Investigating the velocity structure beneath the Southern and Central Atlantic; Implications for evolution of oceanic crust and lithosphere

Thesis submitted for the degree of
Doctor of Philosophy
by

Emily McCarthy
Department of Geology
University of Leicester

2015

Abstract

Presented here is the shear velocity structure of the crust and upper mantle beneath the central and southern Atlantic Ocean from inversion of high resolution group velocity tomography. The path average group velocities from Rayleigh waves were picked using multi filter technique and phase match filtering for 14,000 paths. They were then combined within a tomographic inversion, to obtain the regional variations of velocity structure at a range of short to intermediate periods (14 s - 100 s). These group velocities have depth sensitivities from the surface to approximately 90 km depth, constraining the focus to velocity variations within the crust and mantle lithosphere. Tomographic results highlight short wavelength variations at periods sensitive to shallow depths, implying the possibility for a more complex velocity structure than currently expected for the oceanic region. The results show a clear relationship between increasing group velocities and increasing sea floor age. Group models are then inverted to obtain the shear velocity structure with respect to depth. The shear velocity model highlights slow velocities beneath the ridge, interpreted as the upwelling of asthenosphere between depths between 30 km and 50 km. Models of crustal and lithospheric thickness are extrapolated from the data. These models suggest the evolution of the Atlantic Ocean is more complex than the simple mathematical cooling models. It is suggested that the main control on crustal thickness is tectonic processes associated with the slow spreading rate and not controlled by to the mantle potential temperature. Additionally, results are presented which incorporate 2ψ azimuthal anisotropy in the tomographic inversions. At the longest periods test show that the recovered anisotropy is an artefact of the inversion process, and cannot be interpreted in terms of mantle flow. At the shortest periods there is a possible relationship between the fast direction and the stress field.

Acknowledgements

I would firstly like to thank my supervisors, Dr Stewart Fishwick and Professor Richard England for all their input, discussion and general support over the past 4 years. I would like to thank the Department of Geology and the College of Science and Engineering for funding the PhD without which the project would not have been possible. I would like to acknowledge facilities of the IRIS Data Management System, and specifically the IRIS Data Management Center, which were used for access to waveform and metadata required in this study. The IRIS DMS is funded through the National Science Foundation and specifically the GEO Directorate through the Instrumentation and Facilities Program of the National Science Foundation under Cooperative Agreement EAR-1063471. Thank you also to Dr Pierre Arroucau for allowing the use of the automated code which facilitated the inclusion of more paths in the models.

I would like to thank all the staff in the geology department at the University of Leicester. Especially the clerical and technical staff: Surekha Tailor, Clare Stanga, Kiri Rhodes, Jenna Booth, Dave York, Colin Cunningham and Nick Marsh for some fantastic conversations about rugby. A special mention must go to Gail Andrews who I think was as sick of my questions about the building work as I was with the building work, thank you for all your understanding and help. And thank you to Dr Andrew Myers for all the technical Linux support and answering my stupid questions.

A special mention must go to Dr Valerie Maupin for all her invaluable discussion about group velocity to shear wave inversions and anisotropy, without which my understanding would be much less. Also a big thank you to the staff at SEIS UK, especially Dr Alex Brisborne (Now at BAS) for all his help in the early stage when I was first learning coding and Dr Victoria Lane ("$\$vl$")who is and function in my PERL scripts after all her help when I was learning the language.

Thank you to the British Geophysical Association for hosting the post graduate research in progress conference every year. This has given me opportunities to speak about my work on a friendly platform, gain input from others and spark good discussion. Thank you also to the Elite PhD courses run by the University of Copenhagen for allowing me to attend such an interesting course.

I must acknowledge my support network for the past 4 years. Firstly the PhD community in the department past and present. Many a Friday night in the pub has been needed along with the fantastic banter and conversation at tea break. Especially thank you to my house mate for the last 4 year (and before) Nicola Clark, we've been through a lot but always come out the other side thanks to gin or three! Thank you for everything, you've been a fantastic friend and put up with a lot (especially Sven)! To my office mates, especially Oliver Knevitt and Amy Stephens, with whom a pot of tea, a coffee break and or a meltdown have always been an option, we've got through this last week together! And thank you to Amy for lending the office Jonny as "office dogs body", thank you Jonny for your help this last week. To Rob, Laura, Tom, Sarah, Charlotte, Nyree, Jen, and Geddes, with whom many a night out on the town or a night in with a few geeky board games was spent. I must acknowledge Paul for the enlightenment that you can do inversions using the "inversion button" on the calculator, this really helped after 3 and half years of not realising it was so simple! And also Helena for a little of piece of Britain in my new home in the Netherlands, much tea and cake!

A special thank you must also go to Vincent Perrier who has given me a place to stay in Leicester this past month and shared his scotch collection with me, a new bottle is coming your way! To Claire Pickett who's PhD writing up survival packs has always made my day, you have been a fabulous support on the end of the phone. Without rugby I may not have made it through these past 4 years, thank you to everyone I have played with, Stoneygate Ladies and the University of Leicester. To my coaches Matt Weir and Jonno Arkle who have played me even when I was too busy to make it to training, thank you for letting me get my frustration out on the pitch. A special thank you to my rugby buddy Dr Di who has been a fantastic support with advice and a bottle of wine on hand when ever I've need it. I don't think my Thursday hang over will ever be the same again! And thank you also to all those who have been around but have moved away from Leicester during my Phd, you know who you are.

I would like to thank Sven for being my right arm and for all his love and support during these 4 years. You have been an amazing and I wouldn't trade you for the world! Thank you to my family, my Mum, Dad and Smell Bear for never stopping believing in me, all the proof reading and just being there as you always are.

Finally I would like to dedicate this thesis to my Grandmother
Cecilia Bridget McCarthy
September 24th 1926 - September 30th 2014
who said to me two weeks before I submitted "Don't be too clever, I don't associate with clever people".
May you always keep them entertained behind the pearly gates, I hope you can still get the snooker up there!

Contents

List of Tables

List of Figures

Chapter 1

Introduction

The theory of plate tectonics has remained one of the biggest and most controversial theories in Earth Sciences of the 20th century since its proposal in 1915 and acceptance in the 1950s (Wegener, 1966). It was the South Atlantic Ocean that triggered the debate with a jigsaw-like fit between the two continents, suggesting the two were once joined. Since the widespread acceptance of the theory, studies of plate motions, spreading centres and cooling rates have been numerous, looking at both localised and global problems. Although there are mathematical models which try to explain the evolution of oceanic crust and lithosphere, evolution is not uniform globally and different models fit observed data in different oceanic settings. There is still no one model fits all situation.

The focus of this project has been primarily on the shallow velocity structure beneath the southern and central Atlantic Ocean with the goal of resolving the crustal thickness (Moho depth) and lithospheric thickness to investigate the evolution of the region in comparison to the other oceans.

The Atlantic Ocean is the world's second largest ocean after the Pacific. It has a slow spreading rate along the mid ocean ridge (MOR) in comparison to the Pacific and the Indian Oceans respectfully. The MOR is a high broad topographic feature in the centre of the region (figure 1.1 a). There are twelve ocean islands in the region, most of which are associated with volcanism. Four of these islands lie on or near the ridge. Penedos de São is thought to be linked to a core complex in the Central Atlantic. The

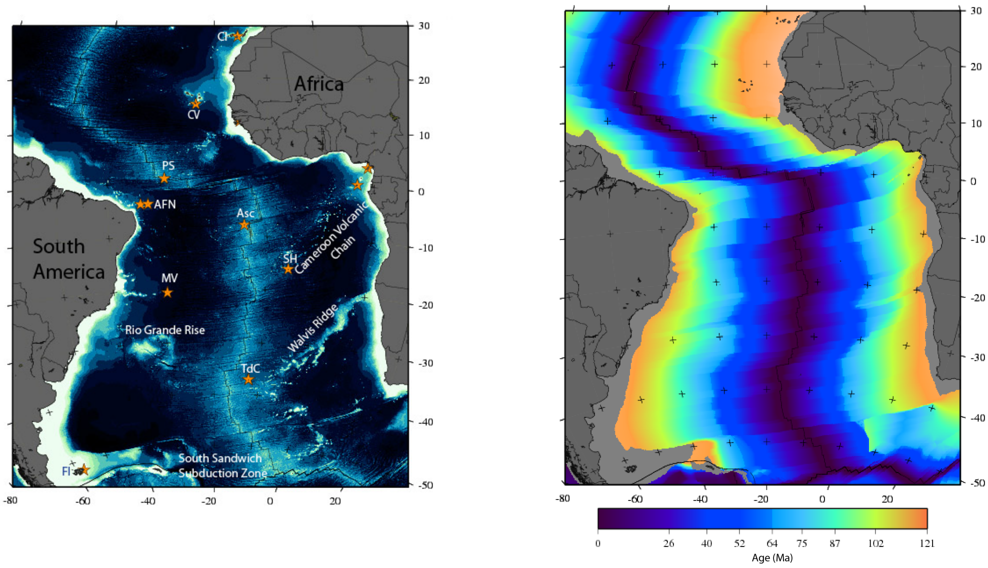

(a) **(b)**

Figure 1.1 (a) Topographic relief of the Southern and Central Atlantic highlighting key topographic features and ocean islands (stars): CI - Canary Islands, CV - Cape Verde Islands, PS - Penedos de São, AFN - Arquipelago de Fernando de Noronha, Asc - Ascension Islands, SH - Saint Helena, MV - Ilhas Martin Vaz, TdC - Tristan da Cunha and FI - Falklands Islands (b) Sea floor age from Müller et al. (2008) model for the Southern and Central Atlantic

three islands (Ascension, St Helena and Tristan da Cunha) along the southern ridge are hotspot islands linked to volcanism from the ridge itself. The Tristan da Cunha hotspot is thought to be the most active and linked to volcanism since the Cretaceous. The Walvis Ridge feature and Rio Grande Rise have both been linked to the hotspot.

Rifting began in the South Atlantic around 150 Ma during the late Cretaceous as part of the break up of Gondwana. Rifting propagated from the south, northwards towards the Central Atlantic. The North Atlantic and South Atlantic joined together in a shearing event which resulted in the formation of the Central Atlantic. The mechanisms related to the rifting vary along the Mid Atlantic Ridge (MAR). To the south of the Walvis Ridge and Rio Grande Rise, magmatic processes are thought to be the driving force causing the breakup. In contrast the central region (north of the Walvis Ridge and Rio Grande Rise) is considered to be amagamatic in the early evolution of rifting (Blaich et al., 2011). These differences should be reflected in the present day structure of the crust and mantle.

Spreading in the Atlantic is thought to have varied little in comparison to other ridges from between 2 cmy^{-1} and 3 cmy^{-1} half spreading rate (Colli et al., 2014; Müller et al., 2008). The age of sea floor is shown in figure 1.1 b. The spreading rate of the Atlantic is considered slow in comparison to the East Pacific Rise and Southeast Indian Ridge which are 15 cmy^{-1} and 5cmy^{-1} respectively.

1.1 Significance of the project

Although the Atlantic Ocean is one of the three largest oceans in the world, the Southern Atlantic region is the least studied out of the Pacific, Indian and Atlantic Oceans. The Pacific Ocean is in the best geological setting for seismic studies, it has an abundance of large earthquakes due to the tectonic setting of subduction in the region, and due to its fast spreading rate it has a abundance of oceanic crust and lithosphere for evolution studies.

A few studies of surface wave inversion and thermodynamic cooling models have been combined in the Pacific region (e.g. Harmon et al., 2009; Maggi et al., 2006a; Ritzwoller et al., 2004) but a study of this kind has not yet been done in the Atlantic. The oceanic lithosphere of the Atlantic is younger than that of the Pacific and therefore, a comparison of the two may further the understanding of the evolution of oceanic lithosphere.

Studies of the Atlantic Ocean have been geodynamic in nature looking at the break up of the margins and the continent - ocean boundaries (e.g. Blaich et al., 2011; Colli et al., 2014; Torsvik et al., 2009). Seismology studies have focused primarily on the North Atlantic looking at the evolution due to the Icelandic plume and the associated velocity structure (e.g. Pilidou et al., 2005). Detailed studies done in the South Atlantic have focused on the deeper structure (50 km - 300 km) using waveform inversion data (e.g. Colli et al., 2013; Heintz et al., 2005; Mocquet & Romanowicz, 1990).

In continental studies, receiver functions are the most commonly used technique to determine depth of the Moho and the base of the lithosphere, however, in oceanic settings the lack of ocean bottom seismometers limits the use of the technique for oceanic crust and lithosphere (Romanowicz, 2009). Surface wave tomography is a technique which has been used in many cases at observing the subsurface of oceanic lithosphere (e.g. Maggi et al., 2006a; Ritzwoller et al., 2004). The use of surface waves reduces the need for an even distribution of seismometers.

Beneath the south east Atlantic Ocean initial tomographic work shows that temperatures at depths greater than 100 km are colder than those predicted by the widely accepted plate model. This suggests that velocity-age relationships are still observed beneath the depth previously predicted by the plate model (Fishwick & Crosby, 2009). This could have implications towards the boundary layer between the conducting lithosphere and the convecting asthenosphere. A more detailed velocity study may help to constrain the velocity structure in the region and the depth associated with the LAB.

The focus of short to intermediate period group velocities (14 s - 100 s) of Rayleigh waves will improve the understanding of shallow lithospheric structure, essential to interpret structures at the base of the lithosphere. Presented here is a shear velocity model for the South and Central Atlantic Ocean from Rayleigh wave group velocities. In bringing together the thermodynamic models and observed data we can try to further understanding of oceanic lithosphere and plate tectonics.

1.2 Project outline

This project is split into four sections, a literature review, group velocity tomography, discussion of shear velocity structure and anisotropic structure. These are brought together in the final chapter and linked to the evolution of the crust and lithosphere of the Central and South Atlantic with a focus on the South Atlantic.

Group velocity path average dispersion curves for 14,000 Rayleigh waves were picked and combined in a tomographic inversion to obtain the group velocity dispersion maps for the Central and South Atlantic. Statistical tests were run on the models to determine the best residual fit to the data and the effects of parametrisation of the inversion on the final model.

The dispersion models were combined and inverted for shear velocity structure beneath the region with respect to depth. Extensive tests were carried out to determine a suitable starting model for the velocity inversion which would, limit the biasfrom the starting model but which would resolved the structure beneath the region.

The group velocity dispersion path average data was also inverted to include the anisotropic component. A series of tests were run to test the parametrisation of the inversion and to determine if the anisotropy recovered was real or a product of the inversion.

The crustal and lithospheric thickness were extrapolated from the shear velocity models. An estimate of mantle potential temperature is also determined for profiles in the South Atlantic from comparison of the half space cooling model to the low velocity zone.

Chapter 2

Background

2.1 The oceanic crust

Oceanic crust is generated by melt from a decompressing asthenosphere rising from depth beneath the mid ocean ridge. It is formed in layers; the upper layer is formed of pillow basalt which cool quickly due to the hydrothermal circulation of sea water. The lower layer is composed of dyke intrusions and banded grabbros which are thought to cool slower from conductivity as they are not reached by the circulating sea water (Morgan & Chen, 1993). Although oceanic crustal formation is thought to be initially uniform, there are many studies looking at the variations in thickness and geochemical composition, which suggests it is not so simple (e.g. Bown & White, 1994; Cannat et al., 1995; McKenzie & Bickle, 1988).

Variations in oceanic crustal thickness tend to be associated with transform faults

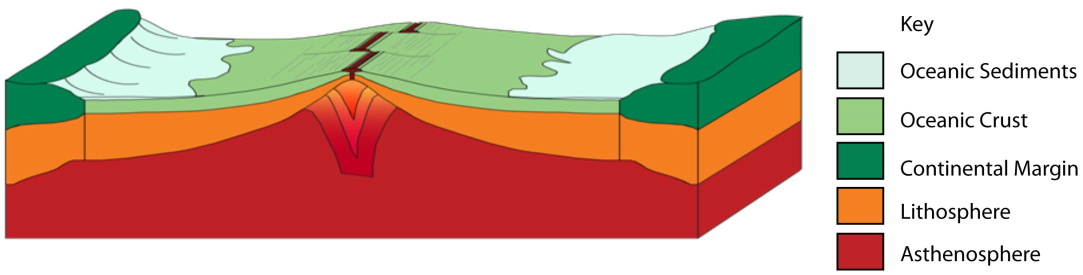

Figure 2.1 Schematic cross section through oceanic crust, lithosphere and asthenosphere with respect to depth showing the generalised structure consistent with geophysical data sets.

(thinner crust) and with hotspots (thicker crust). Hot spots are associated with under plating of magma beneath the crust, which results in anomalously thick crust in the hotspot region. Crust formed along a transform fault is thought to be up to 3 km thinner than crust formed at the centre of the ridge segment. This is thought to be linked to a thicker lithospheric layer beneath the transform faults causing less melt than beneath ridge segments, where the lithospheric thickness is less (Cannat et al., 1995). Slow spreading ridges are observed to have more large transform faults along their length, therefore the thinning of crust beneath these can play a role in the overall thinner average crust (Bown & White, 1994). Crust formed at slower spreading ridges also tends to be thinner due to the depth at which the magma chamber forms and the loss of heat due to conduction at shallow depth (Bown & White, 1994). Both these processes can affect the regional average of crustal thickness.

Variation in mantle potential temperature (T_m) can influence the thickness of oceanic crust. At fast spreading ridges the influence of T_m is greater than seen at slower spreading ridges because the heat loss from conduction being negligible at fast spreading ridges (Bown & White, 1994; McKenzie et al., 2005). Therefore, conductive cooling observed at slow spreading ridges means the melt volume generated is reduced in comparison to fast spreading ridges (Bown & White, 1994). Duncan & Green (1980) show that chemically a second shallower stage of melting is required for basalts observed in ophiolites, which have higher Al_2O_3 and CaO than would be expected from a ultramafic mantle source. They conclude that a second stage of melting, by which depleted lithosphere is incorporated in the melt, could account for these anomalous signatures. Therefore a single magma chamber may not be the case. Imaging of magmatic processes beneath ridges can be more tricky, compared with models based on chemical compositions.

The base of the oceanic crust exhibits a sharp seismic signal due to the significant increase in velocity observed at a sharp boundary from oceanic crust to depleted lithosphere (Brune, 2013). This sharp boundary is the Moho. The Moho was first identified in 1909 by Mohorovicic using refraction seismology and became widely acknowledge in the mid 20 s (White, 1988). It was observed that the continental Moho was at much greater varying depths compared to the oceanic Moho. Exact compositions have been determined for oceanic crust due to sampling from deep ocean drilling programs (e.g. Neo et al., 2009).

2.2 The oceanic lithosphere

The evolution of oceanic lithosphere is thought to be a simpler process than the evolution of continental lithosphere; it is younger than the lithosphere seen beneath most continents and according to some authors could be up to 200 km thinner than in cratonic regions (Fishwick, 2010; McKenzie et al., 2005; Pasyanos, 2010). Whilst the lithosphere beneath oceans is thought to be better understood than that beneath cratonic regions, there are still discrepancies between the data and models. There is general agreement that the thickness of oceanic lithosphere is between 50 km and 100 km on average compared with up to 300 km for continental cratons (Fishwick, 2010; Ritzwoller et al., 2004; Romanowicz, 2009; Zhang & Lay, 1999). Rheologically lithosphere is thought to be weak below the 600 °Cisotherm, which is the region where earthquakes are observed to stop occurring (Anderson, 1995; McKenzie et al., 2005). McKenzie et al. (2005) suggest that the rheological variations between oceanic and continental lithosphere are small. It is agreed that oceanic lithosphere is formed at mid ocean ridges along with oceanic crust. Partial melting and the formation of oceanic crust has depleted the iron content leaving a magnesium rich lithosphere compared with the underlying asthenosphere (Turcotte & Schubert, 2002). The evolution of this mantle and the controls on thickness as it moves away from the ridge axis, however, is still much debated within the literature (Lee et al., 2005; Sleep, 2005).

Many define the lithosphere as the rigid outer layer of the mantle and it is commonly associated with being the conductive tectonic plate floating on convecting mantle below. If we accept that the lithosphere is the rigid upper layer of mantle and crust, we need to compare evidence within the literature as to which properties control the rigid structure. Sleep (2005) favours a thermally controlled evolution defining the lithosphere as the rigid portion of the thermal boundary layer, where heat is transferred purely by conduction. If the lithosphere and its evolution was thermally controlled, as models such as McKenzie (1967); Turcotte & Oxburgh (1967) calculate, the thickness of the lithosphere would be age dependant. In contrast authors (e.g. Jordan, 1975; Lee et al., 2005) suggest the rigid structure is more strongly controlled by the chemical evolution of the lithospheric mantle (see section 2.2.2).

2.2.1 Thermal evolution

Observations of oceanic lithosphere (see section 2.3) indicate there is a relationship between age of lithosphere and geophysical properties. Over the years many models based on a thermally controlled evolution have been published and compared to observed data in the major oceans. Here we discuss the most widely accepted and tested models.

Half space cooling model

The half space cooling model (HSC) was proposed by Turcotte & Oxburgh (1967) to account for the thermal evolution of oceanic lithosphere. The model is simple and uses the idea that lithosphere evolves in a half space where the basal temperature is the geotherm of the mantle potential temperature. It is a very simple mathematical model (see equation 2.1) linking the distance from the ridge (and age of lithosphere) with the depth to the base of the lithosphere based on a fixed mantle potential temperature and thermal coefficient (Turcotte & Schubert, 2002) (figure 2.2).

$$T = T_m \operatorname{erf}\left(1 + \frac{z}{2\sqrt{\kappa t}}\right) \tag{2.1}$$

Where T_m = mantle potential temperature, z = depth, t = time, κ = thermal diffusivity, with an error function erf (Turcotte & Schubert, 2002).

There is no external heat source at the base of the plate modelled in Turcotte & Oxburgh (1967)'s HSC, only the heat produced at the spreading ridge is taken into account (Doin & Fleitout, 1996). The thickness of the plate will therefore, infinitely increase with respect to sea floor age (Forsyth, 1977). The HSC proposed by Turcotte &

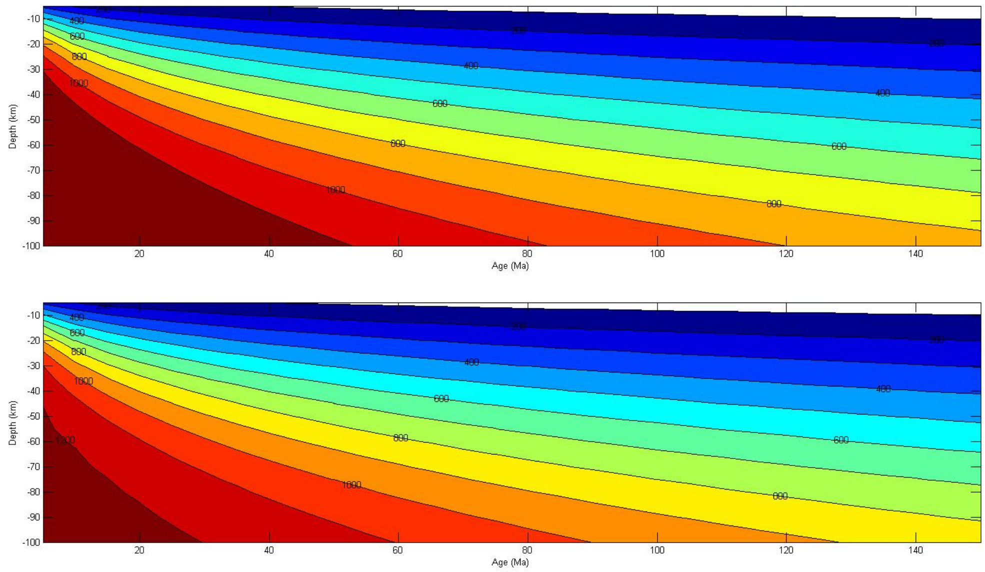

Figure 2.2 Modelled thermal evolution for HSC model (a) equation 2.1 where T_m=1200 °Cand κ = 1x10^{-6} and (b) equation 2.2 where T_m=1200 °CT_s=2 °Cκ = 1x10^{-6} α_T=2.9x10^{-5} and C_p=1350 J Kg^{-1} K^{-1}. Isotherms are plotted at 100 °Cintervals.

Oxburgh (1967) assumes a non adiabatic mantle, however, the mantle is semi adiabatic. Faul & Jackson (2005) proposed a similar model based on equation 2.1, which took into account an adiabatic mantle beneath the rigid slab (Equation 2.2). This means there is an increase in temperature within the mantle from T_m as the convection of the asthenosphere transitions from the conduction of the lithosphere. This increases the number of variables in the model.

$$T = T_s + (T_{ad} - T_s)\ \text{erf}\left(1 + \frac{z}{2\sqrt{\kappa t}}\right) \tag{2.2}$$

Where T_s = Temperature at the Sea floor (2 °C) and T_{ad} = T_m(1+ α_T [gz / c_p]), where g = acceleration due to gravity, α_T = coefficient of thermal expansion, c_p = specific heat at a constant pressure (Faul & Jackson, 2005).

It is agreed by many within the field of thermodynamics and plate cooling that the HSC model is a good fit for the structure and properties of the oceanic lithosphere for ages up to 80 - 100 Ma. However, it is after this age that cooling patterns begin to vary and it is observed that heat flux and topography begin to flatten more than predicted (Faul & Jackson, 2005; Goutorbe, 2010).

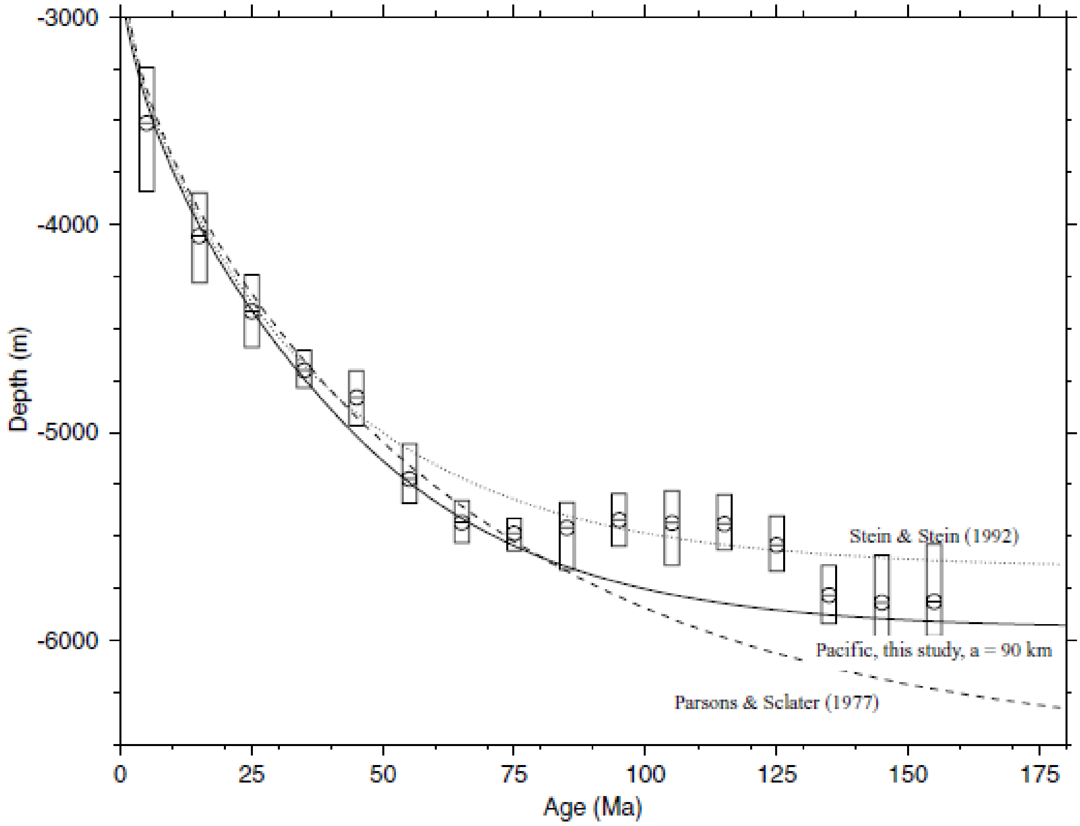

Figure 2.3 Plot taken from (Crosby et al., 2006) showing the varying ocean floor depths with respect to age for the Pacific Ocean, based on different lithospheric thickness's from different data sets.

The plate model

The plate model (PM) was derived by McKenzie (1967) as a cooling slab of finite thickness and has since been developed by many more as a proxy to describe the thermal evolution of the lithosphere (Crosby et al., 2006; Parsons & Sclater, 1977; Stein & Stein, 1992). The basic principle of this model follows a similar cooling pattern to the half space cooling model until about 80Ma where its vertical growth is limited by a finite thickness set within the model (Doin & Fleitout, 1996; Goutorbe, 2010). The evolution of this model has progressed with added data to refine observations (e.g. figure 2.3). The main observable used in these studies is heat flux and observations are discussed further in section 2.4.1. The plate model is a good fit to observed data for both heat flow, ocean depth and topography (up to 120Ma); however, it does not fit seismic observations (Section 2.4.2)(Forsyth, 1977; Goutorbe, 2010; McKenzie et al., 2005).

Other models

Although both the HSC model and PM explain to some extent how oceanic lithosphere evolves, others have attempted to include additional parameters to produce alternative models. Both the half space model and the plate models assume the temperature of the asthenosphere (T_m) is constant from ridge axis along the profile. Lago et al. (1990) looked at subsidence on a regional scale and demonstrated how focused studies show variations from global subsidence models of 50% or more. To account for this T_m must vary along the ridge from 900 °Cto 1450 °C, which is not physically plausible. In response Lago et al. (1990) introduced a second temperature variable into the model; T_r, the temperature of the rising mantle beneath the ridge. T_r is greater than T_m which is the matle away from the ridge section, interacting with the base of the lithosphere away from the ridge. To reasonably fit variations in subsidence the value of T_r only varies by up to 200 °Calong the ridge compared with the previous conclusion of a variation in a single T_m values of 550 °, suggesting it maybe more reasonable assumption.

Doin & Fleitout (1996) introduced the idea of a heat flow across a geotherm, to account for flattening of plates, which is thought to be a result of heat interaction and thermal instabilities at the base of older lithosphere. This model would allow the plate to continue thickening after 80 Ma, but in a different style to the half space cooling model. It produces a better model for thermal structure, however, it only represents the conductive aspect of the geotherm and is likely to require a higher T_m than may be reasonable (Goutorbe, 2010).

As the HSC model fits observed data from oceans as well as the other models up to 80 Ma, it is therefore thought that there are other processes occurring after 80 Ma that affect the flattening of the lithosphere (Ritzwoller et al., 2004). McKenzie (1967) tried to explain this by the plate model, with a finite lithospheric thickness reaching a set basal temperature at around 80 Ma and therefore, beginning to flatten. The flattening may, however, also suggest a reduction in subsidence which may be effected by; convection flow and plumes from the underlying asthenosphere, a new injection of heat or the topography of the sea floor, sea mounts (Ritzwoller et al., 2004). Sediment deposition and distribution are also possible contributors to the subsidence and flattening processes undergone by the oceanic lithosphere, changing the isostatic pressure (Winterbourne et al., 2009). Instabilities at the base of the plate where the transition between convective and conducive cooling occurs, have also been suggested to contribute to the flattening (Ritzwoller et al., 2004).

No model as yet fits every region, as evolution of lithosphere varies significantly, parameters must also vary significantly from region to region (Faul & Jackson, 2005). For the purpose of most studies modelling the lithosphere by the HSC model is a reasonable assumption due to the ratio of 100 km of lithosphere on top of 3000 km of mantle (Korenaga & Korenaga, 2008). There is a question of further complicating a model to fit a data set for example, constraining the thickness of the lithosphere in the plate model. By designing a model to fit the subsidence and heat flow it would expected to fit well because the model was designed to constrain the variations at older ages with the flattening of the heat flow and subsidence data. This must be considered when analysising suitable models.

2.2.2 Chemically controlled evolution

In contrast to a thermal control, others (e.g. Jordan, 1975; Lee et al., 2005) favour a geochemically controlled rigid lithosphere. The lithosphere is thought to be dehydrated and depleted in iron and rare earth elements, therefore, different in rheology to the underlying asthenosphere (Lee et al., 2005). The thickness of a geochemically controlled lithosphere would not be age dependant. Many conclude there is a uniform layer beneath oceans which is the geochemically depleted mechanical boundary layer where conductive cooling occurs and that the age dependant thickening observed is the thermal boundary layer (e.g. Fischer et al., 2010; Lee et al., 2005). The reduction in heat flux and subsidence with respect to age in lithosphere is credited to the effect of convective instabilities within the thermal boundary layer (Lee et al., 2005; Sclater et al., 1981). The base of the thermal boundary layer marks the complete transition within the mantle from cooling by conduction to cooling wholly by convection, with a region of convective instability between the base of the thermal and mechanical boundary layers (Lee et al., 2005).

The question still remains as to the evolution of the chemically depleted mechanical boundary layer. Some propose it evolves with the thermal boundary layer until instabilities occur and then flattens out due to the interaction with the underlying convection and the thermal boundary layer (e.g. Sclater et al., 1981). It is also argued that the chemically controlled, mechanically strong layer is formed at mid ocean ridges at a thickness of up to 100 km during dehydration and depletion of up welling mantle, forming a strong, rigid, uniform thickness layer beneath the ocean (e.g. Lee et al., 2005).

2.3 Asthenosphere

The asthenosphere is defined as the upper mantle beneath the lithosphere, it is characterised by convective cooling and is thought to be mechanically weaker and ductile in comparison to the lithosphere (Hirschmann, 2010; Karato, 2012). Seismological studies which can image beneath the surface, have shown the existence of a low velocity zone (LVZ) at depths which in oceanic studies correlate with the base of the lithosphere. This is approximately 50 km-100 km in oceanic reagions and in continental regions at depths of up to 300 km. The depth and thickness of the LVZ are seen to vary beneath oceans (Anderson, 1995). The LVZ extends to depths beneath the ocean of 200 km, making a 100 km thick layer of slower velocity mantle. In most seismological studies the LVZ is taken to be the base of the lithosphere and the transition into the asthenosphere. The asthenosphere is thought to extend deeper than the LVZ , incorporating the LVZ within it, but the base of the asthenosphere is hard to define (Hirschmann, 2010).

The cause of the LVZ is still much debated within the literature; is it caused by a chemical or phase change, a thermal change to the properties of the mantle or are there melt pockets causing slower velocities in the zone? Hirschmann (2010) shows that melts at depths within the LVZ are thermodynamically stable. Faul & Jackson (2005) conclude that grain size variations may have an effect on the velocity and attributed to the LVZ. If the LVZ is the transition between the plate and the underlying convecting asthenosphere then it would be assumed that a level of shear would occur at the base of the lithosphere. This is suggested to be a cause of the melt pockets (Hirschmann, 2010).

2.4 Observations of ocean crust and lithosphere

2.4.1 Heat flow and Subsidence

As previously discussed in section 2.2 surface observations of heat flow and subsidence are used as observables to map the thickness of the lithosphere. Using heat flow observations Parsons & Sclater (1977) found that the best fit to the plate model was a plate thickness of 125 km and a mantle potential temperature of 1350 °C. This was using data from the northern Pacific and Atlantic for lithospheric ages between 120 Ma and 160 Ma. Stein & Stein (1992) calculated a best fit model with a thinner plate of 95 km and higher mantle potential temperature at 1450 °C. This study used a larger data set, with lithospheric age varying between 50 Ma and 166 Ma. An assumption was made that lithosphere younger than this has a heat flux which is lower than expected due to hydrothermal interaction. Crosby et al. (2006) removed anomalous lithosphere such as hotspots from the study to create a more refined data set. This was done by correlating gravity data and topography to distinguish between age related depths and dynamic depths. It was found that a plate thickness of 90 km gave the best fit to the data in the Pacific and a plate thickness of 100 km gave the best fit the to data in the Atlantic.

2.4.2 Seismic observations

Seismological studies can image to greater depths beneath the surface and image the entire lithosphere - asthenosphere system. If the boundary is purely thermal we would expect to see a gradual change in the velocity structure of the upper mantle. If there is a geochemical and rheological change then the boundary at the base of the lithosphere will be sharper and better defined in the seismic data. Surface wave tomography is the most common study used in oceanic regions due to the sparse distribution of seismometers through out the regions, most being located on the margins of the region on the continents. Surface wave studies solve the problem of sparse unevenly distributed seismometers as different periods sample to different depths due to the wave length of different periods. The average velocity structure along a path or a tomographic inversion of the region can be modelled to interpret the structure. Ocean bottom seismometers would give an even distribution of seismometers for body wave studies but are expensive to deploy and the amount required is not presently feasible for large scale studies. Ocean bottom seismometers are also noisy and would not detect shorter period data reliably (Duennebier & Sutton, 1995).

Surface wave studies are in agreement that there is a high velocity lid above and the LVZ. The thickness of the high velocity lid is seen to increase with respect to age beneath oceanic basins (Romanowicz, 2009). There is, however, no agreement to the exact the thickness of the high velocity lid seen in different studies (Fischer et al., 2010). The LVZ is seen between 50 km and 200 km depths beneath oceanic basins (Romanowicz, 2009) and is there still debate as to it's origin. A systematic increase in group and phase velocity with respect to age of the lithosphere in all oceans is noted in surface wave studies (e.g Ritzwoller et al., 2004; Zhang & Lay, 1999). This would correlate with the hypothesis of a thermal boundary, increasing in thickness away from the ridge.

Surface waves are sensitive to a variety of depths, and group velocities especially are sensitive to the Moho due to the sharp change in velocity at the boundary. This is observed on the dispersion as a steep gradient at periods from 10 s - 25 s depending on the depth of the Moho (Lebedev et al., 2013). Crustal models which are inferred from surface waves alone are highly none unique due to the amount of unknowns. If the shear velocity at the base of the crust and upper mantle is known the depth is easier to constrain. However, as in most cases if the crustal and upper mantle shear velocities are unknown there is a trade off between shear velocity and depth to the Moho as seen in studies by Chave (1979) and Singh (1988). A combined group velocity and waveform inversion study means the velocity structure down to 200 km can easily be constrained imaging the entire lithosphere asthenosphere system. The addition of receiver function data if available can also help to constrain the structure better than surface wave data alone. Individual studies are looked at in greater detail in the following sections.

Path average estimates

Early studies of group velocities were done when seismometers were especially sparse; therefore a single 1-D inversion was often used to infer structure beneath the oceans along a path or series of paths from source to receiver (e.g. Abe, 1972; Singh, 1988; Yoshii, 1975). These studies looked at a range of periods (10 s-120 s).

Singh (1988) focused a study on the Indian ocean and the thickness of oceanic crust beneath ridges. The study was carried out near and along the Ninety-east ridge to determine shear velocity structure both on and off the ridge. Average group velocities were calculated for on and off ridge paths with a standard deviation of 0.04 - 0.08. As a small portion of the paths were continental and continental shelf, a correction was carried out to remove the effect of the continental portion. Singh (2005) revisits the Indian Ocean with some tomographic mapping but also path averages through the regions and 1-D shear velocity inversions. Both these studies conclude that the crustal thickness beneath the Ninety-east ridge is thicker than expected, approximately 22 km, with the suggestion that magmatic under plating is the cause (Singh, 1988, 2005).

Abe (1972) and Yoshii (1975) are examples of early studies where seismic observations were compared to oceanic evolution models. Abe (1972) focused on 25 paths for both Rayleigh and Love waves on tectonically quiet regions of the Pacific Ocean, all paths travelled through the lithosphere west of the East Pacific Rise (EPR). Average group velocities of Rayleigh waves were seen at 40 s to be 4.0 kms^{-1} and at 150 s to be 3.66 kms^{-1} with again low standard deviations of 0.03 on average. The corresponding estimated depths to 150 s is consistent with later estimates of the LVZ observed below the LAB (Romanowicz, 2009). Some paths which crossed the EPR were also discussed in the study. Average velocities for these paths were seen to be 0.15 kms^{-1} slower, interpreted to be the LVZ at shallower depths than below the tectonically quiet region. With the data from this study no best fit model would fit both Rayleigh and Love waves implying a level of anisotropy in the region (Abe, 1972). Yoshii (1975) studied 27 paths from both the east and west of the Pacific ocean. The velocities were split into 4 regions based on age of lithosphere. It was observed that group velocity increased with respect to age. For the Pacific a best fit maximum thickness of lithosphere was 80 km, however, no model could fit velocities from lithosphere younger than 20 My. This is consistent with studies of heat flow and the unstable younger lithosphere due to the hydrothermal interaction close to the ridge axis. The Pacific was the focus of many studies from around this era, all yielding similar results (e.g. Forsyth, 1975; Leeds et al., 1974; Yu & Mitchell, 1979).

One of the earlier surface wave studies in the Southern Atlantic was by Chave (1979) looking at the shear wave velocity structure of the Walvis Ridge. Similar to the Singh (1988) study the paths were divided into on and off ridge, however, only two stations and events were used to get an on and off ridge great circle path, therefore the data is much more limited. A first order observation made on the Walvis Ridge path group velocities is that the velocities up to 40 s are slower than the average of the Pacific. Canas & Mitchell (1981) take a different approach in the Atlantic to group and phase velocities, they look at the attenuation of Rayleigh waves which is also seen to vary with respect to age. They conclude that the attenuation seen in the Atlantic is higher than that seen at the EPR. There is an age dependence observed in the attenuation of waves with and with respect to age. This becomes more notable below 50 km. Souza (1996) look at 3 paths in the region of the south west Atlantic, two which cross sea floor ages of up to 100 km, and one which travels through a region of similar age (100 Ma). A lithospheric thickness of 50 km is concluded from the path average shear velocity inversion and no azimuthal dependence. A study of single path average which cross lithospheric ages would, however, yield an averaged lithospheric lid and show no age dependence. Souza (1996) conclude that surface wave studies can provide valuable information about the lithospheric structure of the Atlantic Ocean.

Tomography

Studies of oceanic lithosphere from seismic tomography data have been carried out on a variety of scales from global to regional (Maggi et al., 2006a; Ritzwoller et al., 2004; Zhang & Lay, 1999). The focus of each study has been slightly different depending on the data set used and the comparisons made.

Zhang & Lay (1999) use tomography from a global data set to model the phase velocities beneath the major oceans and compare the velocity structure. The focus of their study is the deeper structure below 50 km depth. They show a continuous age related increase in velocity in all 3 major oceanic regions, however, the Atlantic presents a much shallower gradient than the Pacific and the Indian Oceans. The average for each ocean is inverted for a velocity structure using an average crustal structure and PREM starting model. The Atlantic Ocean is seen to have much thinner lithosphere at 105 Ma than the Pacific, consistent with Stein & Stein (1992) but inconsistent with Crosby et al. (2006) where the Pacific plate is modelled at 10 km thinner than the Atlantic. The velocity structure inverted for younger lithosphere (5 Ma) is consistent between all oceans in this study. This varies from previous studies where the younger listhosphere was seen to be unstable, which could suggest the resolution of this study cannot detect variations which regional studies can and this conclusion cannot be drawn from this study. They conclude that the rate of lithospheric thickening is different for each ocean which increases to vary with respect to age, therefore, the evolution may be more complex than a single cooling model, controlled by composition, temperature and partial melting in the asthenosphere. Early global studies concluded that the Atlantic appeared to be homogeneous compared with the Pacific Ocean, however, the resolution of global studies does not pick out the finer detail (less than 1000 km) compared with regional studies (e.g. Mocquet & Romanowicz, 1990)

As with single path studies, many tomographic studies have focused on the Pacific Ocean as it is considered a good test laboratory, having a large expanse of lithosphere with a substantial age range. These studies have been done using regional tomography models. Two studies which compare the seismic data to the thermal evolution of the

Pacific plate are Ritzwoller et al. (2004) and Maggi et al. (2006a).

Ritzwoller et al. (2004) invert group velocities of Rayleigh waves and Love waves for 18 s - 200 s and 20 s - 150 s respectively and produce 2 °x 2 °tomographic maps of the region. These are then combined with phase velocities for 40 s - 150 s before inverting the models to produce a 3-D velocity model down to 400 km based on seismic and thermal parametrisation. Average velocities for group and phase velocity dispersion with respect to ages were compared to the half space cooling model (section 2.1). The shear velocity structure as inverted from the 3-D velocity model was also compared to predictions from the half space cooling model. It was observed that to a first degree the half space cooling model fitted the data, except for a flattening in the data at 70 Ma - 100 Ma which was related to a reheating event. Further deviation from the half space cooling prediction with respect to age were concluded to be instabilities at the base of the thermal boundary layer.

Maggi et al. (2006a) use multimode phase velocity data to model the velocity structure beneath the Pacific and compare the results with various plate models. This study does not see a pronounced flattening between 70 Ma and 100 Ma as seen by Ritzwoller et al. (2004), these results agree more with previous studies e.g. Zhang & Lay (1999). They conclude the flattening effect observed by Ritzwoller et al. (2004) could be due to poor path coverage through the region between 60 Ma and 100 Ma due to the uneven distribution of seismometers. The results best fit the half space cooling model compared with heat flow and subsidence data favouring the plate model.

Studies in the Atlantic are more sparse than those in the Pacific. Mocquet & Romanowicz (1990) produced a 3-D velocity model of the Atlantic from long period Rayleigh waves. It was observed that there was no age correlation between group or phase velocity in the north Atlantic (north of 35 °N). Further south (35 °N to 0 °) a weak correlation between the phase velocity was observed but not the group velocities. This observation was seen to reverse south of the equator with a correlation with sea floor age and group velocity but no correlation with phase velocities. This was thought to be an effect of steep velocity gradient, a result of the slow spreading rate.

Silveira et al. (1998) and Silveira & Stutzmann (2002) modelled the isotropic structure beneath the North and South Atlantic using Rayleigh (and additional) Love wave phase velocities. The path coverage for these studies is sparse in the South Atlantic. Hotspots are picked out as region of negative S-wave velocity down to 200 km. Overall the South Atlantic corresponds to slower velocities than the North Atlantic (Silveira et al., 1998). The negative S-wave velocity anomaly associated with the ridge is observed to depths of 150 km in the North Atlantic and 300 km in the South Atlantic suggesting a deeper asthenospheric source in the South Atlantic. This is suggested to be associated with the presence of hotspots along the South Atlantic ridge (Silveira & Stutzmann, 2002). Neither study correlates the velocity structure to lithospheric thickness or evolution.

Colli et al. (2013) is the most recent and detailed study of the South Atlantic Ocean. The study concludes that a lithospheric structure is resolved to a depth of 150 km where the signature is lost. An anomalously slow region is imaged beneath the Mid Atlantic Ridge but also to the west and the east in regions which correspond to the Rio Grande Rise and Walvis Ridge. The resolution of the model is too poor to confidently constrain lithospheric depth and the boundaries of the LVZ. They do suggest the asthenosphere is thin and dynamic beneath the South Atlantic, being kept hot and buoyant by the influx of hot material from hot spots located in the region.

Shear wave inversions of group velocities

Studies of crustal structure require group velocity data to constrain the upper 50 km. For group velocity studies a secondary inversion is required to obtain the velocity structure with respect to depth unlike phase velocity studies where waveform inversion is done before the tomography, therefore, the tomography is obtained directly for depth not period. Inverting the group velocity data extracted from the tomography adds another level of parametrisation and uncertainty to the model.

Regions of inter-continental and oceanic geology have also been studied for their shear velocity structure. Acton et al. (2010) focus the study on the Indian continent but also invert group velocities for the Indian Ocean. The starting model is AK135 upper mantle velocity and fixed layer thicknesses and no crustal layer to avoid biasing the final model. Due to the smoothing effects of the longer periods no sharp Moho boundary was resolved. The 4.1 km^{-}s contour is taken as the Moho, which sees a 15 km average thickness for the Indian Ocean crust. In this study the thickness seen in the continental regions correlates with receiver function studies done in the region. No receiver function studies were done in the oceanic region of the study to correlate the thickness predicted in the model.

Tang & Zheng (2013) studied the South China Sea and the surrounding region. They use a linearised inversion and each model was iterated 30 times from the starting model. The starting model was a single model inverted from the regional average dispersion with layer thicknesses of 10 km above 100 km and 20 km below. In this study the 4.0 km^{-}s contour was taken as the Moho and the LAB depth was the greatest negative gradient above the LVZ. Neither of these studies include a water layer in the starting model, which would influence the shape of the dispersion curves and the fit to the model. This would suggest a greater error in the inversion for both these studies to confidently be able to resolve the depth to the Moho beneath the oceanic region. The choice of velocity contour for the Moho has an affect on the final interpretation and also adds to the error of interpreation. The constraint in the continental region of reciever functions, however, draws back some error on the continent but not in the oceanic regions where the velocity for the Moho may differ.

Di Luccio & Pasyanos (2007) studied the Mediterranean region and include a water layer in the model. They use a starting model of Crust 2.0 with an IASP91 mantle, alternating inverting for thickness and velocity during iterations with a fixed Vp/Vs ratios. The inversions in this study were done using Rayleigh and Love waves to constrain the final model. The fit to the Rayleigh waves at short periods is not great. The result of the inversions sees thicker sediment and crustal layers than the starting Crust 2.0 model. The study also compares what the group velocities predicted by Crust 2.0 are and how the resulting maps vary from the tomography.

Anisotropy

Most seismic studies are done assuming the earth is isotropic, however, the earth can be anisotropic and it is often observed that anisotropic models have better fit to the data (Trampert & Woodhouse, 2003). Anisotropy within the earth can be seen on a range of scales and caused by a variety of geological features. Anisotropy can be observed in seismic studies using a multitude of techniques. Anisotropy is widely agreed to be caused by a preferred orientation in shape or lattice on a mineralogical scale, for example the preferred orientation of olivine (LPO) in a flow is the fast direction in the direction of a flow. Anisotropy observed in the asthenosphere beneath both oceans and continents is thought to show the flow direction. It can also be a frozen snap shot of a paleo flow in the lithosphere. In oceanic crustal studies anisotropy is thought to be induced by the alignment of minerals in a stress field or by cracks, faults and fissures in the upper crust.

Studies of radial anisotropy detect a region between 80 km and 220 km depths, displaying faster horizontal shear component (S_H) values than vertical shear component (S_V) values beneath the Pacific. This depth does not vary beneath the ocean, implying a uniform thickness of 80 km for oceanic lithosphere (Nettles & Dziewonski, 2008). This scale of radial anisotropy is thought to be unique to the Pacific ocean as the Atlantic and the Indian Oceans exhibit radial anisotropy similar to the Primary Reference Earth Model (PREM)(Ekström & Dziewonski, 1998). Azimuthal anisotropy can also be mapped on a regional to global scale using anisotropic tomographic inversion. Anisotropic tomography has more free parameters in than isotropic tomography.

Crustal studies of anisotropy have tended to be on a very regional scale and close to the ridge or on young oceanic crust (less than 10 Ma). Tong et al. (2004) and Dunn & Toomey (2001) have studied the EPR. Both observe anisotropy in the upper crust aligned parallel (or within a few degrees) of the ridge axis. This anisotropy is not observed at depths below 500 m to 2 km. The anisotropy is thought to be due to hydrothermal venting along the fractures and fissures caused during divergent boundary processes.

Nowacki et al. (2012) look at shear wave splitting along mid ocean ridges to determine the direction of LPO along the ridge. Coverage of data in the Atlantic is poor due to the lack of events of good magnitude. The time difference between the two arrivals is seen to decrease as distance from the ridge axis increases. Many of the events occur along transform faults not ridge segments and therefore results show a correlation between spreading direction and direction of movement of the fault. Blackman & Kendall (2002) suggest that ridge parallel anisotropy is associated with slow spreading ridge due to a concentration of material near the ridge axis in contrast to fast spreading ridges where no variation in orientation is seen on and off ridge.

Maggi et al. (2006b) and Lévěque et al. (1998) look at anisotropy in the Pacific and Indian Oceans respectively. Maggi et al. (2006b) observe a strong correlation of azimuthal anisotropy in the lithosphere with paleo flow direction based on sea floor ages. Anisotropy in the asthenosphere is correlated with present flow direction with a fast direction perpendicular to the ridge axis. Lévěque et al. (1998) do not observe a confident correlation with plate motion and azimuthal anisotropy in the top 100 km, but some regions correlate with paleo flow. Below 100 km there is a correlation observed between plate motion and azimuthal anisotropy before it is lost below 200 km and no anisotropy is observed.

Silveira et al. (1998) and Silveira & Stutzmann (2002) model anisotropy in the Atlantic Ocean. A rotation of azimuthal anisotropy which is not directly ridge perpendicular is observed in the region, azimuthal anisotropy in the South Atlantic is aligned NE-SW in the west and aligned more N-S in the east. This cannot be explained by plate motion and flow direction alone.

Other methods

In contrast to surface wave studies, combined surface wave and multiples of S waves (e.g. SS, SSS, SSSS) inversions support evidence of a none age dependant lithosphere, with a thicker high velocity lid beneath the Philippine Sea (40 Ma) than the Pacific Ocean (140 Ma) (Gaherty et al., 1999). Gaherty et al. (1999) supports a lithosphere which does not thicken away from the ridge as seen in tomographic studies. Gaherty et al. (1999) refer to the boundary between the LVZ and the high velocity lid as sharp, not gradual, implying a geochemical not a thermal boundary.

Receiver function studies (Sp and Ps) are less common in oceanic regions due to the distribution of seismometers. Sp and Ps conversions both require a sharp boundary, usually associated with geochemical change e.g. the Moho. Rychert & Shearer (2009) published a study based on data from stations on ocean islands and continental regions. This study yielded no age dependence on oceanic or continental lithosphere. Kawakatsu et al. (2009) used borehole receivers in the North West Pacific; this study did yield an age dependence of lithospheric thickness. This questions the evolution of lithosphere beneath ocean islands, which have been effected by volcanism associated with the interaction of mantle plumes (Fischer et al., 2010). Both studies suggest a sharp lithospheric boundary, implying some geochemical change.

Hirschmann (2010) suggest that the boundary between the lithosphere and the LVZ is not uniform and in regions where there is a sharp transition observed some melt maybe present but in other regions where no sharp boundary is observed a thermally diffusive transition may be present. The nature of the boundary although studied in depth is not conclusive due to the sparse distribution of studies and the limitation of some studies such as receiver functions in ocean regions.

Chapter 3

Group velocity tomography

3.1 Surface waves and group velocities

Surface waves are characterised by the motion of energy travelling near the surface from an event in a 2 dimensional direction along the surface. They form by the constructive and destructive interactions of body wave multiples (PPP, PPPP, SSS, SSSS etc.) at a free surface (Shearer, 2009; Stein & Wysession, 2008). There are two types of surface waves; Love waves and Rayleigh waves. Love waves are simply the multiples of the horizontally polarised S wave (S_H), these waves constructively interfere and the shear direction is perpendicular to the direction of propagation along the horizontal (figure 3.1). Rayleigh waves are more complicated being produced from the interactions of P wave multiples and the vertically polarised S wave (S_V) at the free surface, not just constructive interference. The two coupled motions (up - down and forward - backward) result in a retrograde elliptical motion in the direction of propagation (figure 3.1). Due to the construction of both wave types the amplitude of the energy decays exponentially with respect to depth from the free surface (Lay & Wallace, 1995; Shearer, 2009).

Group velocities are the packets of energy associated with the surface wave. Each surface wave is composed of individual harmonic components of the energy known as phases. Each phase travels at its own frequency dependant velocity. These harmonics interfere with each other to create packets of energy; the envelopes of energy within

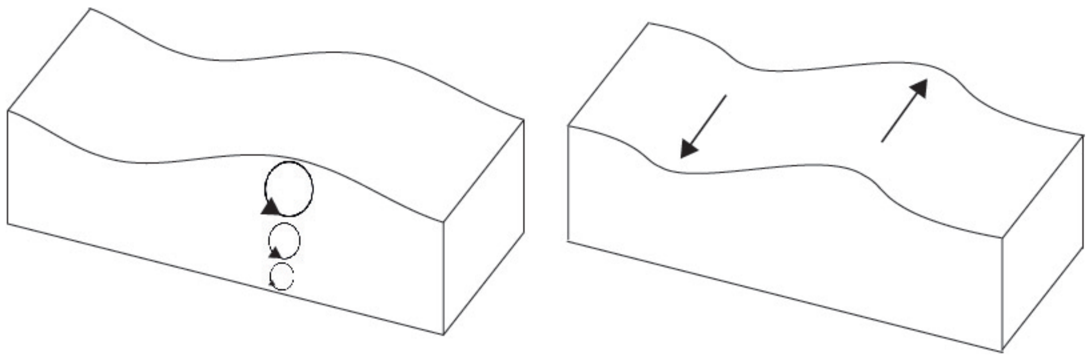

Figure 3.1 Schematic diagram showing the ground motion of Rayleigh waves (Left) and Love waves (Right)

which the phases travel. The velocity of the constructive wave packets is the group velocity which is also frequency dependant. This velocity varies due to the properties or the medium it is travelling through and the phases constructing it (Lay & Wallace, 1995). The energy packets can be seen on the seismogram as the high amplitude arrival spread out over a couple of seconds (Stein & Wysession, 2008). This signal can be broken down using filters for individual frequencies to determine the velocity of the energy packets.

Unlike body waves, surface wave arrivals are not sharp but spread out over a period of time (Stein & Wysession, 2008). The arrivals are spread out due to the varying depths each frequency within the wave is sensitive to and its corresponding velocity, this is known as the dispersion of the wave. The path average dispersion of a surface wave is a reflection of the average velocity gradient with respect to depth. The dispersion of a surface wave varies continuously along its path due to the variations in the medium it travels through and the variations in velocity gradient (for example continental to oceanic transitions). The depth of penetration for each frequency is due to both the wavelength of the energy and also the velocity gradient. As a consequence of this, the period does not directly relate to a single depth but is sensitive to the whole range the wave samples. The lower the frequency the greater the spectrum of depth the wave samples. Each wave packet is sensitive to all velocities from the surface down to the deepest point of penetration with a peak in sensitivity at a specific depth (figure 3.2).

The normal model for velocity structure in the earth is that velocity increases with respect to depth. The dispersion characteristics of this simple velocity model would

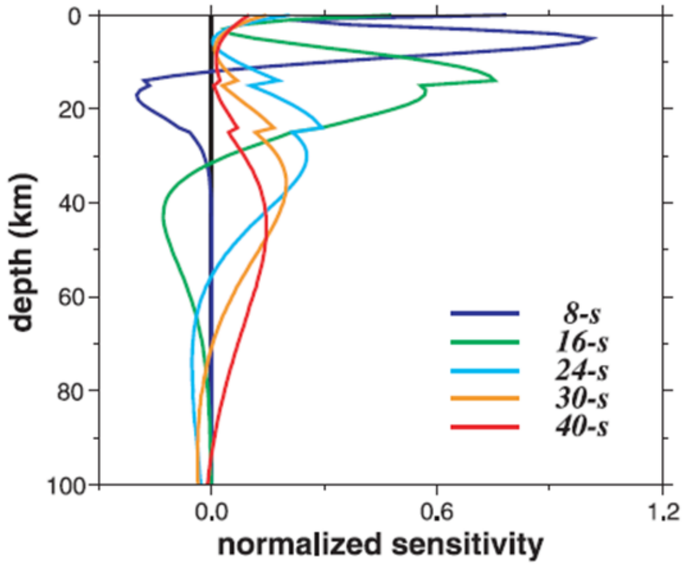

Figure 3.2 Example of sensitivity kernels from Moschetti et al. (2007) highlighting the range of depths which each period can be sensitive to.

see the lower frequency surface waves arriving before the higher frequencies. However, the characteristics of surface waves travelling along paths through predominantly oceanic and continental lithosphere are significantly different, up to periods around 80 s - 100 s where the signatures of oceanic and continental lithosphere are lost to the underlying asthenosphere (Figure 3.3). The Moho can be picked out by a steep gradient at short periods, for oceanic regions this is observed at shorter periods than for continental regions due to the thickness of the respective crusts. There is a decrease in velocity around at 50 s -70 s which is interpreted as the transition from the high velocity lithosphere to the low velocity zone observed at the base of the lithosphere and the top of the asthenosphere, this is not as sharp as the Moho transition. The characteristics of group velocity dispersion can also be uncertain due to the complexities along the great circle paths on which they propagate (Canas & Mitchell, 1981).

Group velocity studies have been used for many years to infer lithospheric structure for both oceanic and continental settings. Group velocity analysis is simpler than phase velocity analysis, due to the uncertainties which can arise with phase velocity analysis which are considered negligible in many group velocity studies (Abe, 1972; Singh, 1988). The initial phase from the source, known as the source phase, is an ex-

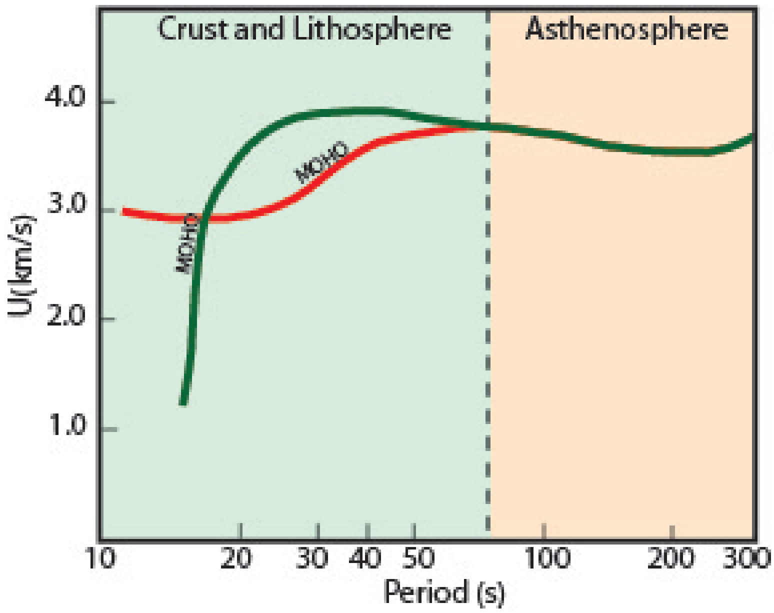

Figure 3.3 Average dispersion curve examples; showing the general characteristics for oceanic (green) and continental (red) paths highlighting the sensitivity to the Earth structure (redrawn from Lay & Wallace (1995))

citation function carried by surface waves due to the convolution of the strain tensor around the source mechanism. There are a variety of factors which can affect the source phase of the signal produced at the source; the depth of the event, the frequency, the source mechanism and the structure of the medium the source originated in. Levshin et al. (1999) studied the effects of the source phase on group velocities from Rayleigh waves where they concluded the effects on periods less than 75 s and from sources at depths of less than 25 km were negligible. The depth error on the source also had significant effects on the correction to the group velocity. They also concluded that a greater path density can reduce the perturbations in tomographic models to 1% compared with 5% in regions with sparser path coverage.

3.1.1 Measuring group velocity dispersion curves

The group velocity dispersion curve is most commonly plotted as a contoured plot of amplitude as a function of period and velocity, and therefore spans both the frequency and the time domains. There are many techniques used to acquire the group velocity dispersion curves for example, moving window analysis and the multi-filter technique

(MFT) (Dziewonski et al., 1969). These techniques have been developed as surface wave analysis has developed.

MFT produces a greater resolution than the moving window analysis by using Fourier transforms. It combines a narrow Gaussian band pass filter about each period with a Fourier transform to calculate the amplitude with respect to period and velocity. The plot, an example of which is shown in figure 3.4 is easy to interpret; plotting thin columns of amplitude associated with each period against velocity. The peaks in amplitude are interpreted as the group velocities at each period, the highest amplitude in general corresponds to the fundamental mode, with higher modes being picked out by lower amplitudes if the energy was significant enough to produce multiple modes (Dziewonski et al., 1969).

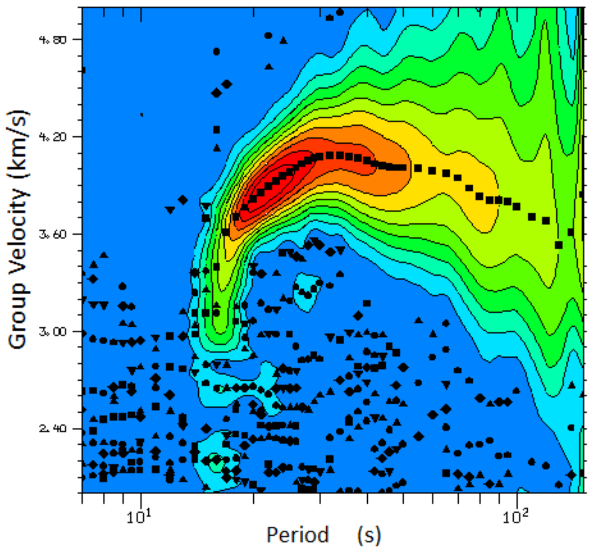

Figure 3.4 Example dispersion curve plotted using the MFT technique.

There are limitations to MFT. The resolution of the plot is controlled by the value alpha (α), which controls the width of the band pass filter used in the Fourier transform. The value of α is increased with respect to the length of the path. As α is increased the resolution in the time domain (velocity) is increased, this causes the resolution in the frequency domain to decrease (Dziewonski et al., 1969). Due to the change in the time domain from the increase in α, the dispersion curve can shift towards low frequencies (Shapiro & Singh, 1999).

A secondary process which can be applied to dispersion curves is a phase match filter (PMF), which was designed to refine group velocities of normal modes by removing the effect of the phase distortions in the signal (Herrin & Goforth, 1977; Russell et al., 1988). It estimates the phase spectrum by reversing the MFT process, and extracts estimated group delays from the dispersion curve, resulting in a refined dispersion curve (Danesi & Morelli, 2000). This process is done completely within the frequency domain (Russell et al., 1988).

MFT is a widely used method and is often combined with a PMF (e.g. Acton et al., 2010; Danesi & Morelli, 2000). By combining MFT with PMF, PMF corrects the bias produced by the spectral amplitude in MFT plots (Wang et al., 2006). PMF also has the advantage of removing multi path signals because it focuses on the individual signals and not the whole spectrum at once (Herrin & Goforth, 1977). The period range of group velocity curves varies with studies dependant on the focus of the study and the noise within the data sets (e.g. Acton et al., 2010; Danesi & Morelli, 2000; Singh, 2005).

3.2 Data

3.2.1 Acquisition

Vertical component seismograms were obtained for paths travelling through the central and southern Atlantic for events occurring between 2000 and 2012. All the data were requested through the IRIS (Incorporated Research Institution for Seismology) database. All permanent station data from the global seismic network (GSN) for the 13 years was processed for stations located around the edges of the region; Africa, South America, the Caribbean and southern Europe, and for ocean island stations within the region e.g. St Helena, Ascension and Tristan da Cunha (Figure 3.5). The stations were chosen so as to limit the portion of path which travelled through the continental regions as much as possible. Due to the distribution of stations and the need for the best path coverage, this was not always possible. There have been a number of temporary arrays set up in the region over the past 20 years, and some of these were incorporated into the data set to enhance path coverage within the region. On the east side; the Cape Verde array (Lodge & Helffrich, 2006), the Cameroon array (Tibi et al., 2005) and the Namibian array (GEOFON, Potsdam) were used. In the west of the region, there have been a number of stations set up as part of the Brazilian lithosphere project (Feng et al., 2004; James et al., 1993). Stations from this project were selected for their location along the coast of Brazil. The Antarctic and Patagonian array (Wiens, 1998) and two arrays in the southern Andes, the SIEMBRA array (Gans et al., 2011) and one in the Aisen region (Miller et al., 2005) were also added to the data set. A few stations further in land were required to optimise the path coverage on both sides of the region.

Figure 3.5 Map showing the distribution of all events (yellow circles) and stations (red triangles) used in the study. Temporary arrays are labelled

The majority of events were from the mid ocean ridge and therefore are shallow sources where only the fundamental mode is induced with enough amplitude to be recorded reliably. Events greater than magnitude 5 from the two subduction zones in the region (Caribbean and South Sandwich islands) were also processed for the 13 years. Figure 3.5 shows the distribution of stations and events across the region. Data acquisition was carried out first by year (starting with 2007) but as the path coverage for the model built up with the addition of new paths, data was acquired based on where there was the most sparse coverage. Temporary arrays and individual stations were requested last based on where path coverage was sparse. For example, the path coverage in the west of the region was more sparse than the east, so the addition of more stations from the Brazilian lithosphere project were introduced along with stations in the southern Andes to try and address the imbalance of path coverage.

3.2.2 Pre-processing

Processing the data was done in a number of steps to prepare it for picking the dispersion curves. Each data request was done through a breakfast request and the data was downloaded in seed format. The SAC file for each path and the station response file (RESP) were converted from the seed files using the program rdseed and the following processing steps were carried out. Scripts were written to automate the processing of the seismograms. A total of 70,423 paths were requested and run through steps 1-4. A list o=of the stations and events which passed step 3 and were therefore included in the models are in Appendicies A and B respectively.

Step 1 was to decimate the sampling rate. The original sampling rate of each file (samples per second) varies depending on the instrument it was recorded on and for the original purpose it was collected. Each sampling rate was decimated so that the final sampling rate of each path was 1 sample per second. This reduces the size of the file for future processing stages and makes the data more manageable.

Step 2 was to ensure the information for each event was in the SAC header information for each path. The information is taken from the Centroid Moment Tensor (CMT) catalogue of events (Dziewonski et al., 1981; Ekström et al., 2012). The magnitude, depth, latitude and longitude were input directly from the catalogue and the distance from the events to the station was calculated before being input. The search for events was done by script for a region -80 to 50 longitude and 50 to -60 latitude. The code does not input information for an event if there is another event in the region within the time period of 2 minutes; this is due to the interference of energy between the two events. These seismograms are left with no header information. Some seismograms obtained did not correlate with information in the CMT catalogue and therefore are also left with no header information. After this step all seismograms with no header information were removed from the data set.

Step 3 was the most important step for deciding which paths were to be included in the rest of the processing and which were not. To minimise the error in picking the dispersion for each path and improve the quality of the data, the signal (the Rayleigh wave portion) to noise (background recording) ratio must not be too low. The higher the ratio the lower the noise error carried into the tomographic models. To calculate the signal to noise ratio, the amplitude of the signal for the Rayleigh wave portion of the seismogram, filtered between 20 s and 40 s, was divided by the amplitude of the 'noise' section, taken from a suitable time after the signal would be expected (this was based on an average velocity and the distance the energy travelled). By taking the noise from within the signal after the peak amplitude, the direct influence of the noise on the signal is considered. Figure 3.6 gives an example of a good signal to noise seismogram where the signal to noise is 6.68 from an event recorded at Namibian station CAPN on 29/03/1998. All seismograms with a signal to noise ratio greater than 3 were passed to the next step.

Figure 3.7 shows the ratio of paths which passed the signal to noise test to those which did not. This step did not, however, remove all poor signals and some curves were un-pickable in MFT, under closer inspection these tended to be incomplete seismograms. Because the amount of data contained in the file, the signal was not coherent

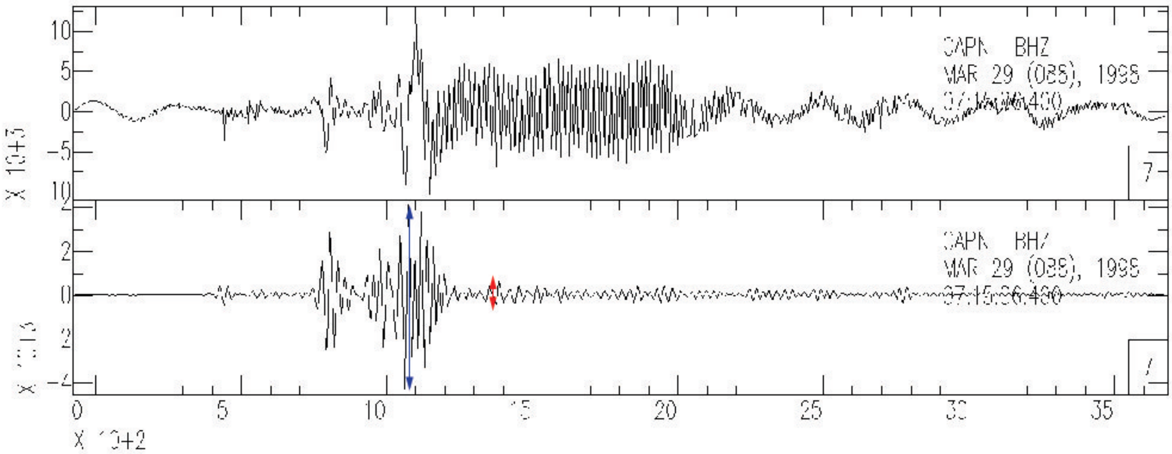

Figure 3.6 Example if signal to noise ration on seismogram (top) shows the raw seismogram data (bottom) the same seismogram bandpass filtered between 20 s and 40 s to focus energy arriving between the periods.The signal (blue) is divided by the noise (red) to obtain the ratio

and although it passed the signal to noise test, the signal was not of the whole event, meaning the data was un-pickable. A step to remove the seismograms less than 1 megabyte was introduced to limit bad signals in step 4.

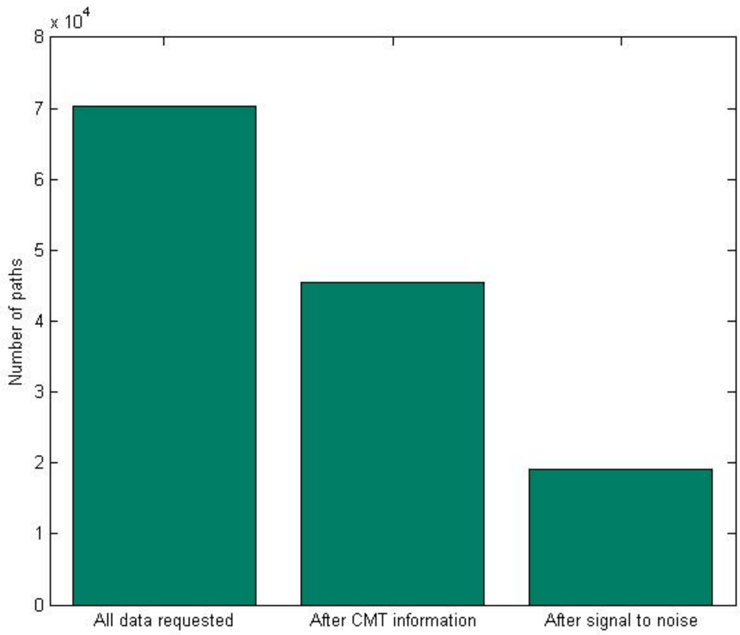

Figure 3.7 Bar graph of reduction in data quantity during processing steps

Step 4 was to remove the response of the instrument from the seismogram. Each instrument has a different and unique response which effects the seismogram and must be removed before the data can be used. This was done using the RESP file for each station and the built in SAC function TRANSFER. TRANSFER removes the instrument response alongside filtering the data through a band pass filter. A number of tests were carried out on the filter parameters for this step. Both wide and narrow band pass filters were tested. It was decided a wide filter was better due to less distortion of the signal. Originally in tests the filter was settled to be $f^1 = 0.005$ $f^2 = 0.01$ $f^3 = 0.25$ $f^4 = 0.5$ (Figure 3.8) but it was later expanded due to distortion of longer periods to $f^1 = 0.002$ $f^2 = 0.004$ $f^3 = 0.25$ $f^4 = 0.5$. f^4 was chosen to be the Nyquist frequency to avoid aliasing the signal. After the instrument response is removed, the seismogram shows the ground displacement as a result of the motion from the wave.

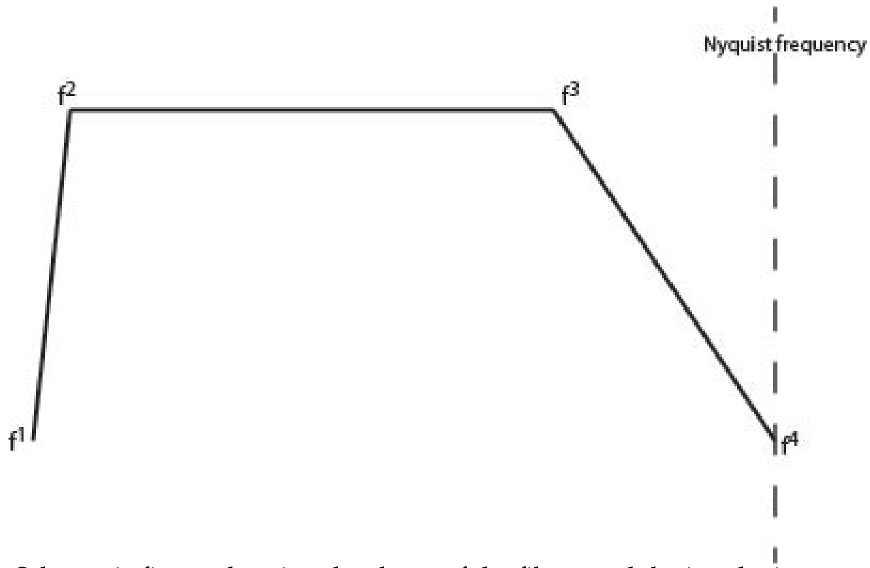

Figure 3.8 Schematic figure showing the shape of the filter used during the instrument response

3.3 Group velocity dispersion curves

The filtering process used to obtain the group velocity dispersion curves is detailed in section 3.1.1, which combines MFT and PMF techniques. 7,502 paths were picked using the open source programs MFT96 and PMF96 from computer programs in seismology (Herrmann & Ammon, 2002). A further 9,534 paths were processed using an automated code (Arroucau et al., 2010).

3.3.1 Do_MFT

DO_MFT is a user friendly program which allows the user to pick group velocities from visual MFT and PMF plots using two sub-programs MFT96 and PMF96. The program allows the user to input certain values and change the plot area for each individual path as discussed below.

Information already in the SAC header file such as the distance, event and station co-ordinates are extracted automatically by the program. The α value must be manually set based on the path length. As explained in section 3.1.1, α controls the width of the band pass filter and is increased relative to the distance travelled to maintain resolution. In DO_MFT there are 3 α value options (table 3.1). These options were interpreted as: for distances of distances of 1500-3900 km an α value of 50 was set, for distances of 3901-7000 km an α, value of 100 was set and for distances greater than 7001 km an α, value of 200 was set. The units of measurement are also required to be manually input in order to calculate the units of the group velocities. All the seismograms used in this study had units of nano metres (nm). The program also required the input of wave type (Rayleigh or Love) before picking the dispersion curve.

Table 3.1 Alpha Values for Group velocity DO_MFT picking

Distance	Alpha
2000	50
4000	100
8000	200

The advantages of DO_MFT are that every path is seen by the picker and any strange or anomalous paths can be looked at in more detail. Paths which have passed the signal to noise ratio test but have too much noise or a scrambled signal can be rejected immediately; the majority of these were subsequently removed by an additional step in the pre-processing of removing all seismograms with a file size less than 1 megabyte. Noise in seismograms was confined to short periods (<10 s) and longer periods (>80 s). This often caused complications in picking the data on the standard plot scale and the shorter and or longer periods were removed from the plot to focus on the coherent portion of the signal (10 s - 80 s). An example of a dispersion curve with poor signal is shown in 3.9. The shorter periods are most likely due to the interference with oceanic waves interacting with the continental margins. The amplitude peaks at shorter periods were not confined to one individual signal but many and made picking tricky at times, with a level of interpretation of the plot. At the longer periods the width of the signal increases and the amplitude contours widen causing more errors. In some cases amplitudes were too high and the coherent signal was again lost at the longer periods. In these cases only the intermediate periods could be picked (20 s - 80 s).

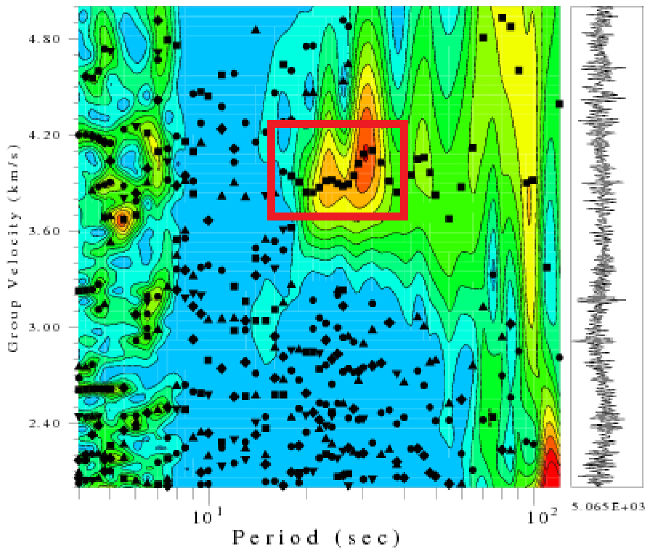

Figure 3.9 Example of noise on MFT plot, example take from an event recorded at station on Tristan da Cunha (TRIS). The red box highlights the coherant signal which would be picked from this path.

Some paths which did not have a bad signal were still noted to be anomalous, for example a higher than average velocity. During the picking of the group velocity dispersion curves a typical velocity range became apparent. Most dispersion curves began around 2.8 kms^{-1} for the shortest periods (<10 s), with a peak at 4 kms^{-1} for intermediate periods (30-50 s) and between 3.6 kms^{-1} and 3.8 kms^{-1} at longer periods (50-100 s). Therefore when a curve was consistently higher or lower than the average velocity it was noted. This may be an indication of a fast or slow velocity region, an anomalously fast or slow recording station or interference between energy from events close together. So other paths travelling through a similar region and to the same station and or from the same event were compared to see if a reason could be found. Discussed here are some examples which were looked at:

Examples:

Anomalously high velocity:

During early stages of processing an event occurring on 05/06/2005 from the South Sandwich islands which was recorded at the Namibian TSUM was noted to be anomalously fast (4.3129 kms^{-1} at 30 s). Comparing this path to another path from the same year (which travelled a similar but not the same great circle) recorded at the same station we see there is a variation of 0.4 kms^{-1} between the two paths. Figure 3.10 shows the two dispersion curves and compares the two paths to the dispersion map for 30 s from all presently picked paths (7,000 paths). We can see the two paths are very similar in the region they traverse and there are no anomalously high velocity zones associated with the faster path (the most northern path). With no reason to remove the path, the path will remain in the data set, it does not effect the tomography and cause a high anomaly.

Anomalously slow velocity:

An event recorded on 22/06/2006 at stations in the Cameroon array (CM) was noted to be consistently anomalously slow. It was plotted against other paths travelling similar great circle paths to the same stations and was noted to still be slow (Figure 3.11). Other stations (and subsequently paths through different regions) recording this event also resulted in slower than expected dispersion curves. On further investigation it was noted that there was a second event which occurred 3 minutes after the event in a similar region of the Mid Atlantic Ridge. With the events being so close in time and geographical location the event should be removed from the data set as the interference of the two events causes too much uncertainty.

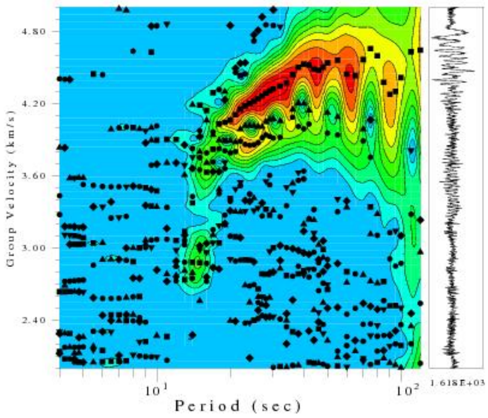

(a)

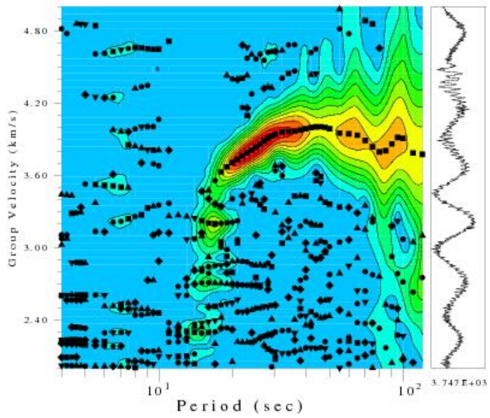

(b)

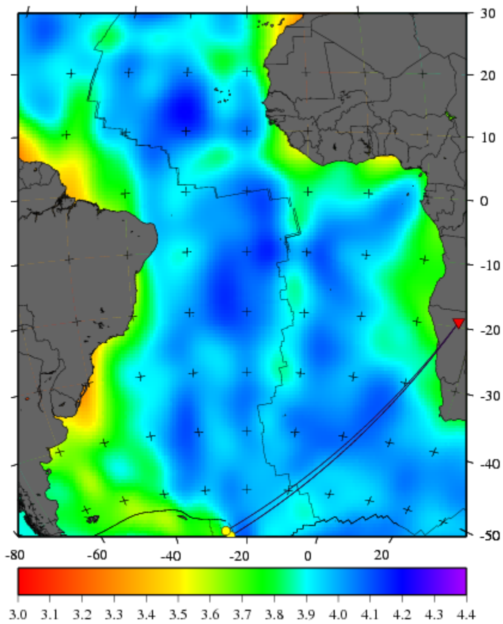

(c)

Figure 3.10 Comparison of dispersion curves for paths from events (a) 05/06/2005 (b) 15/06/2005 to the station TSUM through (c) the tomography for MFT96 picked paths only; the tomography model from when the paths were added

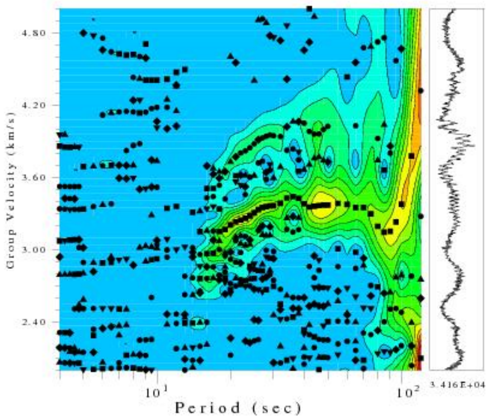

(a)

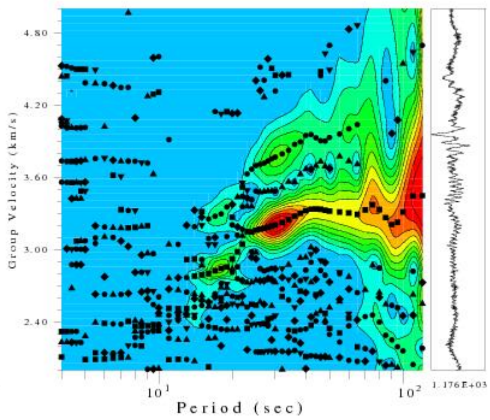

(b) e

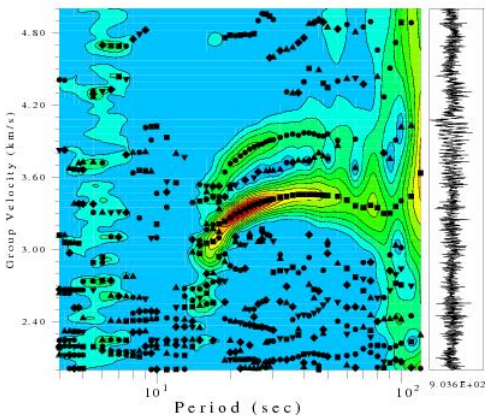

(c)

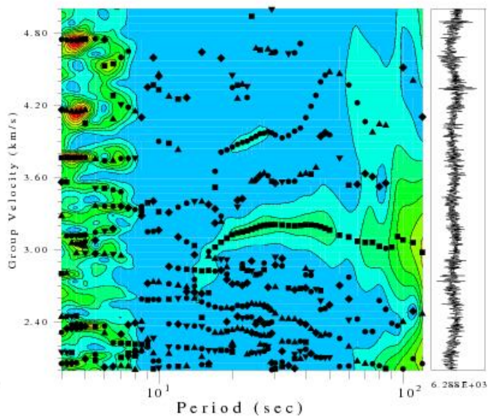

(d)

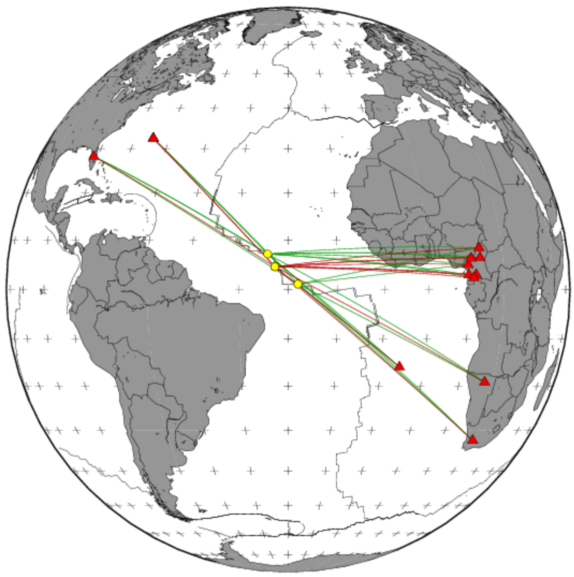

(e)

Figure 3.11 Examples of anomalously slow velocity on dispersion curves for paths travelling from event on 22/06/2006 recorded at (a) CM02, (b) CM23, (c) TSUM and (d) SHEL highlighting two arrivals of energy where the higher amplitude energy is the slower velocity. (e) map showing comparison of great circle paths for slow event and other events from the same region (04/03/2006 and 27/03/2006); the slow paths from event 22/06/2006 are plotted in red and the paths deemed more normal velocities from the other events are plotted in green.

Observations of dispersion curves:

Although most paths followed the same general shape with a peak in the intermediate periods (around 40 - 50 s) it was observed that in some dispersion plots the greatest velocity was at 30 s, with a kink in the dispersion curve around this period. This was noted on a few seismograms of which some examples have been given in Figure 3.12. To see if there was any possible explanation the paths were plotted on the current tomography for 30 s (figure 3.12). Two paths intersect but there is a third unconnected path which does not travel through the same region. The common factor in all three paths is that they cross the mid ocean ridge. An increase in velocity at 30 s is not easy to explain based on the current observations, there is not an anomalous region of high velocity and the mid ocean ridge is seen to be least defined in the 30 s dispersion compared with periods shorter (high velocity region) and longer (low velocity region). There are also no topographic features which correlate with the paths investigated, other than the mid ocean ridge. These paths remained in the data set. It may be a feature on paths travelling through the central Atlantic intersecting the mid ocean ridge.

3.3.2 Automated code

In January 2013 the automated code from Arroucau et al. (2010) was used to pick the group velocities for 2000 to 2004 and 2008 to 2012 along with the temporary arrays. The two main advantages between Do_MFT and the automated code is the acceleration in picking the data; the automated code speeds up the dispersion curve process by 375 %, and the greater variations in α value (table 3.2). A further 8,000 paths were picked using the automated code and combined with the MFT96 picked data to produce final tomography models (section 3.4).

Before the code could be used to continue picking data for this study a comparison of the two programs was required to ensure consistency of the data. The most recent data acquisition at this time was the Namibian array and was therefore used as a test of the MFT96 dispersion data obtained manually against the automated code, to ensure

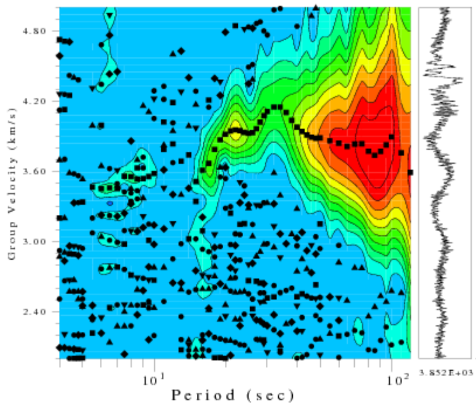

(a)

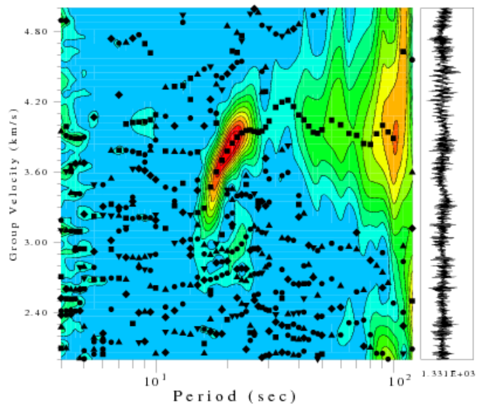

(b)

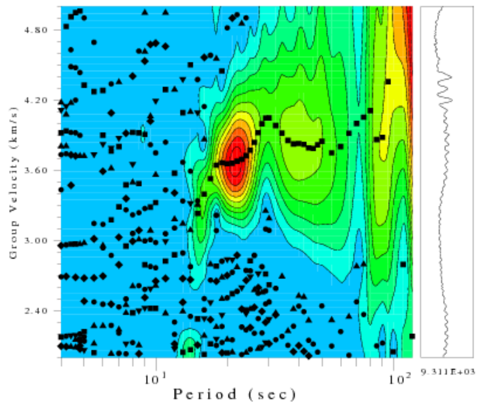

(c)

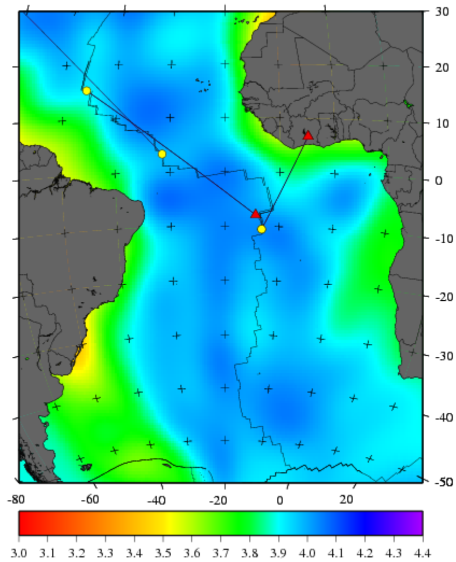

(d)

Figure 3.12 Examples of dispersion curves with unusual shape for events recorded at (a) a station on the Ascension Islands on 11/12/2005 (b) a station in Florida on 19/11/2005 (c) a station in Côte d'Ivoire on 20/02/2006 (d) tomographic model for events between 2005 and 2007 only with paths mapped for events a-c

the consistency of the data.

Comparison study - Namibian array

The Namibian data for 1998 along with a few paths from previously picked data were run through the automated code and the Namibian data was picked using MFT96 for selected events. The examples discussed here are all paths which require an α value of

Table 3.2 Alpha Values for Group velocity automated code

Distance	Alpha
2000	50
3000	75
4000	100
5000	125
6000	150
7000	175
8000	200
9000	225

100 in MFT96 (3900 - 5000 km). Figure 3.13 compares the dispersion plots for a single path recorded on 29/03/1998. The difference between the two plots is the MFT96 plot shows all amplitude peaks for each period, where as the automated plot show the peaks for the amplitudes which have been picked by the code. This does highlight the number of possibilities for picking, especially at shorter periods, increasing the level of error in picking at these periods. The amplitude is also shown to be different between the two plots, this may be due to the filters applied by the different codes.

Figure 3.14 shows a direct comparison of the picked dispersion for both the MFT96 picks and the automated code. There is variability between the picks, where some points correlate better than others. It appears the greatest variability is at the long periods where the dispersion becomes more sinusoidal. Figure 3.15 shows the distribution of the difference between MFT96 pick and the automated pick. The distribution of difference looks normal. However, if the distribution is broken down for each period, this becomes irregular. Figure 3.15 also shows the variability of the difference for each period. There is, as observed from the plots in figure 3.14 greater difference at longer periods but also at periods less than 20 s. This difference at shorter periods was solved by taking all MFT96 picked periods below 20 s and re picking them through the automated code. On MFT96 plots periods shorter than 20 s were harder to pick due to the suspected ocean swell noise.

As seen in table 3.2 the automated code allows for a greater variation of α than was possible using the MFT96 program. A second test was run to determine how much

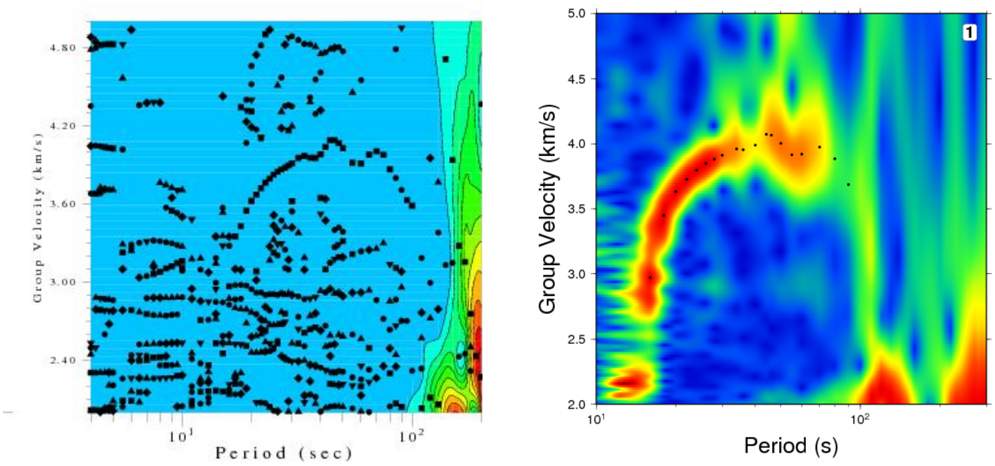

(a) **(b)**

Figure 3.13 Comparison of dispersion plots for event on 29/03/1998 recorded at station WATN plotted using (a) MFT96 and (b) the automated code

variation can be seen in the dispersion curve for 5000 km and 6000 km long paths which were picked using MFT96 with an α value of 100 and picked using the automated code using an α value of 125 and 150 respectively. Having the greater variety in α value would be more accurate as the width of the bandpass filter will be more suited to each path length, as long as it did not effect the consistency in the data. The paths recorded at TSUM on 12/06/2005 and on 06/09/2005 have a path distance of 5516 km and 6137 km respectively. These were picked using the automated code with the corresponding α values to see how much variation there would be from the curves picked using the α value of 100 (as used in MFT96 picks).

It can be seen from figure 3.16 there is less than a 0.04 kms^{-1}) (1%) variation in velocity from an α value of 100 and and α value of 125 for this event. Similarly in figure 3.17 a maximum variation of 1.5% can be seen when the α value is increased from 100 to 150. By having a greater range of α values, this will hopefully enable more accurate results without compromising the consistency of the data. Allowing the α value to change on a more regular basis should tailor the band pass window for each distance better than seen when using MFT96.

Figure 3.18 shows that the differences in velocity at short to intermediate periods (<60 s) are controlled by variations in α, changing the value of α has a greater control on the values than which method is used to pick (auto or MFT96). Where as at

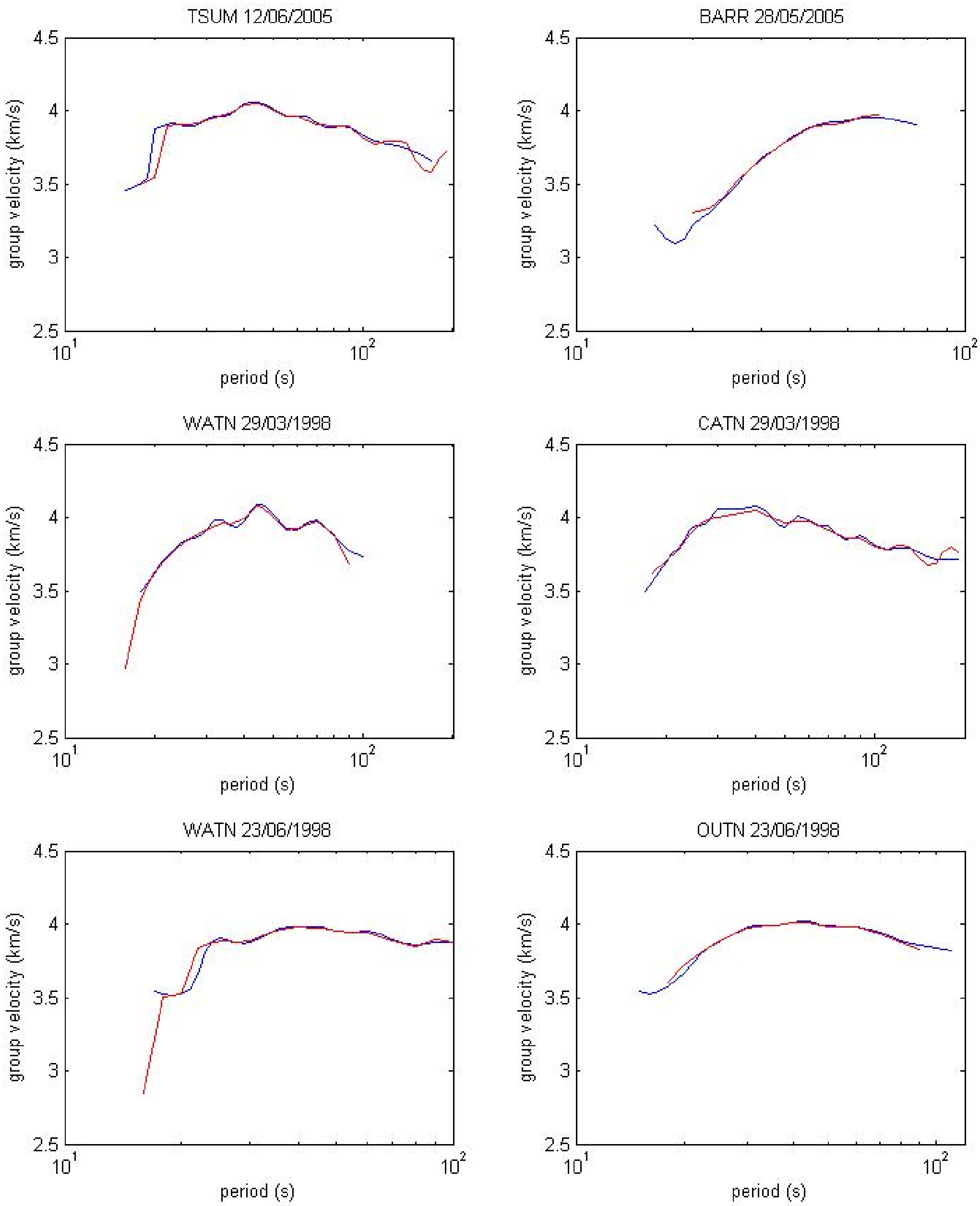

Figure 3.14 Example of comparison dispersion picks between MFT96 (blue) and Automated code (red). The station where the energy for each event was recorded along with the date of the event is plotted above the plot.

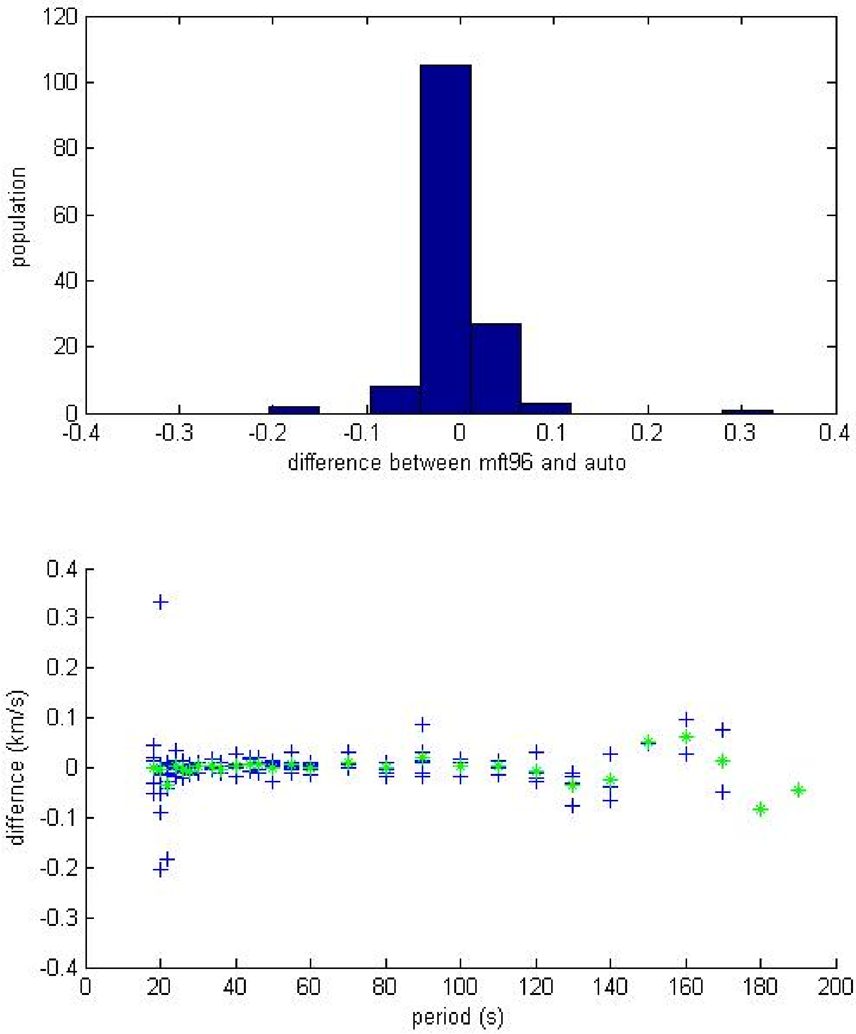

Figure 3.15 (Top) histogram showing the distribution of difference between MFT96 and automated code (Bottom) the difference for individual paths with respect to each period (blue) compared to the average difference for each period(green)

longer periods (>60 s) it is the different method which primarily controls the velocity variations. This suggests there is a trade off between consistency at shorter periods and the accuracy of picking the data using the most appropriate α value for the band pass filter. The variation in values is $\pm$ 0.02 kms^{-1} for periods less than 120 s. This is approximately 1.25 % of the average velocity at the shortest periods (<20 s) and 1 % of the velocity at intermediate periods (>20 s). Based on this study earlier variations between paths travelling through similar regions are as great as 0.9 kms^{-1} which is a

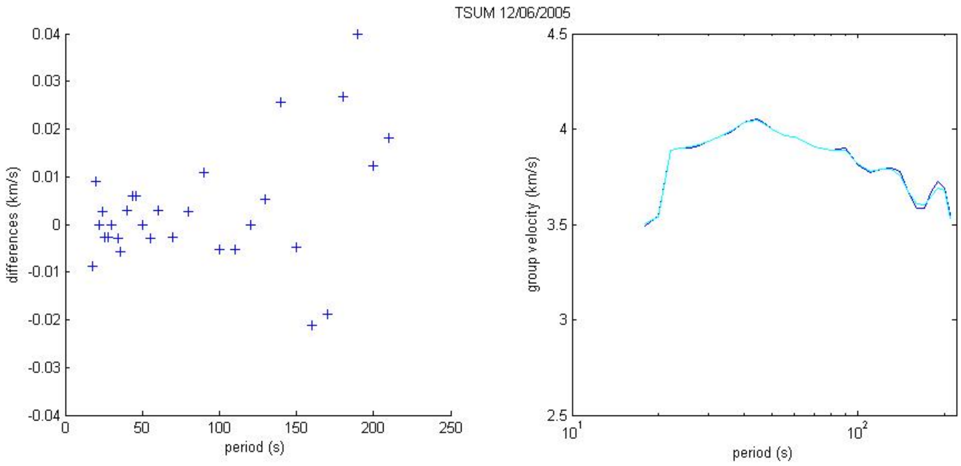

Figure 3.16 Comparison of velocity from picks with the automated code for a path with a length of 5516 km for different α values of 100 (dark blue) and 125 (light blue)

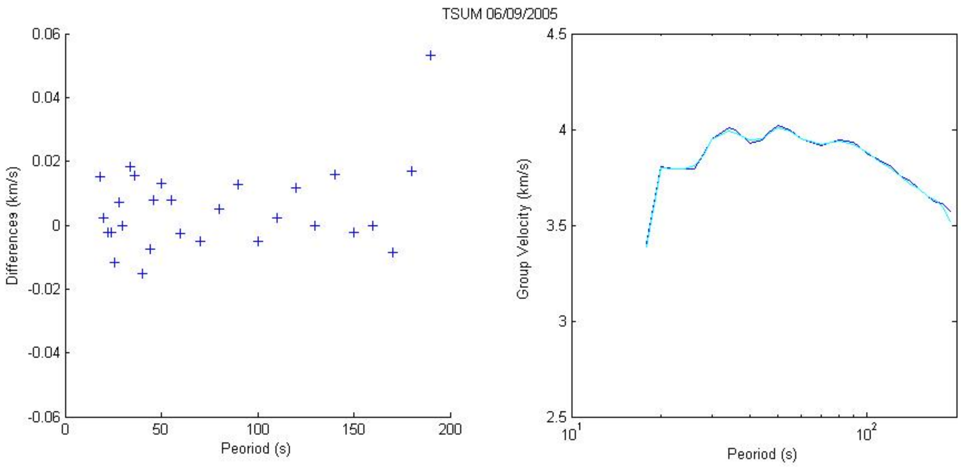

Figure 3.17 Comparison of velocity from picks with the automated code for a path with a length of 6137 km for different α values of 100 (dark blue)and 150 (light blue)

23 % variation in velocity. A velocity variation of 1% related to a more accurate band pass filter for the distance of the path seems reasonable compared with much greater regional variations in the data. The remaining data was picked using the automated code and an α value related to the path distance.

3.4 Tomographic models

Equation 3.1 shows Hooke's Law and the linear relationship between stress (σ) and strain (e) of a medium through the elastic moduli tensor (c). The elastic moduli tensor

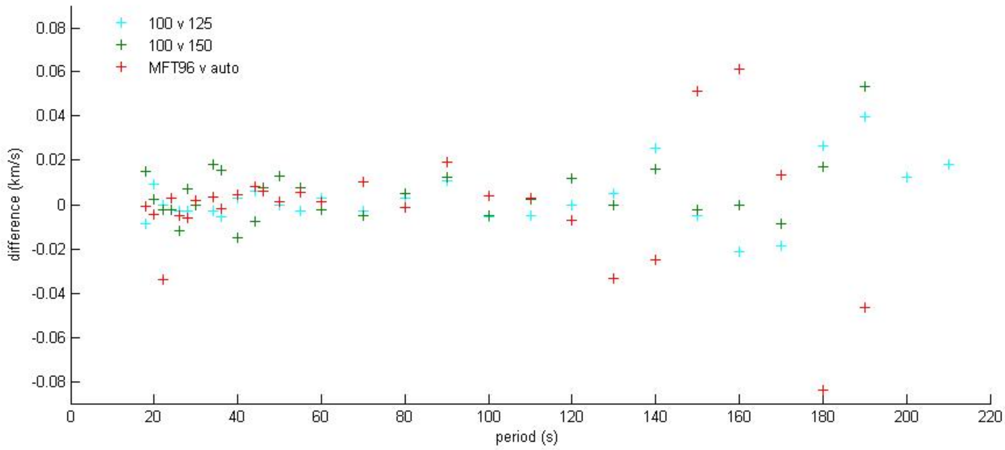

Figure 3.18 Comparison of differences in velocity between varying the α value and between MFT_96 and the automated code.

can be up to 81 terms independent for an anisotropic medium but is reduced to 2 (λ and μ) when the medium is assumed to be isotropic. Thus the inversion for an isotropic inversion is reduced to two unknown elastic constants in the elastic moduli tensor.

$$\sigma_{ij} = c_{ijkl}e_{kl} \tag{3.1}$$

The elastic moduli tensor (c) can be written as a matrix C_{mn} with 21 independent terms where m and n represent the combinations of the indices terms i, j k and l. Equation 3.2 shows the symmetric matrix associated with a isotropic medium. Any medium with more than 2 independent elastic constants is considered anisotropic.

$$c_{mn} = \begin{pmatrix} \lambda + 2\mu & \lambda & \lambda & 0 & 0 & 0 \\ \lambda & \lambda + 2\mu & \lambda & 0 & 0 & 0 \\ \lambda & \lambda & \lambda + 2\mu & 0 & 0 & 0 \\ 0 & 0 & 0 & \mu & 0 & 0 \\ 0 & 0 & 0 & 0 & \mu & 0 \\ 0 & 0 & 0 & 0 & 0 & \mu \end{pmatrix} \tag{3.2}$$

The path average velocity data from the dispersion curves discussed in section 3.3 were combined and inverted using an isotropic tomographic inversion code (Fishwick et al., 2008) to recover the velocity structure of the southern and central Atlantic with respect to period. Equation 3.3 shows the formula used for the weighted, damped least squares inversion as used by the code. The code takes a predetermined starting model (m) and inverts it for perturbations in velocity within the region, based on individual paths from the data (d) (Fishwick et al., 2008). The inversion builds up the perturbations and recalculates the models for each path. A single path travelling at a slower velocity than the model would be assigned a slower velocity to fit the path residual to the data, which would be spread out over the path length within the recalculated model. If more slower velocity paths were added to the region, the slow velocity region in the model would be more focused with in the region to best fit all paths and less spread out along the initial slow velocity path. The resulting model (ω(m)) maps these pertubations for the given region.

$$\omega(m) = (d - G_m)^T W_d(m)(d - G_m) + \epsilon^2 m^T m \tag{3.3}$$

The more paths within the model the better the perturbations within the model can be resolved. The model region can be split into smaller regions to resolve more detailed velocity structure. The tomographic code uses a continuous spline function with evenly spaced points or nodes to recover the structure. The spacing of the nodes has a direct relationship to the resolution of recoverable structure. A smaller node spacing would recover finer details in velocity structure, however, the smaller the node spacing the greater the influence noise has with in the data and can lead to non-unique solutions. A larger node or spline spacing eliminates the bias from the noise due to the larger amount of data contributing to the structure for each node. The trade off between resolution and reliability depends on the amount of data and the regularity of the spatial distribution of the path coverage (Bodin & Sambridge, 2009). The number of paths in the model can also affect the choice of node spacing, in regions of sparse path coverage smearing along paths can be seen which mask the true perturbations in the model.

The inversion was done for the region between 64 °N, 54 °E, 80 °S and 90 °W. This region was chosen to incorporate all the data and to ensure that no paths, stations or events were outside the region. The code assumes that the path travelled from source to receiver is a great circle. Each path was allocated a weighting (W_d) based on the errors in picking the dispersion curve, the amplitude width and the noise levels; poorer data was allocated a lower weighting and therefore would have less influence on the final model. The weighting allocated ranged from 0.01 (best data) to 0.09 (worst data). The outputted error for the two picking methods were different and therefore, a correlation between the two methods (MFT96 and the automated code) was done. A linear relationship was found which allowed the weighting values to be assigned.

The damping parameter is ϵ. If $\epsilon = 0$ the model is the best fit solution, however, in most inversions due to parametrisation and uncertainties there is no complete solution and the damping parameter has to be subjectively chosen as a trade off between the data fit and the plausibility of the model. A higher ϵ value or over damped model minimises the under determined part of the solution but not the misfit to the data. A low or under damped model minimises the misfit to the data but the solution remains under determined. These models are displayed on a trade off curve, which would ideally be an 'L' shape with the best solution being the corner of the curve. Most trade off curves resemble a hockey stick or backwards 'J' shape where there are a few solutions possible, the picking of a solution is therefore done on an individual basis for each inversion run.

The tomographic models were inverted from a homogeneous starting model of an average velocity for each period. Dispersion maps were produced for the following periods; 14 s, 16 s, 18 s, 20 s, 22 s, 24 s, 26 s, 28 s, 30 s, 34 s, 36 s, 40 s, 44 s, 46 s, 50 s, 60 s, 70 s , 80 s, 90 s and 100 s.

3.4.1 Initial inversions

Model progression

Along side picking dispersion curves the tomographic code was run on a regular basis to produce dispersion maps for periods 20 s, 30 s, 50 s and 70 s. This was to ensure the code was working and the models seemed reasonable and to track the improvement of the models. As more data are incorporated into the inversion, this changes the resolution of the outputted model by increasing the path coverage and also of individual regions, where a large influx of paths is added to that region (for example, the Cameroon Array). Figures 3.19 to 3.22 shows 4 steps of evolution for these models from the first inversion (2007 data only) to the combined model from final inversion with all the picked dispersion curves (MFT_96) and the automated code. These test runs were inverted at 6 °spline spacing to focus on the broadest structures in the region. The path coverage for the first few inversion runs were not sufficient to support a smaller spline spacing.

In figure 3.19 we see sensitivity to shallow structure, seeing a clear contrast between the oceanic and continental regions. There is very little change between the first two models (a and b). Model c looks very different to a and b due to a greater resolution in the southern region. The damping parameters selected for this model were most likely less than what had been selected for a and b; the contrast in the intensity of the model velocities from a and b is less. This may also be due to the variations in path coverage between models b and c. By model d we see a clear definition of the ridge as the path coverage is better. The ridge here is defined as a high velocity region, highlighting the contrast in the topography of the ridge compared with the surrounding sediment covered basins.

For 30 s in figure 3.20 we see a less clearly defined contrast between ocean and continent in model a. Between model a and model b one of the most noticeable changes is the high velocity region associated with the Cameroon volcanic line, the resolution in this region is altered by the influx of data from stations deployed as part of the 2005 and 2006 Cameroon array. The definition between the ocean and continent is also becoming more pronounced. This definition increases into model c where the ocean basin and continental shelf regions are being defined alongside cratonic signatures. There is, in contrast to figure 3.19 no ridge defined in the model. Model d sees less change from model c implying the data set is robust and the region is well defined with more data not affecting the overall model. There are small regions such as the slow velocity associated with the Walvis Ridge which have changed between the two models.

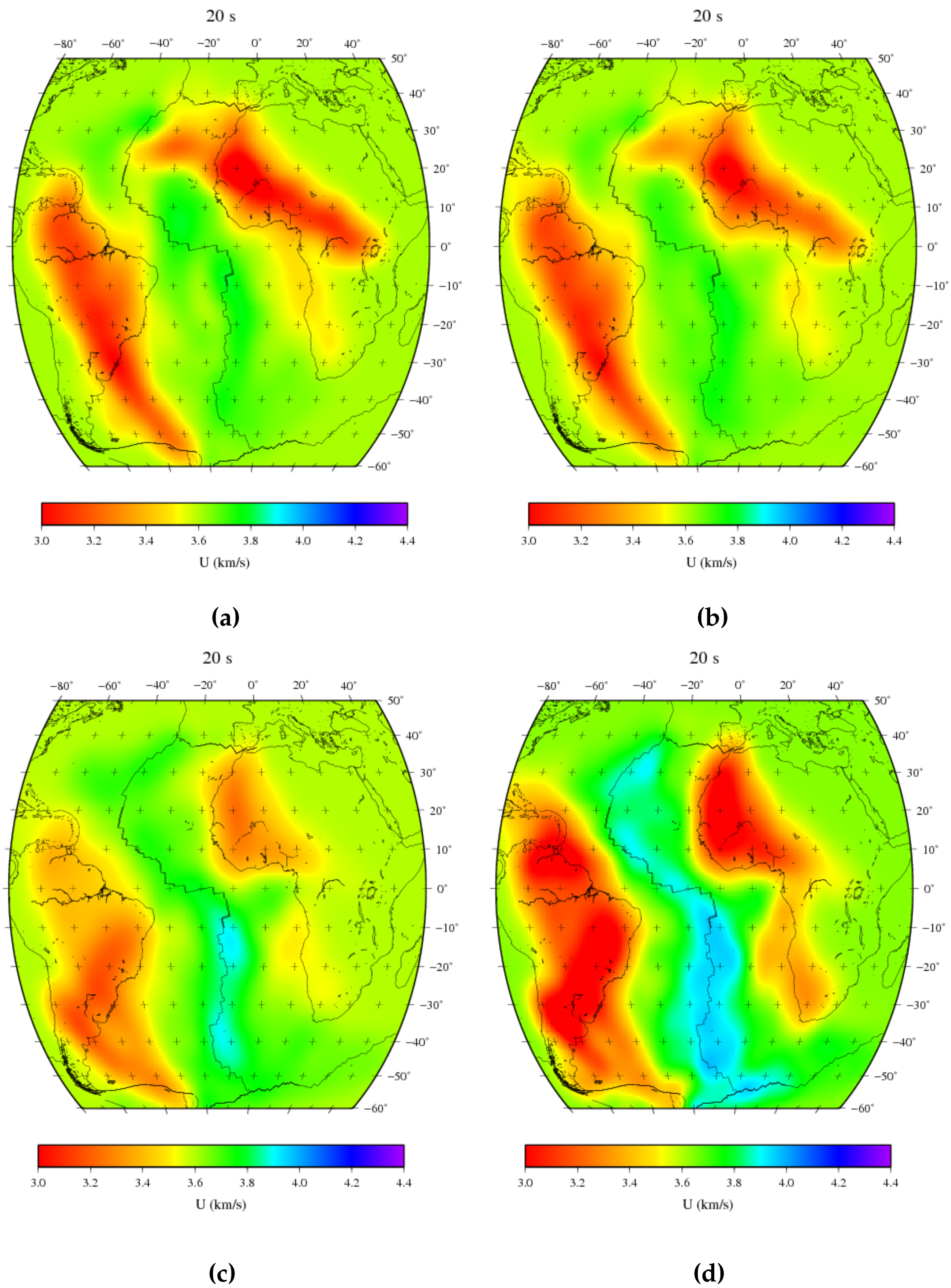

Figure 3.19 20 s tomographic model at 6 °inversion spacing showing the progression as more data was added; (a) 2007 events only (b) 2005-2007 events (c) all data picked with MFT_96 and (d) all data; combined MFT_96 picked data with auto picked data

For 50 s (figure 3.21) models a and b the trade off curve is very limited and there

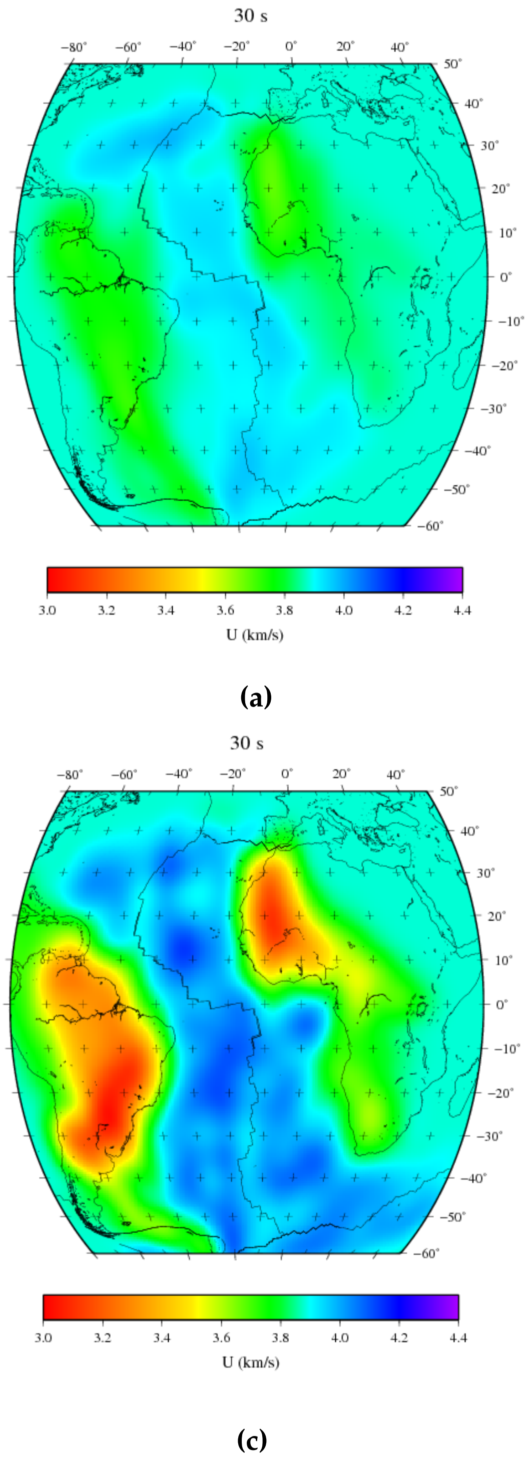

Figure 3.20 30 s tomographic model at 6 °inversion spacing inverted showing the progression as more data was added; (a) 2007 events only (b) 2005-2007 events (c) all data picked with MFT_96 and (d) all data; combined MFT_96 picked data with auto picked data

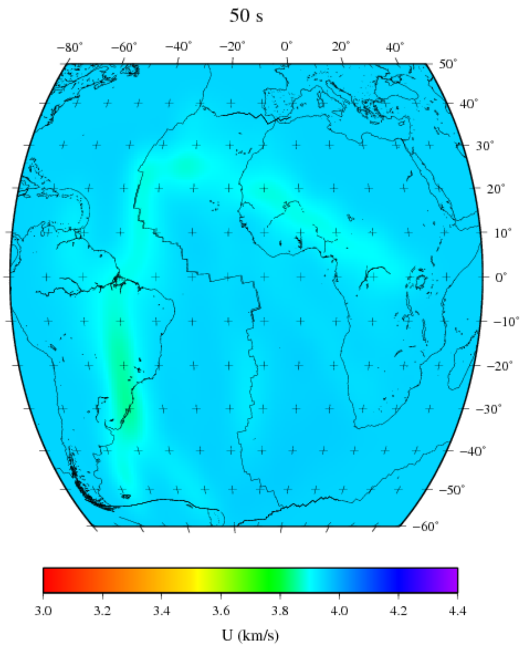

(a)

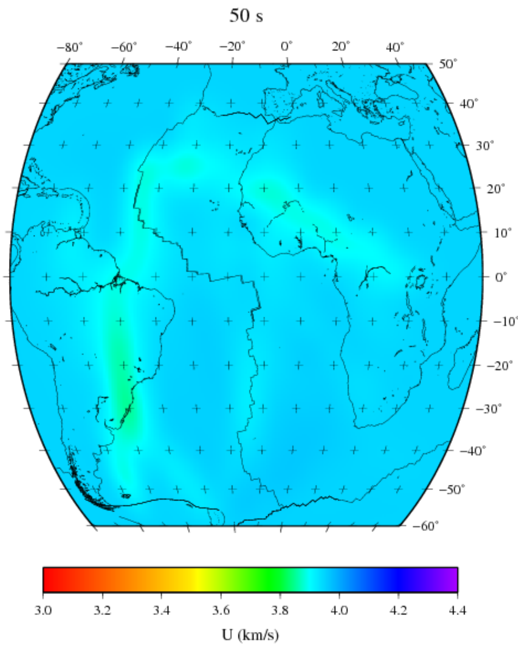

(b)

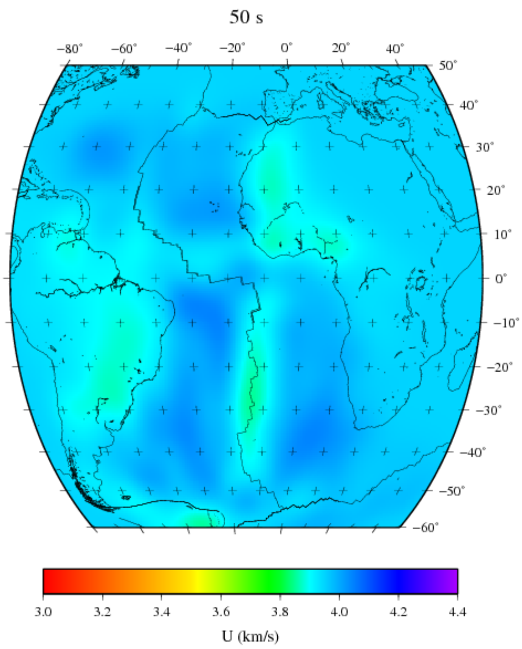

(c)

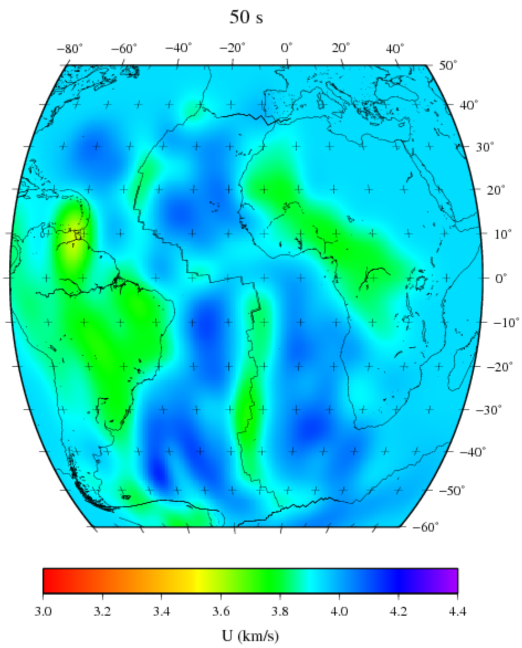

(d)

Figure 3.21 50 s tomographic model at 6 °inversion spacing invertedshowing the progression as more data was added; (a) 2007 events only (b) 2005-2007 events (c) all data picked with MFT_96 and (d) all data; combined MFT_96 picked data with auto picked data

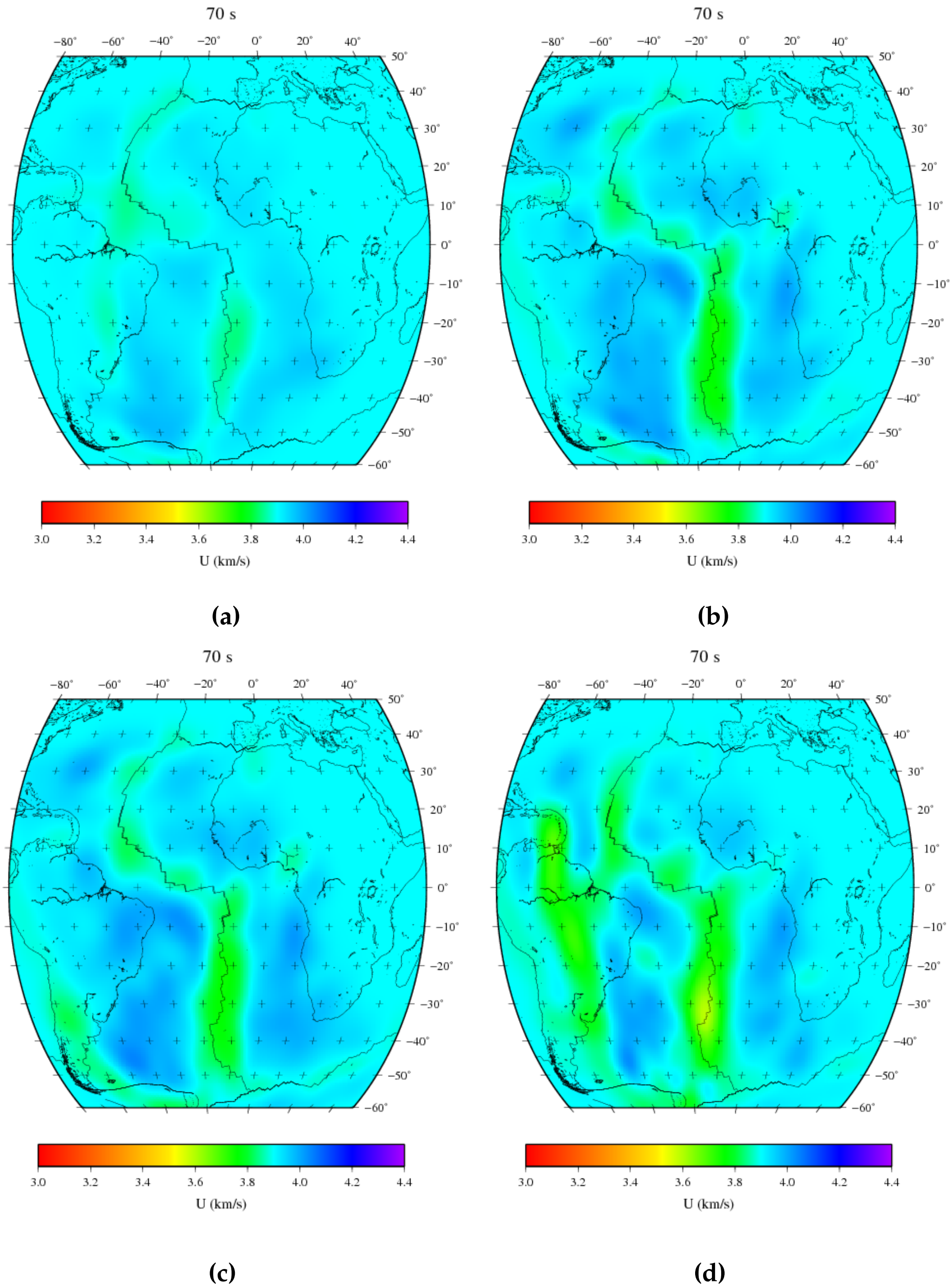

Figure 3.22 70 s tomographic model at 6 °inversion spacing inverted showing the progression as more data was added; (a) 2007 events only (b) 2005-2007 events (c) all data picked with MFT_96 and (d) all data; combined MFT_96 picked data with auto picked data

is little variation from the starting model until we get to model c. Here we start to see less contrast between the continental and oceanic regions, compared with the models for 20 s or 30 s. The southern region resolves features better than the north due to the path coverage, as with 20 s. By model d we are seeing a slow velocity region beneath the ridge, most likely associated with the shallow asthenosphere.

For 70 s (figure 3.22), similar to 50 s see very little contrast in model a between ocean and continent. By model b we are seeing the ridge defined as a slow velocity region. The model changes very little between b and c. We see the influence of some slow paths travelling through South America in model d. The contrast seen in these models is what would be expected compared with shorter periods because of the depth sensitivity being predominately in the lithosphere and therefore having less of a crustal influence associated with the contrasts between ocean and continent seen in figures 3.19 and 3.20.

All data 4 °models

All the periods were then inverted at 4 °spacing to get an initial model for all the data. A selection of these models are shown in figures 3.23 and figure 3.24. An initial interpretation of the models can be made from these which can be tied to geological features. We see the ridge dominating the shortest periods (figure 3.23 a and figure 3.23 b), the ridge is the highest topographic feature of the ocean floor and therefore we see this in the high velocity feature in contrast with the surrounding water. The ridge is formed of oceanic crust with surrounding ocean basins with slower velocity sediments. From 18 s (figure 3.23 b) onwards, the contrast between the oceanic and the continental regions becomes more apparent with slower velocities dominating the continents. At 18 s (figure 3.23 b) we can correlate regions of faster velocity to ocean islands (for example: 3 °S, 35 °W) and the Cameroon volcanic chain. From 18 s (figure 3.23 b) to 26 s (figure 3.24 d) we see the fast velocity ridge region spread out from the ridge to the entire oceanic region, showing the sensitivity to the crustal and upper lithosphere velocities.

We see very little change between the models from periods of 30 s (figure 3.24 a) and 50 s (figure 3.24 b) in the basin and shelf regions, but see the sensitivity to the continental crust is lost as the contrast between the oceanic and continental regions become less pronounced. The ridge is also less defined as a region than in the shorter periods implying the sensitivity of 26 s and 30 s is lower crust and lithosphere where we would not expect to see the topographic or crustal signatures associated with shallower sensitivity. The ridge region begins to become a slower velocity region at longer periods (figure 3.24 b to figure 3.24 c) which would be interpreted as the low velocity zone at the base of the lithosphere as we sample deeper the structure. The lithosphere beneath the ridge would be expected to be thinner than the surrounding ocean basins due to the up-welling of asthenosphere feeding the spreading ridge and cooling of the plate. At 100 s (figure 3.24 d) we see the sensitivity is more towards the asthenosphere, seeing widespread slower velocities.

3.4.2 Analysis of residuals

As discussed in section 3.3.1 some of the paths are singularly anomalous . The tomographic inversion tries to fit all the data; however the residual fit of some paths is greater than others. The tomographic code calculates the residual for each path as a percentage misfit relative to the model. The initial models discussed in section 3.4.1 were all chosen to be slightly over damped, and therefore, closer to the starting model. This was to focus on the broader structure. To ensure a more reliable model the higher residuals (paths with the least fit to the model) have been removed from data set before the final model was produced.

The mean and standard deviation (σ) for the residuals for each periods were calculated for the initial model containing all the data. The shape of the histograms is not entirely normally distributed; there is a large percentage of residuals which fall close to 0% and some outliers which are up to 40%. This distribution has caused the function of the data to be broader than would be expected for an otherwise narrow distribution of residuals. Figure 3.25 shows the distribution of 14 s, 20 s, 30 s, 50 s, 70 s and 100 s residuals. From this we can see that 14 s has a wide and broad distribution of re-

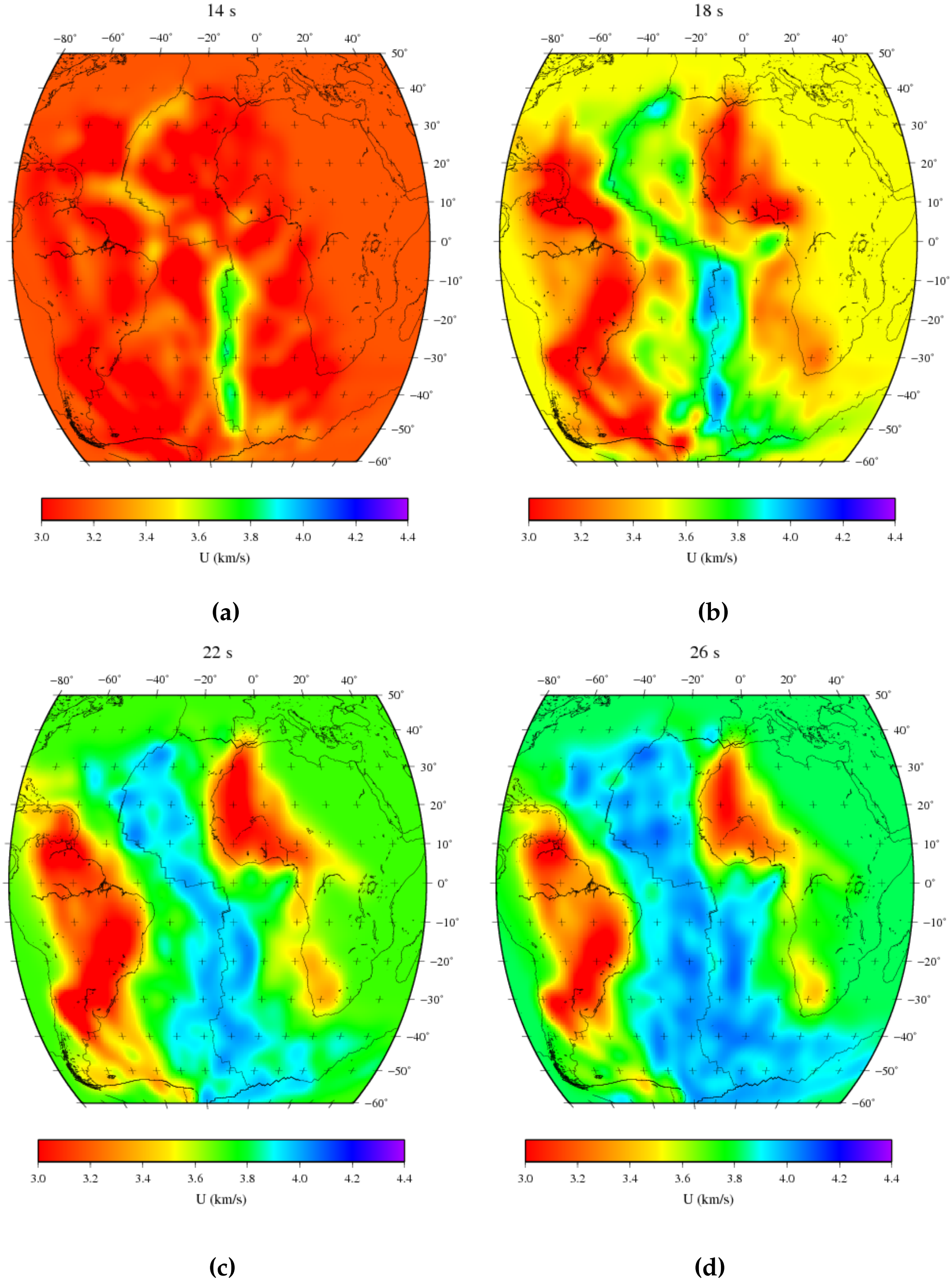

Figure 3.23 4 °tomographic initial models from all data picked for short periods (a) 14 s, (b) 18 s, (c) 22 s, and (d) 26 s; sensitive to the crustal structure

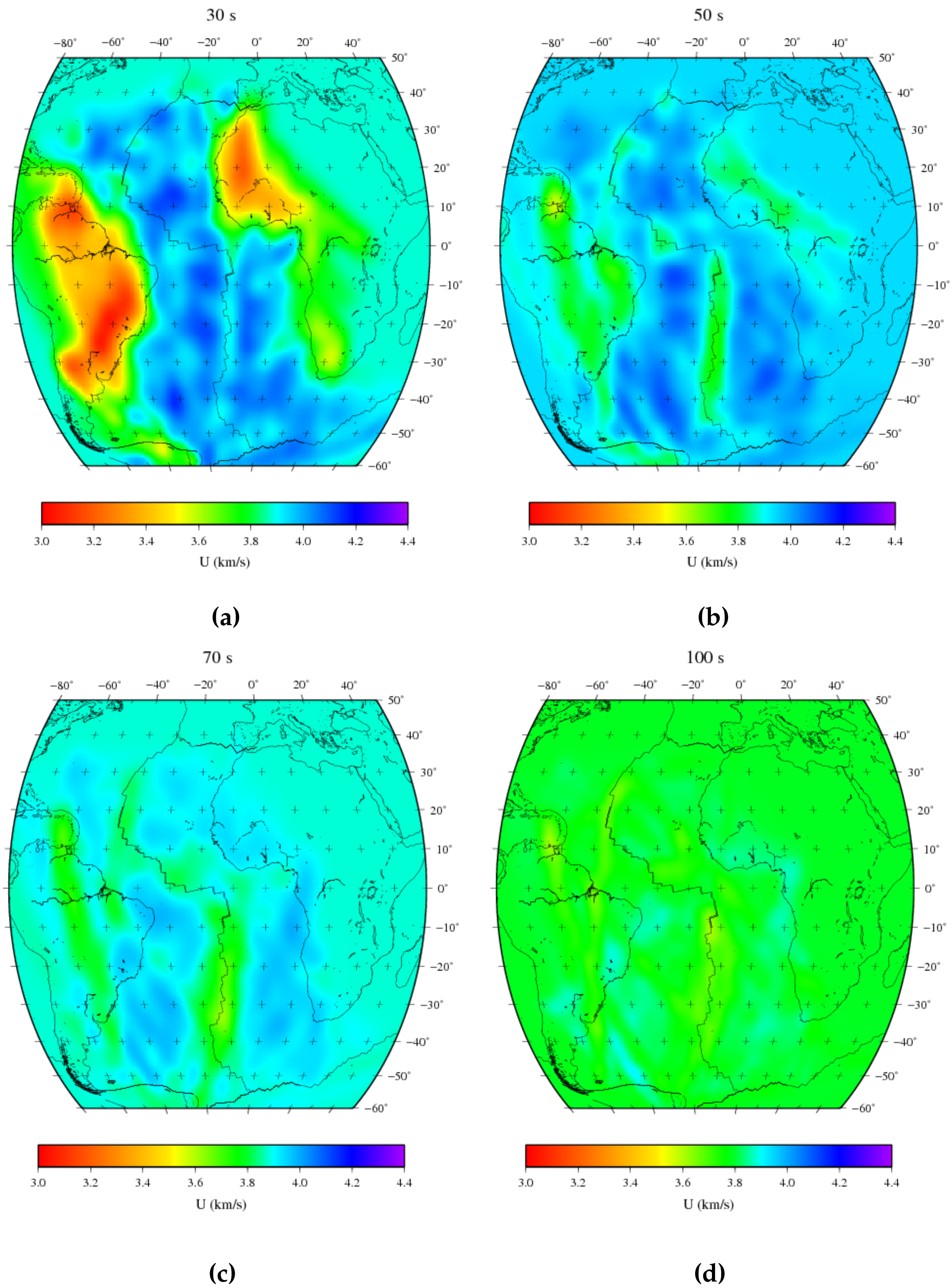

Figure 3.24 4 °tomographic initial models from all data picked for intermediate periods (a) 30 s, (b) 50 s, (c) 70 s, and (d) 100 s; sensitive to the lithosphere and asthenosphere

siduals compared with the other periods which follow the more narrow distribution described. This is reflected in the mean and σ values for the periods. The 14 s period data contains the lowest number of paths of any of the models. With fewer paths the model will be less well constrained which explains the larger standard deviation. The narrow shape for the other periods is due to the high density of paths with a low residual. The majority of paths with a low residual is what we would hope for, showing the model is constrained with most of the data. The Gaussian distributions highlight a slight skewness in residuals in these models (3.25).

The 3rd standard deviation (3σ) has been highlighted for each period by a red bar, statistically 99% of the data should lie within 3σ. Any path with a residual greater than 3σ for that period was removed from the final data set. Figure 3.26 shows the variations of 3σ with respect to period before the residuals were removed from the model. For example 3σ for 30 s is 7.11% therefore any individual path with a percentage misfit greater than 7% was removed before the final inversion was run. 7.11% residual would equate to a ± 0.27 kms^{-1} variation in velocity between the model and the path. This residual value is greater than the variations between the different methods of picking the data(MFT96 and the automated code) and therefore the picking method has not had a great effect on the model compared with expected natural variations between travel paths.

Figures 3.27 to 3.28 show the paths removed for each period based on 3σ. The number of paths removed has varied for each period. The distribution of paths removed varies also depending on the period, for shorter periods (20 s figure 3.27 b to 44 s figure 3.28 b) with sensitivity to the crustal structure the trend of paths removed is through the continental regions (predominately South America). Also at some shorter periods (20 s figure 3.27 b to 44 s figure 3.28 b) we see a trend of some paths which are travelling predominately through transition regions, parallel to a boundary between oceanic and continental lithosphere(for example paths travelling west to east between 0 and 10 °N) are removed. The energy in these paths most likely does not take the assumed great circle route but is likely to travel south of its projected path in the faster velocity oceanic region.

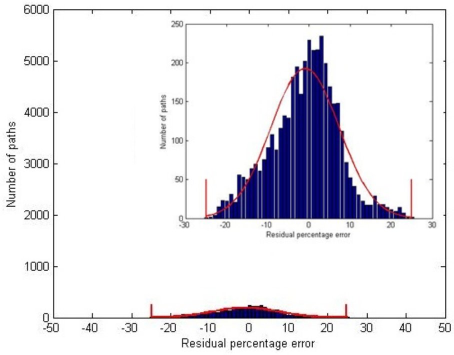

(a) 14 s

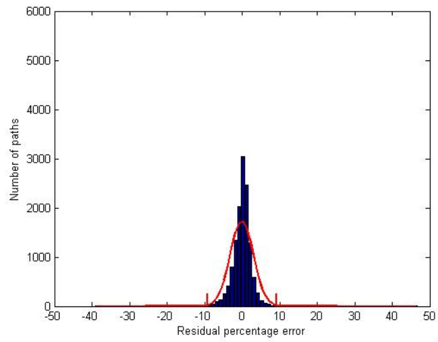

(b) 20 s

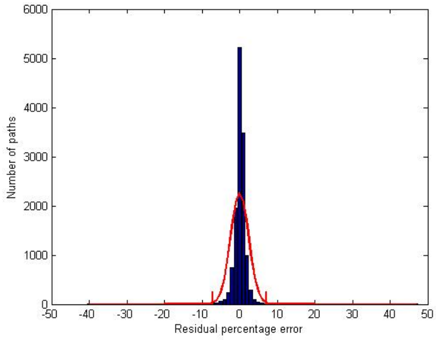

(c) 30 s

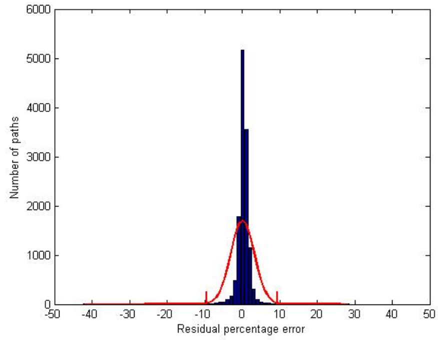

(d) 50 s

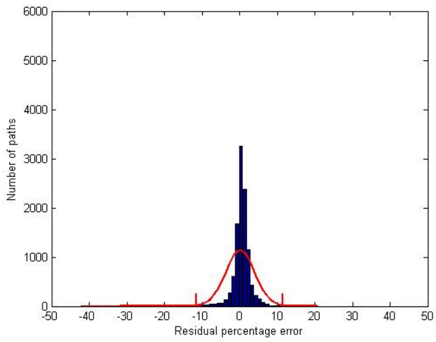

(e) 70 s

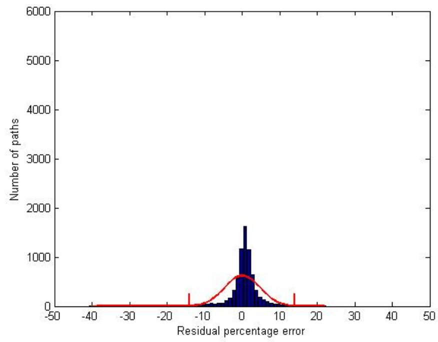

(f) 100 s

Figure 3.25 Distribution of residuals from initial models shown in blue (figure 3.23 and 3.24) for periods (a) 14 s, (b) 20 s, (c) 30 s, (d) 50 s, (e) 70 s and (f) 100s for initial models. Gaussian distribution is plotted as a red line. The red vertical bars highlight the 3 σ value for each period.

As the low velocity region beneath the ridge becomes more prominent (44 s figure 3.28), we see more paths travelling through the ridge region have been removed. The velocity structure of this region is most likely a factor, with some paths travelling outside their projected great circle path in the faster adjacent lithosphere not the slower asthenosphere beneath the ridge. Some stations also seem to have a lot of paths to

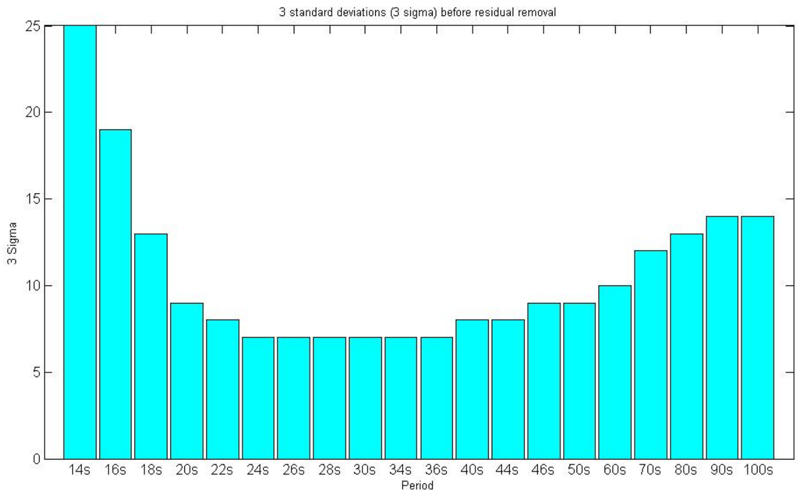

Figure 3.26 3σ value for each period for the initial models

them being removed due to their residuals not fitting (South Africa 30 °S, 20 °E). This could be due to the station being on the edge of the region defined by the model and therefore not enough data to constrain the fit for the paths to the model. It could also be due to timing errors with the instrument or an error in the location of the event. Some of these paths may not need to be removed for reasons as discussed but to ensure a consistent approach all outliers above 3σ are removed irrespective of possible cause of misfit.

Once paths with a residual greater than 3σ were removed , the data was inverted again and the mean and standard deviation were calculated for the new model. For 30 s the new 3σ value after removing the outliers is 4.14%. This now means there is a possible variation in velocity of 0.15kms^{-1}. Table 3.3 shows the maximum variation in velocity associated with the 3σ for each period for the final data set used in the final inversions.The skewness in the residuals distribution in figure 3.25 has also been removed where in figure 3.29 shows a more normal distribution in the fit of data to the model.

From table 3.3 it is clear that 24 s to 60 s have the lowest error with 99% of paths in the model deviating no more than 0.2 kms^{-1} and 20 s to 80 s all fit within an error of 0.3 kms^{-1}. This gives an idea of which models are the most robust from the fit of the data to the model. The error is an inverse correlation to the final number of paths in each

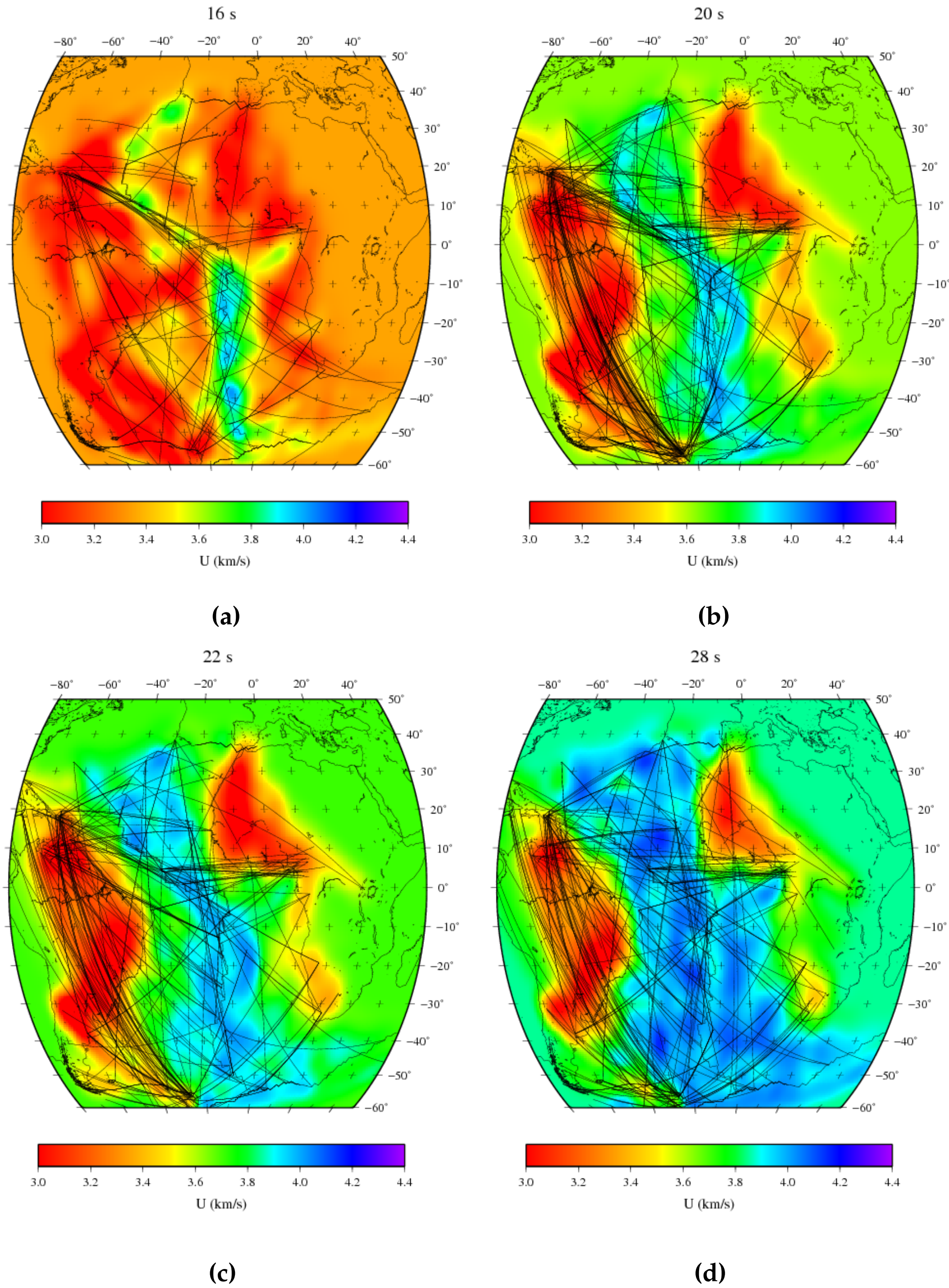

Figure 3.27 Initial tomography models with paths for residuals higher than 3σ plotted as black great circle lines for each period (a) 16 s, (b) 20 s, (c) 24 s and (d) 28 s. These paths were removed from the data before the final model

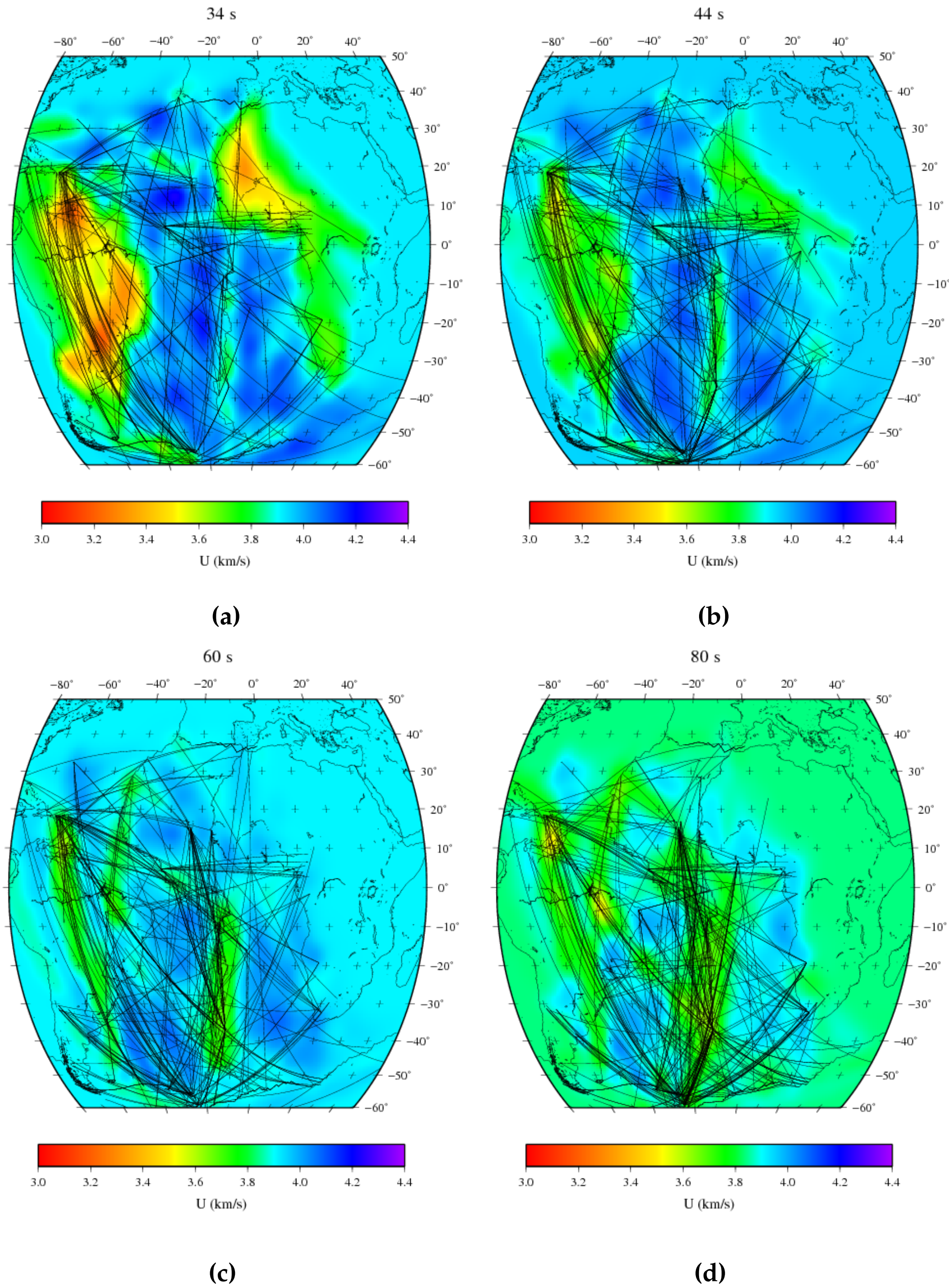

Figure 3.28 Initial tomography models with paths for residuals higher than 3σ plotted as black great circle lines for each period (a) 34 s, (b) 44 s, (c) 60 s and (d) 80 s. These paths were removed from the data before the final model

model, the greater the number of paths (figure 3.31) the lower the velocity error due to the residuals. By removing paths with a greater than the initial 3σ, the variations in path average velocity between the data and the model have been improved. 14 s is not a good fit to the model even after removing the residual misfits greater than σ. The model for 14 s has the lowest number of paths in the model, but also had such a high 3σ value from the initial model that fewer paths were removed from the final data set. There is also a correlation between the number of paths removed from the final model and the improved fit to the model. Initial interpretations would show that the most reliable and robust models based on fit to the model from individual paths are for periods 22 s to 70 s ($< 0.25\%$ kms^{-1}).

Table 3.3 Final velocity errors from residual 3σ

Period (s)	Error (kms^{-1})	Period (s)	Error (kms^{-1})
14	$\pm$ 0.79	36	$\pm$ 0.16
16	$\pm$ 0.36	40	$\pm$ 0.12
18	$\pm$ 0.39	44	$\pm$ 0.16
20	$\pm$ 0.26	46	$\pm$ 0.16
22	$\pm$ 0.22	50	$\pm$ 0.16
24	$\pm$ 0.19	60	$\pm$ 0.20
26	$\pm$ 0.19	70	$\pm$ 0.23
28	$\pm$ 0.15	80	$\pm$ 0.27
30	$\pm$ 0.16	90	$\pm$ 0.34
34	$\pm$ 0.16	100	$\pm$ 0.38

3.4.3 Final Path coverage and models

The final dispersion maps are shown in figures 3.32 a to 3.39 a. Focus is on the oceanic structure and therefore the continental regions have been greyed out to focus on the region of interest. There is little variation between the initial maps (figures 3.23 and 3.24) and the final maps (figures 3.32 to 3.39) which shows that the outliers which were removed were not strongly affecting the recovered tomography. Due to that number of paths in the models at short periods, 14 s and 16 s (figure 3.31 and 3.32) these models were derived from inversions at 4 °spline spacing. All the other models

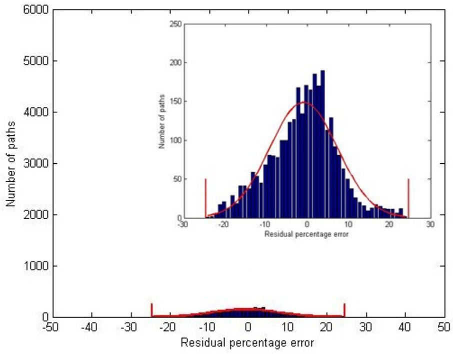

(a) 14 s

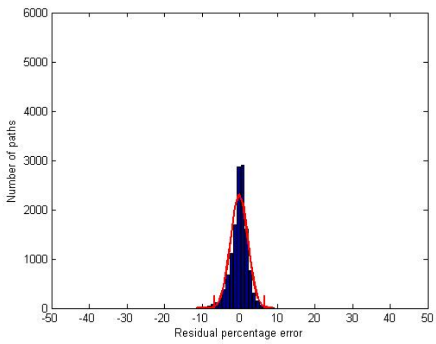

(b) 20 s

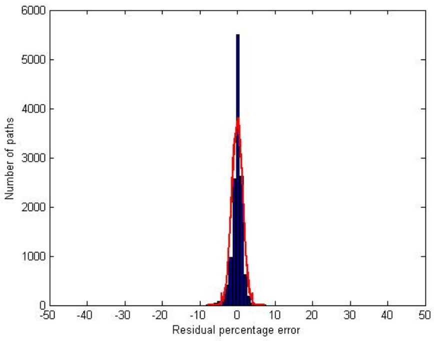

(c) 30 s

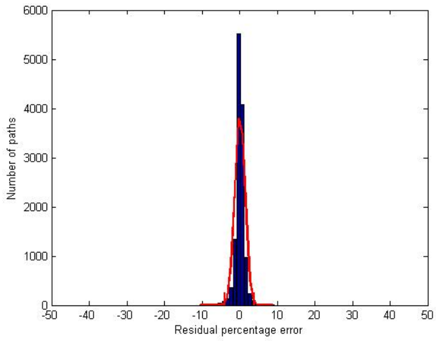

(d) 50 s

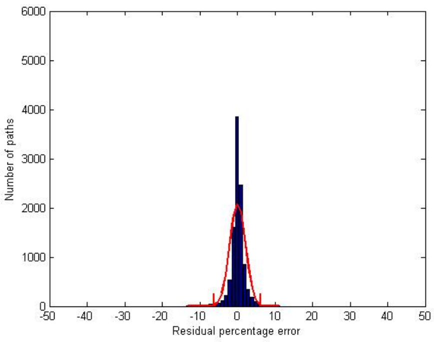

(e) 70 s

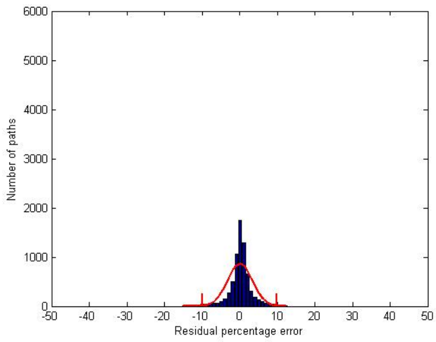

(f) 100 s

Figure 3.29 Distribution of residuals for final models for periods shown in blue (a) 14 s, (b) 20 s, (c) 30 s, (d) 50 s, (e) 70 s and (f) 100s. Gaussian distribution is plotted as a red line. The red vertical bars highlight the 3 σ value for each period.

have been inverted for a 3 °spline spacing. 3 °spline spacing makes the maps sensitive to the structure greater than 350 km laterally, therefore looking at the broad features seen in the region.

The path coverage for the final models is different for every period, which means that the recovered tomography varies from period to period. Figure 3.31 shows the

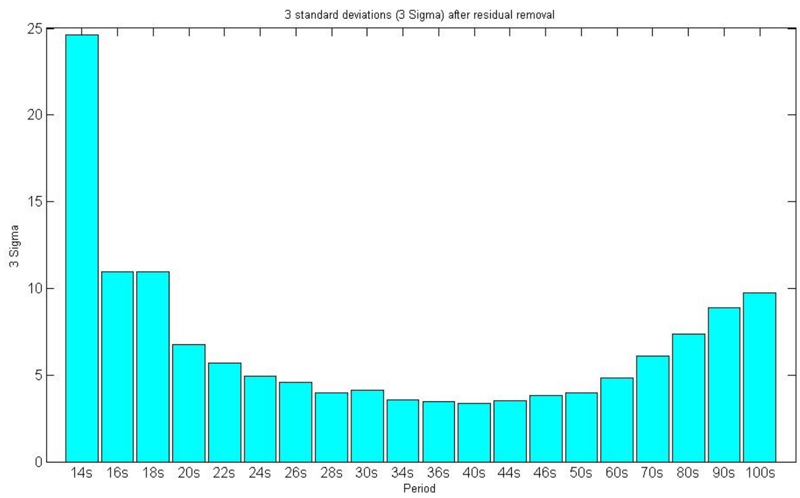

Figure 3.30 3σ value for each period for the final data 4 °models after the residual paths were removed

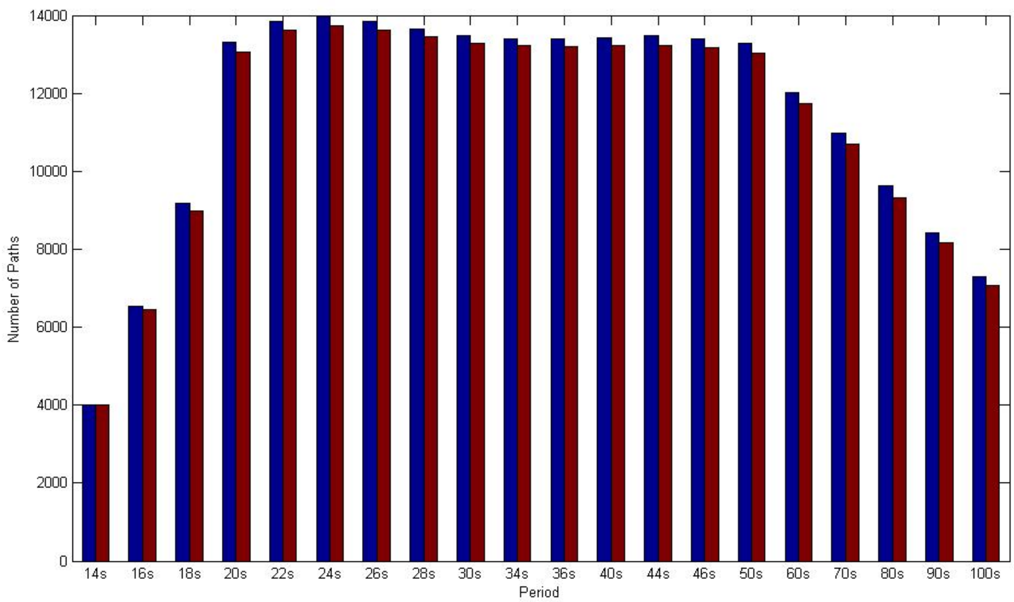

Figure 3.31 Number of paths for each period for the initial (blue) and the final (red) models

number of paths for the initial inversions and the final models for each period. The periods with the highest number of paths in the inversions are 20 s to 50 s, it is the models at these periods where the best path coverage is assumed and therefore the best recovery of the velocity should be seen. The robustness of the models and recovery of structure is discussed in further depth in the section 3.4.4. At the shortest periods (14

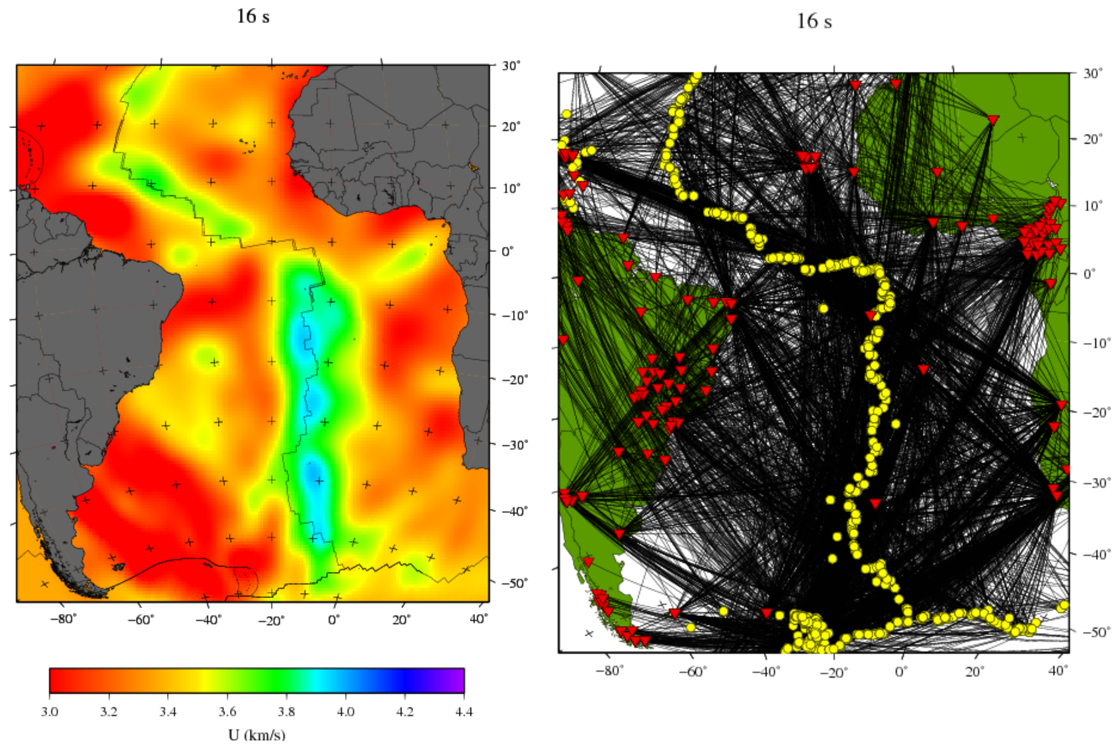

Figure 3.32 (a) Final dispersion map and (b) final path coverage for 16 s

s and 16 s) there is the least number of paths input into the inversions, this is due to the noise seen on the dispersion curves at these shorter periods. The tail off of paths at longer periods is also due to the increasing width of the group velocity signal and the uncertainties with the picking of the velocity peak.

From 20 s to 60 s (figures 3.34 b to figures 3.37 b) there is a high density of paths in the South Atlantic, between 0 °and 40 °south. This is the region where the most features are recovered in the intial and final models, the velocity structure of the mid ocean ridge, the sea mounts and ocean islands. Due to the distribution of seismometers in the west of the region compared to the east of the region, the azimuths of the paths are different; there are more clusters of stations in Africa compared to the less clustered distribution in South America. The paths travelling to South America from the ridge are slightly more perpendicular than the angled direction to the east of the ridge where there is a station gap between 5 °south and 18 °south. This may affect the recovery of

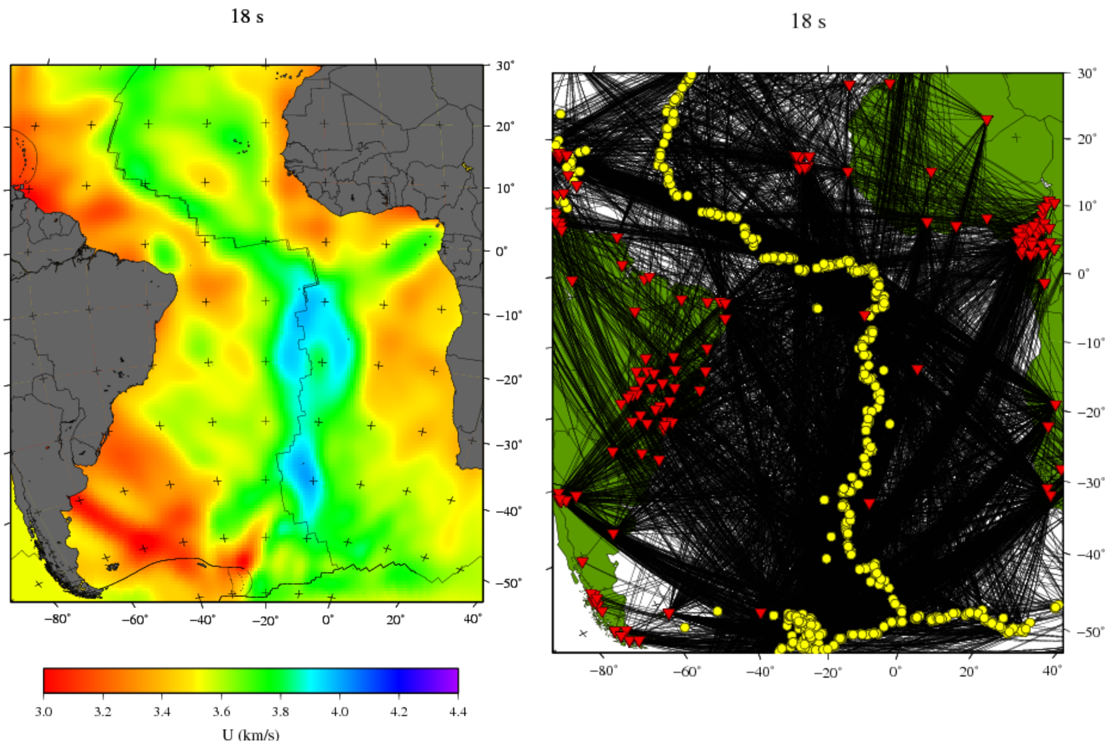

(a) **(b)**

Figure 3.33 (a) Final dispersion map and (b) final path coverage for 18 s

structure of velocity in different directions, for example, the Cameroon volcanic line showing as a high velocity region could be due to the high density of paths travelling parallel to the line towards the Cameroon seismic array. The distribution of the stations and azimuth of paths must be taken into account when interpreting the velocity structure recovered.

3.4.4 Reliability

The reliability of the models presented here were tested for the effect of the choice of damping parameter on the velocity structure and the recovery of the velocity structure due to the spatial distribution of path coverage. As discussed at the start of the section, the choice of damping parametrisation value can be subjective, depending on the shape of the trade off curve. The less sharp it is the more ambiguous the choice of damping values. The difference in velocity between the lowest reasonable damping

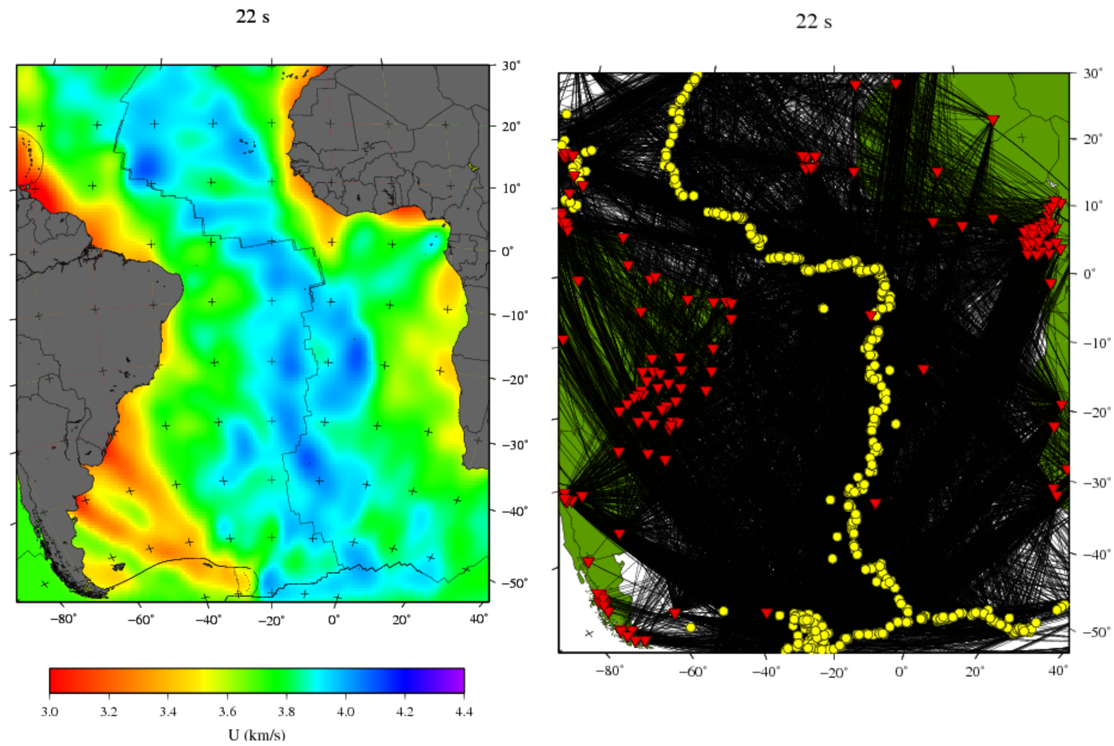

(a) **(b)**

Figure 3.34 (a) Final dispersion map and (b) final path coverage for 22 s

value and the highest was mapped to see how great an effect changing the damping value would have on the velocity model. If choice of damping is reasonable, we would expect to see little effect on the variations in the model. Regions showing large variation in velocity would suggest ambiguity in the model with more than one possible solution in the inversion. It could highlight regions where data is not as robust, causing the ambiguity in the inversion.

Difference Maps

Figure 3.40 to figure 3.48 show the difference maps for each period based on the individual damping values. The chosen damping value for the final model (section 3.4.3) is shown on the trade off curve in blue for each period and the maximum and minimum damping values deemed reasonable are shown in red. The maps show the difference in velocity between the model with the highest damping value (maximum) subtracted

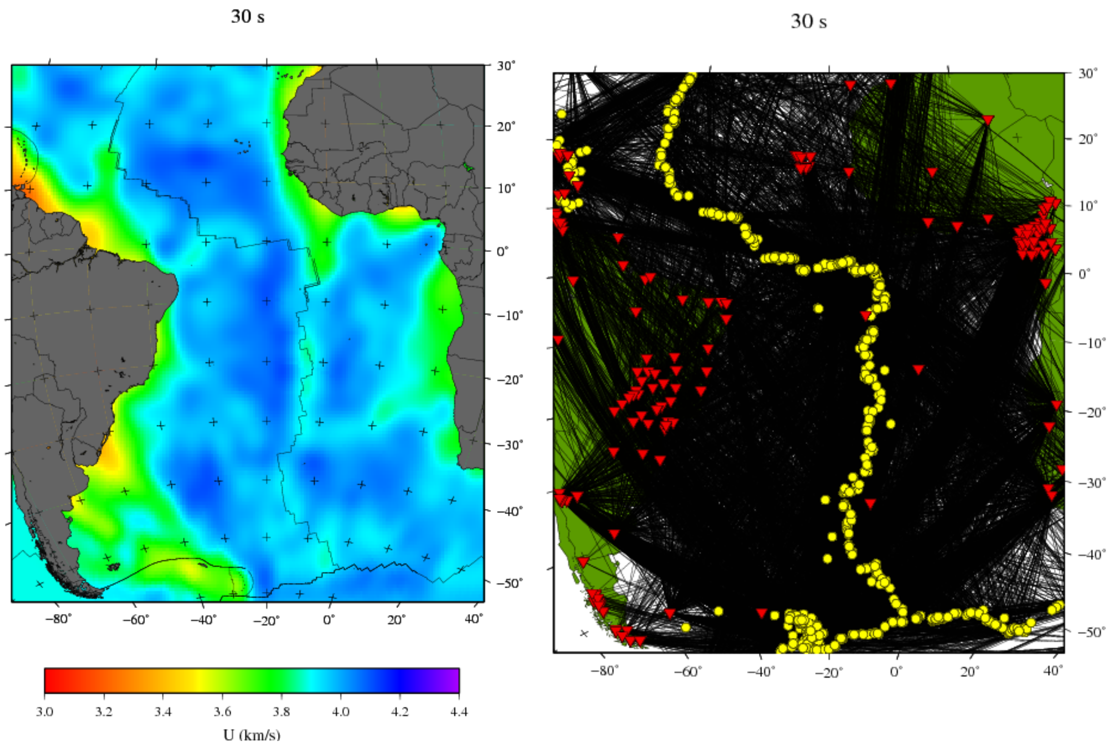

(a) **(b)**

Figure 3.35 (a) Final dispersion map and (b) final path coverage for 30 s

from the model with the lowest value (minimum). The contours on each map show ± 0.1, 0.2, 0.3 and 0.4 kms^{-1} difference in velocity between the two models; white areas represent regions with no velocity variation between damping values.

The shorter periods (14 s to 28 s) have flatter, shallower shaped trade off curves, providing a wider selection of possible damping values. The shape of these curves at the shortest periods (14 s - 18 s) is most likely due to ambiguity in the model due to the sparse path coverage. Figures 3.40 and 3.41 show a large variability in velocity; up to 0.4 kms^{-1} in some regions. Although this is a reflection of the path coverage, the depth sensitivity of these periods also has the most variable velocity structure of the top few km's; deep sedimentary basins adjacent to an igneous dominated mid ocean ridge. The water layer also plays a dominant part in the velocities at these periods. There is no consistent pattern observed between these 3 periods where velocity variations are positive or negative.

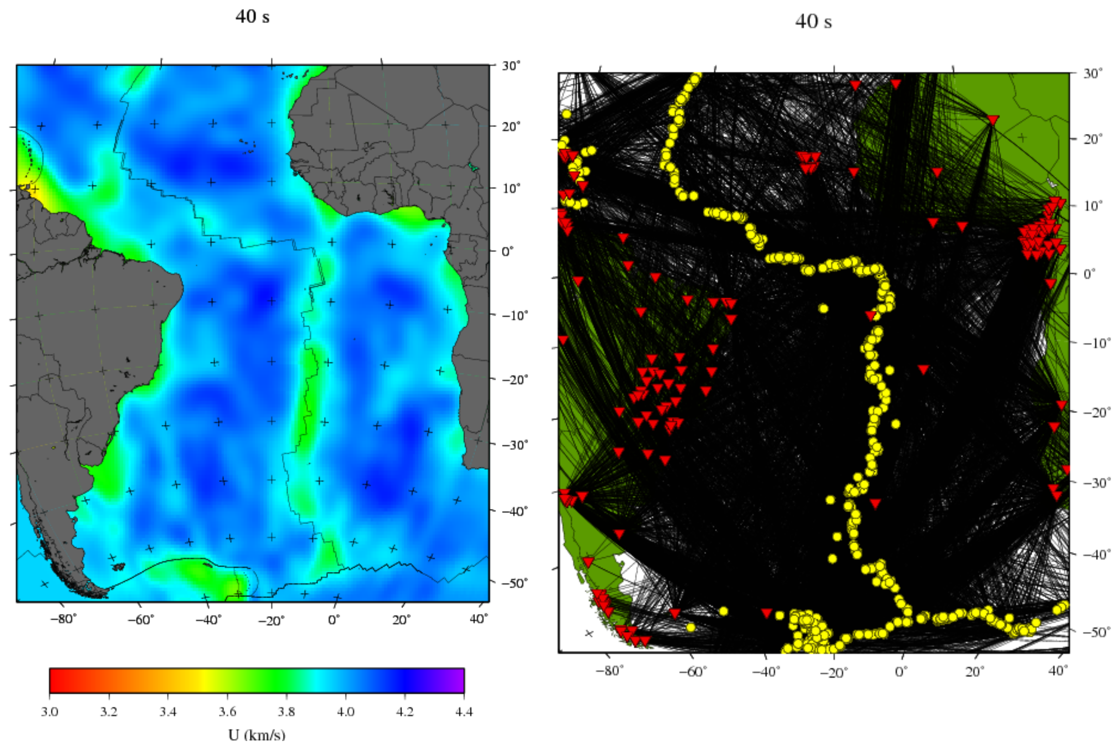

(a) **(b)**

Figure 3.36 (a) Final dispersion map and (b) final path coverage for 40 s

The misfit of the trade off curves improves at 20 s (figure 3.42), this coincides with the improvement in the path coverage in the model (figure 3.31). At 20 s to 28 s (figures 3.42 to 3.43) a significant reduction in the velocity variation for these periods can be seen, compared with the shorter periods (14 s - 18 s). The curves are still shallow in shape which is most likely due to the variable velocity structure at the depth sensitivity ranges for these periods, meaning the fit to the data is still variable due to regional variations in the velocity structure.

The trade off curves have a much sharper bend for intermediate periods (30 s - 70 s). The shape of the curve is due to the better fit to the data alongside the smaller velocity variations observed in the velocity structure. These periods are now sensitive to the lithospheric structure where it is assumed there is less velocity variation compared with the crust. In addition, the misfit to the data increases as the period increases. Although the curve is sharper for these periods there are still a few possible damping

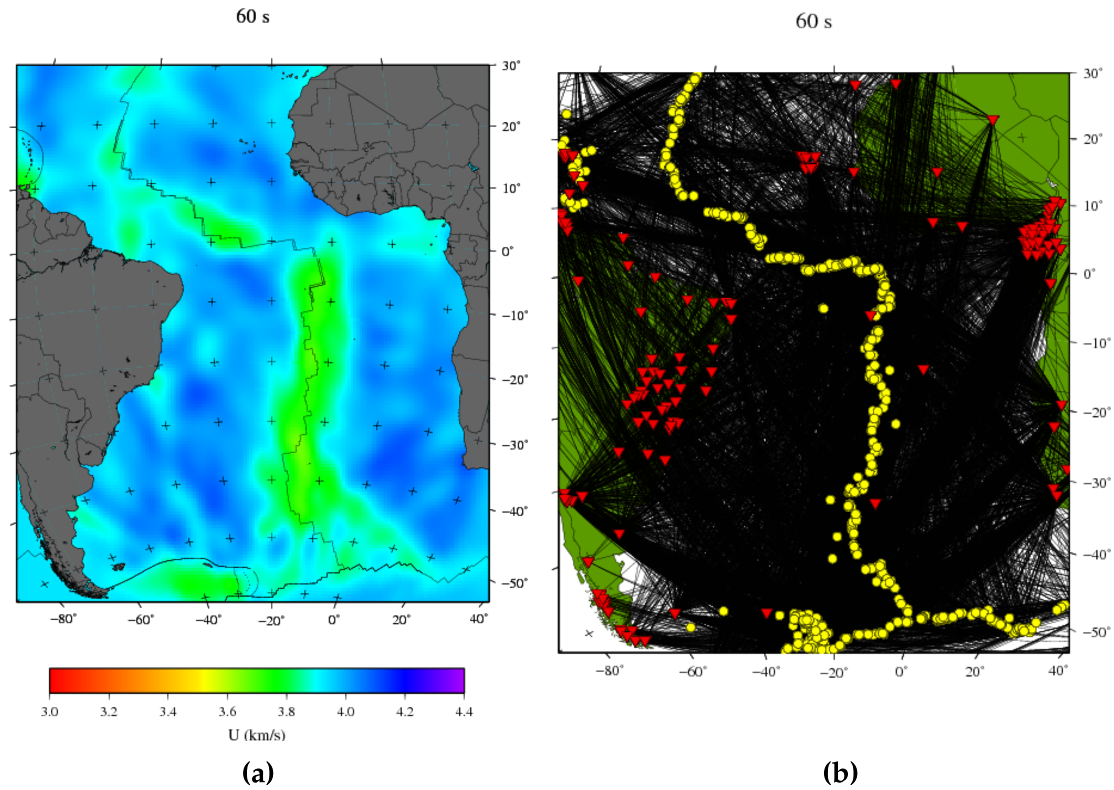

Figure 3.37 (a) Final dispersion map and (b) final path coverage for 60 s

values which could be selected. It is observed that the velocity variation between the maximum and minimum damping is less the 0.1 kms^{-1} across most of the region. This is a variation in velocity of approximately 2.6 %, which lies within the 99% of residuals discussed in section 3.4.2. The maps highlight that the choice in damping parameter for the model is therefore within error of the data itself.

At longer periods where the ridge is defined in the models as a region of low velocity (44 s - 70 s) there is a negative velocity variation, implying that the ridge becomes less defined as less damping is applied to the model. The opposite appears to be true about the sedimentary basins and abyssal plains where we see a positive difference between the least and most damped models. There are no single regions which consistently stand out to be anomalous at all periods. A region to the east of the Atlantic (0 °, 0 °, 10 °S, 10 °E) does highlight a small region of high positive velocity variation for periods 28 s to 40 s (figures 3.43, 5.7 and 3.45) which could highlight a region of uncer-

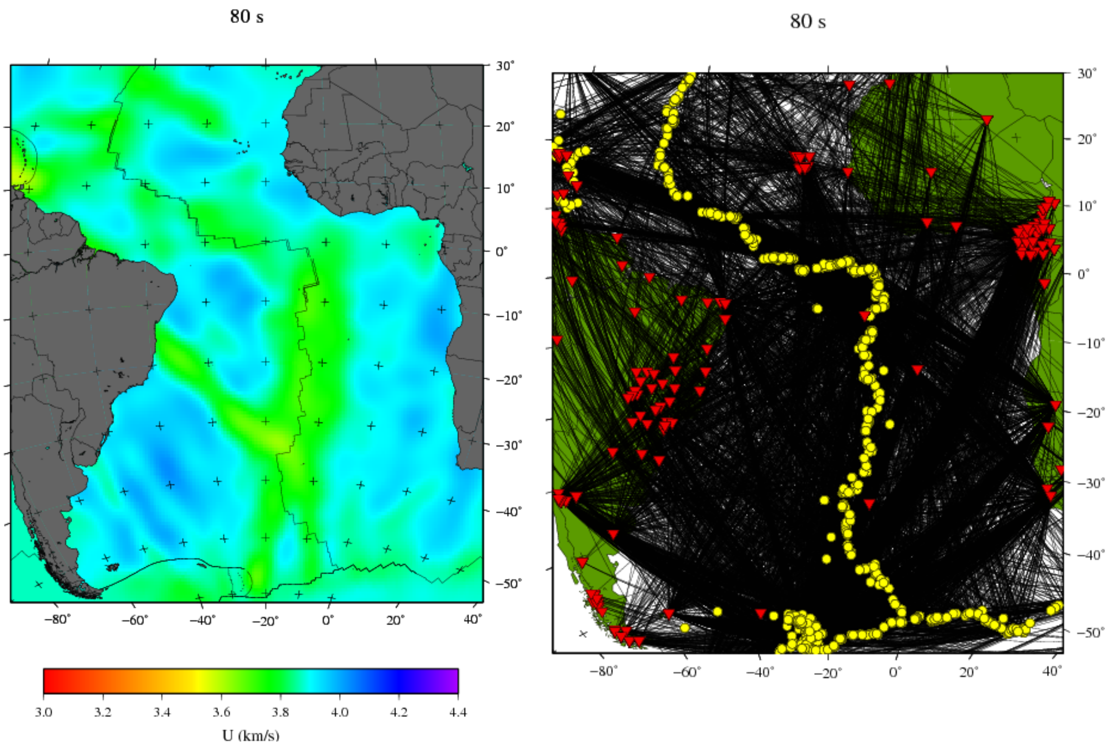

(a) **(b)**

Figure 3.38 (a) Final dispersion map and (b) final path coverage for 80 s

tainty, but may also be linked to the velocity structure of the Cameroon volcanic line as the feature is not seen at all periods. The other region which has a higher velocity variation is the continental margin around the southern tip of South America. There are both positive and negative velocity variations seen in the region. This could be linked with poor path coverage; since it is on the margin of the model or uncertainties in the velocity structure of this region, due to the transition between continental shelf and oceanic basin.

At the longest periods (80 s - 100 s) the velocity variations observed are not as large as those observed at the shortest periods despite the number of paths in the models being similar. This is most likely due to the homogeneous velocity structure at the depths which the longer periods are sensitive to compared with the velocity structure of the depths the shortest periods are sensitive to. There are some linear regions which highlight where paths orientated in a particular direction begin to dominate the velo-

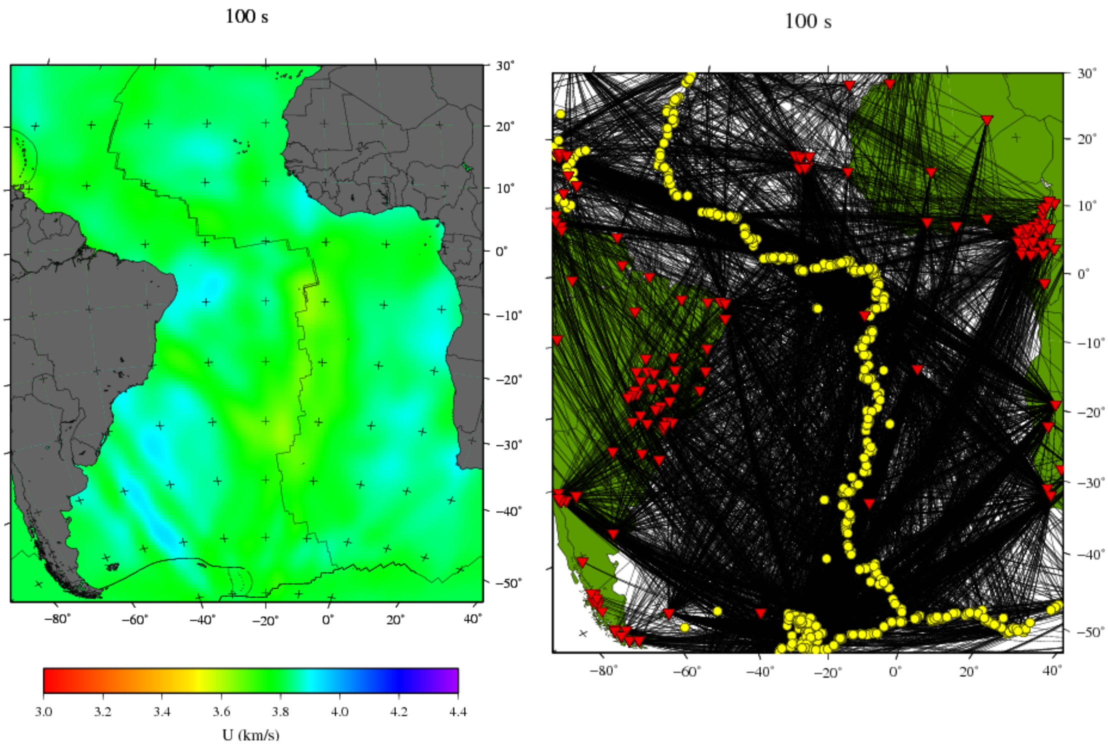

(a) **(b)**

Figure 3.39 (a) Final dispersion map and (b) final path coverage for 100 s

city structure. The trade off curves for these longest periods do not flatten off towards a constant misfit, which is likely to be due to the greater error with in the data.

Due to the shape of the trade off curves and the amount of velocity variation between models, the most robust data and consistent models are for periods 20 s - 70 s. This is consistent with residual percentages, number of paths for the models and the lack of variation in the difference maps.

3.5 Discussion

In this section we have inverted group velocity path average data for tomographic velocity maps with respect to period. There is more variation between oceanic structure and continental structure seen at shorter periods than longer periods. The ridge feature at the shortest periods (14 s -18 s) is picked out as a high velocity feature with a low

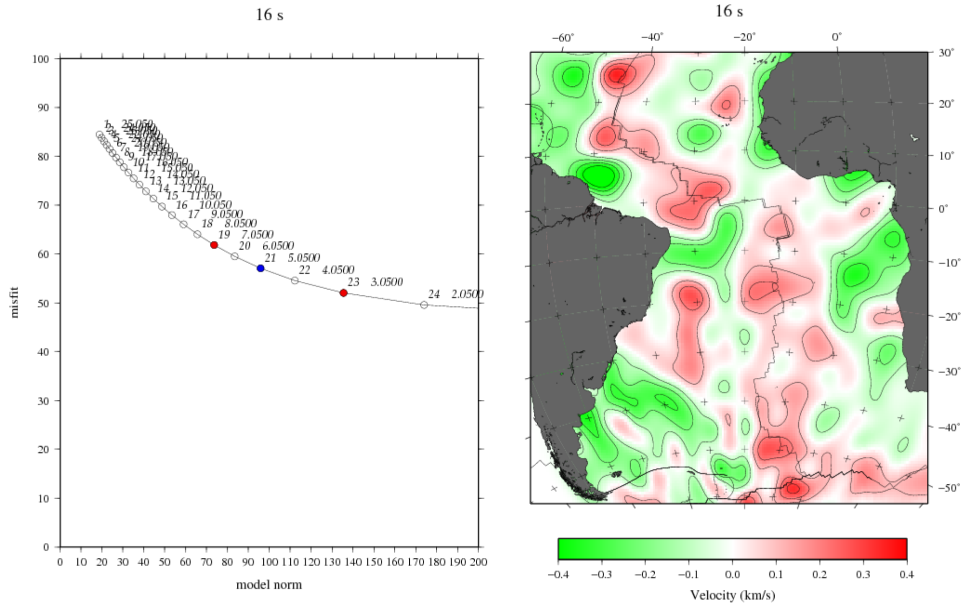

(a) **(b)**

Figure 3.40 Difference map for 16 s between two damping values (19 and 23) shown on (a) trade off curve in red to map (b) the variability in velocity across the region depending on which damping values is chosen. Final model damping value is show on (a) trade off curve in blue

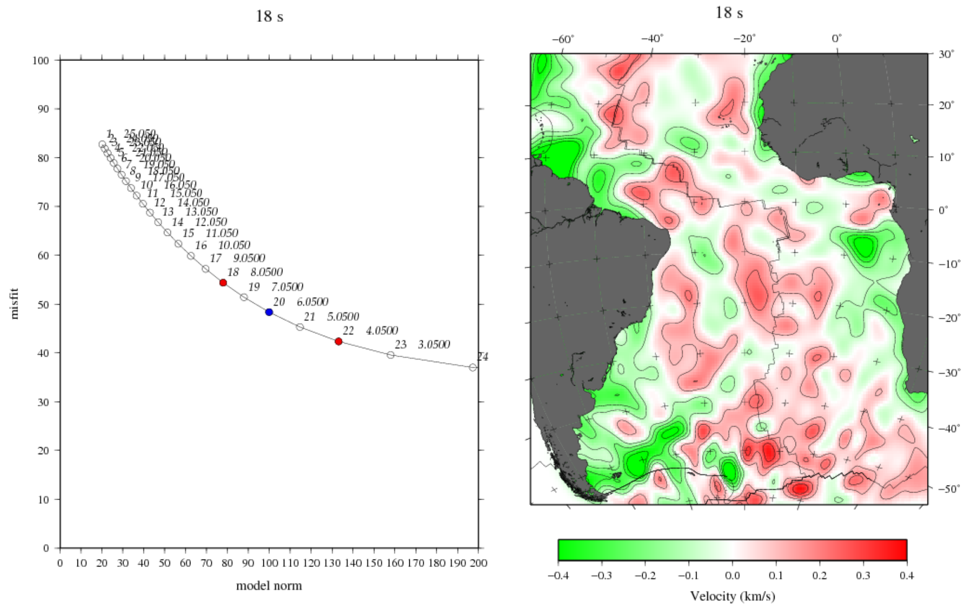

(a) **(b)**

Figure 3.41 Difference map for 18 s between two models (18 and 22) shown on (a) trade off curve in red to map (b) the variability in velocity across the region depending on which damping values is chosen. Final model damping value is show on (a) trade off curve in blue

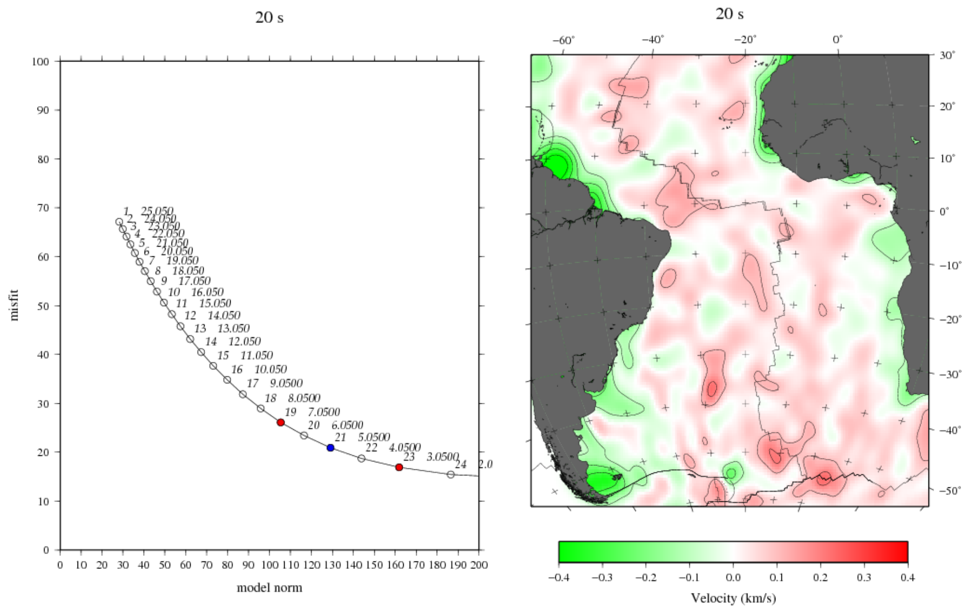

(a) **(b)**

Figure 3.42 Difference map for 20 s between two damping values (19 and 23) shown in red to show variability in velocity across the region depending on which model is chosen.

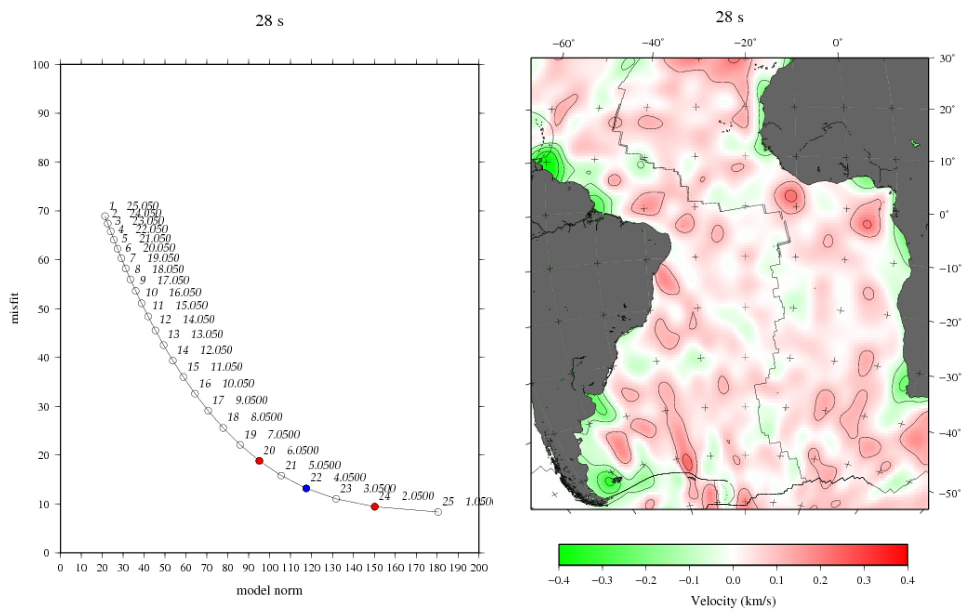

(a) **(b)**

Figure 3.43 Difference map for 28 s between two damping values (20 and 24) shown on (a) trade off curve in red to map (b) the variability in velocity across the region depending on which damping values is chosen. Final model damping value is show on (a) trade off curve in blue

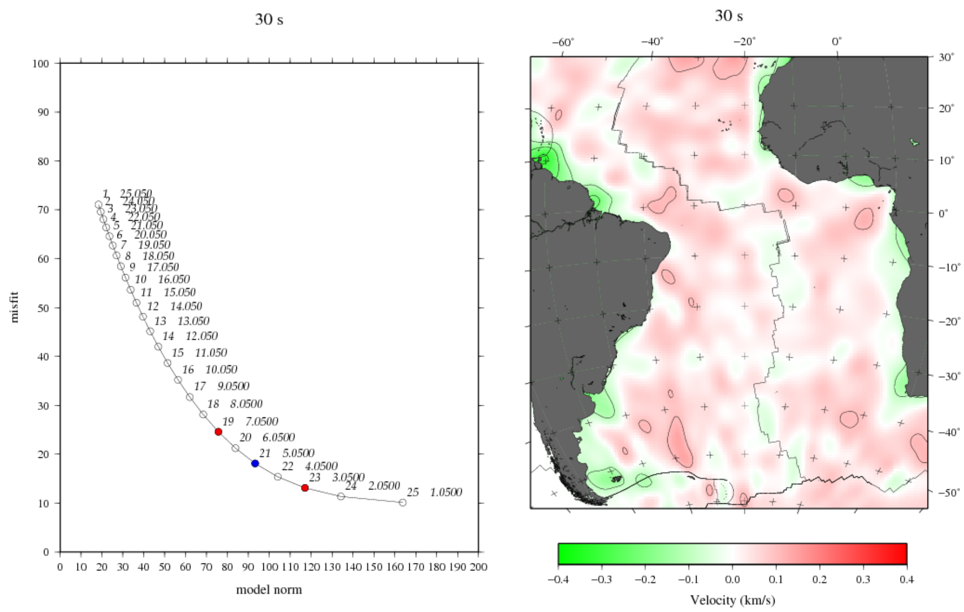

(a) **(b)**

Figure 3.44 Difference map for 30 s between two damping values (19 and 23) shown on (a) trade off curve in red to map (b) the variability in velocity across the region depending on which damping values is chosen. Final model damping value is show on (a) trade off curve in blue

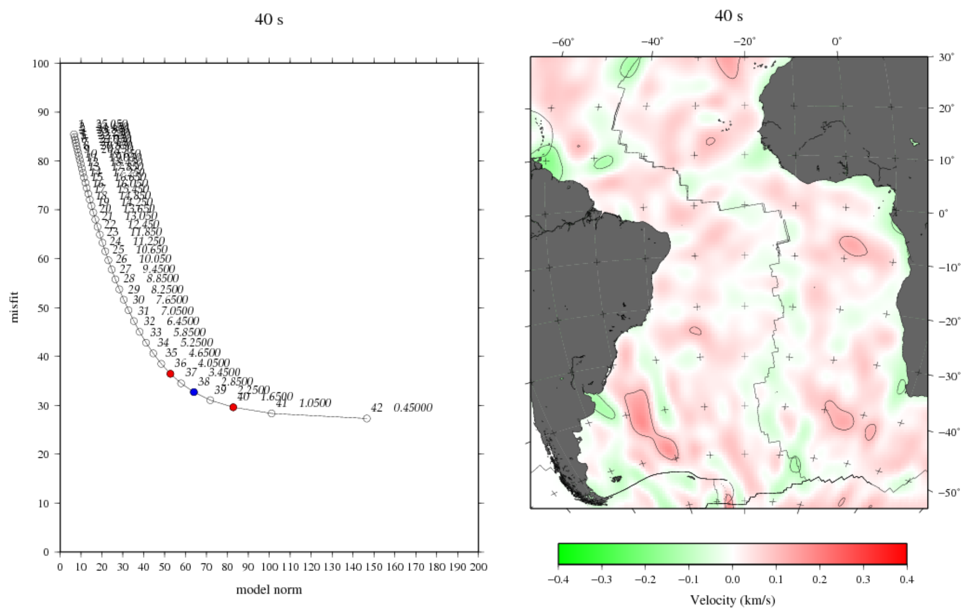

(a) **(b)**

Figure 3.45 Difference map for 40 s between two damping values (36 and 40) shown on (a) trade off curve in red to map (b) the variability in velocity across the region depending on which damping values is chosen. Final model damping value is show on (a) trade off curve in blue

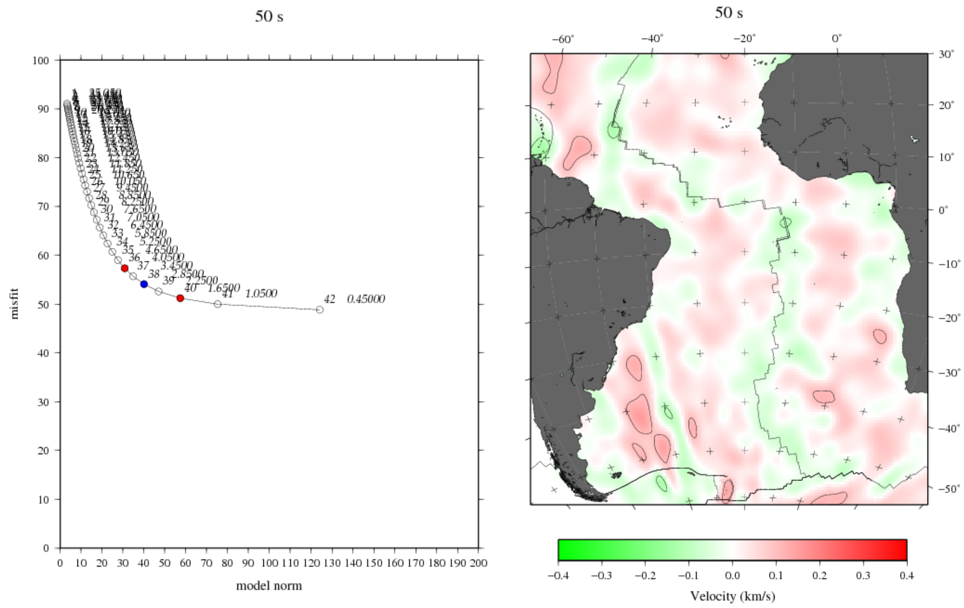

(a) **(b)**

Figure 3.46 Difference map for 50 s between two damping values (36 and 40)shown on (a) trade off curve in red to map (b) the variability in velocity across the region depending on which damping values is chosen. Final model damping value is show on (a) trade off curve in blue

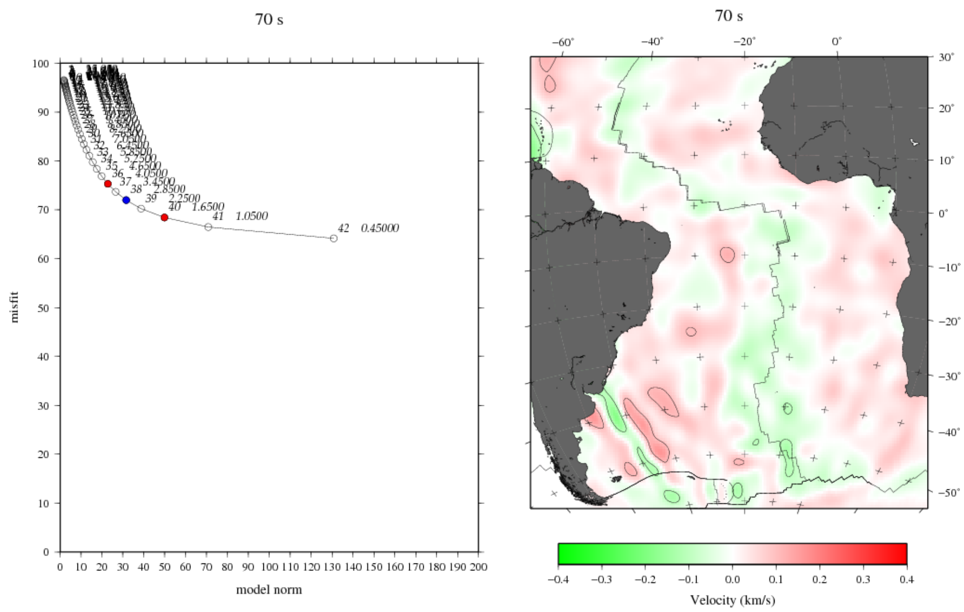

(a) **(b)**

Figure 3.47 Difference map for 70 s between two damping values (36 and 40) shown on (a) trade off curve in red to map (b) the variability in velocity across the region depending on which damping values is chosen. Final model damping value is show on (a) trade off curve in blue

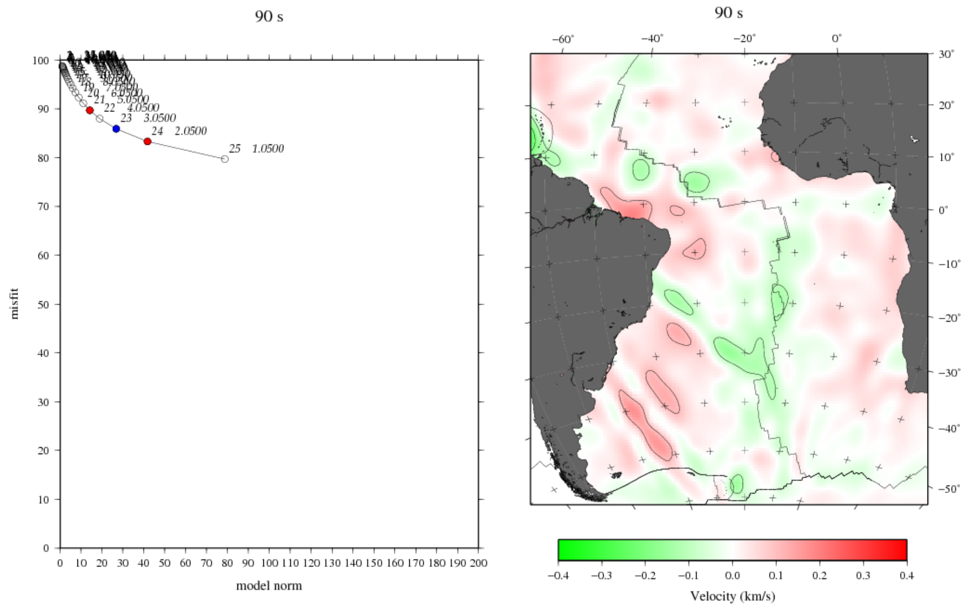

(a) **(b)**

Figure 3.48 Difference map for 90 s between two damping values (21 and 24) shown on (a) trade off curve in red to map (b) the variability in velocity across the region depending on which damping values is chosen. Final model damping value is show on (a) trade off curve in blue

velocity surrounding basin structure(figure 3.32 and figure 3.33). The ocean islands are also well defined as regions of fast velocity. The contrast between the topographic high volcanic features in contrast to the slower velocity sedimentary features is clear. There is a lot of variability in the velocity structure in the sedimentary basins at the shortest periods between 3.2 kms^{-1} and 3.5 kms^{-1}. This becomes less from 22 s (figure 3.34), where less slow velocity features are modelled. At 30 s the Walvis Ridge is modelled as a region of slower velocity but the Rio Grande Rise is not, this may suggest the controls on the Walvis Ridge is more thermal. The continental shelf regions are also picked out at 30 s by regions of slower velocity (figure 3.35).

The ridge is characterised by a slow velocity anomaly associated with the asthenosphere from 40 s in the southern Atlantic, whereas the entire length of both the central and southern Atlantic ridge is only resolved from 60 s (figure 3.36 and figure 3.37). This may be due to a shallower asthenosphere in the south Atlantic compared to the central Atlantic, however, it may also be due to the path coverage and the recoverability of the feature being better in the south. At 40 s the Walvis Ridge and Rio Grande Rise regions are associated with fast velocities. This is in contrast to the slow velocity features recovered by Colli et al. (2013). These fast velocity features are not as pronounced by 60 s. At longer periods, the pronounced asymmetry, which is observed by Silveira et al. (1998) of fast phase velocities beneath the east and slower velocities to the west is absent. By the longest periods (90s and 100 s) there is a uniformity to the structure with some smaller regions of slow velocity off the coast of Africa and South America in contrast to the dominant asthenospheric structure.

The path coverage is good for the region in contrast to previous studies. Mocquet & Romanowicz (1990) included 200 paths in their model of the Atlantic region and Silveira & Stutzmann (2002) included 1300 Rayleigh waves and 600 Love waves for the North and South Atlantic. Colli et al. (2013) performed a full wave form inversion on 4000 paths, resolving a higher resolution model focussed on the South Atlantic. The resolution of the Colli et al. (2013) model begins at 100 km and therefore compliments the group velocity model presented here resolving the shallow structure above 100 km.

The path coverage at shorter periods (14 s -18 s) is not ideal and the reliability of these models along with the model for the longest periods (90 s- 100 s) is less. The best periods for reliability and path coverage are 20 s - 80 s. This is reflected in the error calculated in table 3.3, the number of paths included in each model (figure 3.31) and the variations in the difference maps (section 3.4.4).

Chapter 4

Velocity Structure

In the previous chapter, frequency time analysis provided estimates of the group velocity dispersion for 14,000 seismograms. These were then combined within the tomographic inversion to provide information on the regional variations in group velocity for periods from 14 s to 100 s. The next step is to obtain the velocity structure with respect to depth as this information is much more useful for interpreting crustal and lithospheric structure. As discussed in section 3.5 the velocity dispersion map for each period is sensitive to a range of depths, the depth and range of sensitivity increases with respect to the period length. Additionally the sensitivity for each period varies dependant on the velocity structure which it is travelling through and therefore, a direct comparison of period map to a particular depth has limited validity.

A dispersion curve for each individual point in the region can be extracted from the group velocity tomography and inverted to obtain a 1-dimensional (1-D) shear velocity structure. By combining these 1-D models a 3-D velocity model of the region can be constructed for further interpretation (e.g. Acton et al., 2010; Eaton & Darbyshire, 2010). The specific approach taken to convert the group velocity dispersion curves into shear velocity - depth models is the key focus of this chapter. Complications for this approach include; the inclusion of a suitable water layer, the effect of the starting model on the results, and the choice of an appropriate parametrisation and regularisation scheme.

Previous work taking this approach includes studies in Hudson Bay (Eaton & Darbyshire, 2010), India (Acton et al., 2010) and the South China Sea (Tang & Zheng, 2013). Oceanic regions are more complicated compared to continental regions because a water layer must be taken into account. Rayleigh waves are sensitive to the water layer due to the P wave component. The depth of the water layer is important for fitting shorter periods (Lay & Wallace, 1995). In studies where a water layer has not been included (e.g. Acton et al., 2010; Tang & Zheng, 2013) the resulting crustal thickness modelled is thicker than the expected oceanic crust. For example Acton et al. (2010) observed the crust in the Indian Ocean to be up to 15 km thick in places. However, this study focused on the Indian continent and the interpretation of the oceanic crust is limited.

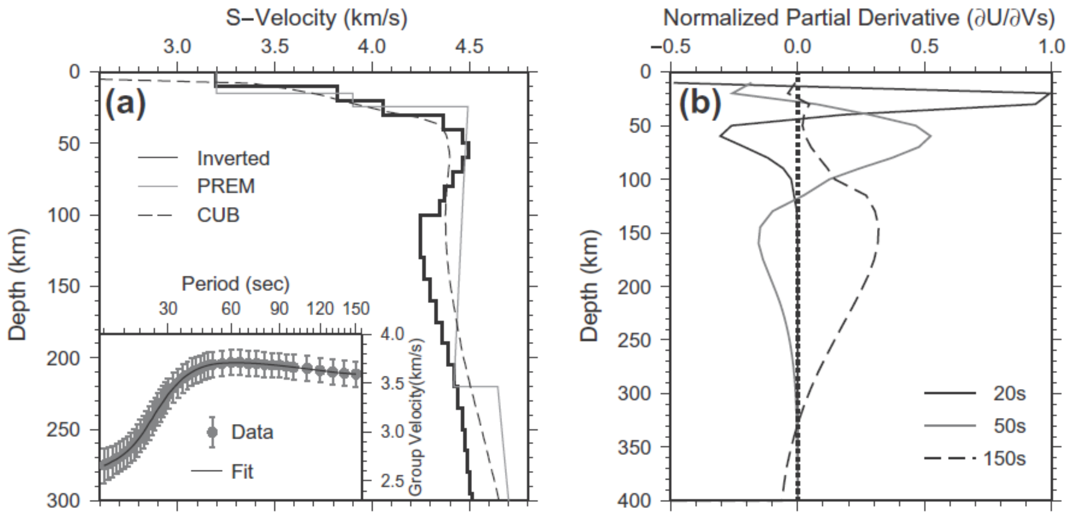

Figure 4.1 Figure taken from Tang & Zheng (2013) showing (left) the average starting model velocity structure and (right) the partial derivatives for 20 s, 50 s and 150 s, highlighting the negative oscilations

Additionally, a significant challenge in modelling the shallow structure is the instabilities of the group velocities seen at shorter periods when inverted. Figure 4.1 shows the partial derivatives for an inversion by Tang & Zheng (2013). This shows a negative portion of the 20 s period sensitivity kernel between 50 km and 100 km. A change in the velocity model in the inversion to fit this period would either be a positive change above 50 km or could result in a negative velocity change at 50 km to 100 km. This can result in geologically unreasonable models such as high velocities in the crustal structure or lower velocities at depth. It is sometimes hard to differentiate between an anomaly and a stable inversion. The partial derivatives must be considered when interpreting the velocity model.

The two key programs used from the Computer Programs in Seismology package (Herrmann & Ammon, 2002) are sdisp96 and surf96. sdisp96 takes a given velocity model and calculates the group and phase velocity dispersion curves which would be expected for the velocity structure in the input model. The input model can be anything from a simple half space (although this structure would have no dispersion associated with it) to a velocity model of varying layers such as CRUST 2.0 or PREM. The output can be plotted as a single dispersion curve for the 1-D velocity model. The periods output are variable and can be chosen and set by the user.

surf96 is a programme to invert dispersion curves to obtain a 1-D shear velocity model with respect to depth. The choice of starting model is important to the inversion because the model is inverted from the starting structure. A linear least squares inversion was chosen to invert the velocity structure. It means the fit to the data is improved on each iteration by inverting the previous model in the iteration sequence. This can be iterated for a chosen number (n) iterations to improve the residual fit. The choice of other parametrisation and regularisation are also important to the resulting output model. These are further discussed in the following section.

There is a trade off between a degree of *a priori* knowledge in the starting model and biasing the resulting output model by the use of this prior knowledge. The inversion needs freedom to fit the data without too much bias from a starting model. Having a single velocity half space model (e.g. Acton et al., 2010) of mantle velocity may not give enough *a priori* information for the inversion to resolve a 10 km thick crustal layer through a 300 km thick profile. There are many Earth models and crustal models which add different levels of *a priori* information to the inversion. The choice of model in this study is discussed in section 4.2.2 along with tests assessing the affect on the final model. In addition to the starting model the inversion can be run for a flat or spherical Earth model.

The choice of starting model affects the regularisation of the inversion, the number of layers, the layer thickness and velocity. In surf96 there is the option to fix the velocity and invert for layer thickness or to fix the layer thickness and invert for velocity. The choice of starting model influences the approach taken in the inversion. For example, if you have a single half space velocity of equal layer thickness, inverting for layer thickness is counter intuitive and therefore setting the inversion to invert velocity only is sensible to gain an output model with variable velocity for the velocity structure. If *a priori* knowledge is used for a crustal layer, setting the inversion to invert for layer thickness would give the inversion freedom to stray from the original *a priori* model and fit the data for a varying crustal thickness.

Unlike the inversion for the tomography where a series of models were run with different damping parameters and a final model was chosen from a tradeoff curve, the inversion with surf96 requires a single damping value to be chosen at the start of the inversion. The damping value controls how much each iteration of the model varies from the starting model to fit the data. A lower damping factor would decrease the misfit to the data on each iteration more than a higher damping factor. It would also cause greater variation from the original starting model. Testing is therefore done on a series of damping factors (see section 4.2.1). The inversion can also be set with smoothing or no smoothing depending on what the resulting output model required is.

A weighting can be applied to each layer within the starting model, to either fix the velocity and thickness of the layer to that of the starting model, or to increase the emphasis to change that layer within the inversion. It was decided that the only layer to change the weighting for in this study was the water layer. This was fixed with a weighting of 0 and therefore the velocity and thickness were not allowed to vary. This is because the average depth of the water layer is known and should be included. All the parametrisation and regularisations were tested and are discussed in section 4.2.1.

4.1 Forward modelling - Predictions from Crust 2.0

Prior to inverting the group velocities, an initial test was done to compare the tomography dispersion maps with *a priori* information. The following section discusses a comparison with dispersion characteristics obtained from forward modelling of Crust 2.0 model (Bassin & Masters, 2000). The Crust 2.0 model was compiled using reflection and refraction data published before 1995 to produce a global 2 °model of crustal thickness. In regions, where the data is poor, the structure is estimated based on a statistical method using the age of the crust and the geological setting. Crust 2.0 has seven layers; ice, water, soft sediment, hard sediment, upper, middle and lower crust along with an upper mantle velocity for any given point of latitude and longitude. The sedimentary thickness is within an error of 1 km and the crustal thickness is within a error of 5 km. The water depths are interpolated from the ETOP05 model. The mantle velocities for Crust 2.0 were extended to 200 km depth above a half space asthenospheric velocity (4.8 kms^{-1}).

The dispersion characteristics of the Crust 2.0 model were calculated using sdisp96 for all periods modelled in chapter 3 (14 s to 100 s). Figure 4.2 shows the variation in velocity between the Crust 2.0 dispersion from 30 s to 40 s (a) and 50 s (b). The main region of variation is along the continental margins; the velocity structure in the oceanic region is negligible. The variations between 30 s and 50 s (figure 4.2) are small under oceanic regions, seeing the stronger mantle signature which in the crust 2.0 model is uniform. Therefore, to show dispersion maps for periods greater than 30 s would result in no additional insights between the crustal structure modelled by this study and Crust 2.0.

Figures 4.3 and 4.4 show the velocity dispersion maps calculated from the Crust 2.0 model compared to the tomographic velocity dispersion maps using the data obtained from chapter 3. The overall distribution of velocities are similar in the tomographic models and the Crust 2.0 predictions, which is promising. At the shortest periods (14 s and 16 s) the ocean islands are clearly picked out as faster velocities as well as the ridge itself (figure 4.3). This corresponds to the broad features seen in the tomographic data. The mid ocean ridge in the northern region is also much less of a broad feature than the southern region in both the Crust 2.0 velocities and the tomographic models. At 16 s there is a larger variation in velocities and the continental shelf feature is defined as a slower velocity for Crust 2.0 (figure 4.3 c).

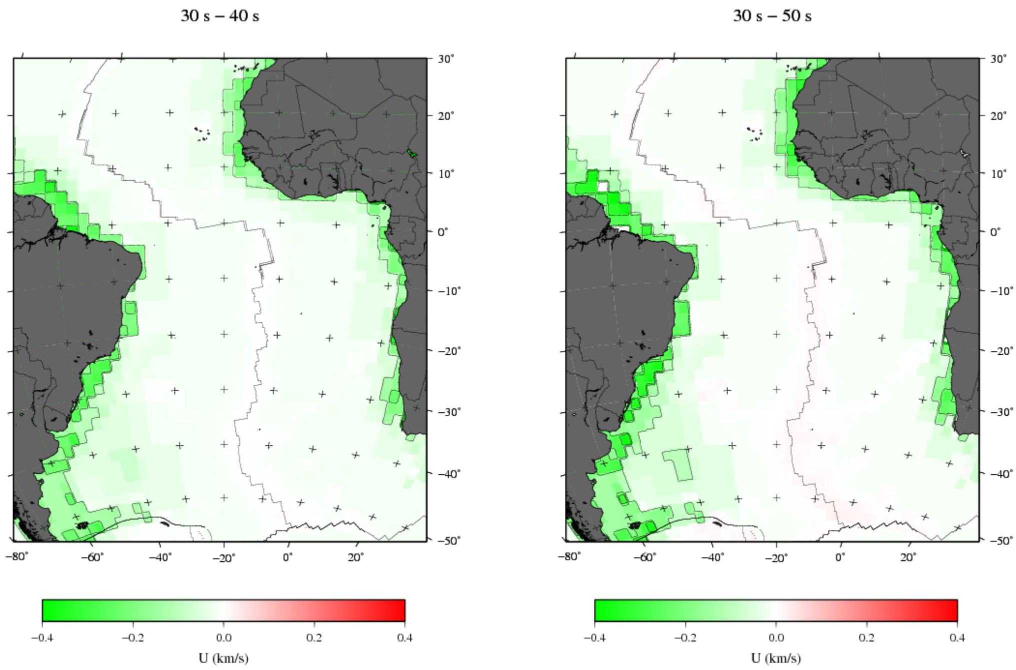

(a) **(b)**

Figure 4.2 Difference maps between Crust 2.0 dispersion maps for longer periods between (a) 30 s and 40 s and (b) 30 s and 50 s highlighting the small variations associated with the crustal structure at these periods

The fast velocity from the ridge begins to spread out at the longer periods (20 s - 30 s) with the ridge and ocean islands becoming less defined (figure 4.4 a and c). There is no definition of the Cameroon Volcanic line (either fast or slow) in Crust 2.0 as observed in the tomography at 30 s (figure 4.4 a and b). Other topographic features such as the sea mounts (e.g. Walvis Ridge) and the mid ocean ridge are still defined down to 30 s but not as clearly as the shortest periods (figure 4.4 a and c). At the longer periods we do not see a low velocity region beneath the ridge in the Crust 2.0 predictions as seen in the tomographic inversions. This is due to the uniform mantle beneath the Crust 2.0 model as previously stated.

To compare the predictions from Crust 2.0 with the tomography data more quantitatively, the tomography velocities were subtracted from the Crust 2.0 predicted velocities to produce velocity difference maps which can be seen in figure 4.5. At 14 s the velocities for the tomographic model are predominately faster than Crust 2.0 (figure 4.5 a, green areas), while at 16 s this relationship is reversed (figure 4.5 b, red dominated areas). However, given the similar depth sensitivity of these two periods, it is very difficult to explain this feature with a reasonable velocity structure. This may suggest an error is in the dispersion data, most likely linked to the residual uncertainties for 14 s (section 3.4.2.)

As the periods increase, the differences become more defined with a positive variation beneath the ridge and at the edges of the oceanic regions. There are still variations of up to 0.4 kms^{-1}. At 20 s (figure 4.5 c) the continental shelf and sedimentary basin regions have a very positive anomaly associated with them, the velocities observed in the tomographic model is much slower (up to 0.4 kms^{-1}) than the velocities in Crust 2.0. Slower velocities than the predicted velocities at this period, which is still predominately sensitive to shallow depths would suggest either, slow crustal velocities, slow underlying mantle velocities or thicker crust than Crust 2.0. By 30 s (figure 4.5 d) we observe the ridge and sea mount as a clear positive difference which has become more dominant compared with the surrounding negative features, suggesting the velocities observed are slower than Crust 2.0 predicts.

Although a direct comparison of the dispersion maps for Crust 2.0 and longer periods was deemed unnecessary, mapping the differences highlights the variations between a uniform mantle and the observed tomographic models. Figure 4.6 show the velocity differences at 50 s and 70 s, which shows the ridge being the dominant positive anomaly. The dispersions maps for Crust 2.0 and the tomographic models are different but they diverge more after 50 s as the effects of the crustal layers become less and the mantle signature becomes greater.

The most notable differences between Crust 2.0 and the dispersion from the tomography occur close to the ridge and the continental margins. The likely cause of these discrepancies are variable crustal thickness and a heterogeneous mantle. It is therefore clear that the group velocities must be inverted from the tomography to obtain the velocity structure with respect to depth.

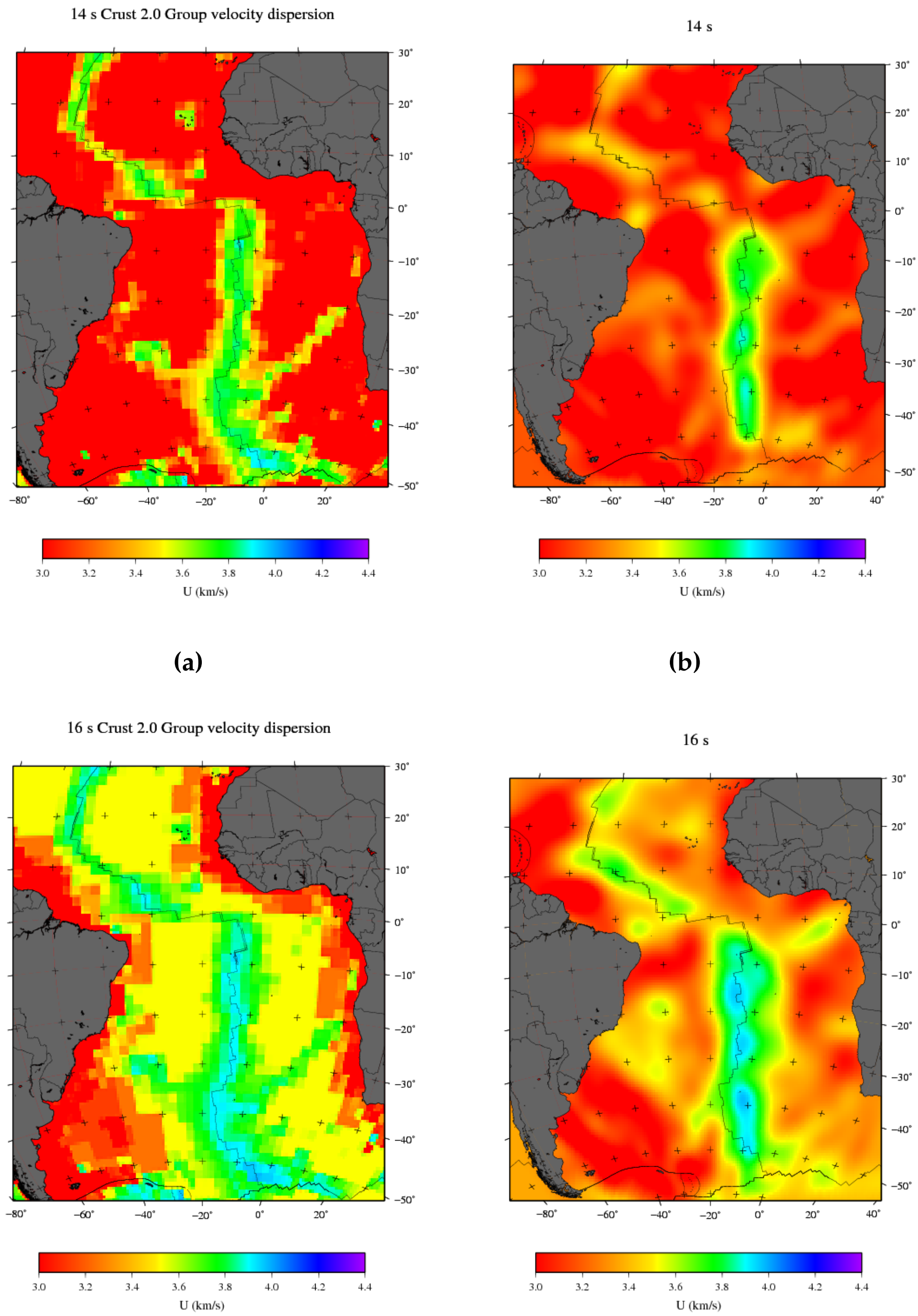

(a) (b) (c) (d)

Figure 4.3 Crust 2.0 dispersion maps and the final tomography models for comparison respectively for (a and b) 14 s and (c and d) 16 s

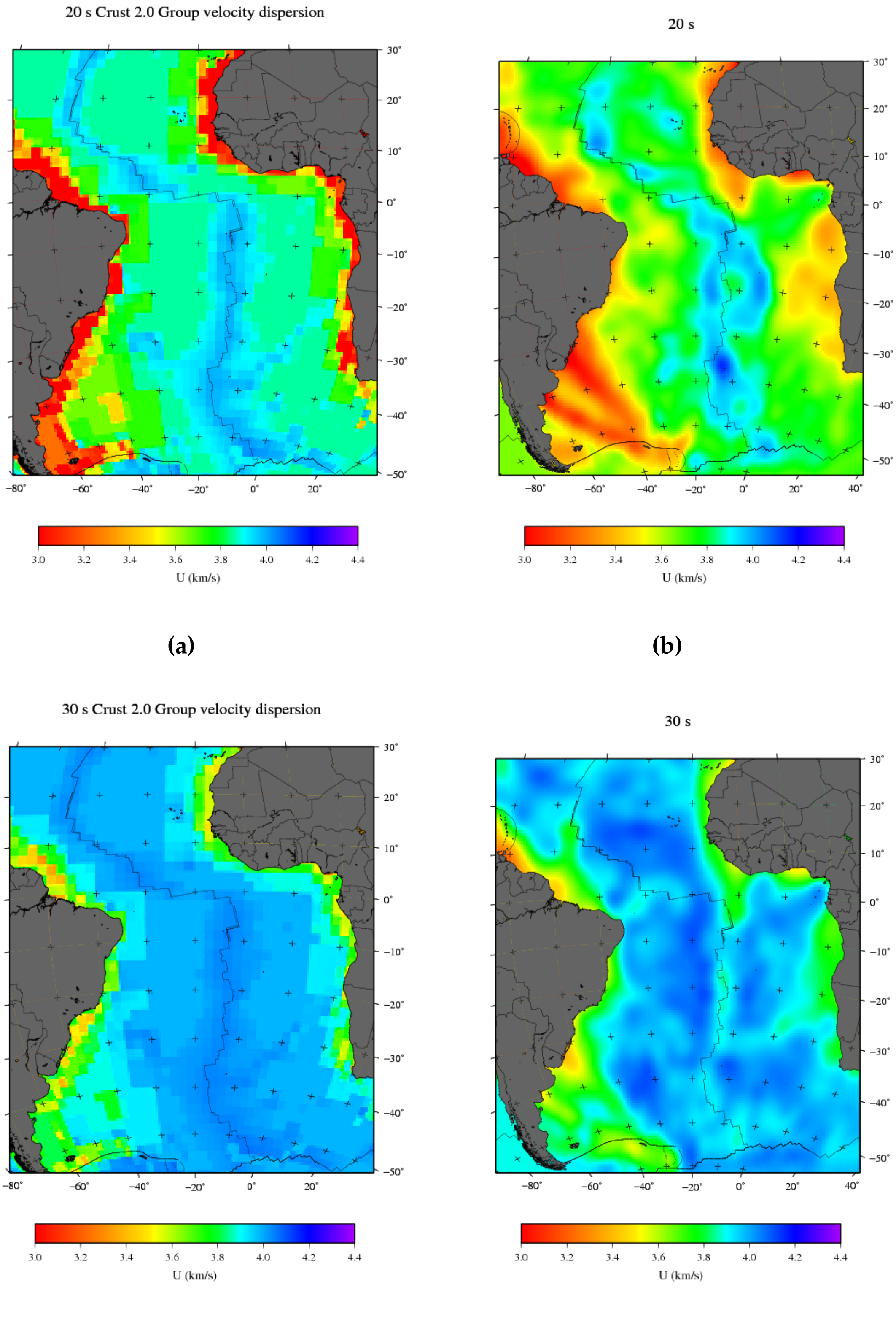

(a) **(b)**

(c) **(d)**

Figure 4.4 Crust 2.0 dispersion maps and the final tomography models for comparison respectively for (a and b) 20 s and (c and d) 30 s

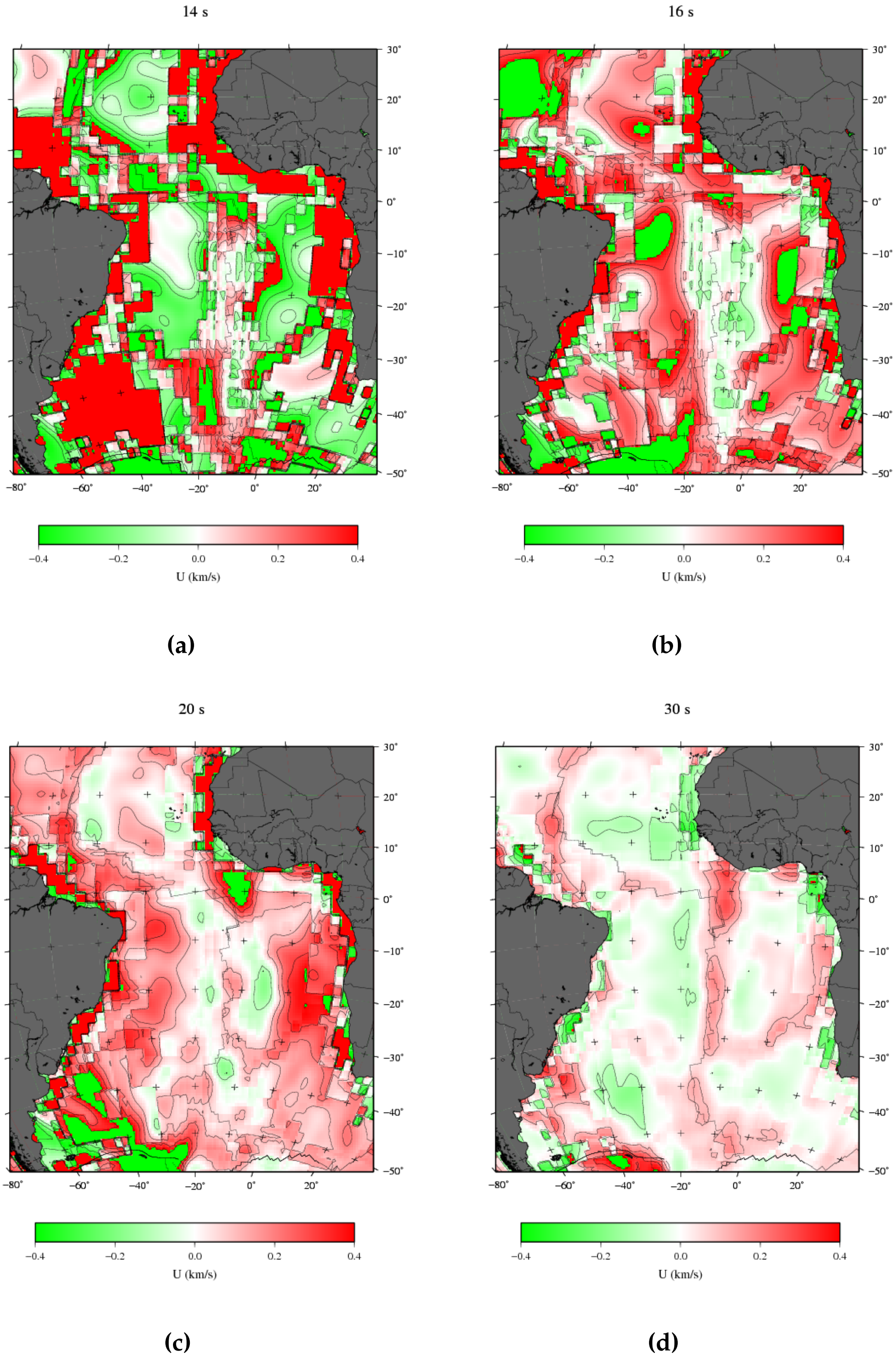

Figure 4.5 Difference maps between Crust 2.0 dispersion models and the tomographic dispersion models for further comparison highlighting crustal velocity structure variations for (a) 14 s (b) 16 s (c) 20 s and (d) 30 s

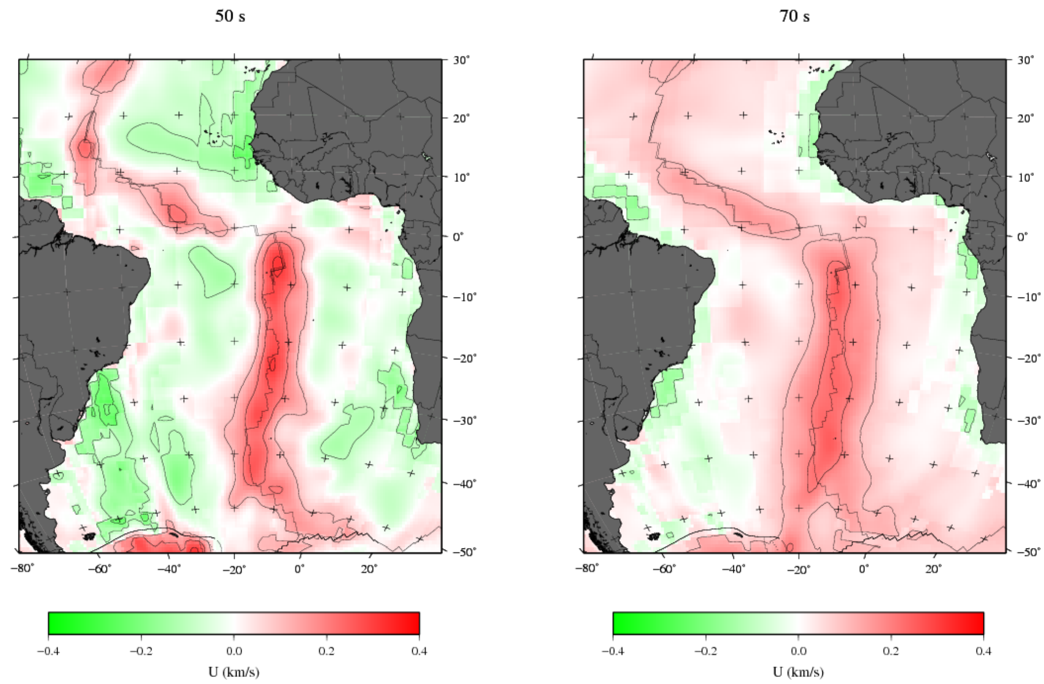

(a) **(b)**

Figure 4.6 Difference maps between Crust 2.0 dispersion models and the tomographic dispersion models highlighting mantle velocity structure variations for (a) 50 s and (b) 70 s

4.2 1-D inversion

Before inverting for the shear velocity structure with respect to depth, a suitable starting velocity model and parametrisations must be tested. A series of tests were carried out to determine which parameters to use in the inversion and what was a suitable starting velocity model. These tests are discussed in the next two sections (4.21 and 4.2.2). A profile along the latitude of 20 °south was chosen to carry out these tests because of the good path coverage for all points and the geological settings it traverses; continental, shelf, basin and ridge.

The velocity dispersion curve which will be inverted is composed for each 1D profile (latitude and longitude) of the group velocity at that point extracted from each group velocity dispersion tomography map with respect to period. Each velocity is also assigned an error value. The error value was taken from the difference maps in section 3.4.4. Because these maps show the difference between the maximum suitable damping value and the minimum and the value chosen lies between the two, the error assigned to each point was half the difference. The initial dispersion curve consisted of a group velocity value for each of the following periods; 14 s, 16 s, 18 s, 20 s, 22 s, 24 s, 26 s, 28 s, 30 s, 34 s, 36 s, 40 s, 44 s, 46 s, 50 s, 60 s, 70 s, 80 s, 90 s and 100 s.

4.2.1 Model parameter tests

Damping parametrisation

As with the tomographic inversion the damping of the shear velocity inversion is a trade off between the misfit to the data and the deviation from the starting model. There is more constraint on the inversion with a higher damping value as opposed to a lower damping value. The damping values were tested for 1, 2, 3, 4, 5, 10, 15 and 20 for a simple half space starting model of 4 kms^{-1}. The test runs were performed for a single iteration for the 20 °south line with no smoothing.

Figure 4.7 shows the results of the tests. The greatest variation between models with different damping parameters is seen at 50 °west within the continent of South America. Different responses to the damping values are seen in the abyssal plain region, 30 °west and 5 °east (figure 4.7 b and d) which could suggest the dispersion curves for each of the points are still variable and the velocity structure could differ from the east to the west. 12 °west is the ridge region where less variation between models is noted.

There is a key feature on all the models; a jump in velocity at 50 km depth and 120 km depth. These features were tested by changing the model layers, extending the 2 km layers to a depth of 90 km and reducing the number of 20 km layers at the base of the model (figure 4.8). The jump in velocity continues to occur at the change in layer thickness, from 2 km thick to 5 km thick and to 20 km thick layers. This must be considered during interpretation, as the structure of the layers needs to be reasonable for the expected velocity structure. 2 km thick layers at shallow depths are required to try and define shallow structure (for example the 10 km thick crust). But at deeper depths thicker layers are reasonable and reduce the total number of layers in the model. A model with 150 layers increases the processing time for the inversion unnecessarily.

It may also highlight velocity variations at depths which are too small to be reasonably detected given the wavelength of the longer periods.

The initial damping value chosen was 5; from these simple tests the variation in the model was deemed reasonable. As more variable velocity layers were included in the velocity structure, a damping of 5 was found to not constrain the crustal structure. This was investigated and is discussed further in section 4.2.2.5.

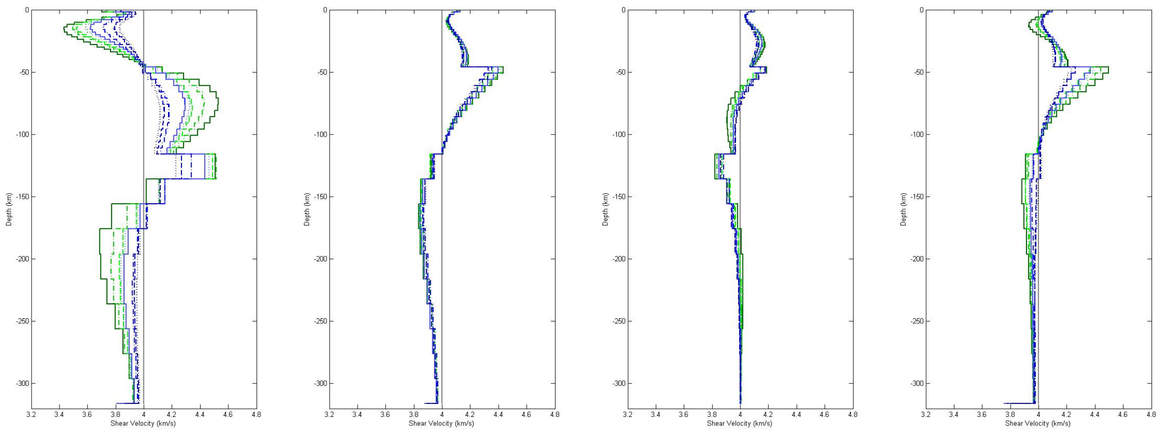

(a) **(b)** **(c)** **(d)**

Figure 4.7 Damping tests for points along the 20 °south profile (a) 50 °west (b) 30 °west (c) 12 °west and (c) 5 °east for damping values of 1 (dark green solid), 2 (medium green dot-dashed), 3 (medium green dashed), 4 (light green dotted), 5 (blue solid), 10 (dark blue dot-dashed), 15 (dark blue dashed) and 20 (blue dotted)

Flat or Sperical Earth model

The inversion can be performed for a flat Earth or a spherical Earth. A flat Earth would make the inversion simpler, not taking into account the curvature of the Earth and the convergence of points at depths. The size of the region and depth of the model are key in deciding which Earth model to use. If inverting for just the shallow structure a flat Earth would suffice because there is not the convergence of profiles at depth to considered. The same applies to the size of the region, a small region would not be affected by the curvature of the Earth in the same way that a large region would. The simple single half space starting model was inverted for both a flat and a spherical Earth model to see what affect the change in Earth model had on the resulting velocity

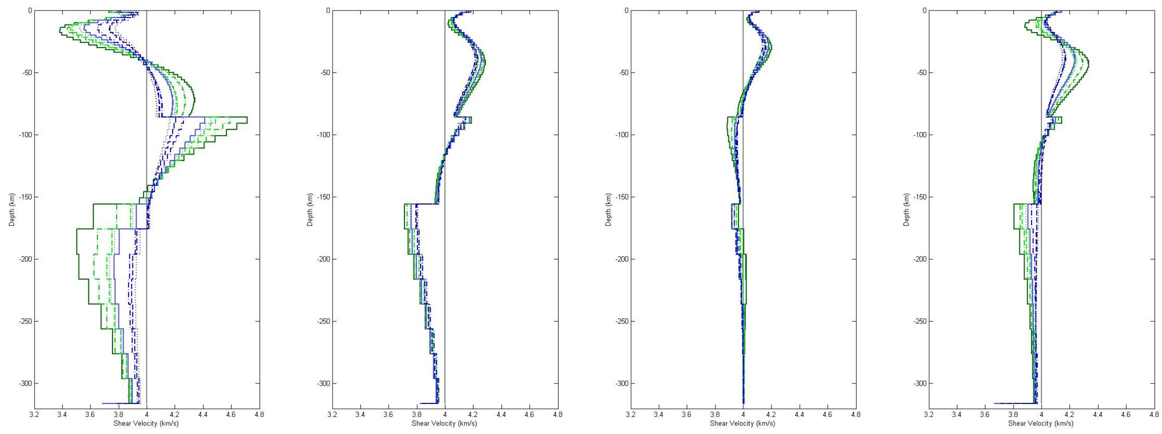

(a) (b) (c) (d)

Figure 4.8 Damping tests for points along the 20 °south profile extending the 2 km layers to 90 km depth (a) 50 °west (b) 30 °west (c) 12 °west and (c) 5 °east for damping values of 1 (dark green solid), 2 (medium green dot-dashed), 3 (medium green dashed), 4 (light green dotted), 5 (blue solid), 10 (dark blue dot-dashed), 15 (dark blue dashed) and 20 (blue dotted)

model. Each point was inverted for 10 iterations at a damping value of 5. The results can be seen in figure 4.9. It is at depths greater than 100 km where the change in velocity structure linked to the starting model is most apparent. Also at shallower depths for 50 °west and 5 °west there are variations between the models. There is no geological link to these two regions, although both exhibit a good fit to the data. The spherical model has a better overall residual fit to the data compared with the flat Earth model (figure 4.10). It was decided based on these tests that a spherical Earth model would be used given the size of the region. It is most appropriate theoretically and it has the best fit to the data (figure 4.10).

4.2.2 Starting model

A series of tests were carried out to determine which starting model to use. As discussed earlier, there is a need to balance allowing freedom in the inversion to fit the data and a starting model which is close enough to a real Earth to counter the possible instabilities in the inversions of group velocities. A series of tests were run using the 20 °south profile for various starting models to observe what the effects were on the inversions and how well the final model fitted the data. A good fit to the data is

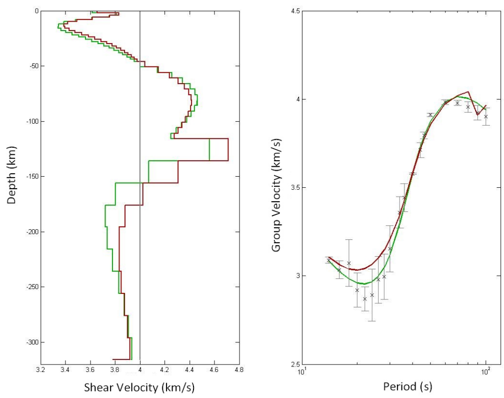

(a)

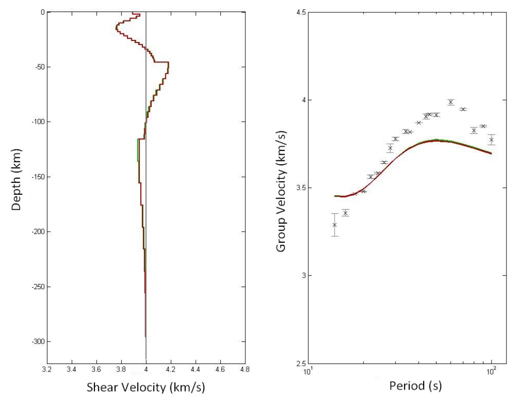

(b)

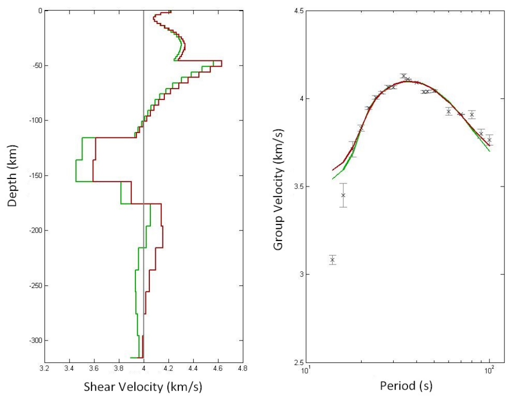

(c)

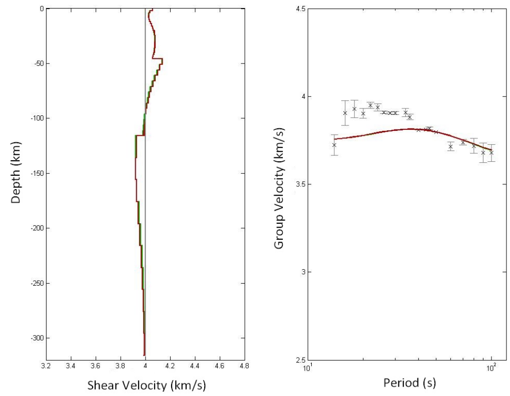

(d)

Figure 4.9 Inverted 1-D models for test profile 20 °south for spherical (green) and flat (red) Earth models at (a)50 °west, (b) 38 °west, (c) 20 °west, (d) 14 °west, (e) 10 °west, (f)5 °west, (g) 10 °east and (h) 20 °east inverted for 10 iterations

desired alongside a reasonable velocity structure. Due to the diversity of tectonic features/velocity structure (e.g. sea mounts, the mid ocean ridge and continental shelf) along the profile, the crustal and mantle velocities and crustal thickness in the starting model are important. The tests were run to find the best starting model from; (i) a single half space velocity with no water layer (as seen in Acton et al., 2010), (ii) a single half space velocity with the addition of a uniform water layer of 4 km, (iii) a starting model inverted from the regional average velocity and a half space starting model with a water layer of 4 km (e.g. Tang & Zheng, 2013), (iv) PREM with a uniform water layer of 4 km, and (v) Crust 2.0. Crust 2.0 has a water layer which varies across the region, and no water layer in continental regions.

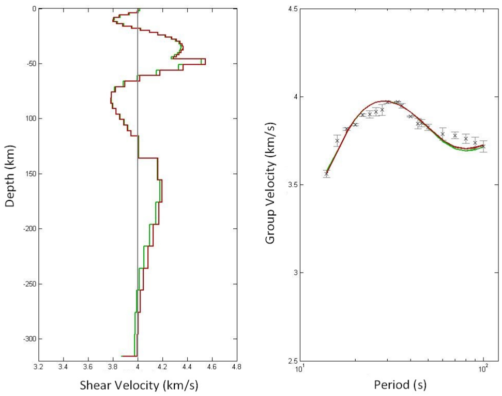

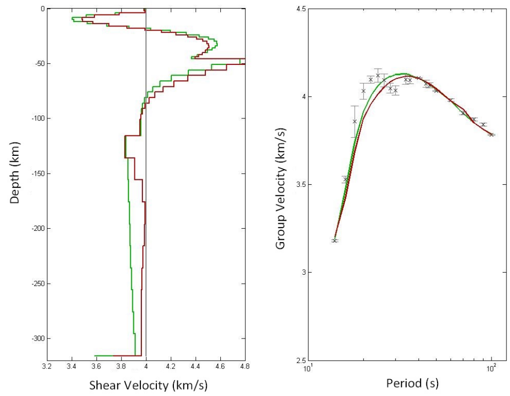

(e) **(f)**

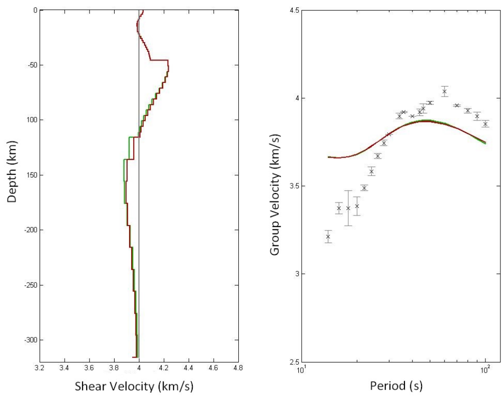

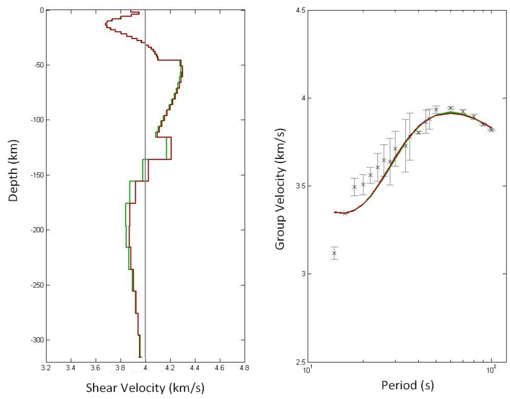

(g) **(h)**

Figure 4.9 Continued

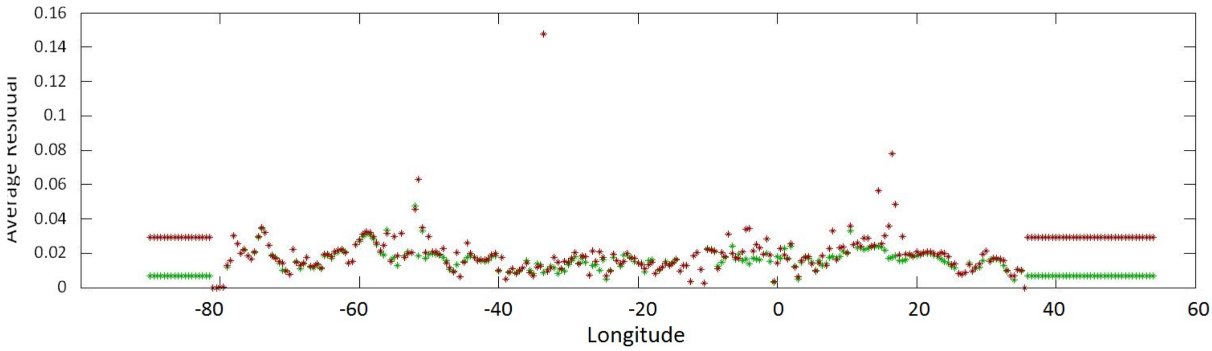

Figure 4.10 Average residual fit (km/s) to the final model for each point along the 20 °south profile for the spherical model (green) and the flat model (red). Flat ends show the end regions where the model is out of the range of the tomographic data and is therefore the regional average inverted for depth.

(i) Half space; no water layer

The first model tested is the simplest starting model, a single velocity consisting of 23 layers of 2 km to allow as much variation in the shallower structure, 14 layers of 5 km and 10 layers of 20 km to take the model to a depth of 316 km. 4 kms^{-1} was chosen as an average between crustal and mantle velocities. Starting with the simplest model reduces the amount of bias towards structure in the starting model. The half space model was inverted for both 10 and 20 iterations to see how much the fit improved to the data based on the number of iterations run. The damping applied to the inversion was 5 and there was no smoothing applied to the inversion to allow each layer more freedom in the inversion.

Running 20 iterations provides an overall better fit to the data along the profile than 10 iterations, however, it is still not a good fit for all the models (figure 4.12). Some locations show a reduction in velocity at shallower depths. In contrast there are some points, for example 14 °west and 10 °east (figure 4.11d and g) where there is little or no velocity below 4 kms^{-1} at shallow depths. These velocity models coincide with poor data fit. The models output are not geologically reasonable as variations in crustal structure are not modelled.

(ii) Half space; including water layer

The next test took the simple single velocity structure and added a water layer. The water layer is 4 km thick, based on the average depth of the water in the Atlantic abyssal regions. There is a small improvement along the profile to the residual fit of the data (figure 4.14) but the structure recovered by the inversions is still too fast at shallow depths (figure 4.13). The inclusion of the water layer appears to have increased the velocities in some of the models at shallow depths from the half space model without a water layer and not constrained the velocities to more reasonable slower crustal velocities (figure 4.13). Again there are points where there is virtually no fit to the data. To obtain a crustal structure of the region a level of bias towards slower velocities at shallow depths is required.

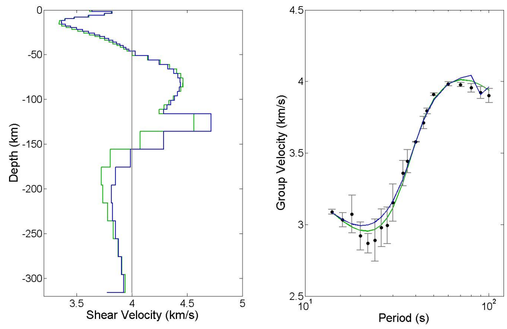

(a)

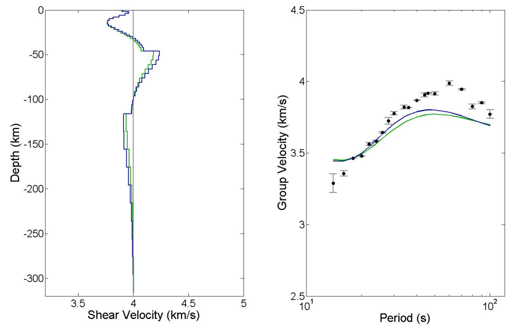

(b)

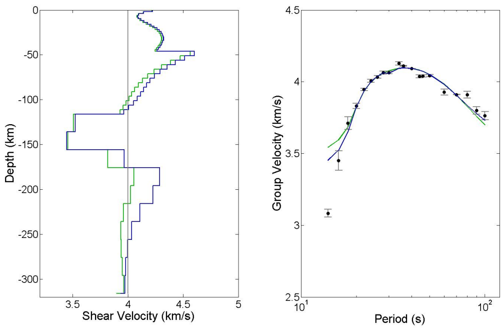

(c)

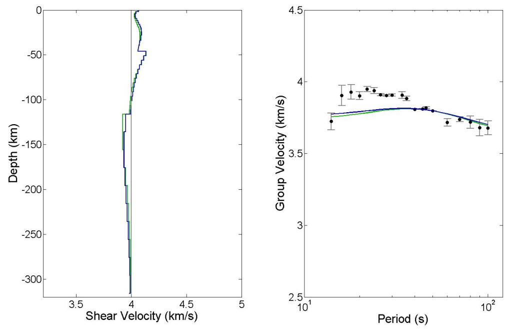

(d)

Figure 4.11 Inverted 1-D models for test profile 20 °south for a half space starting model at (a)50 °west, (b) 38 °west, (c) 20 °west, (d) 14 °west, (e) 10 °west, (f) 5 °west, (g) 10 °east and (h) 20 °east inverted for 10 iterations (green) and 20 iterations (blue)

(iii) Regional average

To obtain slower velocities at shallower depths the next step was a simple model based on regional average structure of the region from the dispersion data to try and maintain little bias by using *a priori* knowledge. The regional average group velocity for each period were combined to produce a dispersion curve (figure 4.15 a). This regional dispersion curve was inverted using a smoothed inversion, and a half space with a water layer of 4 km as a starting model. The inversion was iterated until the residual fit to the data did not change from the previous iteration. By running n number of iterations until the average residual does not change, the model can no longer be improved with further iterations (figure 4.15 b). The resulting regional starting model velocities are still at 4 kms^{-1} at the crustal depths and therefore the improvement to the geological structure is minimal (figure 4.15). However, this velocity model was then used for an

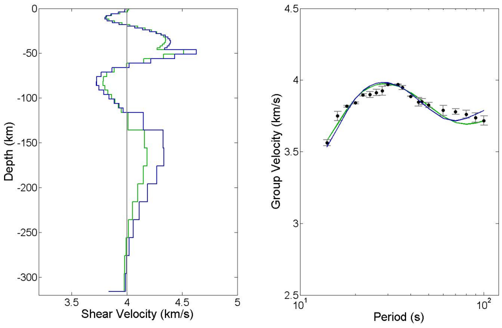

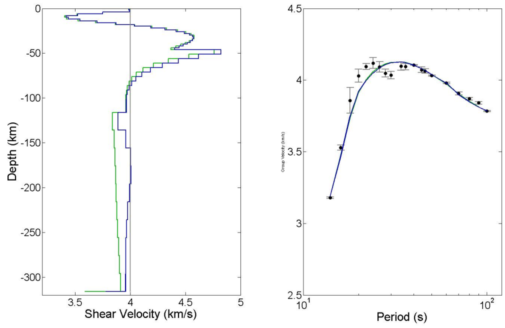

(e) **(f)**

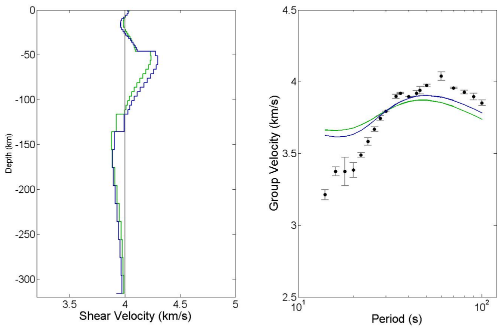

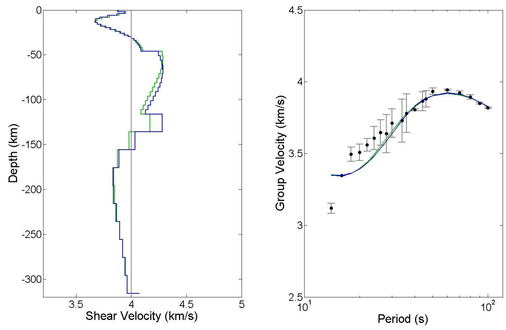

(g) **(h)**

Figure 4.11 Continued

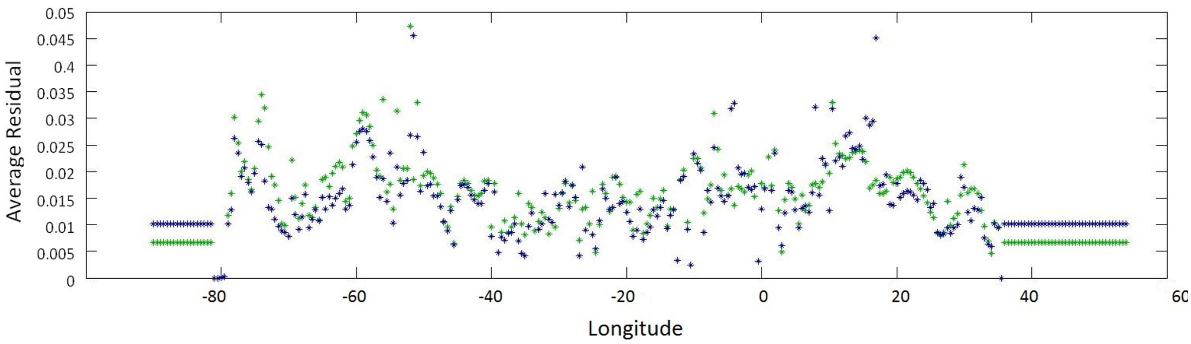

Figure 4.12 Average residual fit (km/s) to the final model for each point along the 20°south profile for a half space starting model after 10 iterations (green) and 20 iterations (blue). Flat ends show the end regions where the model is out of the range of the tomographic data and is therefore the regional average inverted for depth.

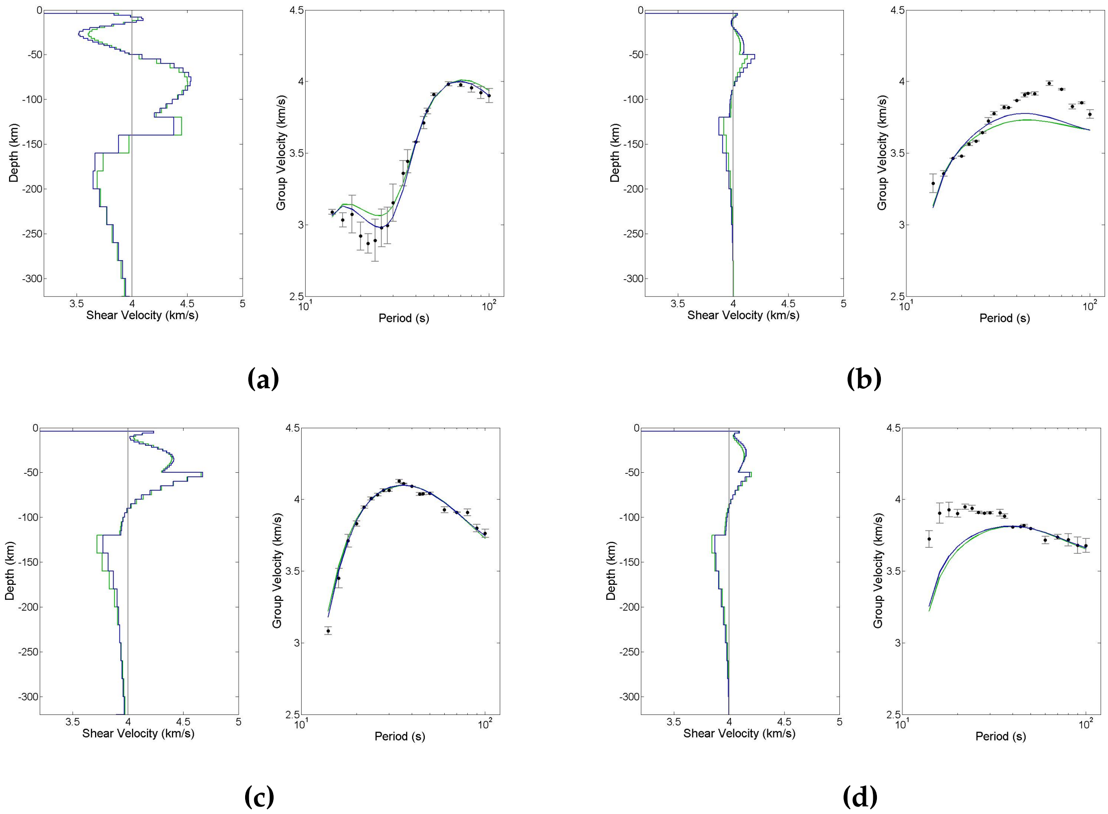

Figure 4.13 Inverted 1-D models for test profile 20 °south for a half space starting model with a 4 km water layer at (a) 50 °west, (b) 38 °west, (c) 20 °west, (d) 14 °west, (e) 10 °west, (f) 5 °west, (g) 10 °east and (h) 20 °east inverted for 10 iterations (green) and 20 iterations (blue)

inversion along the profile to investigate if the change in starting model varied the velocity structure and by how much.

The model from the regional average was then used as the starting model for the inversion. An unsmoothed inversion was run for 10 iterations, 20 iterations and for $\text{residual}_n - \text{residual}_{n-1} = 0$, so that each point was inverted for n iterations (figure 4.17 b). The output models (figure 4.16) are overall comparable with the velocity models from the single half space with water (figure 4.13). The most notable point where an improvement to the dispersion curve fit is 38 °west (figure 4.16 b) where there is least variation from the starting model. There is an overall improvement to the fit of the data to the models for all inversions run. The best improvement to the fit of the data is for n iterations, where as a set number of iterations does not fit so well (for example between -60 and 40 and 10 and 20).

There is still not a well defined crustal structure from this starting model. The

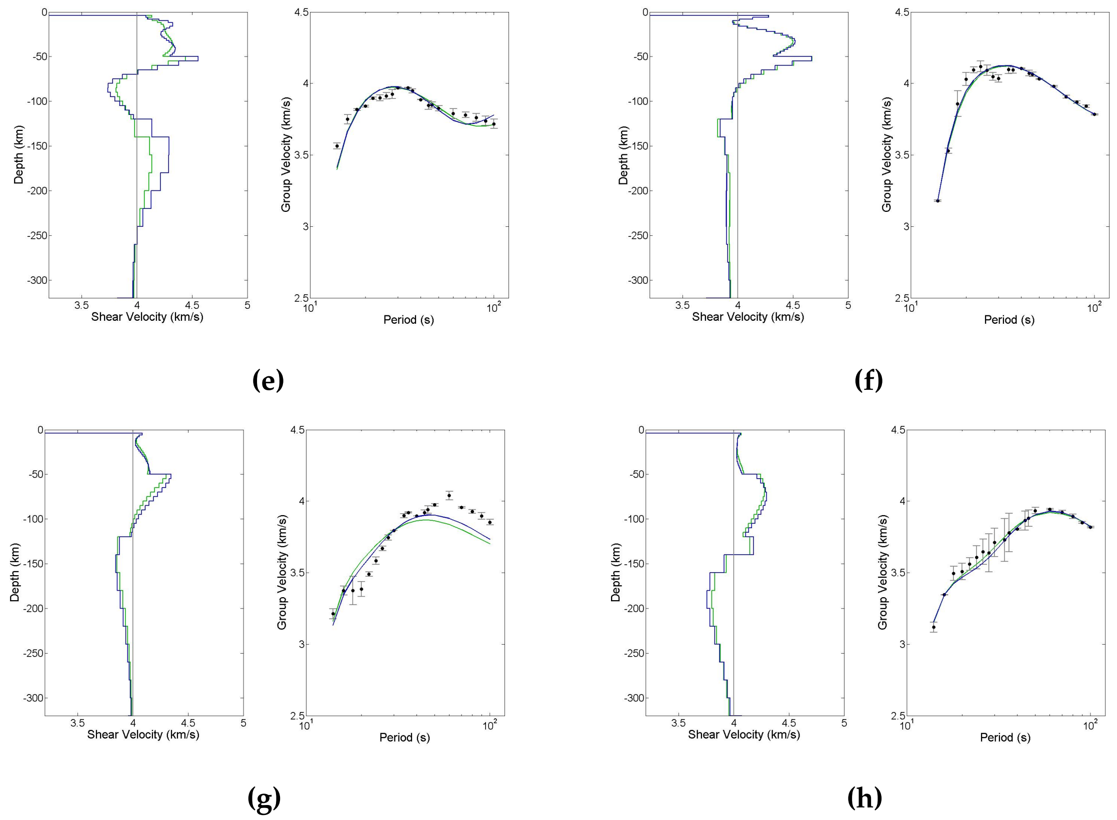

Figure 4.13 Continued

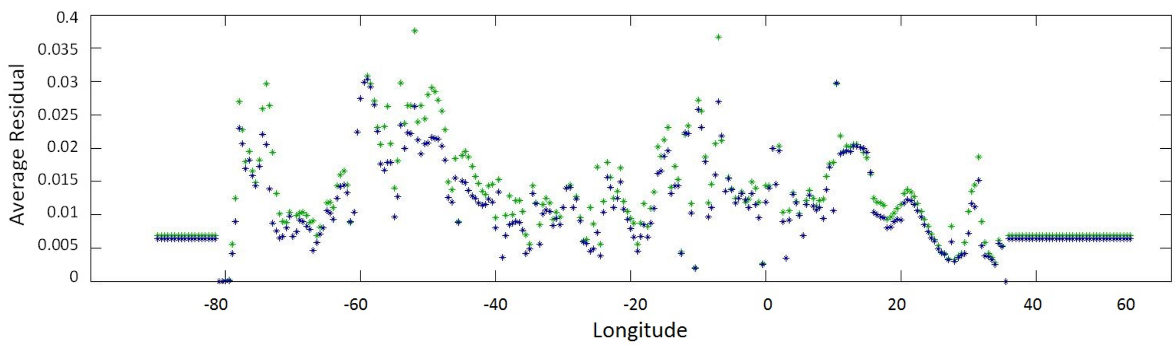

Figure 4.14 Average residual fit (km/s) to the final model for each point along the 20 °south profile for a Half space starting model with a 4 km water layer after 10 iterations (green) and 20 iterations (blue). Flat ends show the end regions where the model is out of the range of the tomographic data and is therefore the regional average inverted for depth.

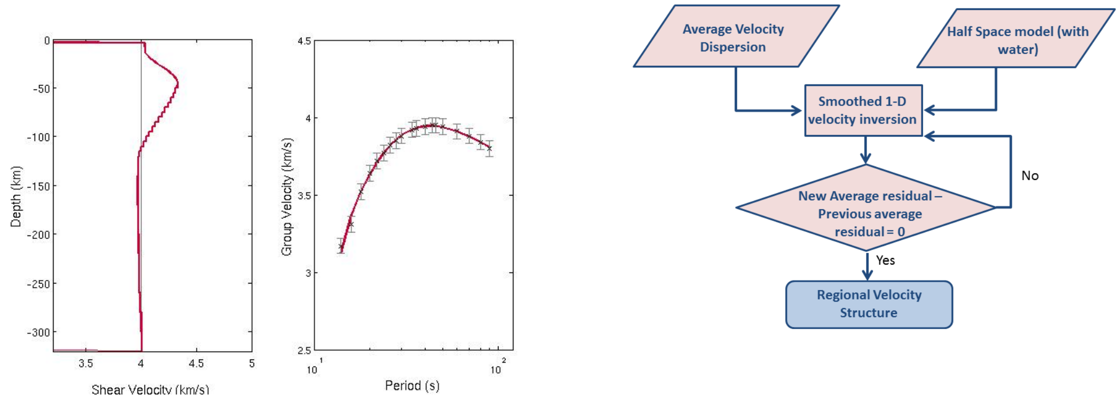

(a) (b)

Figure 4.15 Inverted model from average group velocity (a) (left) velocity structure for the starting model (red) against the starting Half space model with a 4 km water layer (grey) (right) the average velocity for each period (grey) against the velocity for each period for the average starting model. Final average residual fit 0.015 km/s. (b) Workflow illustrating the process of inverting for the regional average velocity structure

comparable output velocity models between the half space with a water layer and the regional average model show that the data is robust to the point that two different starting models result in similar structure. However, to obtain a crustal structure, *a priori* crustal structure is required in the starting model.

(iv) PREM

The Preliminary Reference Earth Model (PREM) was developed to give a reference model of elastic properties as a suitable starting model for geophysical studies (Dziewonski et al., 1981). It is a 1-D Earth model with a global weighted average for the crustal thickness and velocities due to the large lateral variation in the vertical structure of the top 100 km. The crustal thickness is 19 km, which is thicker than average oceanic crustal thickness. A 4 km water layer was added to the model and the approximate isotropic mantle velocities were used because the profiles are 1D and therefore, anisotropy varitaions cannot be modelled. The velocity values used for each layer can be seen in Appendix C. The number of layers in PREM are less than the previous models tested and are variable. The inversion was therefore alternated for layer thickness and layer velocity. This results in the need to run two iterations, one for thickness and one

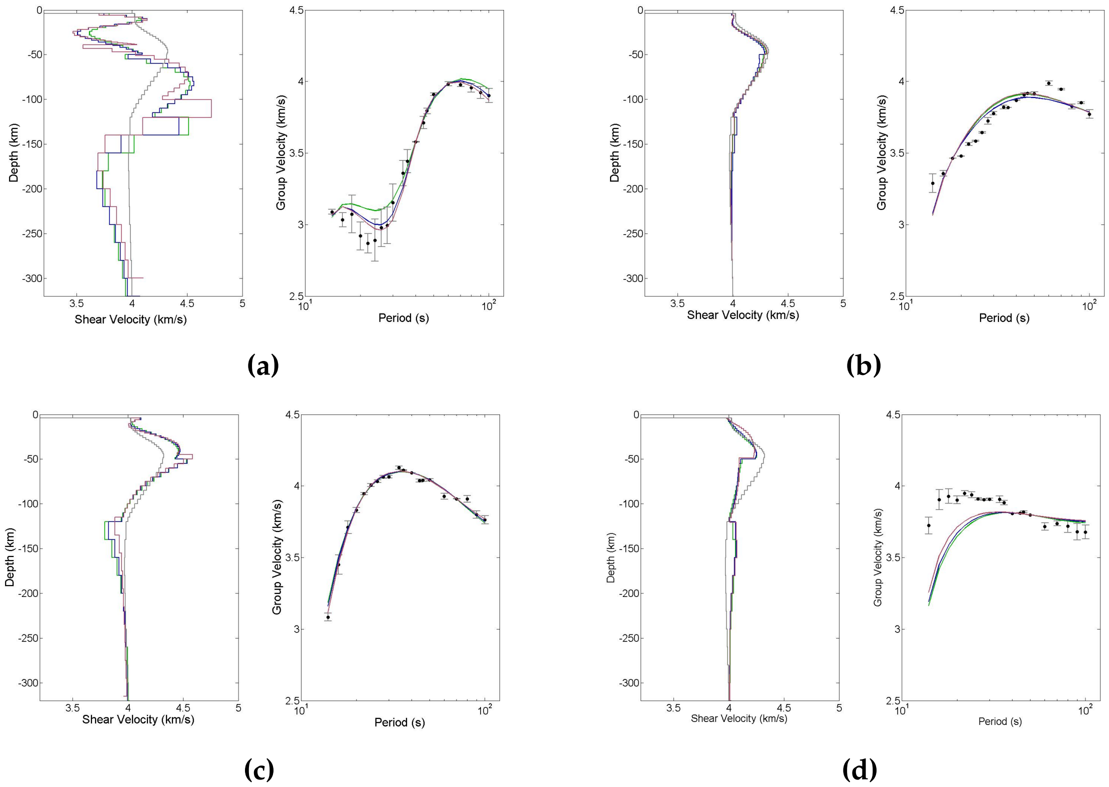

Figure 4.16 Inverted 1-D models for test profile 20 °south for regional average starting model at (a) 50 °west, (b) 38 °west, (c) 20 °west, (d) 14 °west, (e) 10 °west, (f) 5 °west, (g) 10 °east and (h) 20 °east inverted for 10 iterations (green), 20 iterations (blue) and n iterations until residual fit does not change (pink)

for velocity before calculating the difference to the residual fit.

The previous test showed that the average residual for the data would be improved along the profile by allowing each point to be inverted for n iterations until there was no change in residual from the previous model (residual$_n$−residual$_{n-1}$ $= 0$). PREM was therefore used to test if the variation in residual could be a small value (e.g. 0.01) and not a variation in residual of 0. This would reduce the number of iterations but the average residual fit may be too significantly higher than $_n$−residual$_{n-2}$ = 0 to be a reasonable parameter. It was tested for residual$_n$−residual$_{n-2}$ $= 0$, residual$_n$−residual$_{n-2}$ $= 0.001$ and residual$_n$−residual$_{n-2}$ $= 0.01$. The nukber of iterations per cycle has now inceased to 2 (thickness and velocity) and therefore the residual will be compared every 2 iterations. These results are seen in figure 4.18.

There are variable results to the fit across the region and there is a greater fit to the data for residual$_n$−residual$_{n-2}$ $= 0$. Some points have a good fit to the data by

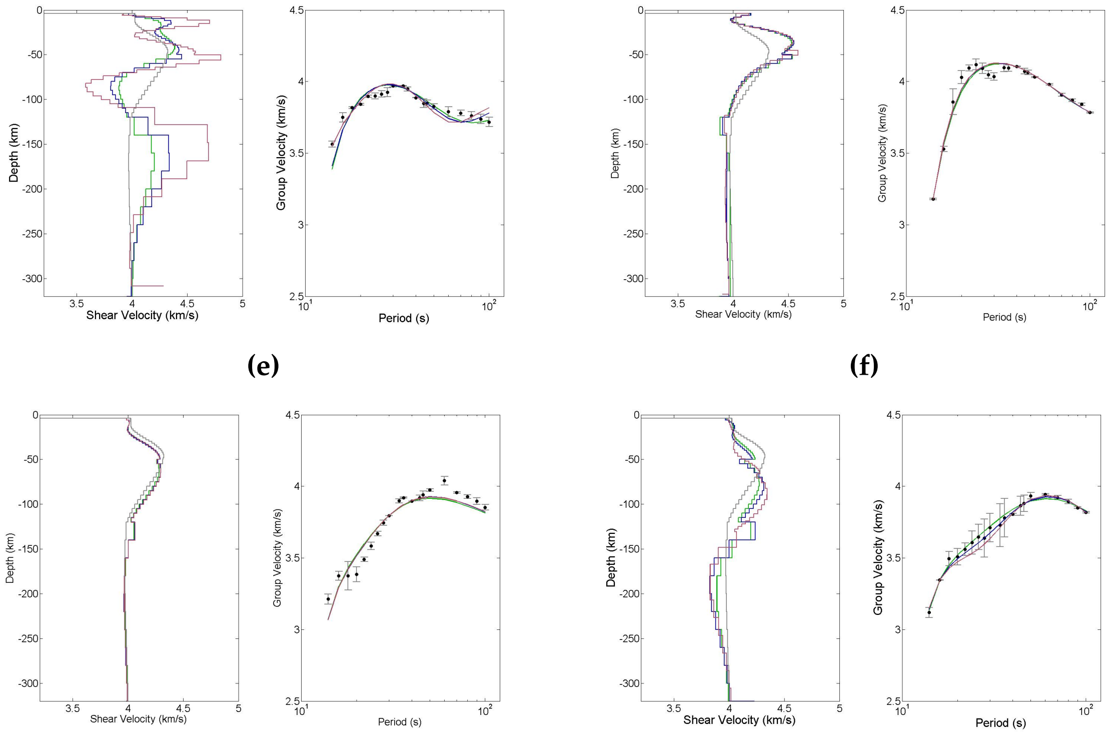

(e) **(f)**

(g) **(h)**

Figure 4.16 Continued

residual$_{n-2}$ $= 0.01$ (e.g. 20 °west - figure 4.18 c) and others show little improvement to the fit, although not good after residual$_n$$-$residual$_{n-2}$ $= 0.01$ (e.g. 38 °west and 10 °east - figure 4.18 b and g). There are other points where there is a great improvement to the data fit from residual$_n$$-$residual$_{n-2}$ $= 0.01$ to residual$_n$$-$residual$_{n-2}$ $= 0$. Overall the improvement to the average residual is significant (figure 4.19 a).

The inversions overall result in a thinner crustal structure across the region, however, the resulting models are not all geologically reasonable. 14 °west (figure 4.18 d) gives a velocity at shallow depths (between 10 km and 20 km) faster than the lowest mantle velocity (approximately 4.7 kms^{-1}). This is geologically unreasonable but it is trying to fit the observed faster shorter period data due to the topographic signature of the mid ocean ridge. 2 °east (figure 4.18 h) which is located on the African continent is another example of a poor geologically constrained output model. To fit the data to the water layer (which in the African continent is none existent) the inversion has increased the crustal velocities to that of mantle velocities (4.2 kms^{-1}) effectively re-

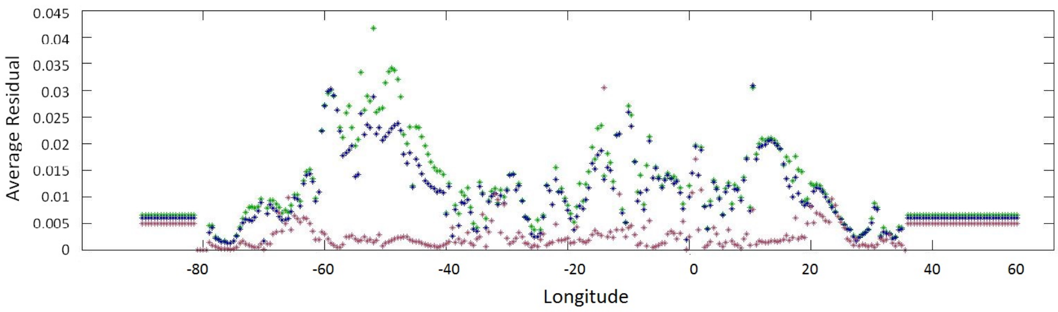

(a)

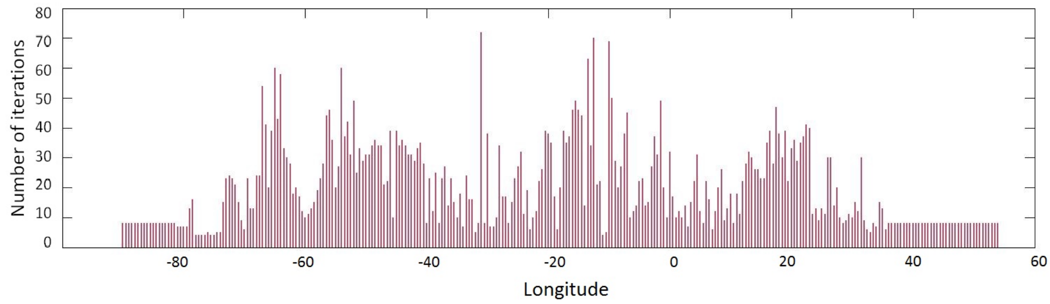

(b)

Figure 4.17 (a) Average residual fit (km/s) to the final model for each point along the 20 °south profile for regional average starting model after 10 iterations (green) and 20 iterations (blue) and n iterations until residual fit does not change (pink) (b) corresponding number of iteration (n) for each point along the profile.

moving the crust. This is also observed for 5 °west (figure 4.18 f) where a water layer is expected due to the point being in the abyssal region east of the mid Atlantic ridge. The problem with using a single velocity model for every point in the region is the variable crustal structure and thickness of the water layer. All models inverted so far have had a single uniform water layer across the region when converted to a 3-D model. Taking a model which contains *a priori* crustal knowledge but has variable structure and water layer may be better.

(v) Crust 2.0

Crust 2.0 was then tested as a possible starting model, however the velocity of the mantle extracted from Crust 2.0 is a single value based on sub Moho estimates and is therefore not suitable for the whole 300 km. For this reason for each 1-D model the Crust 2.0 mantle velocity was extended only 30 km beneath the Moho, and from this

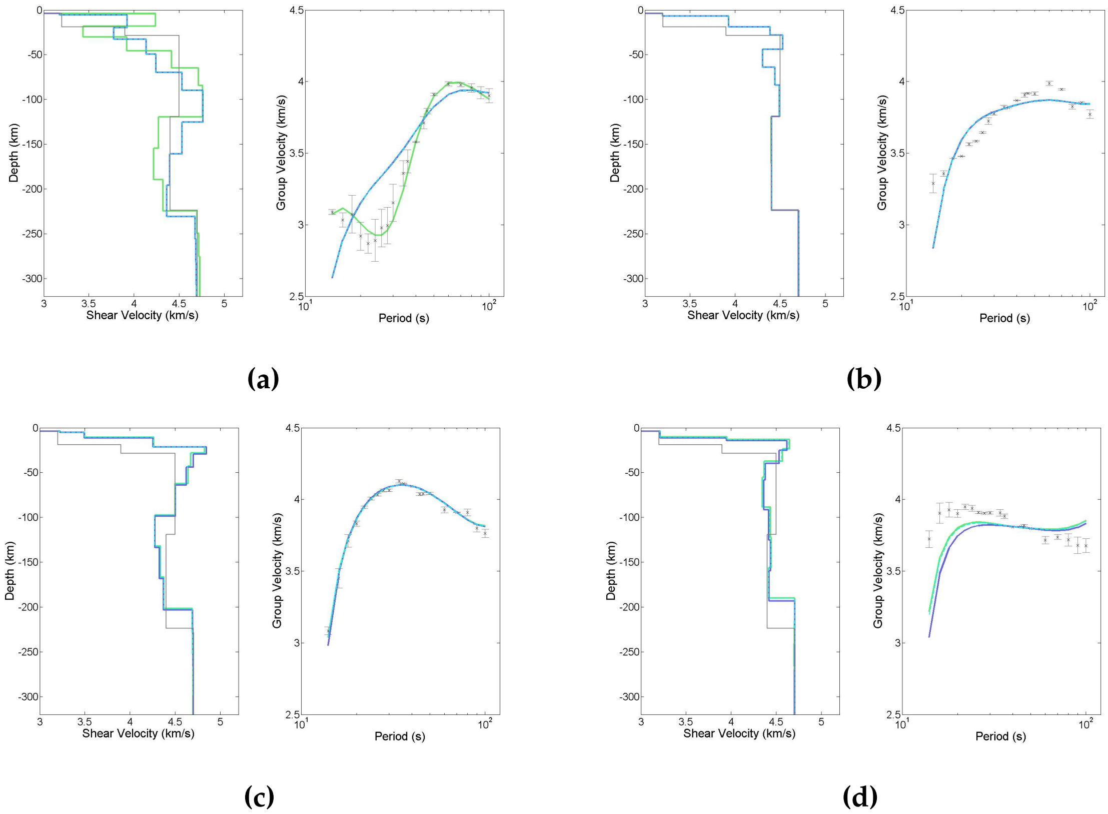

Figure 4.18 1-D profiles for test profile 20 °south for PREM starting model at (a)50 °west, (b) 38 °west, (c) 20 °west, (d) 14 °west, (e) 10 °west, (f) 5 °west, (g) 10 °east and (h) 20 °east inverted for n iterations until residual fit change by 0.01 (blue) 0.001 (red dashed) and 0 (green)

depth the PREM velocity structure was used down to 300 km. Figure 4.20 shows the velocity structure for varying crustal thickness, the models were constructed so that by 100 km depth the velocity structure was uniform beneath the variable crustal structure.

The dispersion data (14 s - 100 s) was inverted for 20 °south profile with the corresponding Crust 2.0 model for each point. The results can be seen in figure 4.21. The overall geological structure observed is better and the fit to the data is also significantly better (figure 4.22). There were some points which again gave cause for question (e.g. 5 °west - figure 4.21 f). The velocity just below the crustal layer (which in this model is now existing) the velocity increases to above 5 kms^{-1} which is not geologically reasonable. The fit to the data is, however, very good. The jump in velocity at 10 °west (figure 4.21 e) could be explained by the topographic fast velocity feature of the ridge, also seen in the PREM results, but 5 °west is in the abyssal region. The damping value was altered up to 50, where there was some reduction to the high velocity but nothing

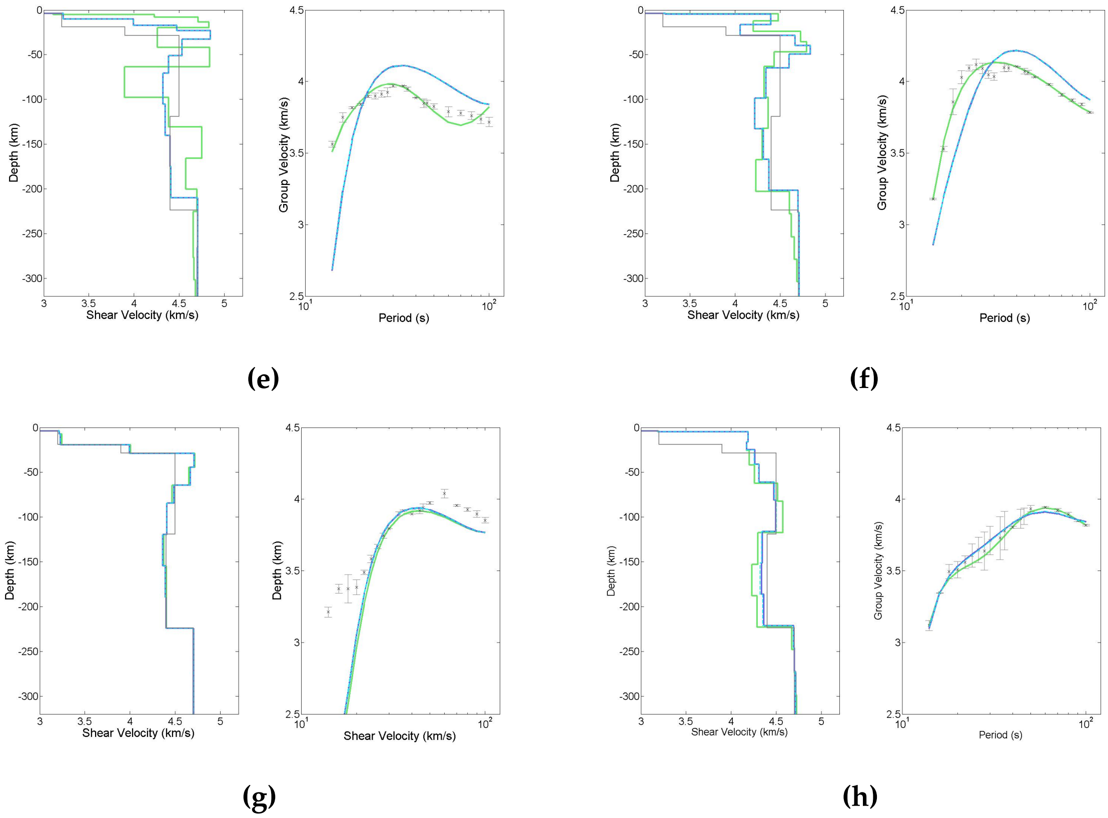

Figure 4.18 Continued

significant. This also increased the number of iterations run.

One aspect that was considered was the uncertainties in the information from the 14 s tomographic model. Looking at the residual fit for 14 s, the error (or 3σ value) for the final model is 0.79 kms^{-1} (19%). This error is unreasonable to fit the group velocity in the shear velocity inversion. If the group velocity for 14 s is up to 0.79 kms^{-1} slower in some regions, this could explain the fast velocities in the shear velocity model, as the inversion has tried to fit data which should be 0.79 kms^{-1} slower. The differences in the Crust 2.0 dispersion and the tomographic model in comparison to the other periods would also suggest that the velocities for 14s in the tomographic model are faster than expected. Due to the uncertainties with the 14 s dispersion data, the 14 s group velocity from each dispersion curve was removed.

Figure 4.23 shows the new models for the 20 $^{\circ}$south profile. By removing the 14 s data the oscillations observed in the models have been removed (e.g. figure 4.21 b, e, f and h) and the velocities are now more geologically reasonable. There are still

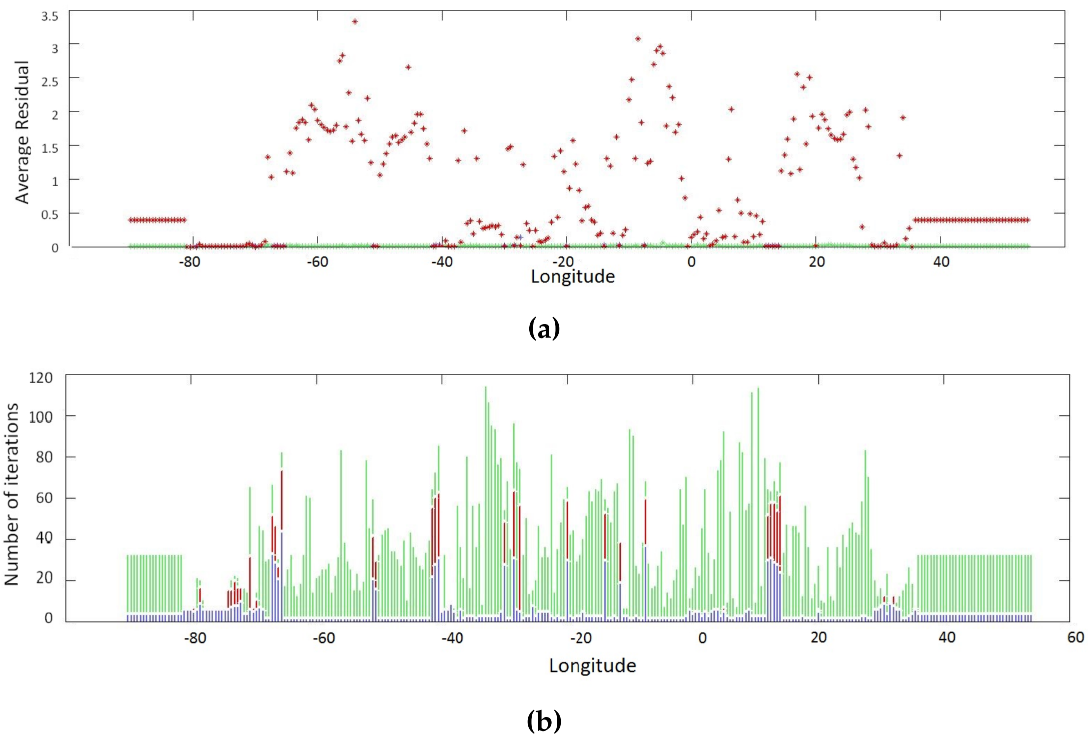

Figure 4.19 (a) Average residual fit (km/s) to the final model for each point along the 20 °south profile for PREM starting model for n iterations until residual fit change by 0.01 (blue) 0.001 (red) and 0 (green) (b) corresponding number of iteration (n) for each point along the profile for 0.01 (blue) 0.001 (red dashed) and 0 (green)

variations between the starting model and the output model, especially in the top 100 km where the focus of the study is. The residual fit to the data was also improved along the profile by removing 14 s (figure 4.22 a).

Summary of models

In summary (table 4.1), a starting model was chosen after a series of tests to determine how much *a priori* knowledge was required in the starting model to obtain a reasonable geological model of the crustal and upper mantle structure. The tests were run to see if models with little bias from *a priori* information could obtain a reasonable velocity model for the Atlantic or if the crustal structure would be too thick. It was concluded that to obtain a reasonable crustal structure, unlike the structure seen in previous studies (e.g. Acton et al., 2010; Tang & Zheng, 2013) a model with a *a priori* crustal structure was required.

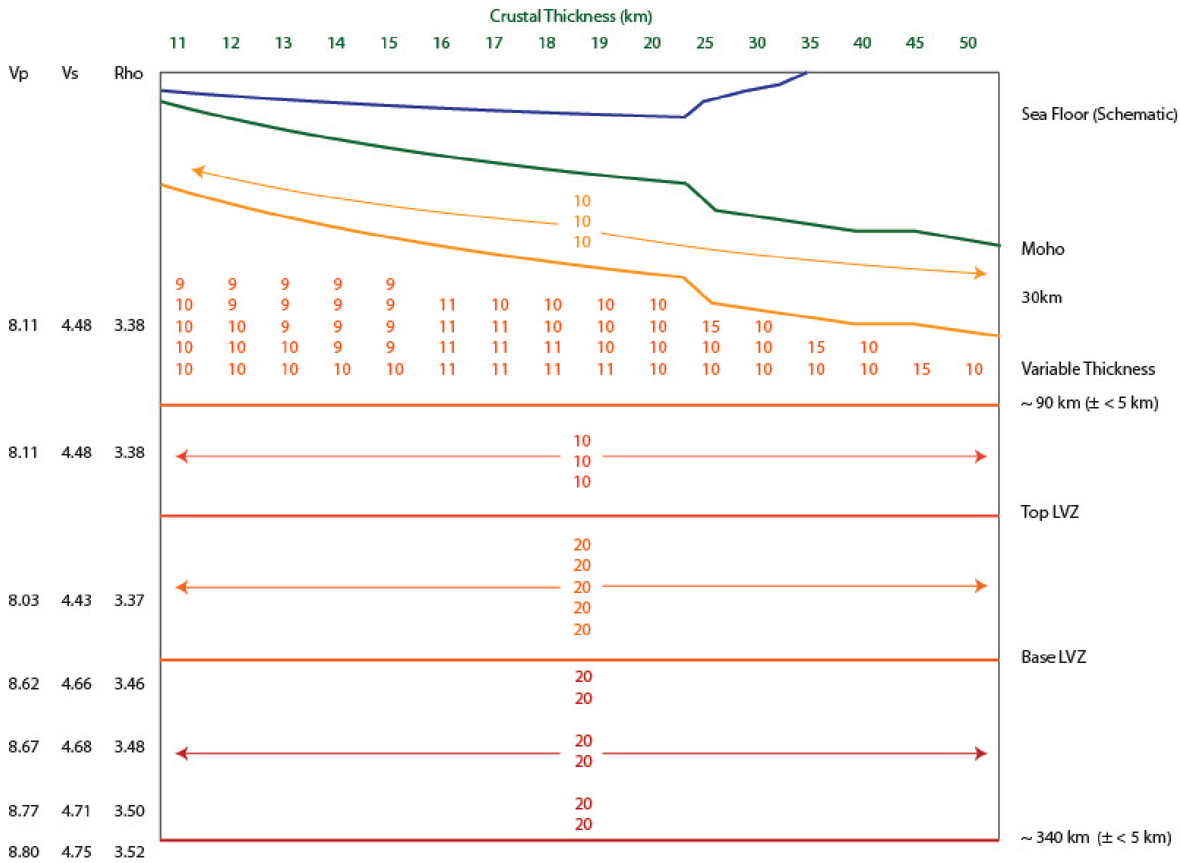

Figure 4.20 Velocity structure for Crust 2.0 model down to 300 km based on variations in crustal thickness. Above the yellow line the velocity extracted from Crust 2.0 is used for each layer. Below the yellow line the velocity used for each layer is shown on the left hand side. The values within the plot show the layer thickness associated with each corresponding velocity. Above 90 km the layer thickness (orange) is varied between 9 km and 15 km to allow each model to be uniform from 90 km. Where as below 90 km the layer thickness is the same regardless of crustal thickness.

Although PREM has a crustal structure and resolved a reasonable model, Crust 2.0 contained more regional information with an oceanic crustal thickness and the variation in water depth, which PREM did not include. From tests carried out in section 4.1, the velocity structure modelled beneath the South Atlantic has variation from Crust 2.0 and therefore a new regional velocity model can be determined from this starting model with *a priori* knowledge. The Crust 2.0 starting model also has the best overall residual fit to the data for the 20°south profile (table 4.1). PREM was on average a less good fit to the data than the average starting model; this is most likely due to the thicker crust which PREM has in comparison to a model, which fits the regional average.

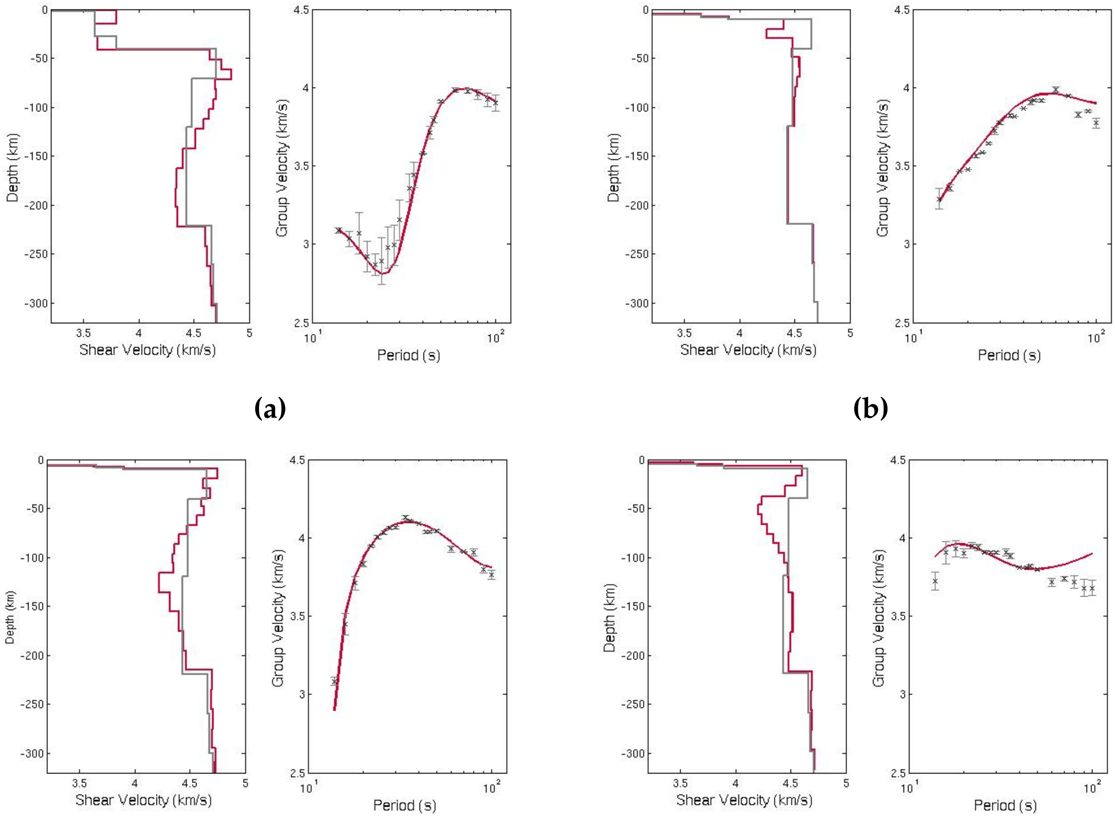

(a) **(b)** **(c)** **(d)**

Figure 4.21 Inverted 1-D models for test profile 20 °south for Crust 2.0 starting model for all data at (a)50 °west, (b) 38 °west, (c) 20 °west, (d) 14 °west, (e) 10 °west, (f)5 °west, (g) 10 °east and (h) 20 °east inverted for n iterations, the starting model is in grey and the final model is in red

Table 4.1 Summary of starting model tests

Model	*a priori* information	Average residual fit
(i) Half space	None	0.014
(ii) Half space with water	Water layer	0.01
(iii) Regional Average	Water layer	0.0031
(iv) PREM	Water Layer and 15 km thick crust	0.0064
(v) Crust 2.0	Regional water layer and oceanic crustal thickness	0.001

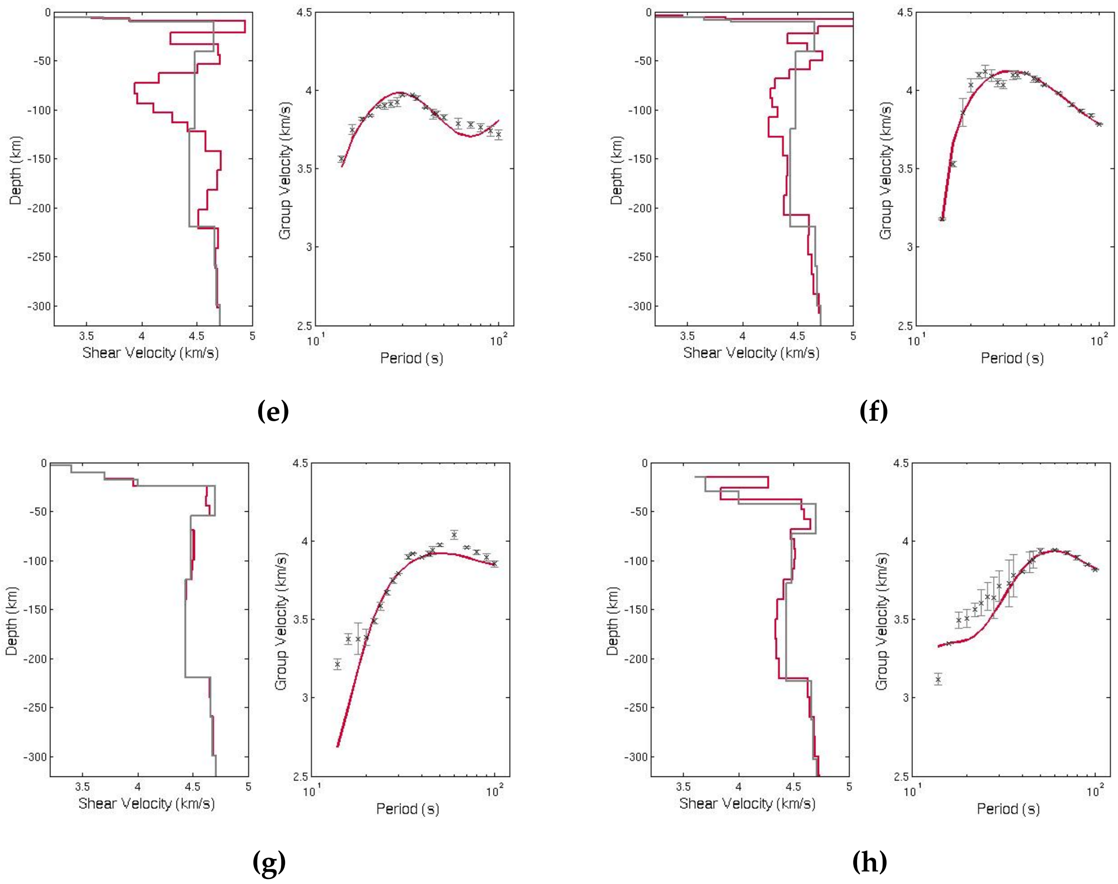

Figure 4.21 Continued

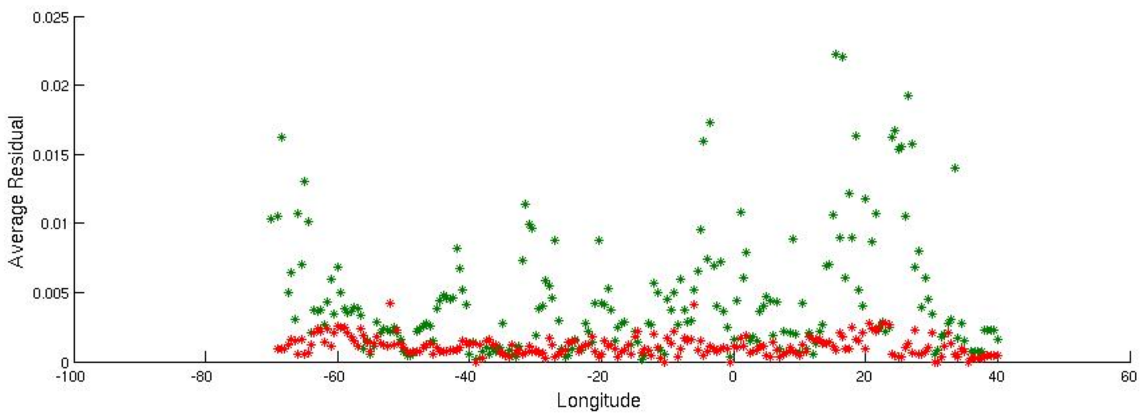

Figure 4.22 Average residual fit (km/s) to the final model for each point along the 20 °south profile for Crust 2.0 with all data (green) and without 14 s (red).

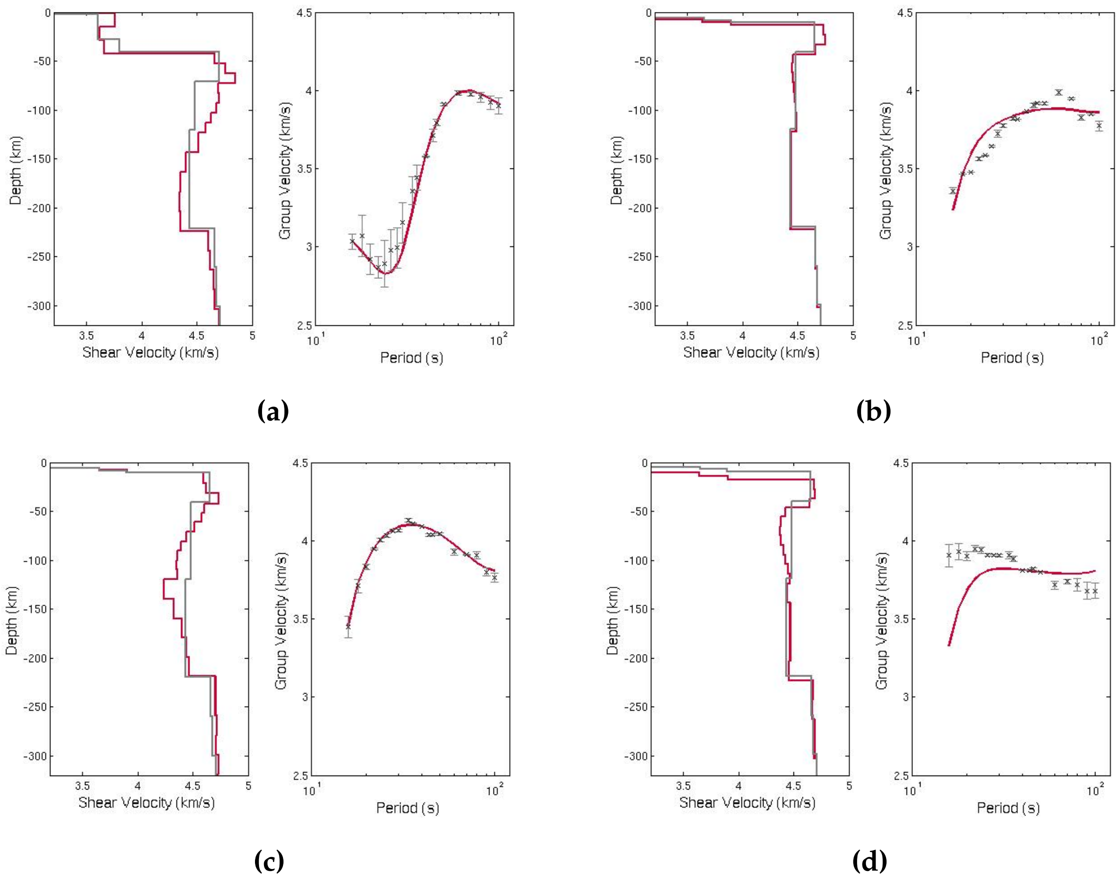

Figure 4.23 Inverted 1-D models for test profile 20 °south for Crust 2.0 starting model with the group velocity for 14 s removed from the data at (a) 50 °west, (b) 38 °west, (c) 20 °west, (d) 14 °west, (e) 10 °west, (f) 5 °west, (g) 10 °east and (h) 20 °east inverted for n iterations, the starting model is in grey and the final model is in red

4.3 20 °south 2-D profile comparison

The 1-D velocity profiles along 20 °south were combined into 2-D profiles for the regional average starting model, PREM and Crust 2.0, excluding 14 s (figure 4.24). The velocity structure does vary between the three profiles due to the starting velocity model. The velocity structure for the regional average model (figure 4.24 a) exhibits overall slower mantle velocities than PREM and Crust 2.0 which have more similar starting velocities. The overall structure of the three models is similar with an up welling slower velocity beneath the ridge (12 °west). The South America continent (from 40 °west) is also defined in all three models as a region of deeper slow velocity. This region is likely to be better resolved because more paths cross in this region in the tomographic model compared with west Africa. Also on all three profiles, features oc-

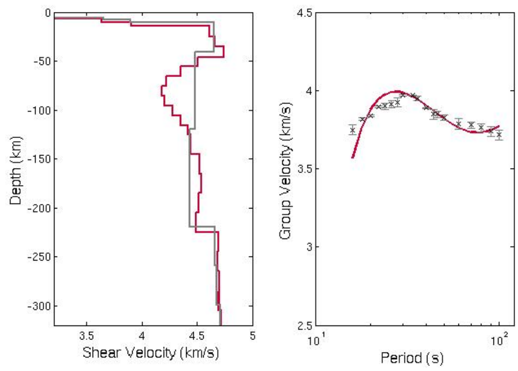

(e)

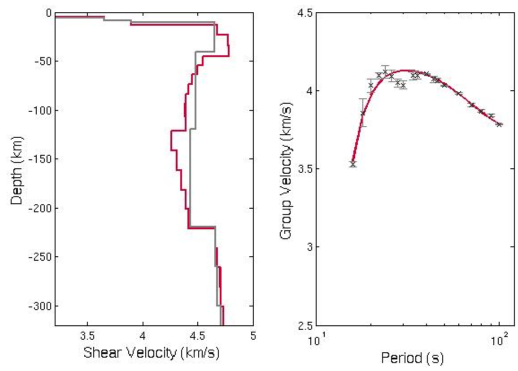

(f)

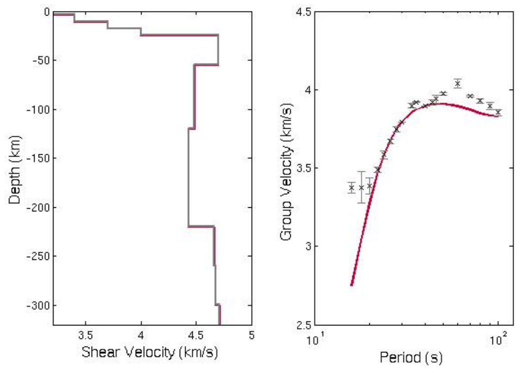

(g)

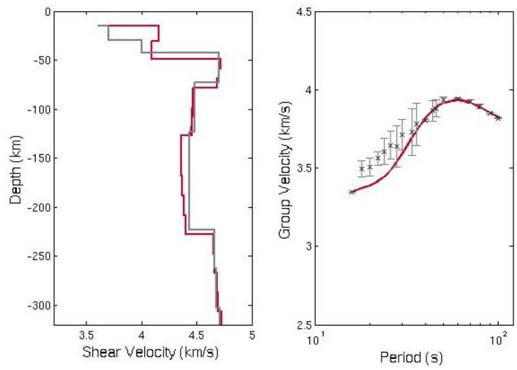

(h)

Figure 4.23 Continued

cur 10 °and 15 °east, where the profile transitions onto the continental region of Africa. These show the robustness of the data, where features not present in the starting models have been resolved from three very different starting models.

The comparison of the three profiles highlights again that the regional average model (figure 4.24 a) does not define a crustal layer, although it is more apparent in places when combined in a profile. The PREM model (figure 4.24 b) exhibits some faster velocities in the shallow depths (around 25 °west), which can be attributed to the 14 s data point included in the inversions and attempts to fit the shortest period. This is not observed in the Crust 2.0 model (figure 4.24 c), excluding 14 s, which would suggest the data set is better without the inclusion 14 s group velocity.

It was concluded that Crust 2.0 would be the best starting model for the region due to the residual fit being overall better to the data than any of the previous models (even before the removal of 14 s). Using Crust 2.0 gave a better overall starting model

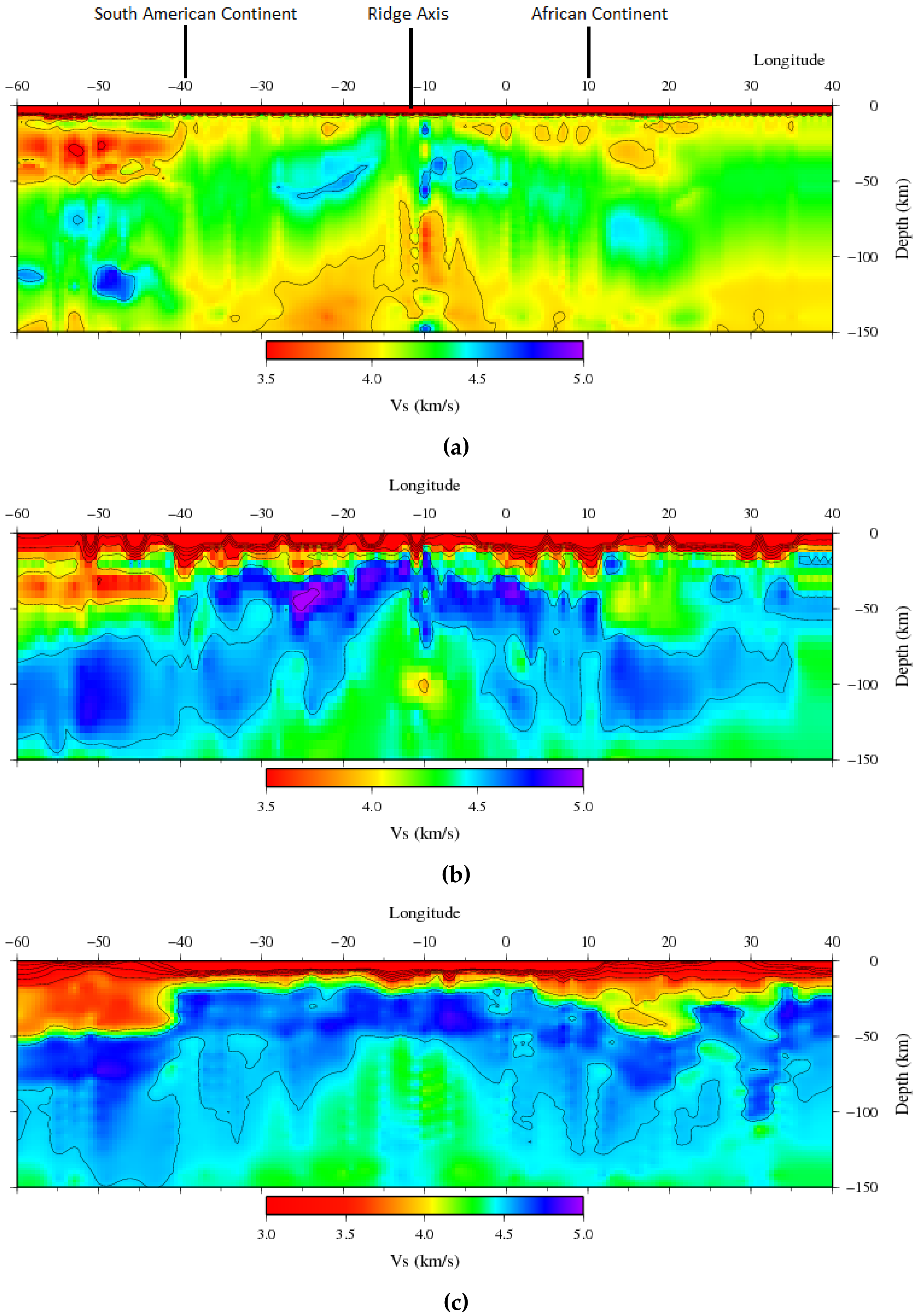

Figure 4.24 Shear velocity profile for (a) regional average starting model, (b) PREM starting model and (c) Crust 2.0 excluding 14 s starting model for the 20 °south profile. Ridge axis is located at 12 °west

across the region, taking into account the variable water depth and crustal thickness. From section 4.1, the velocity structure of Crust 2.0 does not fit the data completely, therefore variations between the starting model and the resulting output model can be highlighted and the velocity structure of the Atlantic Ocean can be refined with the addition of surface waves to refraction data. The Crust 2.0 model is only constructed based on average data, where data is sparse and therefore may not be the true structure for the whole region. The Crust 2.0, excluding 14 s partial derivatives, also give the best depth sensitivity allowing an interpretation of the velocity structure down to 75 km.

4.4 Velocity maps

The dispersion data, excluding 14 s, was inverted with the Crust 2.0 starting model for the whole region with a damping factor of 10 for n iterations. Maps of shear velocity structure for depth were then constructed for the region. The greatest depth, which the maps were constructed for, was 75 km due to the velocity sensitivity of the inversions. The velocity structure was gridded and filtered using a Gaussian filter with a width of 250 km; this was based on the resolution of the tomographic models being no less than 300 km and Crust 2.0 being at 2 °spacing. These maps can be seen in figure 4.26. The velocity is plotted as depth below the sea floor, not below sea level, therefore the shallow depth maps are not a flat cross section.

At 5 km depth (figure 4.26 a), it is observed that the ridge has little contrast in velocity compared to the surrounding velocities. This is due to the depth and the volcanic signature of the crustal velocity of the ridge and oceanic crust at distance from the ridge. There is also little contrast between the oceanic and continental velocity structure. There are regions on both sides of the ridge in the sedimentary basins, where velocities are observed to be faster than the ridge and continental margins. To the west of the ridge, there are faster velocities than to the east. This may be due to the geodynamic setting of the region; the African plate is considered to be stationary, therefore both the ridge and the South American plate motion are westward. This may create an extensional region in the west and a compressional region in the east. The faster velocity region is at between 30 Ma and 50 Ma, where cooling of the oceanic crust should have no effect on velocity. The ocean island signatures observed in the shorter period tomography are not observed at this depth, therefore in the tomography the ocean island signatures are most likely due to the topographic relief and contrast to the water.

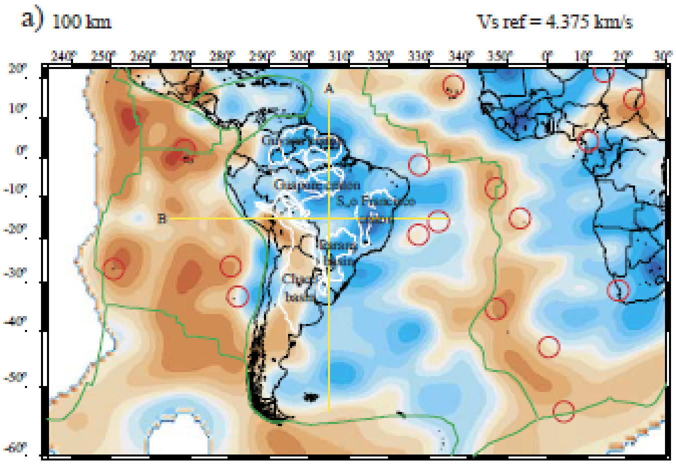

(a)

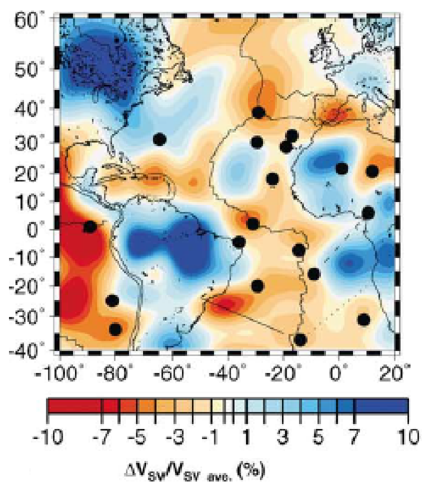

(b)

Figure 4.25 (a) Map from Heintz et al. (2005) showing the velocity pertubations at 100km (b) Map from Silveira & Stutzmann (2002) showing the velocity pertubations at 100km

The velocity structure from 10 km to 20 km (figure 4.26 b-c) is very similar. There is a clear contrast between the oceanic velocity and the continental velocity at these depths and a slower velocity mid ocean ridge feature. There are also slow velocity features away from the mid ocean ridge (closer to continental velocity), some of which correspond with the sea mounts (the Walvis Ridge and Rio Grande Rise). In other regions, where there are no sea mounts, slower velocity structure is observed to a depth of 20 km. This is also observed as regions of slower velocity in the tomography between 20 s and 36 s. The thickness of the crust is discussed in chapter 6 in further detail.

At 30 km (figure 4.26 d) the velocity structure is relatively uniform beneath the oceanic region and the low velocity feature is lost. This would suggest that the slow velocity region beneath the ridge at 10 km and 20 km is be related to magma melt chambers. By 50 km (figure 4.26 e), there is a slower velocity ridge feature, but the rest of the velocity structure is uniform. 75 km (figure 4.26 f) is the greatest depth that the longest periods can reliably resolve. The slow velocity region beneath the ridge has spread out away from the ridge but the majority of the velocity structure is still fast at this depth.

The velocity map at 75 km can be compared to previous studies of the African, South American and South Atlantic region. Heintz et al. (2005) show a similar velocity structure with a narrow region of slow velocity beneath the ridge (figure 4.25 a). This is interpreted as narrow due to the slow spreading rate and therefore thickening of lithospheric structure closer to the ridge. The decreasing velocities away from the Amazon basin are modelled in Feng et al. (2004) with a similar velocity pattern. Silveira & Stutzmann (2002) observe an asymmetry in the velocity structure at 110 km depth, which is not observed in this model (figure 4.25 b).

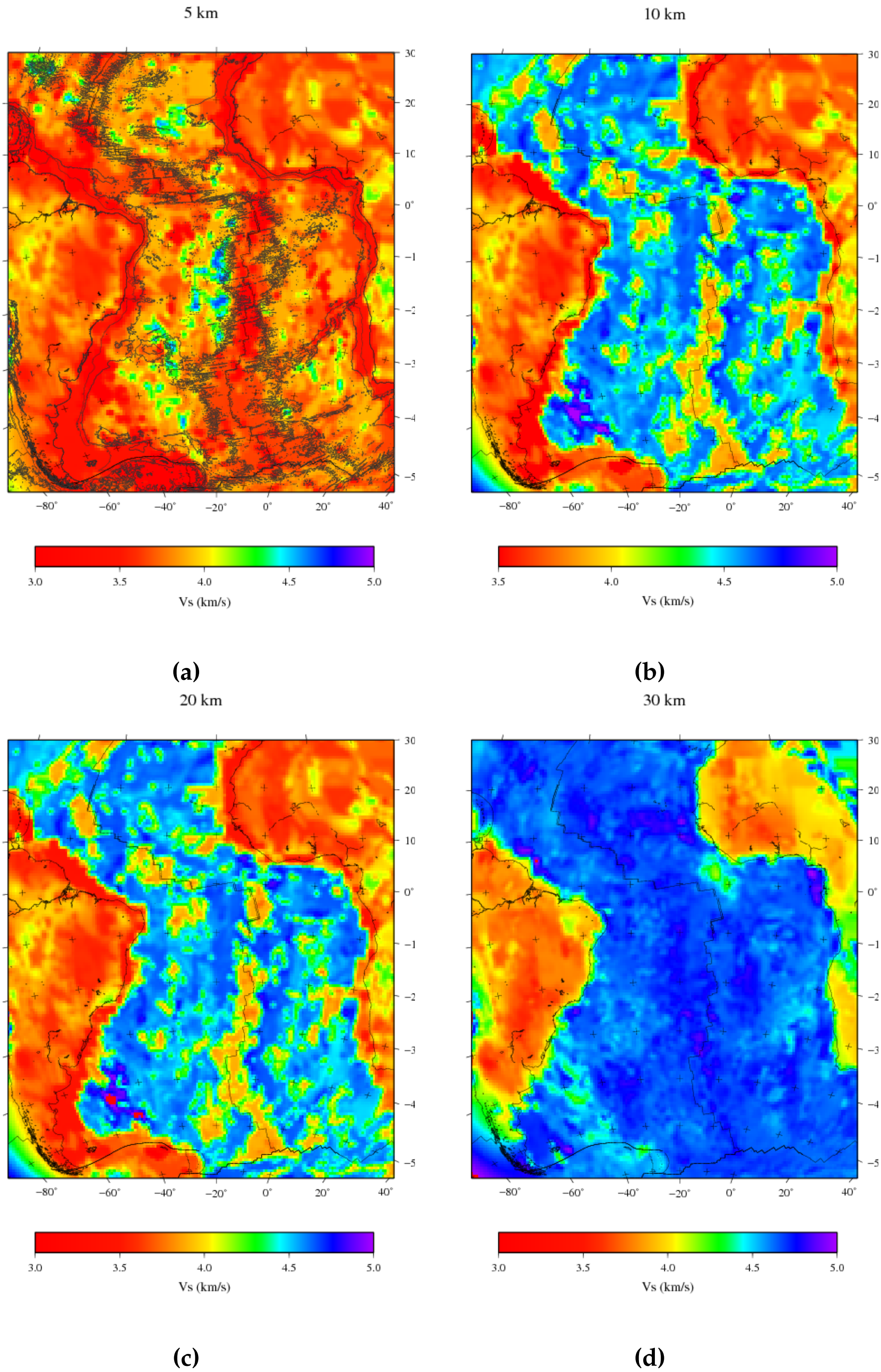

Figure 4.26 Shear velocity maps for (a) 5 km (including topography) (b) 10 km (c) 20 km (d) 30 km (e) 50 km (f) 75 km (stars show ocean island locations)

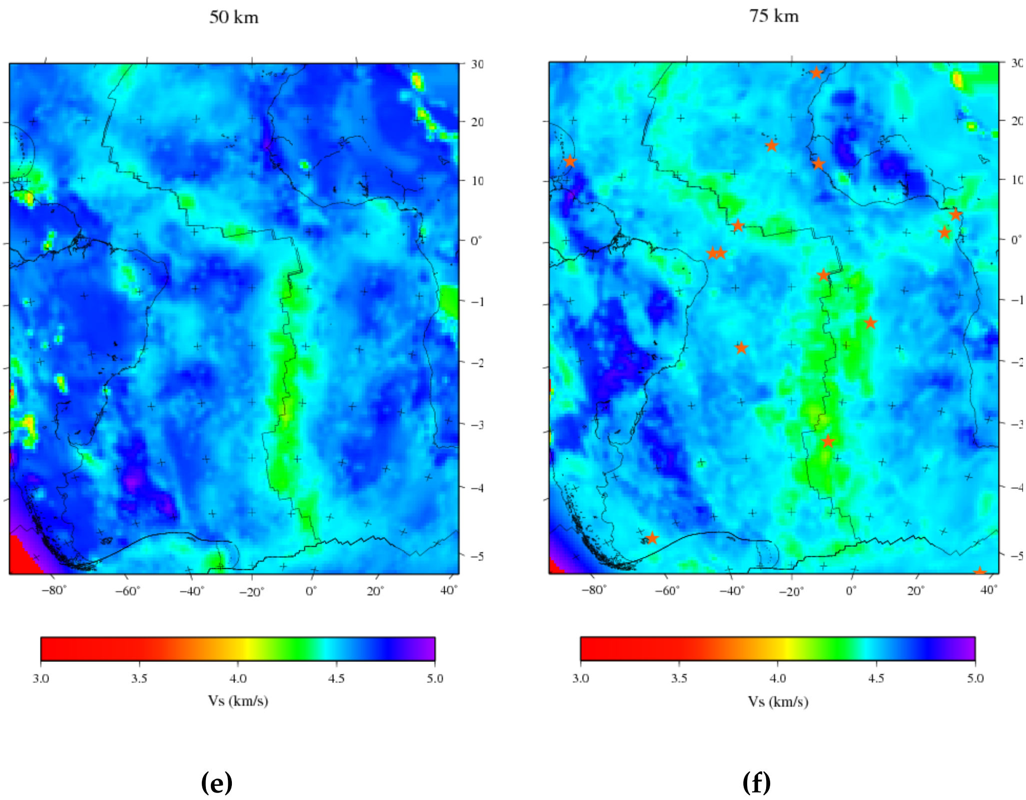

Figure 4.26 Continued

Chapter 5

Anisotropy beneath the South Atlantic Ocean

The work discussed so far in this study (chapter 3 and 4) has investigated the velocity structure of the southern Atlantic assuming the crust and upper mantle is isotropic. The parametrisation of isotropic inversions are simpler than anisotropic inversions as the velocity is assumed to be the same in all directions. However, the Earth's velocity structure is not isotropic and therefore the misfit to the data can be improved by inverting for anisotropic structure (Trampert & Woodhouse, 2003). When a mediumis anisotropic the elastic moduli tensor (c - equation 3.1) can include up to 81 terms.Therefore, when inverting for anisotropy there is a trade off between reducing the misfit due to anisotropic structure and increasing the number of unknown parameters in the tomographic inversion.

Anisotropy is created when the properties (stress and strain) of a medium vary depending on the direction of wave propagation, causing slow and fast directions of travel through the medium. Common causes of anisotropy are heterogeneities in the velocity structure such as a layered structure of varying velocity (e.g. sedimentary bedding), and the alignment of the crystal lattice in a preferred direction (e.g. mantle olivine). There are different types of anisotropy depending on the structure which causes the anisotropy such as, radial anisotropy and azimuthal anisotropy (Stein & Wysession, 2008).

As previous studies have observed, the velocity structure beneath mid ocean ridges can be anisotropic. Azimuthal anisotropic observations are thought to be due to the assumed flow direction, frozen anisotropy and crack/dyke induced anisotropy seen in the asthenosphere, lithosphere and crust respectively (e.g. Dunn & Toomey, 2001; Maggi et al., 2006a; Silveira & Stutzmann, 2002). Variations between Love and Rayleigh wave velocities beneath oceans also imply variations in V_{SH} and V_{SV} (radial anisotropy) which is thought be be associated with small scale convection. It is considered that PREM is a good anisotropic model for radial anisotropy beneath all oceans except the Pacific where larger variations in V_{SH} and V_{SV} are observed (Ekström & Dziewonski, 1998).

A horizontally layered structure will cause transverse or radial anisotropy; such that the P wave velocity travelling parallel to the layered structure is greater than the P wave velocity travelling perpendicular to the structure. The S wave velocities (V_{SH} and V_{SV}) will split parallel to the structure where the S_H is the faster velocity. Perpendicular to the layers both S wave velocities will remain the same.

Azimuthal anisotropy shows the fast velocity magnitude and direction (azimuth from north γ) with respect to the horizontal plane. In regions where the fast velocity direction is vertical or in an isotropic medium, no azimuthal anisotropy would be present. Equation 5.1 shows the surface wave anisotropic velocity variations, where A_i(T) is the surface wave with respect to period T and is dependent on 21 elastic constants. A_1(T) is the isotropic velocity term modelled in chapter 3 and $A_{(2-5)}$(T) are the azimuthally anisotropic terms of velocity associated with the azimuth of the surface wave (ψ) from 0 °.

$$A(T) = A_1(T) + A_2(T)cos2\psi + A_3(T)sin2\psi + A_4(T)cos4\psi + A_5(T)sin4\psi \tag{5.1}$$

Surface waves provide valuable information for anisotropy studies because they sample both the radial anisotropy (the discrepancies between Love and Rayleigh waves) and the azimuthal anisotropy of the structure simultaneously (Trampert & Woodhouse, 2003). Love waves are sensitive to the V_{SH} only whereas Rayleigh waves are predominately sensitive to the V_{SV} and a smaller component of V_P. This makes Rayleigh waves good for azimuthal anisotropy studies (Ekström, 2011). The azimuthal fast direction γ is seen to vary for both Love and Rayleigh wave studies due to the ground motion of the wave. It is considered that Rayleigh waves are described better by the 2ψ variations in velocity where as Love waves are described better by the 4ψ velocity variation (Anderson, 2007; Maupin & Park, 2014). The fast directions of these two components are seen to be at 45 °angles to each other, again due to the V_{SH} and V_{SV} directions the waves are sensitive to. V_P is most anisotropic, therefore although a small component of the Rayleigh wave it also influences the azimuthal anisotropy associated with it (Anderson, 2007).

Complications in wave propagation can be associated with anisotropic structure, can also be caused by refraction of the wave. This is a particular problem at shorter periods, which sample the shallow, heavily layered structure, or for waves with long paths where the curvature of the Earth can refract the wave to simulate an anisotropic medium (Stein & Wysession, 2008). This causes higher uncertainty when interpreting the data.

Several studies show a correlation between the fast direction associated with the 2ψ anisotropy and plate motion, which has led to the use of azimuthal anisotropy data in geodynamic studies, to determine past and present flow directions (Ekström, 2011; Maggi et al., 2006b). There is less of a correlation between 4ψ and geodynamical features. Most studies of azimuthal anisotropy, especially in oceanic regions neglect 4ψ and invert for and interpret 2ψ anisotropy only (e.g. Lévěque et al., 1998; Maggi et al., 2006b). Based on the depth sensitivity of the structure sampled beneath the Atlantic both frozen anisotropy in the lithosphere and flow direction beneath the ridge in the up welling asthenosphere can be expected. This section investigates the added complications of azimuthal anisotropy in velocity models for the Atlantic.

5.1 Tomographic inversions

The tomographic inversion for the anisotropic structure is a least squares weighted and damped inversion similar to the isotropic inversion (equation 3.2) but includes the sum of the components in equation 5.1, where A(T) is model m for m(θ, ϕ, γ), where θ is the latitude, ϕ is the longitude and γ is the azimuthal direction of the fast velocity (Fishwick et al., 2008). This increases the unknowns in an already under determined inversion (Trampert & Woodhouse, 2003).

By inverting for just 2ψ or 4ψ seperately, the parameters in the inversion are reduced and a smaller misfit is produced than when both azimuths are inverted for together (Trampert & Woodhouse, 2003). This is observed in the 4ψ tests run in section 5.2.2. Inverting for azimuthal anisotropy requires the regions extrapolated by the spline function to be sampled in at least 3 directions in order to resolve the 2ψ component reliably (Lévěque et al., 1998). The path coverage in the study area has a good azimuthal distribution. Although a significant part of the data is dominated by east-west sampling the introduction of data in South America (from the Brazilian Lithosphere Project), alongside data from stations in the Caribbean and Europe provides sufficient variations to investigate anisotropic structure. There will be some regions of course, where resolution for resolving the anisotropy is better than others.

The dataset discussed in section 3.4.3 has been used for the anisotropic inversions. Therefore, outliers have already been removed, and the same weighting as in the isotropic inversions were used. The initial inversions were done for just 2ψ due to the lack of correlation between the majority of 4ψ studies and geodynamics.

The isotropic and anisotropic components of the models were inverted for different parametrisation. the inversion for anisotropy were done for 6 °spline spacing. This is broader spacing for the isotropic structure than the isotropic model in chapter 3. The focus of this chapter is on the anisotropic structure and therefore, to attempt to resolve the anisotropy better, the spline spacing was increased to allow more crossing paths at varying azimuths than for the isotropic inversions.

Anisotropic models were calculated at 8 different periods. 18 s and 20 s are the shortest periods with a good path coverage to invert for the shallower crustal anisotropic structure. The data coverage at 16 s was considered too sparse to accurately resolve the anisotropic structure. group velocities at 24 s and 30 s will be sensitive to the slightly deeper structure and the transition from crust to lithosphere. Models at 36 s and 50 s should be sensitive to the lithospheric structure and the asthenospheric structure beneath the mid ocean ridge should be imaged by 70 s and 100 s down to approximately 80 km.

The magnitude of the azimuthal anisotropy is more sensitive to the damping applied to the model than the isotropic structure, and therefore the choice of damping is even more important in the anisotropic inversion (Trampert & Woodhouse, 2003). The results still have an uncertainty in the absolute magnitude of the anisotropy which must be considered in interpretation of the resultant anisotropy. The effect of damping value is considered in detail by analysing the difference maps between models in section 5.2.1.

5.1.1 2ψ Models

The initial 2ψ models are shown in figures 5.1 and 5.2. The isotropic velocity is plotted in terms of absolute velocity variations, using the same colour scale as in chapter 3. The fast direction (γ) of the 2ψ azimuthal anisotropy is plotted using a red bar, the length of the bar is proportional to the magnitude of the aniostropy. The broad isotropic signature plotted beneath correlates with what is observed in the isotropic inversion in section 3.4.3.

The first notable point is the strong ridge parallel anisotropy observed in the short period models (figure 5.1) which was not predicted at such distances (over 1000 km) from the ridge (Dunn & Toomey, 2001). A ridge parallel structure close to the ridge would correlate with crack induced anisotropy, but does not explain the similar structure also observed beneath the basin regions. The models suggest a strong north west anisotropy in the upper lithosphere (15 km- 30 km) which is lost at deeper depths.

The magnitude of the ridge parallel anisotropy is lost with respect to depth and by

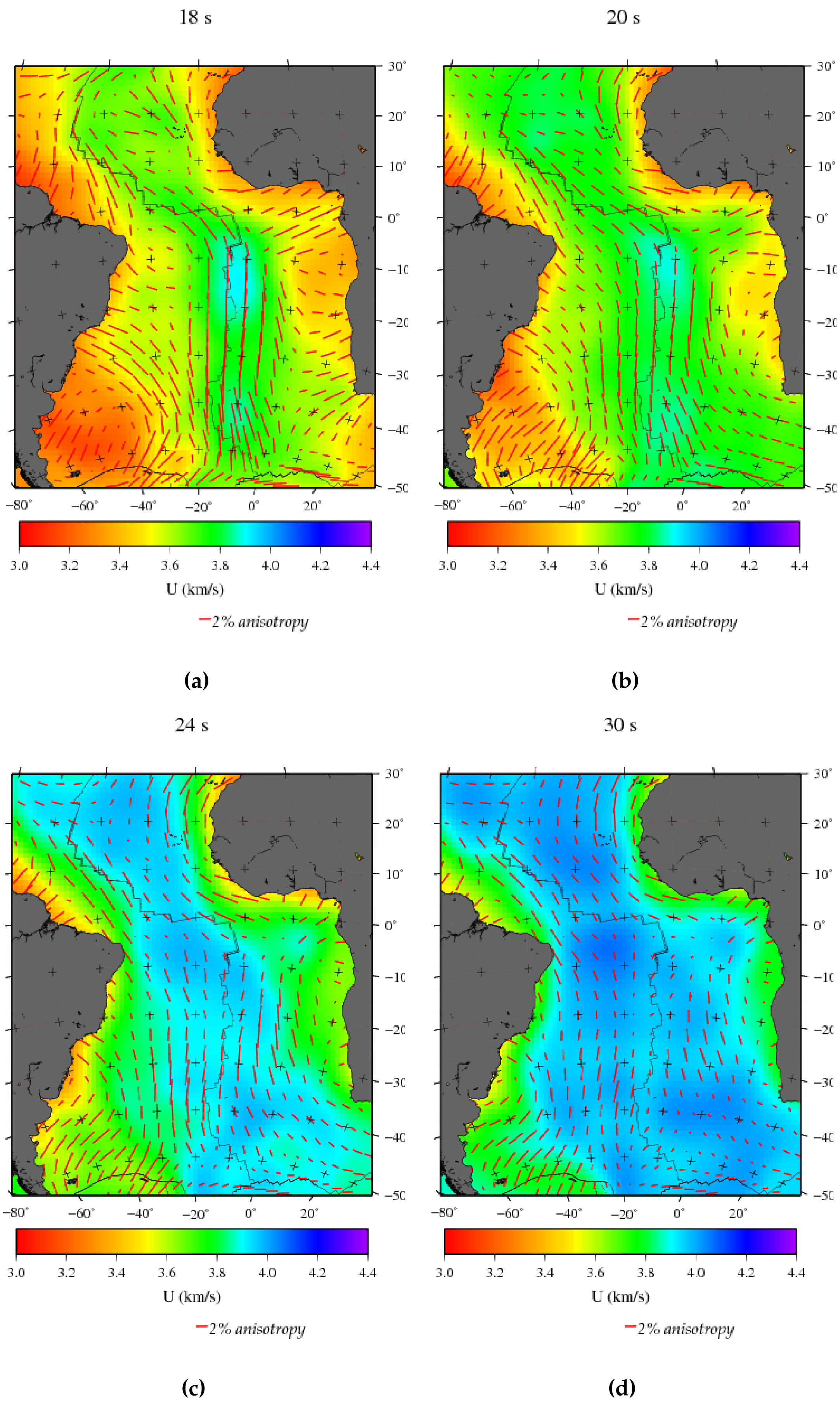

Figure 5.1 2ψ anisotropy plotted in red for short periods (a) 18 s, (b) 20 s, (c) 24 s and (d) 30 s on top of the 6 °spline spaced isotropic structure.

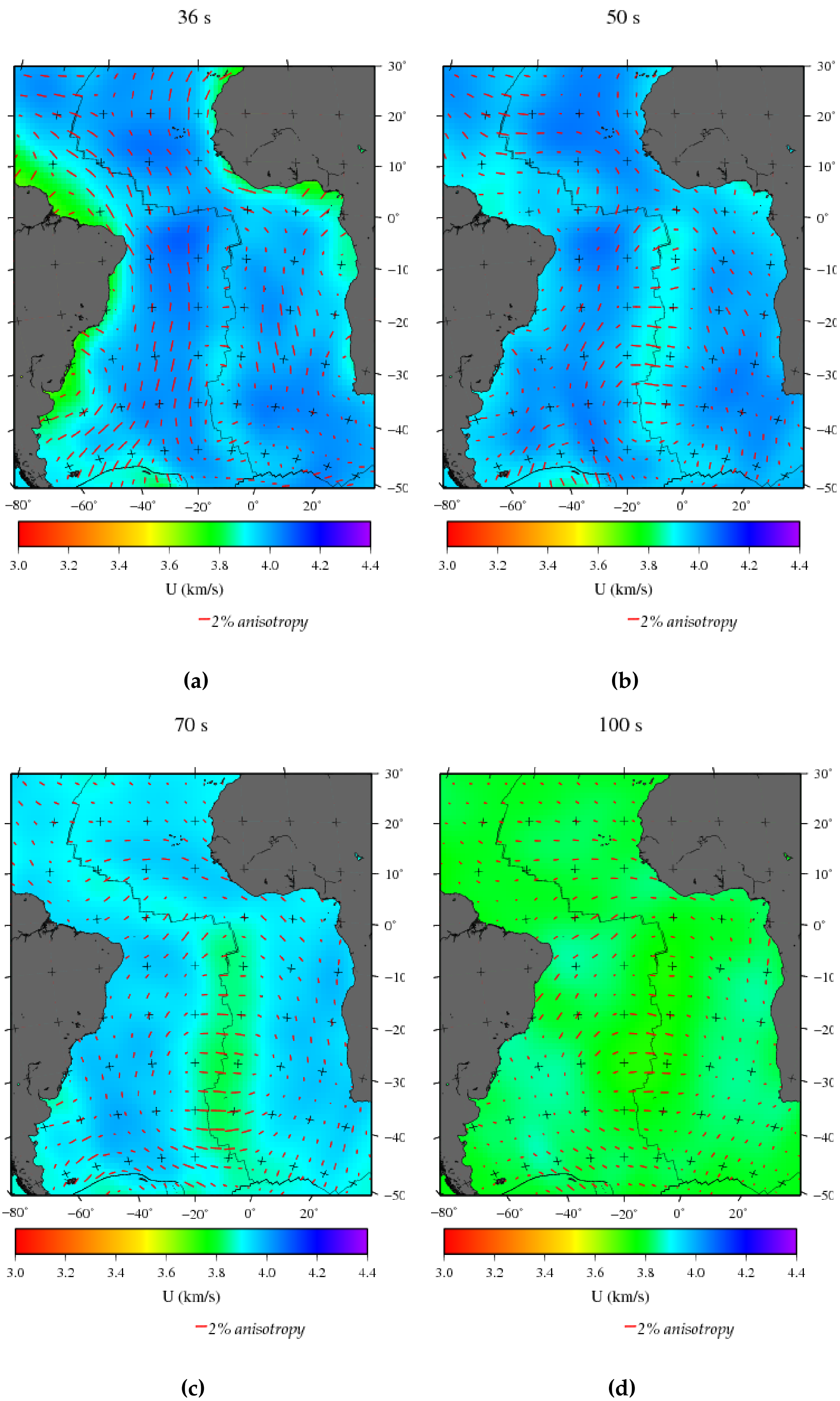

Figure 5.2 2ψ anisotropy plotted in red for intermediate periods (a) 36 s, (b) 50 s, (c) 70 s and (d) 100 s on top of 6 °spline spaced isotropic structure.

50 s it is replaced by the expected ridge perpendicular anisotropy beneath the ridge in the slower velocity asthenosphere. The magnitude of the ridge perpendicular anisotropy in 50 s is greater than the anisotropy seen in 100 s, which may imply a weaker flow or a vertical fow at shallow depths.

The depth sensitivity of 100 s is approximately 80 km maximum and therefore the concentration of the anisotropy seen concentrated beneath the ridge can be considered reasonable if it is asthenospheric flow. There is no correlation to paleo flow (perpendicular to the ridge now frozen into the lithosphere) observed in the lithosphere as off ridge anisotropy observed is ridge parallel and the signature is weaker by 50 s.

5.2 Reliability test

It has been observed before that the anisotropic structure can in places be a result of the inversion and not true anisotropic structure (Lévěque et al., 1998; Maggi et al., 2006b). The magnitude of the anisotropy also requires caution based on it's sensitivity to damping parametrisation (Trampert & Woodhouse, 2003). Three tests were carried out to test the robustness of the model and the trueness of the anisotropy.

The effect of the choice of damping value was tested (as in section 3.4.4), taking the highest reasonable damped model away from the lowest reasonable damped model. This was done for both the isotropic and the anisotropic components.

As seen in most studies, the 2ψ anisotropy from Rayleigh waves is the only anisotropy to correlate with geodynamic processes and the 4ψ anisotropy is considered to not correlate with the 2ψ fast direction (Anderson, 2007). The motion of Rayleigh waves in thought to correlate best with 2ψ anisotropy and Love waves with 4ψ, meaning a correlation between 2ψ and 4ψ in Rayleigh wave on tomography would not be logical (Anderson, 2007; Maupin & Park, 2014). A test to see how much correlation the two azimuths had with respect to orientation and magnitude was carried out. It is assumed that if there is a correlation, the structure is not real anisotropy associated with geodynamical processes due to the 4ψ direction no correlating with the Rayleigh wave motion.

The anisotropic structure was also tested by defining an isotropic model and inverting for anisotropy. Because the model is isotropic any resulting anisotropy can be considered to be a result of the inversion and not true anisotropy. If this structure correlates with the structure seen in the anisotropic models from the data, it could be assumed the structure is not real. Previous studies have run similar tests (e.g. Maggi et al., 2006b; Trampert & Woodhouse, 2003) using a standardised Earth model such as 3SMAC. By using the isotropic tomographic model for the region small scale variations which are not observed in standardised Earth models are taken into account in the inversion.

5.2.1 Difference maps

To test the damping value and the effect of the magnitude of the anisotropy recovered, the lowest damping value was subtracted from the highest damping value and the difference was mapped. The isotropic and anisotropic components were subtracted separately. The isotropic portion of the model was mapped using the same scale as used in 3.4.4. Because the test is to show the sensitivity of the magnitude for the anisotropy, the difference in azimuth was considered negligible and the magnitude was subtracted as a scalar.

The results of the difference maps are seen in figures 5.3 to 5.6. For 18 s (figure 5.3) the region where the anisotropic model exhibits the greatest magnitude of anisotropy, the mid ocean ridge, there is little variation in magnitude for different damping values. This would suggest that the magnitude of anisotropy at the mid ocean ridge is stable in the model and not a result of the choice of damping. There is greater variation in magnitude towards the basin regions, away from the ridge. Refractions of the waves in the sedimentary layers could cause anisotropic effects, causing a greater uncertainty of the structure through choice of damping value. The magnitude of variation in anisotropy in the southern region is in places greater than 2%. This region is sensitive to the choice of damping and any anisotropy in the region could have a error on the anisotropy of $\pm$ 1% which must be considered in the interpretation.

For 30 s (figure 5.4) the variation in magnitude in the eastern region beneath the basin is on the order of 1% which suggests an error associated with the choice of damping of ± 0.5%. It is unlikely at this period that the uncertainty could be caused by refractions in the sedimentary layers. The tradeoff curve is quite shallow which adds to the uncertainty associated with the choice of damping. The variations in magnitude for damping values is greater at 50 s (figure 5.5) and is more wide spread across the region. Beneath the mid ocean ridge where the strongest magnitude is observed in the anisotropic model (figure 5.2 b) there is a large variation in magnitude associated with damping choice. This would suggest an error of ± 1% anisotropy beneath the mid ocean ridge.

The magnitude of anisotropic variations at 100s (figure 5.6) is less than that seen at 50 s. This correlates with lower magnitude anisotropy observed in the anisotropic model for 100 s (figure 5.2 d). The region in the 100 s model (figure 5.2 b) where there is the greatest magnitude of anisotropy again is beneath the mid ocean ridge. This is where the greatest variation in magnitude is observed with a error of ± 0.5% .

5.2.2 Joint inversion for 2ψ and 4ψ

Table 5.1 The precentage misfit calculated from the variance for the chosen tomographic models for the isotropic inversion (chapter 3) the inversion for 2ψ only and the inversion for both 2ψ and 4 ψ

Period	Percentage Missfit		
	Isotropic	2ψ	2ψ and 4ψ
18	43.89	16.66	36.42
20	23.41	21.15	26.46
24	14.86	13.41	18.26
30	18.11	16.64	21.14
36	25.25	27.05	33.39
50	54.03	55.12	62.36
70	71.96	70.88	75.36
100	89.81	84.93	86.76

It is often considered that the 4ψ is associated more with the Love wave propagation

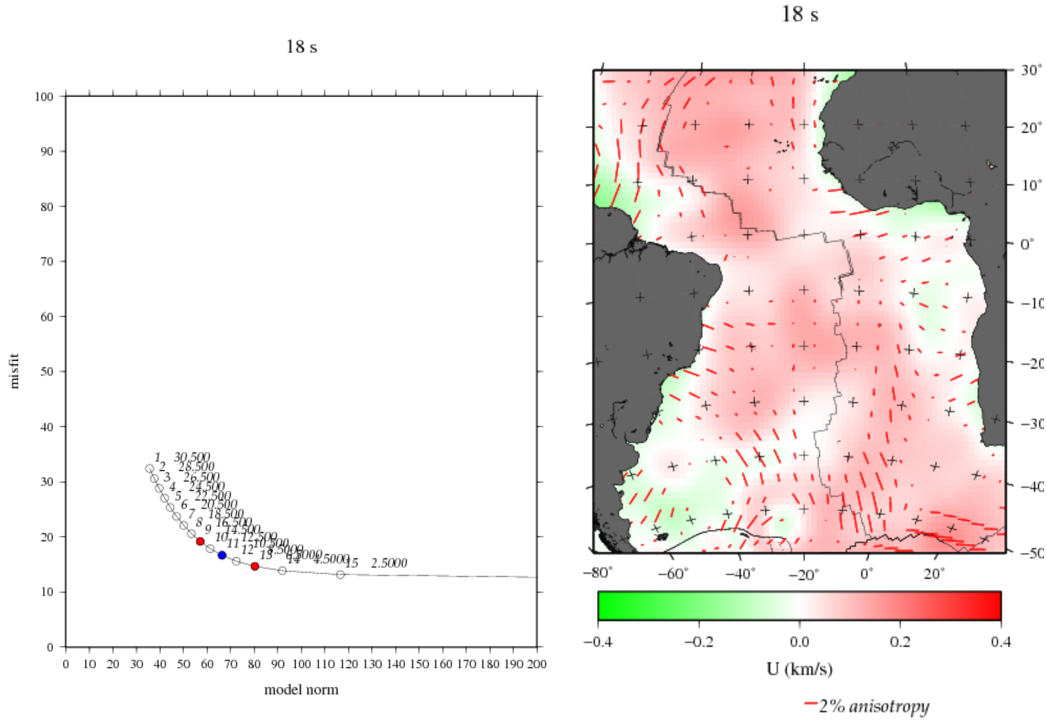

(a) **(b)**

Figure 5.3 Difference map for 18 s between two damping values (9 and 13) shown on (a) trade off curve in red to map (b) the variability in azimuthal anisotropy across the region depending on which damping values is chosen. Final model damping value is show on (a) trade off curve in blue

pattern and therefore there is not expected to be a correlation with Rayleigh wave data (Anderson, 2007; Maupin & Park, 2014). By comparing the azimuth and magnitude of the 2ψ and the 4ψ anisotropy, the variations can indicate whether the 2ψ anisotropy observed is real or a product of the inversion. No correlation between the 2ψ and the 4ψ azimuthal direction would suggest that the 2ψ anisotropy is robust because, the 4ψ inversion for Rayleigh waves only data should not show a correlation to structure. The limitation to this test is the added parametrisation of 4ψ and the requirement for more ray path directions in the spline function to resolve the 4ψ structure. Although the two are compared there is less reliability in the 4ψ due to the path coverage resolution in some parts of the region along with the increase of the unknowns in the inversion.

By inverting for both 2ψ and 4ψ, the misfit to the data is higher compared to inverting for just 2ψ, this can be seen on the trade off curves in figure 5.7 for 30 s due to the added unknowns in the 4ψ terms. This also shows that as 4ψ is not associated with the

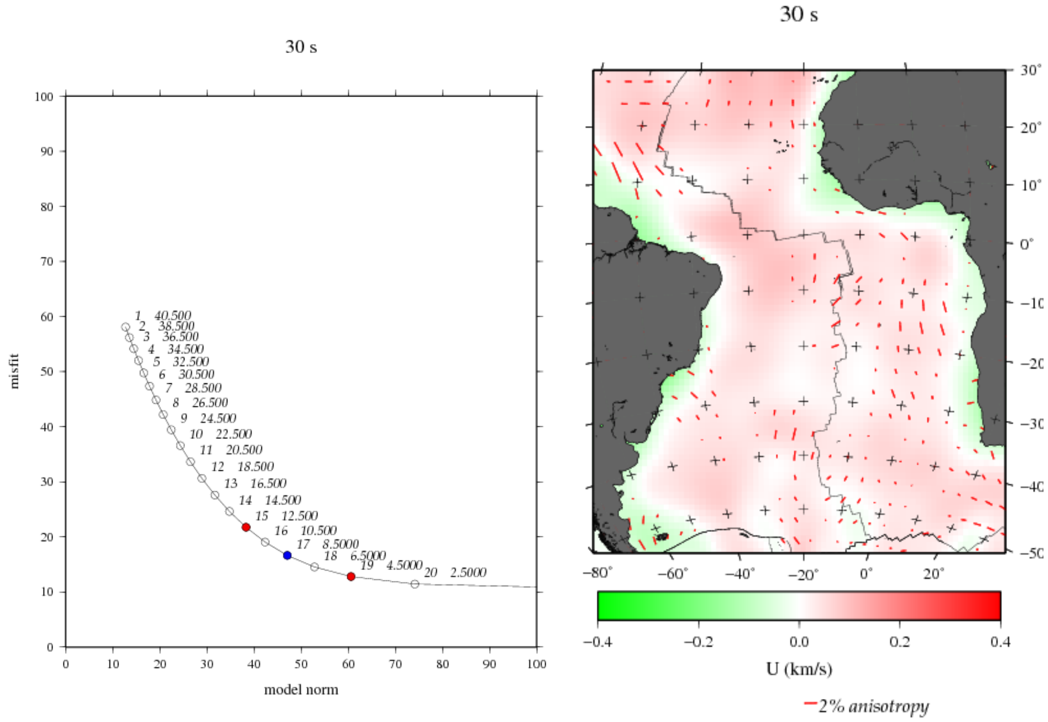

(a) **(b)**

Figure 5.4 Difference map for 30 s between two damping values (15 and 19) shown on (a) trade off curve in red to map (b) the variability in azimuthal anisotropy across the region depending on which damping values is chosen. Final model damping value is show on (a) trade off curve in blue

motion of Rayleigh waves the misfit is greater than just 2ψ which is associated with the motion of Rayleigh waves. Table 5.1 shows the comparison of the misfit of the final model for the isotropic model (chapter 3), the 2ψ only model (section 5.1.1) and 2ψ and 4ψ model. By inverting the data for 2ψ anisotropy the misfit is improved from the isotropic inversion, which suggests that simply inverting for isotropic structure in the region is not enough. The most notable reduction in misfit is for 18 s which suggests the structure sampled at 18 s is more anisotropic than the structure the other periods are sensitive to. The misfit is increased for each period when inverting for both 2ψ and 4ψ which is due to the 4ψ velocity variations not describing the motion of Rayleigh waves (V_{SV}) but Love waves (V_{SV})(Anderson, 2007). Again the most notable increase in misfit is for 18 s.

The 2ψ and 4ψ anisotropy were plotted on the same map for comparison (figures 5.8 and 5.9). The magnitude of the 4ψ anisotropy for 18 s (figure 5.8 a) is large across

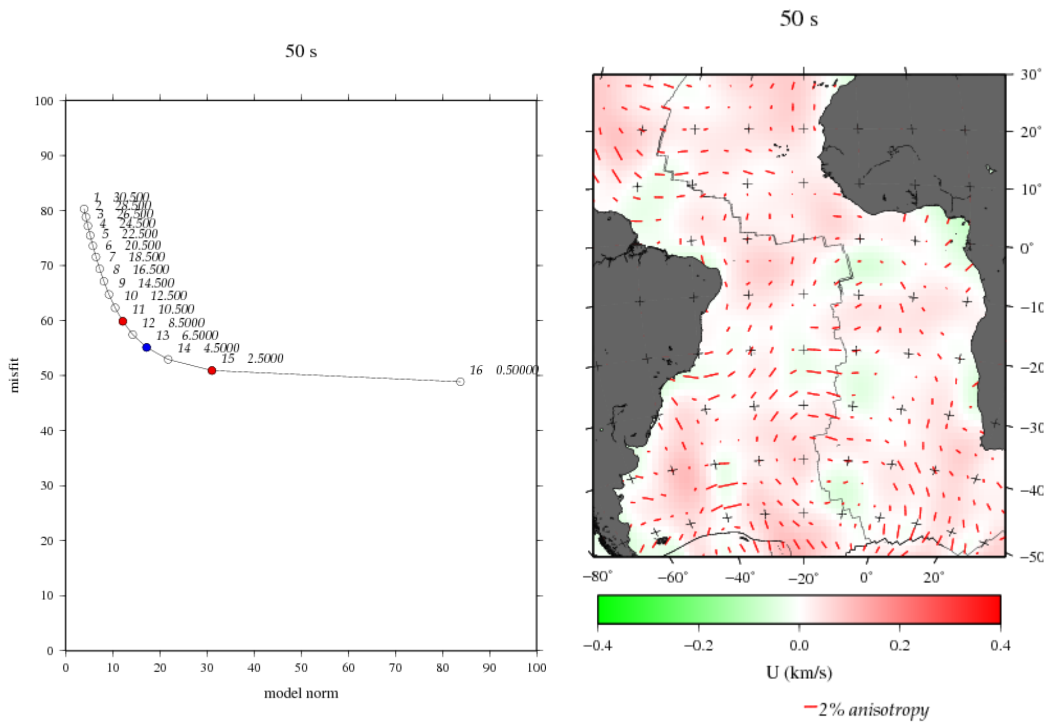

(a) **(b)**

Figure 5.5 Difference map for 50 s between two damping values (15 and 19) shown on (a) trade off curve in red to map (b) the variability in azimuthal anisotropy across the region depending on which damping values is chosen. Final model damping value is show on (a) trade off curve in blue

the region. This may suggest the 2ψ structure is not real as it is also associated with 4ψ, however the increase in misfit from 2ψ could support the 2ψ structure. The path coverage may also not be enough to invert for 4ψ. The magnitude of the 4ψ structure for the rest of the periods does not correlate as well with the 2ψ structure.

For 24 s (figure 5.8 c) there is a correlation between the azimuthal direction of 4ψ and 2ψ anisotropy to the east of the mid ocean ridge but not in the west where the azimuths are off set. The magnitude of the 4ψ anisotropy is greater in the structure towards the continental shelf. This trend continues to 30 s and 36 s but the magnitude of 4ψ becomes weaker as the period becomes longer. There is a more negative correlation between 2ψ and 4ψ for 30 s and 36 s where the magnitude of 2ψ is strong the 4ψ magnitude is weaker. The 4ψ anisotropy seems to become stronger in regions of slower velocity (towards the continental shelf). There is also, a degree of correlation at 50 s, 70 s and 100 s (figure 5.9 b, c and d) with the anisotropy beneath the mid ocean

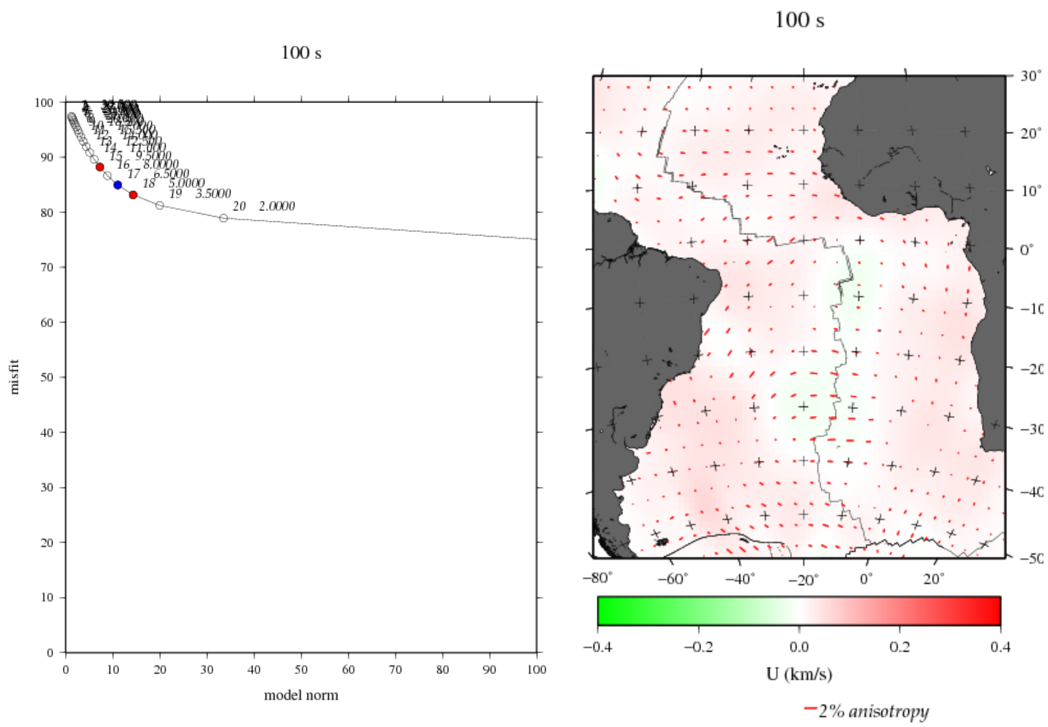

(a) **(b)**

Figure 5.6 Difference map for 100 s between two damping values (15 and 18) shown on (a) trade off curve in red to map (b) the variability in azimuthal anisotropy across the region depending on which damping values is chosen. Final model damping value is show on (a) trade off curve in blue

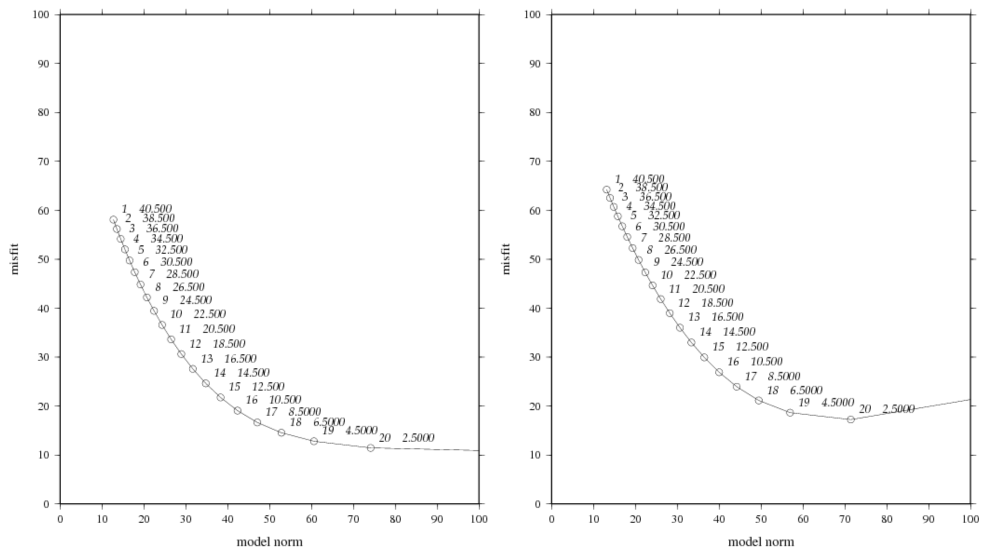

(a) **(b)**

Figure 5.7 Tradeoff curve for choice of damping for 30 s for (a) 2ψ and (b) joint 2ψ and 4ψ.

ridge, which could suggest the anisotropy is not a result of a flow direction.

Tests show the misfit improvement for 2ψ which does suggest a level of anisotropic structure is required to fit the data. The poorer fit to the 4ψ could be due to the path coverage not being sufficient or the added unknowns in the inversion. The tests show some regions, especially 30 s and 36 s where the ridge parallel structure may be real.

5.2.3 Inversion of synthetic structure

The anisotropic structure can sometimes exhibit questionable azimuthal anisotropy based on the isotropic structure, for example the strong ridge parallel anisotropy seen at 18 s (figure 5.1 a) could be the result of the fast velocity ridge and therefore the fast direction is along the fast velocity feature (ridge parallel). The same argument stands for a slow velocity linear feature where the fast direction would be perpendicular to the slow velocity feature. If the azimuthal anisotropy in the models were an artefact of the inversion because of the isotropic velocity structure and not a true anisotropy structure it would be expected to be present in the inversion of an isotropic model. If the anisotropy was not the result of the isotropic structure then no anisotropy would be present in the resulting model from inverting an isotropic velocity model.

The final isotropic model from section 3.4.3 was used to test the anisotropic velocity structure. The path average velocity for each path in the velocity model was calculated and reassigned as the input for the data path in the anisotropic model inversion. Each path was given a equal weighting, if the model is assumed to be the isotropic structure then there is no need to weight the data. The results for the inversion can be seen in figures 5.10 and 5.11.

There is a similar anisotropic pattern in the isotropic model test (figures 5.10 and 5.11) compared to the structure resolved from the anisotropic data inversions (figures 5.1 and 5.2). The ridge parallel structure which is seen at shorter periods (18 s - 36 s) appear to be associated with the velocity structure moving from a fast ridge to a slower continental velocity. At longer periods (50 s - 100 s) the slow velocity ridge feature associated with the up welling asthenosphere beneath the ridge is modelled in the isotropic

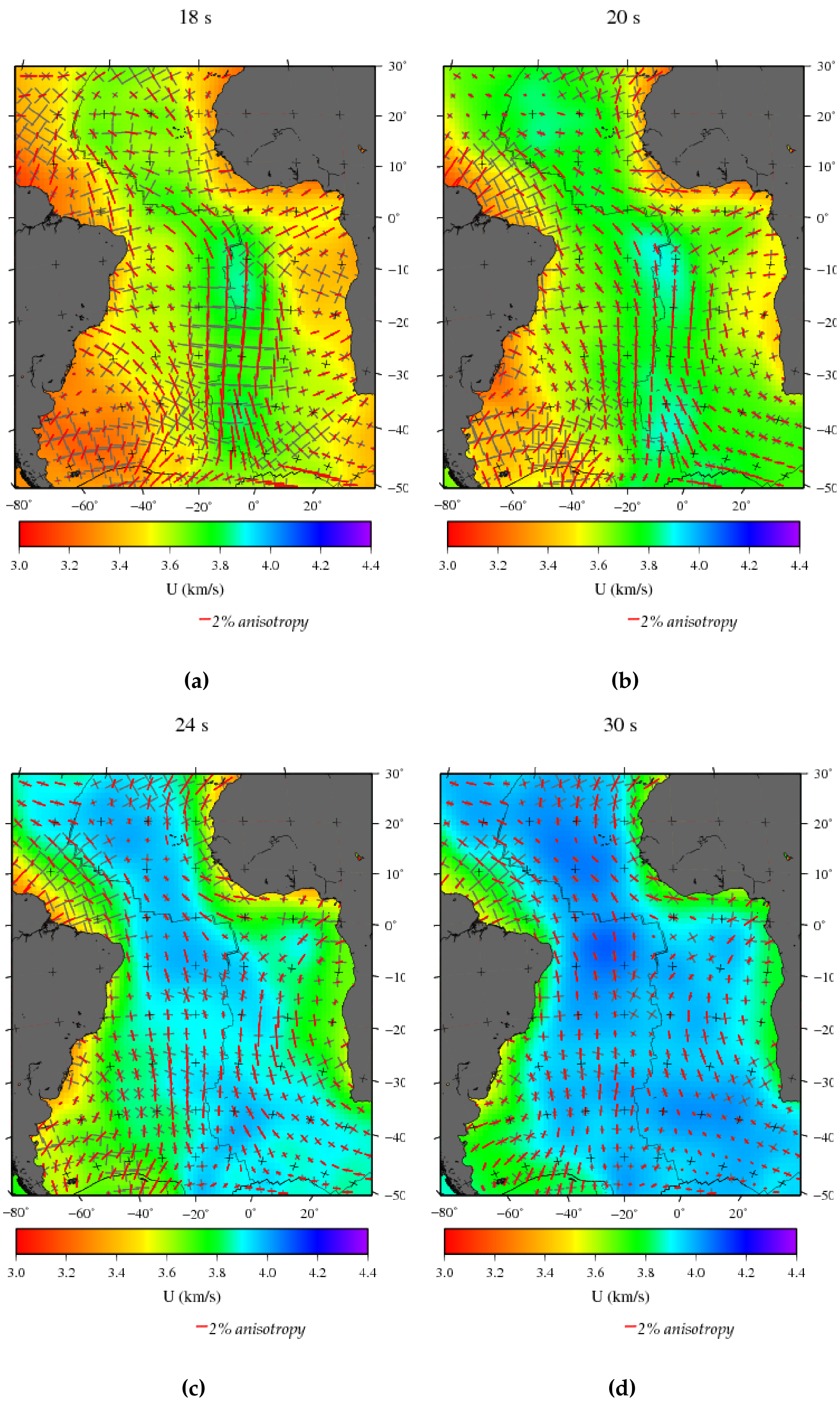

Figure 5.8 Jointly inverted 2ψ anisotropy plotted in red and 4ψ anisotropy plotted in grey at 4 °spacing for short periods (a) 18 s, (b) 20 s, (c) 24 s and (d) 30 s on top of the associated isotropic structure.

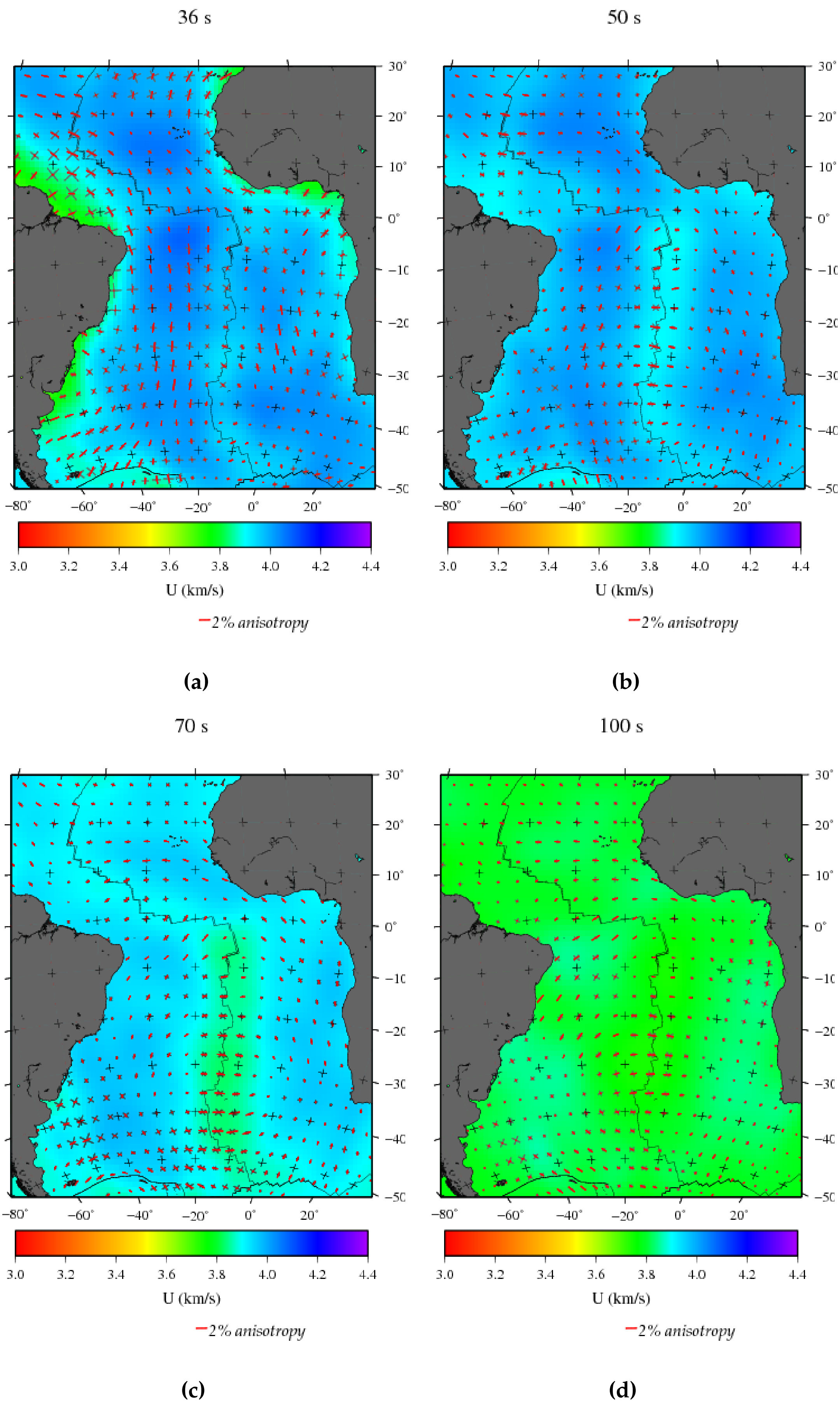

Figure 5.9 Jointly inverted 2ψ anisotropy plotted in red and 4ψ anisotropy plotted in grey at 4 °spacing for intermediate periods (a) 36 s, (b) 50 s, (c) 70 s and (d) 100 s on top of the associated isotropic structure.

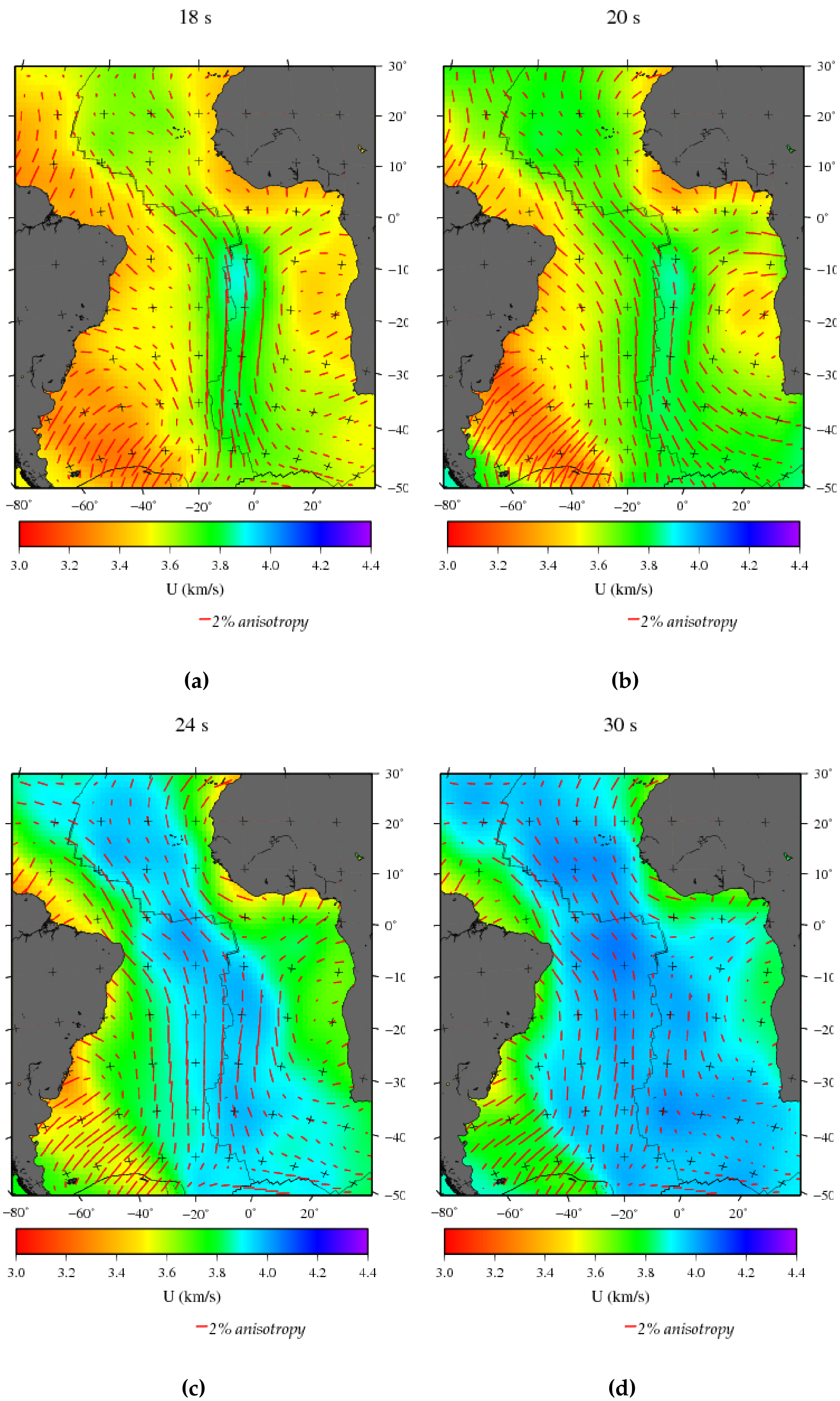

Figure 5.10 2ψ anisotropy plotted in red for a isotropic structure inverted from the isotropic tomography model plotted at 4 °spacing for short periods (a) 18 s, (b) 20 s, (c) 24 s and (d) 30 s on top of the isotropic structure.

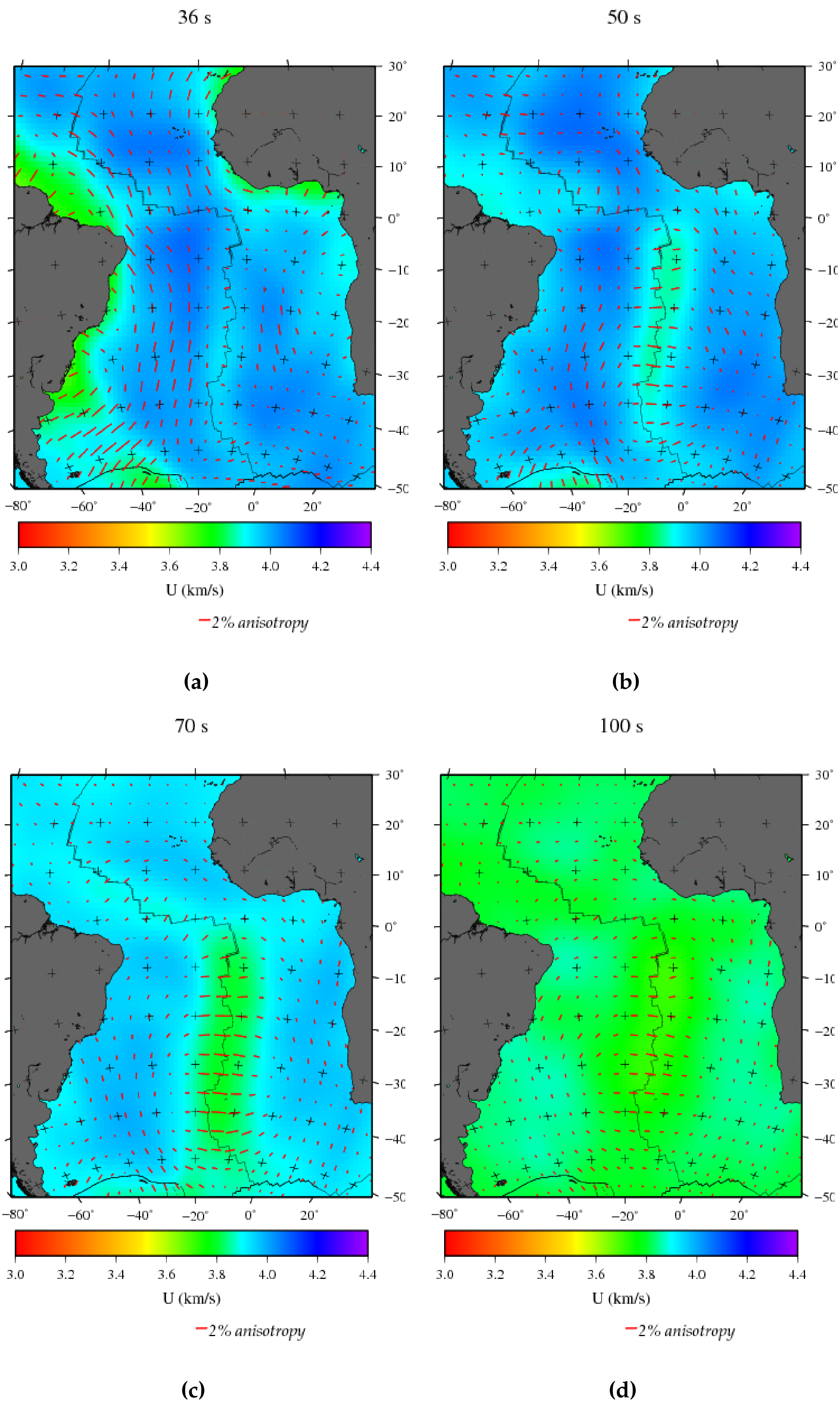

Figure 5.11 2ψ anisotropy plotted in red for a isotropic structure inverted from the isotropic tomography model plotted at spacing for intermediate periods (a) 36 s, (b) 50 s, (c) 70 s and (d) 100 s on top of the associated isotropic structure.

inversions. This would suggest what has previously been interpreted as mantle flow could be associated with the isotropic velocity structure of the region and no anisotropy is present beneath the mid ocean ridge. The low velocity region in these models is concentrated beneath the ridge and are narrow. If periods were extended to sample deeper, the low velocity region may be better trusted as a region of ridge perpendicular anisotropy not associated with a narrow region of slow velocity.

5.3 Final anisotropy structure

The isotropic inversions (section 5.2.3.) resolve similar anisotropic structure to the structure resolved in the models (section 5.1.1). To attempt to model the anisotropy associated with just the real anisotropic structure and exclude the anisotropy obserevd as an artifact of the inversion, the resultant anisotropy was calculated. Where the magnitude of the anisotropy seen in the anisotropic model was greater than the anisotropy associated with the synthetic anisotropic structure, the resultant azimuthal vector was calculated. The results are plotted in figure 5.12 and 5.13.

18 s and 20 s (figure 5.12 a and b) are the only two periods where any large azimuthal anisotropy is modelled from the data but not the synthetic test. This anisotropy if off ridge but ridge parallel. The sensitivity of these periods is to crustal structure and therefore the structure associated with the anisotropy would be crustal not lithospheric. Possible causes of this anisotropy are discussed in chapter 6.

No anisotropy is observed at longer periods, suggesting that the anisotropy observed in the anisotropic models may not be real and there is no paleo flow or present flow observed at this resolution. The structure observed at the longer periods, however, is similar to published models of anisotropy beneath oceans (e.g. Lévěque et al., 1998; Maggi et al., 2006b; Silveira & Stutzmann, 2002). These tests raise the question as to how much anisotropy resolved beneath the oceans can be interpreted as mantle flow. Geodynamic models of plate motion have used data from anisotropic studies to determine flow direction.

These tests may instead show that the path coverage in the region is not well distributed so the azimuthal directions are not resolve in the anisotropy accurately. The same path coverage was used for both the synthetic test and the inversion of data. Both resolved the same structure, however, the structure does change in orientation from ridge parallel to ridge perpendicular. This would suggest that the anisotropy is not a result of a single dominant path direction.

5.4 Anisotropy and stress fields

Anisotropy for periods sensitive to crustal structure (18 and 20 s) has some resultant anisotropy not observed in the modelling of the synthetic dataset. This anisotropy is off ridge and parallel to the ridge, therefore perpendicular to the direction of flow. Anisotropy in the oceanic crust can be induced by the alignment of minerals in a stress field or by cracks, faults and fissures in the upper crust.

Global stress maps were looked at to see if there was a correlation between stress direction and the anisotropy. Richardson (1992) model the torque acting on the tectonic plates. On the African plate ridge push and collision force act on the plate (figure 5.14). The direction of anisotropy of the African plate is consistent with Zoback et al. (1989). The forces modelled in Richardson (1992) for the South American plate are just ridge push which do not correlate with the azimuthal anisotropy. There are no stress directions mapped on the South American plate therefore a comparison cannot be made (Zoback et al., 1989).

Although there is a similarity between the stress directions and the azimuthal anisotropy the structure in the anisotropic models does follow the velocity structure. This may suggest that although it is not modelled in the isotropic inversions from the isotropic dataset, it may still be a result of the tomography and not anisotropy in the crust. Further work would need to be carried out with a more reliable short period data set to test if anisotropy can be resolved and if there is a correlation with the stress field of the plates.

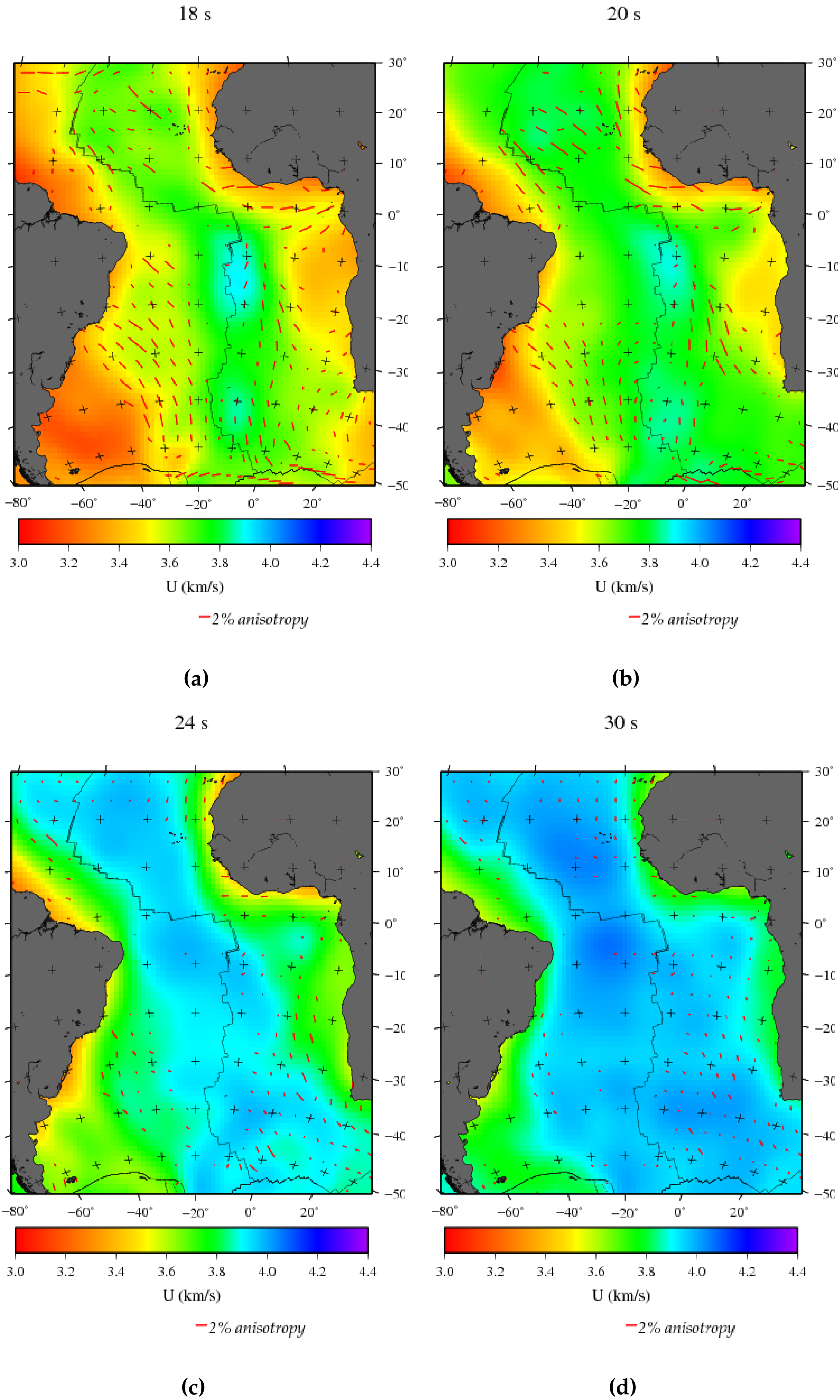

Figure 5.12 The resultant vector for 2ψ anisotropy from the isotropic and anisotropic inversions plotted in red at 4 °spacing for short periods (a) 18 s, (b) 20 s, (c) 24 s and (d) 30 s on top of the isotropic structure from the data inversion.

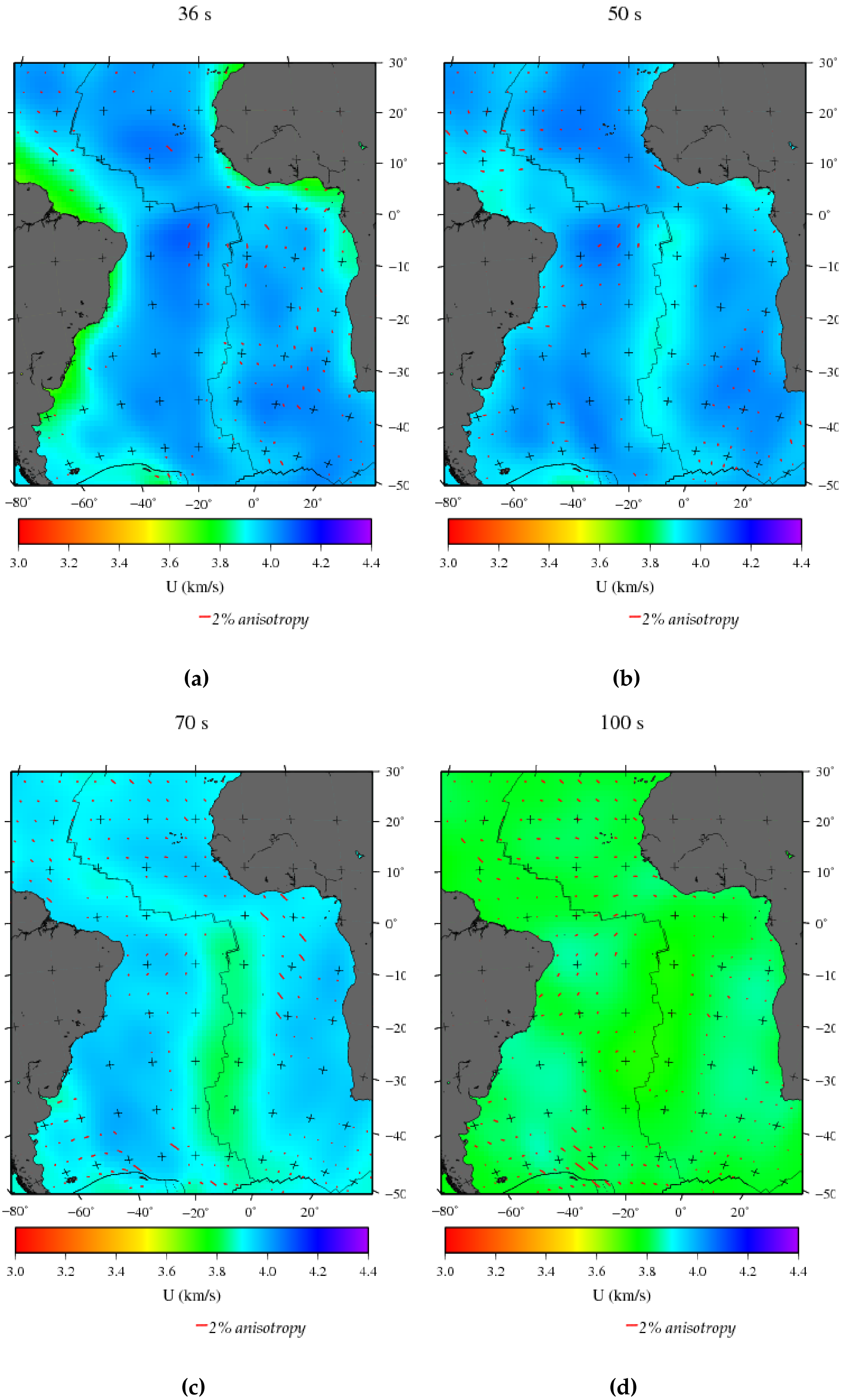

Figure 5.13 The resultant vector for 2ψ anisotropy from the isotropic and anisotropic inversions plotted in red at 4 °spacing for intermediate periods (a) 36 s, (b) 50 s, (c) 70 s and (d) 100 s on top of the isotropic structure from the data inversion.

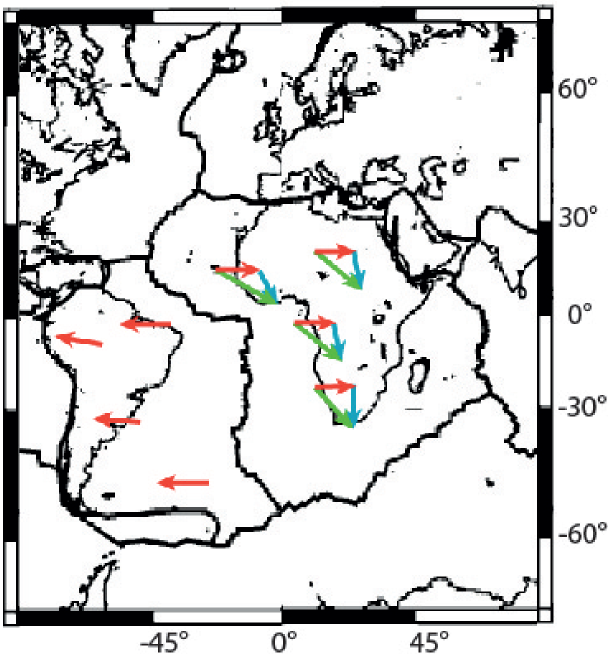

Figure 5.14 Redrawn from Richardson (1992) showing the ridge push force (red) and collisional force (blue) associated with the Torque on the African and SOuth American plates with the resultant from the two in green

Chapter 6

Discussion, Conclusions and Further Work

6.1 Discussion

This study has resolved the isotropic velocity structure beneath the central and southern Atlantic Ocean from surface wave tomography, using measurement of group velocity. Features resolved in the tomography have a horizontal scale of approximately 350 km or larger. The tomographic models have then been inverted in order to find the shear velocity structure with respect to depth, providing the most detailed crust and uppermost mantle structure obtained for the central and southern Atlantic to date. A clear variation can be seen in crustal structure observed in the profiles, from ridge to sedimentary basin, to continental margin and continent (chapter 4). Additionally, a low velocity region is resolved beneath the ridge. This low velocity region occurs at increasing depths as the structure is observed further from the ridge axis. Here the causes and significance of the features observed in the data are discussed in further detail, with a focus on the relationship between group velocities and lithospheric age, the crustal and lithospheric thickness and the relationship to mantle potential temperature (T_m).

Maps of crustal and lithospheric thickness for the whole area are presented. A

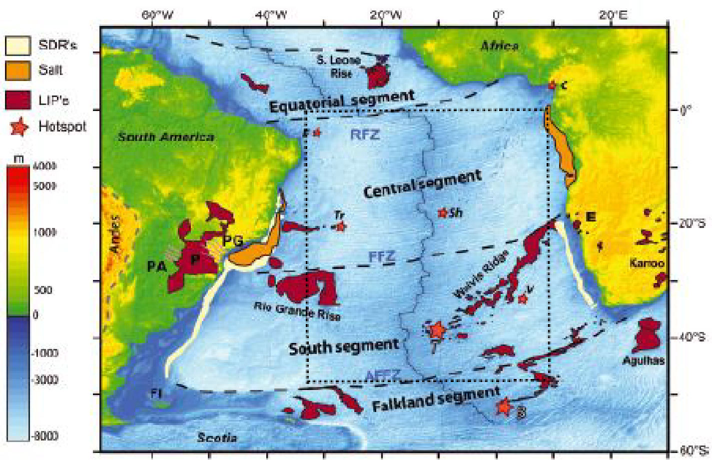

Figure 6.1 Map taken from Torsvik et al. (2009) showing the central and southern segment locations in the southern Atlantic Ocean and highlighting the volcansim associated

more focussed study is done on the southern Atlantic (between 0 °and 50 °), where the path coverage is considered best. The early evolution of the southern Atlantic is thought to differ between the segmented regions, with the southern region being magma dominated in evolution, whereas the central was tectonic dominated with less magmatic influence (Blaich et al., 2011). Associated with the magmatic evolution of the southern segment are the Rio Grande Rise and Walvis Ridge, which are suggested to be large igneous provinces (LIPs) (Torsvik et al., 2009). Figure 6.1 shows the considered geographical seperation between these two regions and the focused region discussed in this study. A comparison of these regions will allow an investigation into whether differences in early evolution of the mantle lithosphere are also reflected in the present velocity structure.

Previous studies have observed asymmetry in the South Atlantic. Colli et al. (2014) and Flament et al. (2014) observe a bathymetric asymmetry, with the African continent being more elevated relative to the South American continent, causing a topographic gradient from east to west. Blaich et al. (2011) observed an asymmetry associated with the continent to ocean transitional margins, where the gradient of the Moho is steep beneath the South American margin and the transition is narrow in comparison to a gentler transition beneath the African margin. This asymmetry is thought to be associated with the initial breakup of Gondwana and not with ongoing present day processes. The magmatism associated with the initial break-up of the southern segment is also asymmetric, the distribution of volcanism for the Rio Grande Rise is concentrated close to the continental shelf of South America (figure 6.1). In contrast, the associated magmatism on the African plate, the Walvis Ridge is elongated from the continental shelf to the mid ocean ridge. This magmatism of both features is associated with the same hot spot, now residing beneath Tristan da Cunha. This explains the asymmetry because the hotspot has continued to feed the crust beneath the Walvis ridge, but material to the Rio Grande Rise ceased on the South American plate as spreading continued (Torsvik et al., 2009). There is also an asymmetry with respect to shear velocity observed in the region. Silveira et al. (1998) observe an asymmetry of phase velocities between 50 s and 170 s, where fast velocities are observed in the east compared to the west of the South Atlantic. Given the various sources of asymmetry in structure, a comparison is therefore also made in this study between the east and west of the region.

6.1.1 Group velocities and lithospheric age

Surface wave velocity is seen to increase with respect to lithospheric age in all oceans (e.g. Mocquet & Romanowicz, 1990; Ritzwoller et al., 2004; Zhang & Lay, 1999). Mocquet & Romanowicz (1990) observe a weak correlation of group velocities with respect to age in the Atlantic south of the equator, but not with phase velocities. Zhang & Lay (1999) observes that the seismic data beneath the Atlantic exhibits much less variation in phase velocities with respect to age than seen in the other oceans. This was thought to be due to a steeper velocity gradient associated with the slow spreading rate in the Atlantic compared with the Pacific and Indian Oceans. There is also an overall decrease in the age dependence as the period increases, which is observed for all oceans (Zhang & Lay, 1999). The longest period group velocities in this study (60 s - 100 s) are the group velocities sensitive to the lithospheric structure.

The longest period group velocities (60 s to 100 s) were plotted with respect to age of the sea floor for the southern Atlantic (figure 6.2). The ages were taken from the Müller

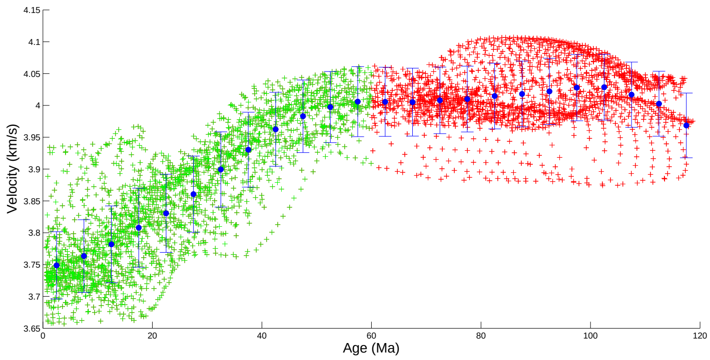

(a)

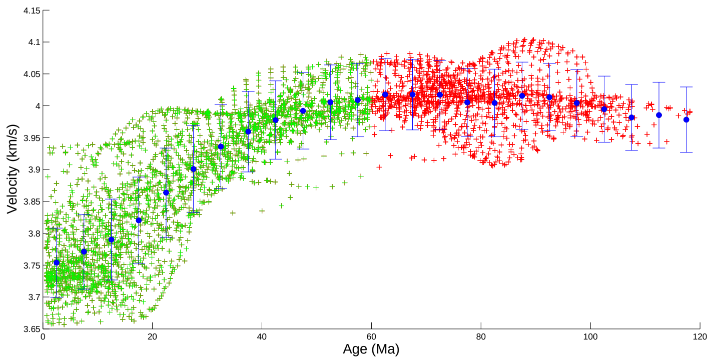

(b)

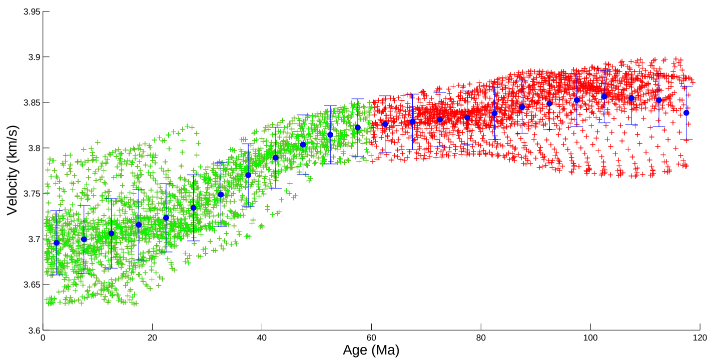

(c)

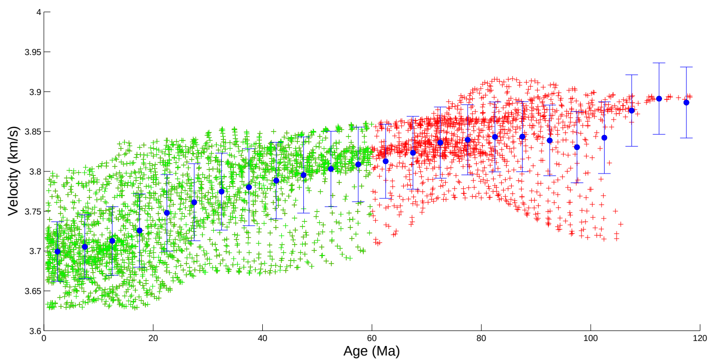

(d)

Figure 6.2 Age versus velocity plots from the tomographic modelled group velocities for 60 s east (a) and west (b) and 100 s east (c) and west (d) where green is < 60 Ma and red is > 60Ma and the blue points are the mean velocity for every 5My bin et al. (2008) model for sea floor age. Due to the asymmetry associated with observations in previous studies, the east and west of the region are considered separately. To further explore the relationship between the age and velocity, the velocities were put into age bins of 5My and the mean average velocity was calculated along with 1 standard deviation. The age-velocity scatter plots for 60 s and 100 s with the mean velocity and standard deviation plotted can be seen in figure 6.2. All the plots show a positive correlation, however, there appears to be a stronger correlation between 0 Ma and 60 Ma (green) and less of a correlation between 60 Ma and 100 Ma (red). There appears to be an overall stronger relationship at 60 s than at 100 s, a similar trend to what Zhang & Lay (1999) observed in phase velocities. The plots for the other 3 periods (70 s - 90 s) can be found in Appendix D. Overall, there is greater scatter in the velocities in the west compared to the velocities in the east.

A linear relationship has been assumed between age and group velocity for periods 60 s to 100 s and the gradient of the line of best fit for the mean values (the m value for the $y = mx + c$) can seen in table 6.1. The linear relationship was calculated for the whole profile (0 - 120 Ma), for younger lithosphere only (0 - 60 Ma) and for older lithosphere (60 Ma - 120 Ma) respectively. From the mean velocity values it does not appear to be a direct linear fit between age and velocity for the whole age span (All Lithosphere). This is reflected in the R^2 values seen in table 6.1. The best fit linear relationship for each period is for the velocities between 0 and 60Ma. The relationship between 60 and 120 Ma is a magnitude smaller, which suggests the controls on the lithosphere may change after this age. The linear relationships do systematically decrease with respect to period.

Two errors can be applied to the group velocities, from chapter 3; the difference maps suggested there was a variation on the velocity values of between $\pm$ 0.05 and $\pm$ 0.01 depending on the model chosen. Whereas, the 3rd standard deviation for each period has a greater error associated, between $\pm$ 0.16 and $\pm$ 0.38 for 60 s to 100 s. These latter errors are similar values to the standard deviations for the age binned velocities, which would be sensible as the error for each velocity is the deviation of the path to the regional average for each period. The difference maps however, suggest that between 0 and 20Ma the velocities would decrease but increase after 20 Ma. This would change the gradient of the linear relationship, however, there would still be a linear relationship. This does not explain the increase in scatter in the west of the region. We can conclude that there is a strong linear realationship between velocity and age, which decreases with period and with age.

Table 6.1 Relationship between age and mean group velocity for the South Atlantic from the isotropic tomographic inversion

Period (s)	All Lithosphere(0 - 0120 Ma)			
	West (kms^{-1}/Ma)	R^2	East (kms^{-1}/Ma)	R^2
60	0.002	0.71	0.0018	0.58
70	0.002	0.84	0.0018	0.7
80	0.002	0.85	0.0014	0.7
90	0.0016	0.87	0.0016	0.93
100	0.0015	0.88	0.0015	0.94

Period (s)	Young Lithosphere(0 - 60 Ma)			
	West (kms^{-1}/Ma)	R^2	East (kms^{-1}/Ma)	R^2
60	0.005	0.99	0.005	0.97
70	0.004	0.978	0.0045	0.97
80	0.0035	0.97	0.0035	0.96
90	0.003	0.98	0.0025	0.98
100	0.0025	0.97	0.0022	0.97

Period (s)	Old Lithosphere(60 - 120 Ma)			
	West (kms^{-1}/Ma)	R^2	East (kms^{-1}/Ma)	R^2
60	-0.0001	0.034	-0.0007	0.78
70	0.0005	0.64	-0.00004	0.0125
80	0.0007	0.73	0.00035	0.09
90	0.0007	0.86	0.001	0.76
100	0.0005	0.52	0.001	0.73

6.1.2 Crustal thickness

The thickness of oceanic crust can be controlled by the spreading rate, presence of transform faults, mantle potential temperature and the presence of intra plate volcanism. Crust formed at slow spreading ridges is thought to be thinner than crust formed at fast spreading ridges (Bown & White, 1994). The number of transform faults along the ridge plays a role in this, where the crust associated with these is thinner (around 3.5 km) due to upwelling lithosphere along the transform faults. This results in an overall thinner average crust (Bown & White, 1994; Gregg et al., 2007). Hotspots can be associated with anomalously thick crust, as they underplate the crust with magmatic material (Bown & White, 1994; McKenzie et al., 2005). The Atlantic is a slow spreading ridge with a current half spreading rate of 2 cmy^{-1} but the ridge has three associated hotspots, the Ascension Islands, St Helena and Tristan da Cunha. The T$_m$ is also thought to be a control on the thickness, where a change in T$_m$ of 12 °Ccan cause a variation in crustal thickness of 1 km (McKenzie et al., 2005). McKenzie et al. (2005) state that the average oceanic crustal thickness is 7.1 km $\pm$0.8 km, which assumes a variation in T$_m$ of 10 °C.

An estimate for crustal thickness can be extrapolated from the shear velocity model by taking the depth to a velocity contour. Acton et al. (2010) take the 4.1 kms^{-1} contour as the depth to the Moho, while Tang & Zheng (2013) take the 4.0 kms^{-1}. These contours were chosen by Acton et al. (2010) and Tang & Zheng (2013) based on a correlation with receiver function data. Both these studies yield thicker crust for the oceanic region than would be expected. This suggests that the choice of velocity may be too fast to obtain a sensible depth the oceanic Moho. Therefore, in this study we compare estimates of Moho depths using the 3.9 kms^{-1} and 4.0 kms^{-1} contours The depths to these contours were extracted from east-west oriented profiles at 1 degee north-south spacing. The depths are gridded, and then crustal thickness was calculated by subtracting the sea floor depth from the depth to the 3.9 kms^{-1} and 4.0 kms^{-1} velocity contour at 0.5 degree intervals.

The crustal thickness maps can be seen in figure 6.3 a and b for the 3.9 kms^{-1} and the 4.0 kms^{-1} contours respectively, along with the starting crustal thickness for the Crust 2.0 model. There is a lot of variation from the starting model of Crust 2.0 (figure 6.3 c) with regions of thicker crust and regions of thinner crust in both maps. The 3.9 kms^{-1} map (figure 6.3 a) seems to be closer to the starting model and provides a more geologically reasonable thickness. The Walvis ridge and Rio Grande rise are

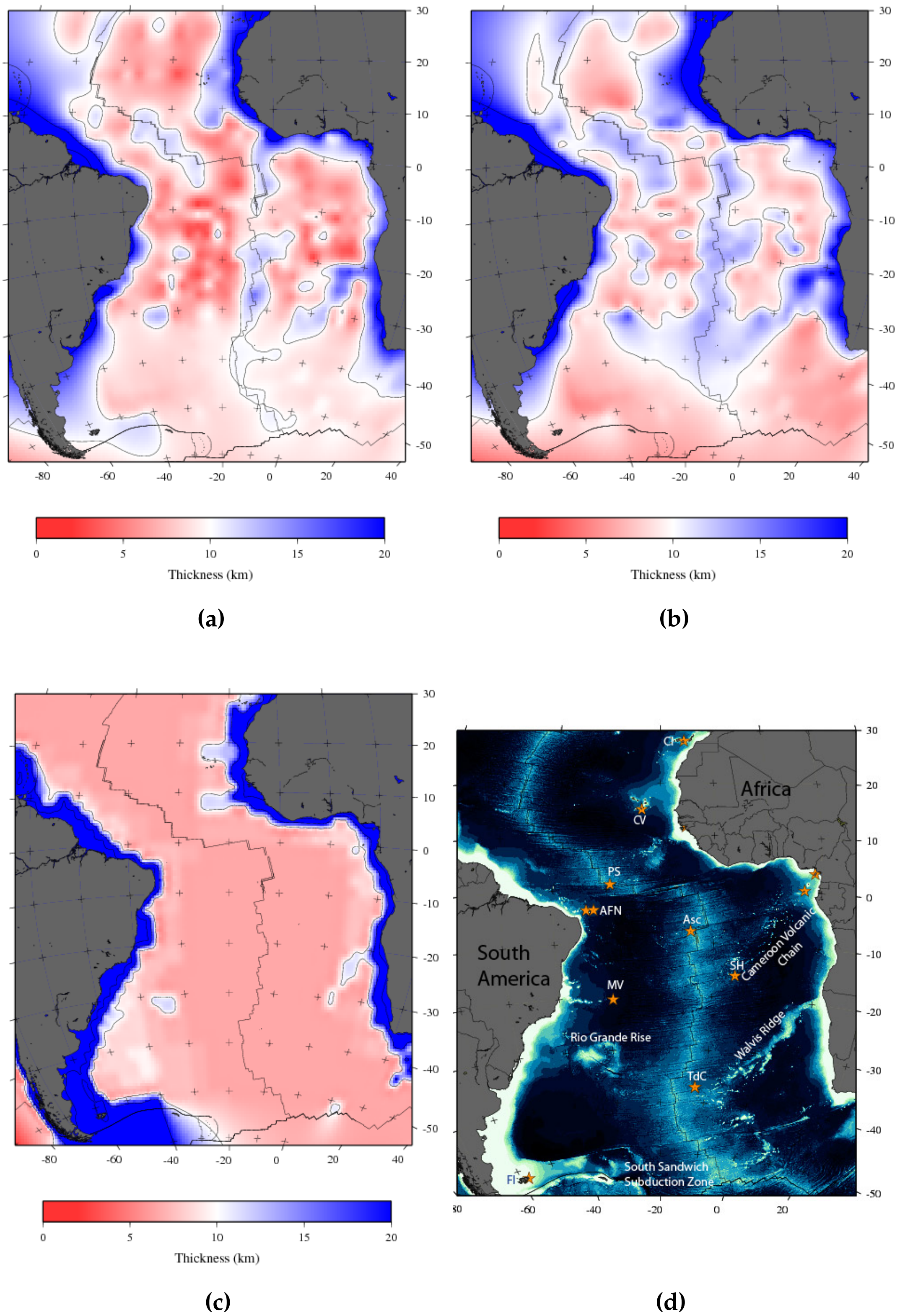

Figure 6.3 (a) Crustal thickness predicted using 3.9 kms^{-1} from velocity model with contours at 10 km. (b) Crustal thickness predicted using 4.0 kms^{-1} from velocity model with contours at 10 km. (c) Crust 2.0 model crustal thickness. (d) Topographic structure of seafloor used to calculated crustal thickness with ocean islands and sea mounts highlighted.

picked out as regions of thicker crust (greater than 10 km) in both models. The ridge itself is picked out as a region of thicker crust in the maps from the inverted model. This is most likely due to the complex velocity structure beneath the ridge. A shallow magma chamber, which is associated with slower spreading ridges would cause a thicker region of slower velocity, thus increasing the depth to the 3.9 kms^{-1} and 4.0 kms^{-1} contours. There is still debate as to when the Moho is fully formed beneath the ridge axis and how far away from the ridge axis it can be confidently recovered, but based on studies of the EPR the formation of the Moho is considered to be complete a few degrees from the ridge axis (Mutter & Carton, 2013). As a result, the thicker structure recovered below the ridge is dismissed until 2 °either side of the ridge axis, where the Moho is assumed to be fully formed and the thickness can be confidently recovered.

Away from the ridge and sea mounts there are smaller regions, which are thicker than 10 km on both maps (but more prominent on 4.0 kms^{-1}) from the inverted model. These regions of thicker crust also correlate with the slow velocity regions seen at shallow depths in chapter 4. There is no correlation between the regions of thicker crust and the ocean islands. These could be continental crustal blocks associated with the initial break-up of South America and Africa, during the formation of the South Atlantic. These blocks would have been stretched during the extension of the continental rifting and therefore would be thinned from 30 km, but still retain the slower velocity signature. O'Reilly et al. (2009) suggest processes linked to rifting of continental cratons can leave wedges of continental lithosphere within the new oceanic crust-mantle system (figure 6.4). If they are continental relics, the velocity of the block may be slower than the surrounding crust which will increase the depth to the 3.9 kms^{-1} and 4.0 kms^{-1} contours. This is a disadvantage to defining a single velocity contour as the Moho, it does not account for variations in crustal velocity across the region.

In the west of the central segment of the South Atlantic, the crustal thickness appears to be on average thinner than that in the east. Table 6.2 shows the average for the two segments, for the east and west along with an overall average. The estimated error is half the average difference between the two crustal thickness maps (3.9kms $^{-1}$

and 4.0kms $^{-1}$). This seemed as a reasonable estimation considering the structure in 3.9kms $^{-1}$ appears more reasonable; some velocity variations with in the region could be accounted for by the error. However, some of the features occur on both maps. Even with the large error there is an asymmetry in the central segment with the west being thinner than the east on both maps (table 6.2). Other error estimations were considered but were deemed not as suitable. The error from the difference maps between suitable tomographic models could have been converted into a thickness, however, this would not have accounted for the error in the shear wave inversion. The tomographic model error was used as the error in the shear wave inversion and therefore, it is the error in the inversion of the shear wave velocities and the choice of velocity contour which needed to be considered. The error is similar to that of McKenzie et al. (2005), which may suggest there are some mantle potential temperature controls on crustal thickness in the region.

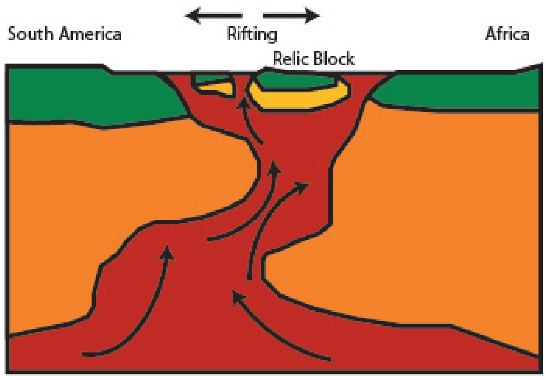

Figure 6.4 Cartoon redrawn from O'Reilly et al. (2009) showing the emplacement of continental lithospheric relics in rifting between cratonic blocks.

Comparisons with previous studies of crustal thickness beneath the oceanic area are limited due to the lack of other regional models. However, studies of crustal thickness of the continental regions have been made, and therefore the margins can be compared. Pasyanos & Nyblade (2007) suggests that the crustal thickness for the equatorial and central segments of Africa is between 10 km and 20 km ±5 km, which is thicker than the crust modelled in this study. The crustal shelf and Walvis ridge are less well defined in the Pasyanos & Nyblade (2007) model for crustal thickness. Assumpção et al. (2013) and Chulick et al. (2013) model the crustal thickness of the South American continent.

Chulick et al. (2013) model little variation off shore of the continent, and predict crustal thickness between 5 and 10 km out to 20 °west. This is consistent with the work presented in this study (figure 6.3). Assumpção et al. (2013) combine various techniques for a detailed crustal thickness model. The receiver function results in the Amazon basin predict a steep Moho gradient from 10 km to 40 km. A similar pattern is seen in figure 6.3, with a thick crust along the continental shelf in the basin. Assumpção et al. (2013) present a series of models for Moho depths from different combined data sets. The group and phase velocity data only derived Moho model also models region of thicker crust north and east of the Amazon basin, which corresponds to regions in figure 6.3. When the group and phase velocity model is refined to include gravity data these regions become less defined inthe Assumpção et al. (2013) model. Blaich et al. (2011) observed that the gradient in the Moho in the transitional margins was steeper on the western flank of the Atlantic, compared to the east. Although the scale of features resolved in this study is large there is evidence that the thickness contours in the west are tighter than in the east. This feature is not observed on the Crust 2.0 starting model (6.3 c) which suggests it has been resolved by the inversion.

Table 6.2 Average crustal thickness for east and west for both segments and the whole region

Region	West thickness (km)		East thickness (km)	
	3.9 kms^{-1}	4.0kms $^{-1}$	3.9 kms^{-1}	4.0 kms^{-1}
Central Region	7 ± 0.7	9 ± 0.7	11 ± 0.7	13 ± 0.7
Southern Region	11 ± 0.7	11 ± 0.7	10 ± 0.7	10 ± 0.7
Average for region	9 ± 0.7	10 ± 0.7	10.5 ± 0.7	11.5 ± 0.7

Crustal thickness asymmetry is observed by localised studies in the North Atlantic and is thought to be associated with the slow spreading rate and the segmentation of the ridge (e.g. Allerton et al., 2000; Cannat, 1996). Figure 6.5 shows a cartoon interpretation of the faulting associated with segmentation at slow spreading ridges which causes magmatic accretion on only one side of the axis and tectonic controlled spreading on the other. The motion of the tectonic side is controlled by the large fault and extension at the base of the foot wall and upper part of the hanging wall. This is thought to only be stable for a few million years and therefore does not explain 40 million years of extension and crustal thinning on the west side (Allerton et al., 2000). Allerton et al. (2000) observe the west of the MAR in the northern region (29 °north) to be asymmetric with the tectonic evolution on the western limb. The size of the region with thinner crust observed in figure 6.3 may also be too large to be explained by this localised process as the region crosses many segments.

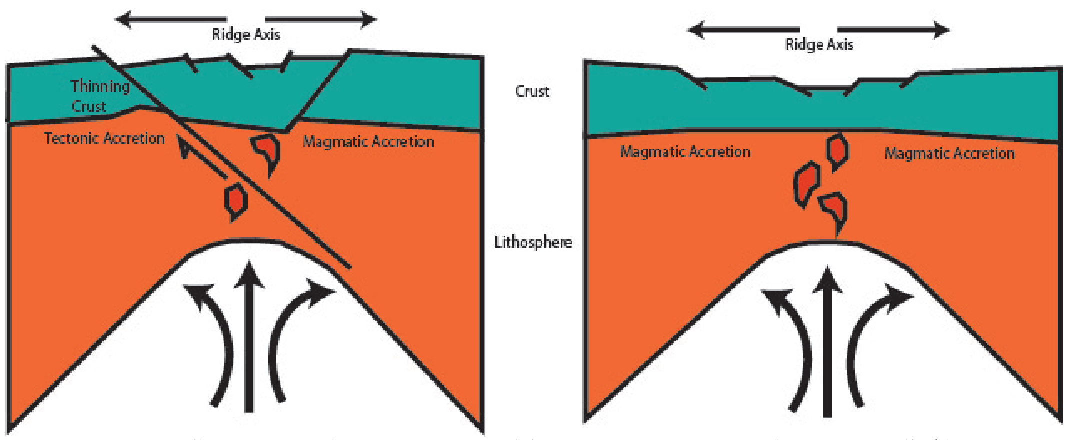

Figure 6.5 Cartoon illustrating short term unstable asymmetric crustal accretion (left) associated with slow spreading ridges compared with stable symmetric spreading model redrawn from Cannat (1996) and Allerton et al. (2000)

The crust of the southern segment is on average more uniform in thickness between the west and east in comparison to the central segment. There is a possibility that the evolution due to volcanism and the Tristan da Cunha hotspot in the south have continued to control the evolution of the southern segment. The difference in west is 2 to 4 km with the southern segment being significantly thicker than the central segment, whereas, the east is up to 1 to 3 km thinner in the east. If the 3.9 kms^{-1} model is taken then the variations in the east are within the error in the crustal thickness and the variation in the west are up to 4km. There is no more transform faulting in the central segment compared to the southern segment therefore this is not the cause of the thinner crust. The observations made here do suggest that the early evolutionary controls do still play a role in the evolution of the oceanic crust, with a more tectonic evolution in the central segment and a more uniform volcanic evolution in the southern segment.

6.1.3 Lithospheric evolution

As a first order comparison of the velocity structure beneath the Atlantic the 4.45 kms^{-1} contour was plotted with respect to depth and age against the 1200 °Cand 1300 °Cisobars calculated from the half space cooling model (HSC) (Faul & Jackson, 2005; Oxburgh & Turcotte, 1969). The 4.45 kms^{-1} velocity contour was chosen because the LVZ of the PREM velocity model goes from 4.45 kms^{-1} to 4.41 kms^{-1} and therefore it was considered a sensible proxy for the base of the lithosphere.

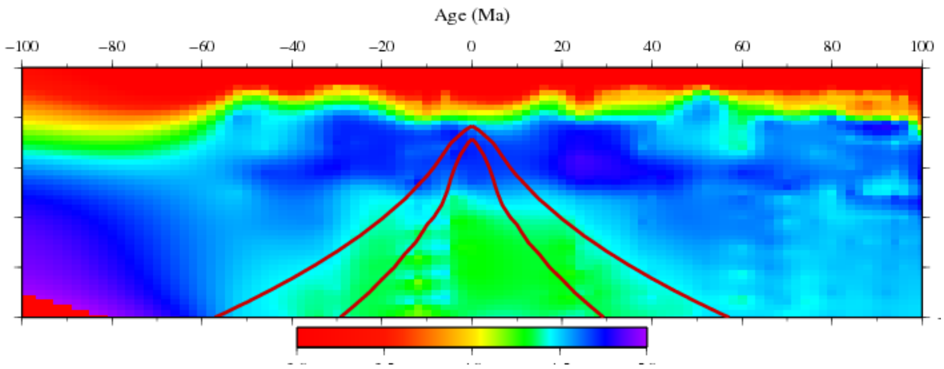

(a)

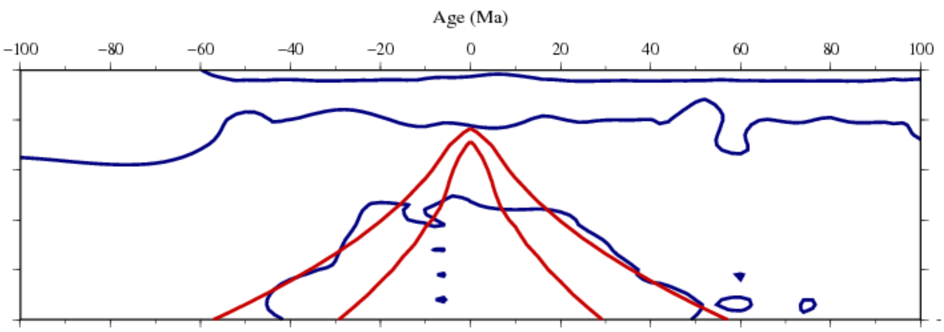

(b)

Figure 6.6 20 °South profile (a) velocity structure compared to thermal HSC model (red) (b) 4.45 kms^{-1} velocity contour (blue) correlated to thermal HSC model (red) for a T_m of 1300 °C

In agreement with Pacific studies (Maggi et al., 2006a; Ritzwoller et al., 2004) this study uses a starting T_m value of 1300 °C, however, other studies have also concluded that 1400 °Cis not unrealistic due to geochemical observations (e.g. Grose, 2012). It is thought that T_m can vary along the ridge axis (McKenzie et al., 2005) and therefore for each profile (5 °spacing) the isotherms were plotted for varying T_m between 1300 °Cto 1400 °Cto see which T_m value fitted best with each profile. Figure 6.6 shows the 20 °south profile (profile D - figure 6.7) with a best fit model of T_m=1300 °C. The best fit model was chosen by the correlation between the 4.45 kms^{-1} velocity contour and the 1200 °Cisotherm, as this is considered the base of the lithosphere through thermal evolution (Ritzwoller et al., 2004). Each profile was looked at independently of other profiles to determine the best fit for that profile without bias. The final isobar fits for profiles A-G can be found in appendix E.

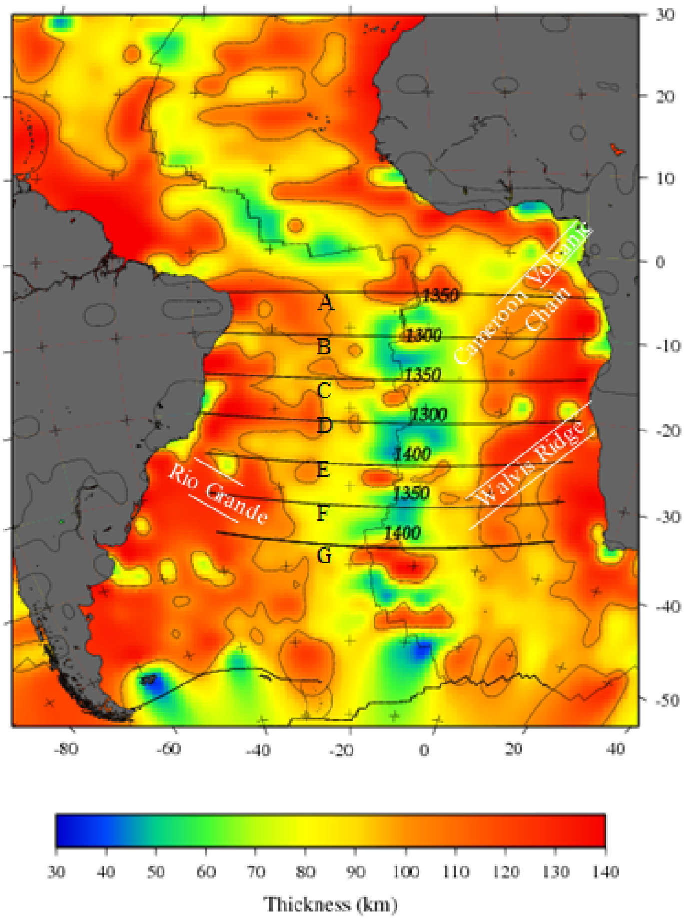

Figure 6.7 Thickness of the lithosphere in the Atlantic Ocean inferred from the 4.45kms^{-1} contour. Mantle potential for the 7 profiles (A-G) looked at in deatil in shown along the ridge axis. Sea mounts are highlighted in white.

The results suggest a variation along the ridge in T_m of 100 °Cfrom 1300 °Cto 1400 °C, this is plotted in figure 6.7 along the ridge axis. A variation of 100 °Cwould correspond according to McKenzie et al. (2005) to a crustal thickness variation of 8 km, which is not observed in this study (table 6.2). Therefore this large variation of mantle potential temperature is not considered reasonable, however, there is a pattern of hotter T_m in the southern region, where there is on average thicker crust and cooler T_m in the central region where the crustal thickness is up to 1 km thinner. This relationship is discussed further in section 6.1.4. Figure 6.7 also shows lithospheric thickness (extrapolated from the 4.45 kms^{-1} contour) for the South Atlantic. The profiles correlate to the profiles fitted for T_m in appendix E and table 6.3.

Crosby et al. (2006) concluded that the lithospheric thickness of the Atlantic was on average 100 km maximum thickness calculated from the plate model using heat flow and subsidence data. Zhang & Lay (1999) concluded the thickness of lithosphere in the Atlantic was a maximum of 85 km from global phase velocity models. The thickness of the lithosphere mapped in figure 6.7 is up to 120 km. This is beyond the reasonable depth sensitivity of the model, however, the 4.45 kms^{-1} velocity contour was plotted at a uniform depth in the starting model of 80 km. Therefore, the depth to the point at which the 4.45 kms^{-1} is plotted in the final model has been increased within the inversion, therefore the variations in thickness can still be considered significant. Although the sensitivity in the model is less at depth, variations in shallow structure affect the structure at depth causing these variations. Some of the thicker lithosphere is associated with continental shelf and therefore could be transitional from oceanic thermally controlled lithosphere to the thicker continental lithosphere.

Previous studies which have looked at lithospheric thickness (not just shear velocity structure) have focussed on the continental regions of the study area. Fishwick (2010) maps lithospheric thickness for Africa, but shows thickness for the east of the Atlantic. The overall shape of the 120 km contour correlates well with the thicker lithosphere (greater than 100 km) modelled in this study. The region off the north of the African continent correlates on a broad scale to the structure resolved by Pasyanos (2010), but they suggest the thickness is up to 180 km, whereas, this study resolves the thickness to a maximum of 140 km. Both studies also resolved a broad feature of thinner lithosphere from the ridge to the Cameroon region but the lithospheric thickness varies between the models (Fishwick, 2010; Pasyanos, 2010). This feature has not been resolved clearly in this model (figure 6.7). For South America Feng et al. (2007) estimate the lithospheric thickness for the Atlantic at between 50 km and 100 km but resolution of the model is poor for the oceanic regions. This study predicts thicker lithosphere, closer to 140 km.

Overall there is general agreement between previous studies around Africa for regions where thicker lithosphere is predicted. There is less correlation on the South American side of the region but velocity maps (Chapter 4) correlate with previous studies (e.g. Feng et al., 2004; Heintz et al., 2005) which would suggest the resolution of the lithosphere is reasonable and the differences in lithospheric thickness are caused by the parametrisation used.

6.1.4 Mantle potential temperature and crustal thickness

As previously discussed McKenzie et al. (2005) state there is a relationship between the mantle potential temperature and the crustal thickness. In this section this relationship is investigated in more detail for results from this study. The relationship between the predicted T_m and the associated crustal thickness for the profiles previously discussed is looked at in more detail. Table 6.3 shows T_m predictions from this study (6.1.3) and prediction based on the (McKenzie et al., 2005) relationship between crustal thickness and T_m, where T_m has been calculated based on the crustal thickness from this study (6.1.2). Due to the error associated with the crustal thickness there is an error on the predicted T_m of 8.5 °Cbased on the relationship defined by McKenzie et al. (2005). Both the first order comparison of the 4.45kms^{-1} contour derived T_m and the T_m derived from crustal thickness suggests that T_m in the southern segment is higher than the central segment. The Tristan da Cunha hot spot could be associated with this variation. Silveira et al. (1998) suggest the source of upwelling asthenosphere in the South Atlantic is deeper compared to the north. A higher T_m could be the result of a deeper source, for example, upwelling hotter material from depth. However, the question is, is the variation to the depth of asthenospheric source (assuming a higher T_m corresponds to a deeper source) along the ridge associated with that predicted (table 6.3) reasonable on the scale and does this tie to crustal thickness? By comparing the average T_m for the southern and central segments it would suggest that the asthenospheric source becomes more shallow in a northern direction along the ridge axis. As this study presents a better resolution model compared to Silveira et al. (1998), the variation in asthenospheric source depth has been modelled on a more regional scale, whereas, Silveira et al. (1998) compared the North Atlantic to the South Atlantic. The model shown here fluctuates on a smaller scale (approximately 500 km) and appears to become overall shallower towards the north of the ridge. The observations made here could therefore, expand in further detail on those which were observed by Silveira et al. (1998) along the ridge. A high resolution deeper mantle study of the region would be required to test if variation in depth of the base of the low velocity zone beneath the ridge axis tied to the predictions of deeper source asthenosphere.

The crustal thickness for the profiles where the 4.45 kms^{-1} velocity contour predicts a T_m of 1350 °Cvaries by 2 km ±0.7 km. However, the variations in crustal thickness for those profiles observed to have a best fit T_m of 1300 °Cand 1400 °Cis only 1km ±0.7 km. This is within a more reasonable error. There is, however, too great a variation in the crustal thickness (2km) for the control to be T_m alone. Bown & White (1994) suggest that the crustal thickness at slow spreading ridges is controlled by more processes than just T_m. Other controls could be linked to the asymmetry in the region, such as the segment faulting and tectonically controlled spreading instead of magmatic in the west.

Although to a first degree the 4.45 kms^{-1} contour does fit the isotherms, there is a level of uncertainty at depth in the model due to the reduced sensitivity of group velocities. A combined study of group velocities and phase velocities may help to define the deeper thermal structure and refine the shallow structure due to the depth sensitivities of phase velocities being greater than that of group velocities.

Table 6.3 Mantle potential temperature comparison from the values based on comparison between 4.45 contour and HSC and values based on relationship between mantle potential and crustal thickness from crustal thickness values (1km is associated with 12 °Cchange in T_m) where 7.1 km thick crust is associated with 1300 °C(McKenzie et al., 2005)

Latitude	Average thickness (km)	T_m (from data) (°C)	T_m relationship from McKenzie et al. (2005) (°C)
5 °S	9± 0.7	1350	1334± 8.5
10 °S	7± 0.7	1300	1298± 8.5
15 °S	7± 0.7	1350	1298± 8.5
20 °S	8± 0.7	1300	1316± 8.5
25 °S	8± 0.7	1400	1316± 8.5
30 °S	8± 0.7	1350	1316± 8.5
35 °S	9± 0.7	1400	1334± 8.5

6.1.5 Joint inversion of group velocities and phase velocities

The features in the model below 75 km are not as well resolved due to the length of the periods used in the inversion (16 s - 100 s). This is shallower than the LAB as mentioned in section 6.1.3, however a thickness which correlates with previous studies is observed. By combining group and phase velocities a better resolution of the LAB can be achieved as the group velocities can resolve the shallow structure and the phase velocities the deeper in more detail. The surface wave tomography model of Fishwick (2010) extends into the eastern part of the study region discussed in this chapter. This earlier work used a waveform inversion to obtain the path average velocity structure in the upper mantle, with the 3SMAC crustal model above, and the PREM velocity structure below the sensitivity of the data. The velocity structure along each path was combined into a tomographic inversion to obtain velocity structure with respect to depth.

Tomographic models of the same or similar regions can differ significantly due to the parametrisation and regularisation of the inversion, as well as the distribution of data (e.g. Maggi et al., 2006a; Ritzwoller et al., 2004). Here, we take the shear velocity model of Fishwick (2010) and use forward modelling calculations to calculate the group and phase velocities along a profile (20degrees south). We first make a comparison of the group velocities estimated from the previous tomographic study with the group velocities described in Chapter 4. Figure 6.8 shows the difference between the group velocities from this study and the group velocities from Fishwick (2010). There is a variation along the profile, however, the maximum difference is 0.2 kms^{-1} which is within the error of the residual outliers in the models.Given the similarities in group velocities it was considered reasonable to use the longer period (40 s - 160 s) phase velocities calculated from theFishwick (2010) tomography as additional data to enhance the resolution of the models presented within this thesis The 1-D inversions were run the same as in section 4.4, the group and phase velocities were inverted with Crust 2.0 as the starting model for n iterations until there was no change in the residual.

The profiles for these two models can be seen in figure 6.9. Somewhat surprisingly, the joint inversion has refined the velocity structure of the crust more than the deeper structure. The new model suggests thinner crust between 3 °E and 10 °E, the region associated with the Walvis ridge. The joint inversion for this profile has not improved definition to the base of the lithosphere, however, it has removed the high velocity region below the ridge. It is thought this feature in the group velocity only inversion could be due to the inversion not being able to resolve to this depth. The faster velocity layer is therefore a relic of instabilities in the estimation of the group velocities in the inversion. By combining the two data sets this depth has now been resolved and the low velocity zone is defined to a depth of 150 km.

There is a better residual fit to the group velocity only inversion compared to the joint inversion (figure 6.10). This is most likely due to the added data in the inversion which it needs to fit. The places where the fit is worst is around the ridge and on the continent of Africa (figure 6.10). The African continent is where the modelled group velocities from Fishwick (2010) and this study correlate least well. This is due to the path coverage variations and the different focuses of the two data sets. Path coverage for this study is sparsest on the African continent and path coverage in the Fishwick (2010) model is sparsest towards the ridge. Therefore the resolution of each model is worst at the ends of the profile, where the residual fit is highest.

A combined study using the same ray paths would be best to correlate the data and get the best fit. The relationship between the 4.45kms^{-1} and the isotherms still suggest a T_m of 1300 °C. When assuming a thermally controlled LAB the velocities should also be converted to temperature for a better analysis of T_m (e.g. Ritzwoller et al., 2004).

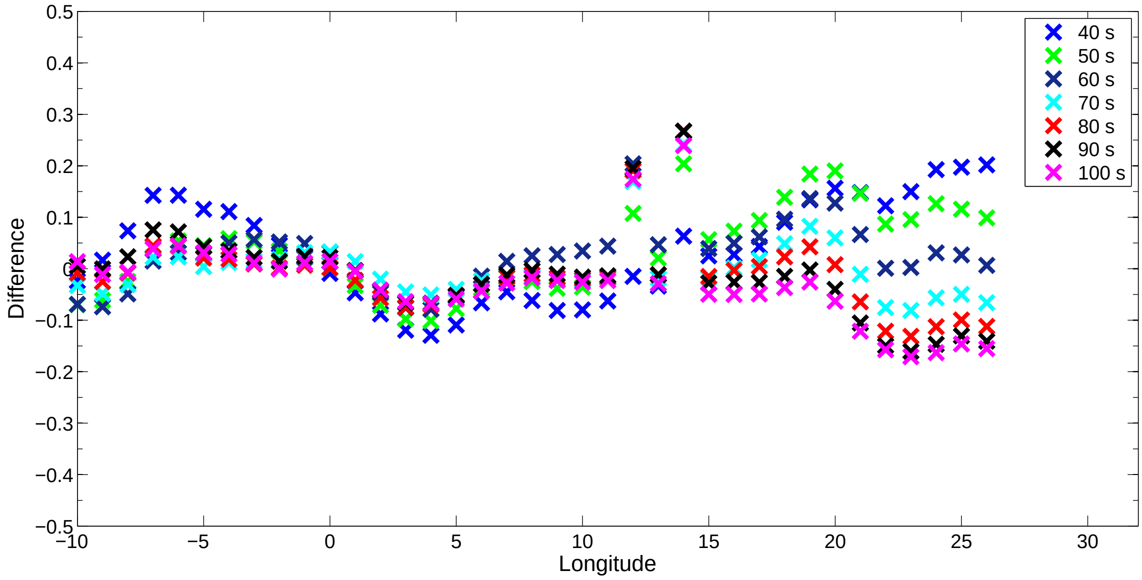

Figure 6.8 Differences between group velocities from tomographic inversions in this model and Fishwick (2010) group velocities for periods 40 s - 100 s

6.2 Conclusions

- Group velocity data was extensively tested for reliability and fit to the model (Chapter 3). Model parametrisation is important in recovering the best structure. Tests showed that 20 s to 80 s periods were best quality data with least variation between damping values and error associated with standard deviation from path residuals (table 3.3). 14 s was a poor fit and the model produced was not reliable, this resulted in the data being removed from the final inversions.

- There is a positive correlation between group velocity and sea floor age (table 6.1, figure 6.2 and Appendix D). This correlates with previous studies. There is a slight asymmetry in the linear relationship with the west increasing slightly faster than the east. The relationship is stronger at the intermediate periods (60 s - 80 s)

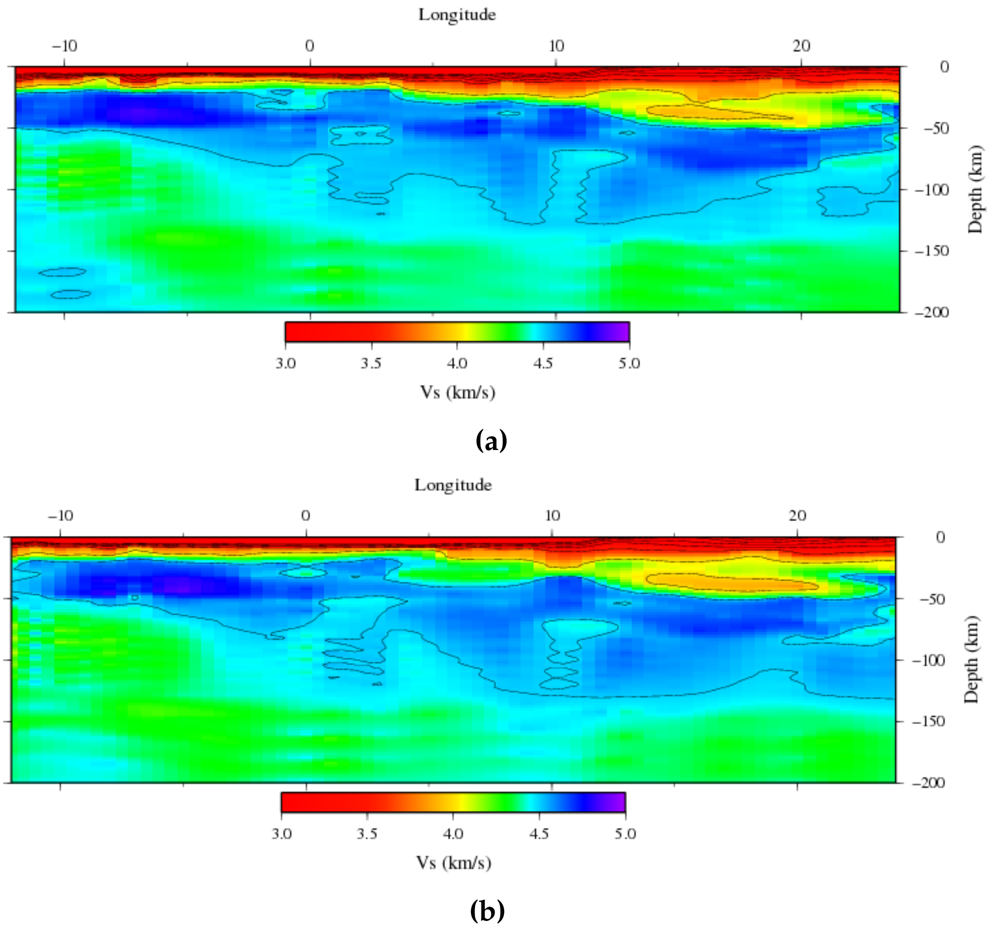

Figure 6.9 20 °south shear velocity structure from the ridge east for (a) group velocities in this study only (b) joint inversion of group and phase velocity data

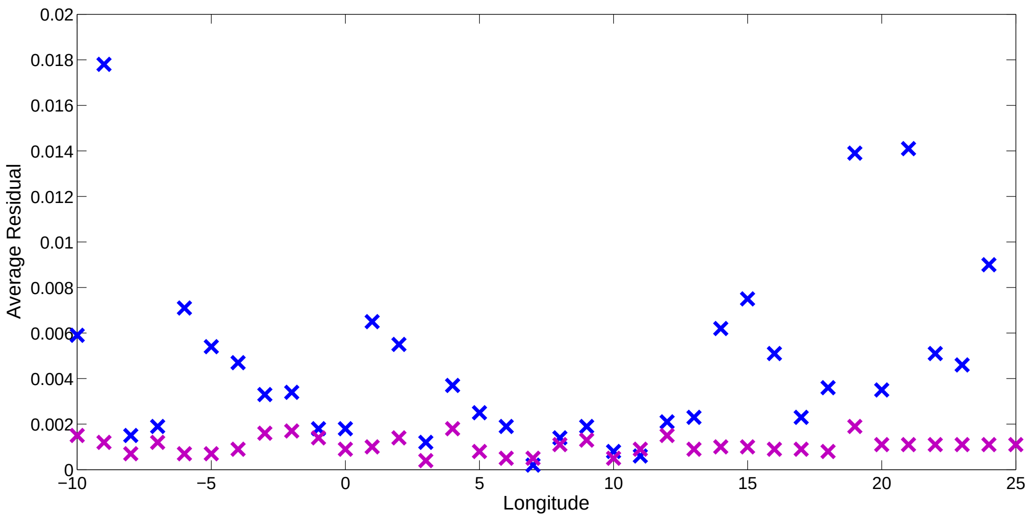

Figure 6.10 Residual fit of the 1-D inversion to the data for the 20 °south profile for the group velocity only inversion (red) and the joint inversion (blue)

and decreases at longer periods (90 s- 100 s) suggesting as previous studies have that this relationship is associated with lithospheric evolution.

- Inverting group velocities is complicated and balance is required between a high quality data set and a suitable starting model for the inversion. Tests were run on the starting model and Crust 2.0 was chosen as the most suitableto invert the data (table 4.1). There are instabilities in inverting group velocities only which is why a high quality data set is required. 14 s was removed due to its poor quality fit to the group velocity tomographic models (Chapter 4).

- There is a clear variation between the central and southern segments which suggests the evolution of these regions differ. The crust is thicker in the south and the mantle potential is greater than observed in the central segment. The Tristan da Cunha hot spot is likely to play a role in this variation in the Atlantic (table 6.2 and figure 6.3)

- Asymmetry in crustal thickness is observed between the east and the west sides of the Atlantic (table 6.2 and figure 6.3). This variation is prominent in the central segment. Asymmetry may be due to the evolution of oceanic crust at slow spreading ridges and the interactions between magmatic and tectonic controlled accretion of the crust at segment ends. The southern segment is associated with more magmatism than the central segment and therefore supports the hypothesis that the central segments thin crust in the west was caused by tectonic driven spreading on the west limb of the ridge segments in this region.

- The recovery of anisotropic structure from surface waves has been shown in this study to be difficult (Chapter 5). At the shortest periods it is tempting to relate the fast direction of anisotropy to the principal stress direction in the crust (e.g. figure 5.14), the direction of anisotropy seen at 18 s and 20 s correlates to Richardson (1992) and Zoback et al. (1989) directions of stress. At longer periods anisotropy would normally be interpreted as geodynamical features (e.g. Maggi et al., 2006a; Silveira & Stutzmann, 2002). However, the results from synthetic tests (section 5.2.3) show that the majority of the anisotropy can be related to the interaction between the isotropic velocity structure and path coverage within the tomographic inversion. As such, no strong tectonic or geodynamic interpretations can be made.

6.3 Further work

- A joint inversion of group velocities and phase velocities from the same data set would help to constrain the velocity structure across the South Atlantic and therefore a phase velocity dataset would need to be compiled and a joint inversion for shear velocity structure for the region obtained. This would enable modelling of the deeper structure to test the suggestion from this project that the depth of the asthenospheric source varies along the ridge axis. This would offer more insight into the velocity structure beneath slow spreading ridges to draw comparisons with the extensive studies carried out on the EPR, a fast spreading ridge. Taking the velocity structure constrained in this study, a waveform inversion study could be done using this velocity structure for the top 50 km.

- A thermal conversion to allow a direct comparison of the structure modelled in the tomography with the mathematical models which try to explain the lithospheric evolution should be done. This should be done on the jointly inverted data which should have better resolution at depth of the LAB. This would also facilitate a better comparison of the slow spreading Atlantic with the fast spreading pacific.

- A more reliable short period group velocity data set, maybe for smaller regions in the South Atlantic could be compiled and inverted for anisotropy. This would help to constrain if there is anisotropy in the oceanic crust caused by the stress field of the plate. By focussing the study on a smaller region it would increase the reliability of the shorter periods by including shorter average path lengths. Shorter periods attenuate first which means that they are less reliable on longer paths.

Appendices

A. Stations

List of Stations used in the study

Name	Latitude	Longitude
ABPC	9.4608	-64.8207
ABRA	-31.499	-66.2383
ABVI	18.7296	-64.3325
AGPR	18.4675	-67.1112
ALAC	-46.5063	-73.063
ANWB	17.6685	-61.7856
AOPR	18.3466	-66.754
APOB	-18.5471	-52.0251
APOB2	-18.5081	-52.074
AQDA	-20.48	-55.7
ARPC	9.7438	-63.7972
ARRO	-30.4076	-69.2454
ASCN	-7.9327	-14.3601
AUA	12.5056	-70.0106
B151	12.9915	-67.6513
BAK01	-47.184	-71.9735
BAMB	-20.0398	-46.0308
BARR	-31.6495	-69.4159
BB15B	-21.0413	-48.5308
BB16B	-21.0337	-48.5857

BBGH	13.1434	-59.5588
BBSR	32.3713	-64.6963
BDFB	-15.6418	-48.0148
BEB	-1.45034	-48.4443
BEB4B	-21.082	-48.5073
BGCA	5.17636	18.4242
BLWY	-20.143	28.611
BOSA	-28.6141	25.2555
BOZA	-31.7511	-68.4351
BRAN	-21.359	14.749
BSFB	-18.8313	-40.8465
BTBT	11.4989	-62.501
CAL01	-45.4793	-71.6035
CALI	-31.2831	-69.4195
CANB	-22.9681	-50.3778
CAPC	7.3429	-61.8256
CAPN	-21.759	13.968
CART	37.5868	-1.0012
CASP	-31.207	-69.6285
CAUB	-8.17683	-36.0102
CBYP	18.2717	-65.8566
CCP2	10.8792	-69.8328
CCUB	-18.425	-51.212
CDSB	-18.7655	-52.8393
CDVI	17.7317	-64.7147
CM01	2.389	9.834
CM02	2.698	13.289
CM03	3.519	15.034
CM04	2.979	11.959
CM05	2.942	9.914

CM06	2.385	11.268
CM07	3.87	11.456
CM08	3.909	9.863
CM09	4.234	9.328
CM10	4.223	10.619
CM11	3.98	13.188
CM12	4.481	11.634
CM13	4.588	9.462
CM14	4.422	14.358
CM15	5.034	9.933
CM16	5.48	10.572
CM17	5.546	12.312
CM18	5.723	9.355
CM19	5.975	11.232
CM20	6.225	10.054
CM21	6.467	12.62
CM22	6.477	13.268
CM23	6.37	10.793
CM24	6.523	14.288
CM25	6.76	11.811
CM26	7.265	13.548
CM27	7.359	12.667
CM28	8.469	13.237
CM29	9.347	13.385
CM30	9.757	13.95
CM31	10.327	15.262
CM32	10.619	14.372
CMLA	37.7637	-25.5243
CMPA	-19.5792	-54.1688
CMPC	7.6508	-64.0731

CNG	-26.2917	32.1883
CORB	-17.7433	-48.6892
CPD	18.0368	-65.9151
CPUP	-26.3306	-57.3309
CRJB	-6.1702	-50.1546
CRP4	9.7882	-69.5829
CRPR	18.0064	-67.1096
CRPR	18.4675	-67.1112
CRTA	-13.4321	-44.5819
CRTB	-13.4321	-44.5819
CRZF	-46.43	51.861
CS6B	-5.49448	-36.6709
CS6B	-5.49448	-38.6709
CUBA	11.8499	-65.418
CULB	18.3264	-65.3006
CUPC	10.1576	-63.8264
CVNA	-31.4821	19.7617
CVNA	-31.482	19.762
DBIC	6.67016	-4.85656
DECP	-62.9771	-60.6699
DKSS	11.7515	-63.7699
DODT	-6.186	35.748
DRKS	11.9992	-62.6685
DWPF	28.1103	-81.4327
EDPC	6.7126	-61.6392
EFI	-51.6753	-58.0637
ELCO	-47.2538	-72.5314
ELEF	-61.2198	-55.139
FCPC	9.6502	-66.8342
FDF	14.735	-61.143

FELL	-52.0568	-70.0047
FNL01	-46.5516	-72.2219
FREI	-62.1947	-58.9841
GNSB	-15.2644	-49.0855
GO09	-51.2707	-72.3381
GRGR	12.1324	-61.654
GRM	-33.313	26.508
GRM	-33.3133	26.5733
GRTK	21.5115	-71.1327
GTBY	19.9268	-75.1108
HAMB	-53.614	-70.9309
HOPE	-54.2836	-36.4879
HUMP	18.1421	-65.8488
HVD	-30.605	25.4967
HVD	-30.605	25.497
ICM	17.8934	-66.521
IFE	7.54667	4.45692
IGAB	-23.2524	-46.1164
IGCB	-1.1272	-47.6085
ITAB	-27.3082	-52.3411
ITPB	-15.9887	-39.6282
JATB	-17.8929	-51.4929
JEI01	-46.8354	-72.0094
JMPC	9.8872	-67.3968
JNRB	-15.4678	-44.5052
JOSE	-46.7472	-72.5432
JUQB	-24.093	-47.7163
KOWA	14.4967	-4.014
KTWE	-12.814	28.209
KUKU	6.19232	-0.36842

LAPC	8.985	-65.7719
LAPO	-45.7027	-71.8333
LBTB	-25.0151	25.5966
LEON	-23.435	18.743
LMPC2	9.3555	-67.3833
LNEG	-46.5773	-72.6423
LOWI	-63.247	-62.1808
LPAZ	-16.2879	-68.1307
LSZ	-15.2779	28.1882
LTL	30.5374	-90.766
MACI	28.2502	-16.5082
MAHO	39.8959	4.2665
MAIO	15.2306	-23.1772
MAPC	7.4169	-65.1881
MAYE	-48.2631	-72.4265
MBAR	-0.6019	30.7382
MBO	14.391	-16.955
MELI	35.2938	-2.935
MGP	18.0076	-67.0891
MHTO	13.9497	-66.491
MILO	-51.5678	-72.6199
MING	16.8628	-24.9365
MLOS	14.976	-24.338
MNPC	8.9876	-62.7444
MOPA	-23.5173	31.3977
MOPC	6.5861	-66.8426
MORF	37.3043	-8.65267
MPG	5.11011	-52.6445
MPG	5.11	-52.644
MPR	18.2117	-67.1398

MRP3	10.3061	-69.6911
MSKU	-1.6557	13.6116
MTDJ	18.226	-77.5345
MTE	40.3997	-7.5442
MTOR	28.4948	-9.8487
MTP	18.0972	-65.5525
MTP	18.0972	-65.5527
MUPC	8.3274	-64.2946
MZM	-11.434	34.035
NOVB	-28.6105	-49.5582
NUPB	-20.6628	-47.6859
OBIP	18.0428	-66.6062
OHIG	-63.3212	-57.8982
OTAV	0.2376	-78.4508
OUTN	-20.151	15.689
PAB	39.5446	-4.3499
PACB	-21.6074	-51.2618
PALA	-46.2957	-71.8321
PAPC	8.0344	-62.655
PATM	14.8693	-24.4241
PAZB	-15.1369	-50.8634
PCDR	18.5145	-68.381
PDCB	-12.5306	-39.1238
PESTR	38.8672	-7.5902
PFPC	8.3276	-65.9443
PFVI	37.1328	-8.82683
PJOR	16.9841	-25.1943
PKA	-29.67	22.757
PLCA	-40.7328	-70.5508
PMOZ	32.823	-17.1972

PMSA	-64.7744	-64.0489
PNP7	8.0742	-69.3024
POPB	-22.4565	-52.8368
PORB	-13.3304	-49.0787
PP1A	-17.6003	-54.8796
PP1B	-17.6003	-54.8796
PPP6	8.9413	-69.46
PRAT	-62.4798	-59.6641
PRCB	-17.2702	-46.8188
PRPC	8.5019	-63.625
PTGA	-0.7308	-59.9666
PUCM	19.4403	-70.6814
PVAQ	37.4037	-7.7173
RCBR	-5.8274	-35.9014
RCP5	9.2649	-69.4978
RIMA	-45.3111	-72.3269
ROPC	9.9092	-66.3847
RPPC2	8.9494	-66.4365
RPPC	8.9485	-66.4361
RRS01	-47.4767	-72.5414
RTC	33.9881	-6.8569
SABA	17.6205	-63.2426
SACV	14.9702	-23.6085
SALA	16.7328	-22.9357
SALM	-52.5494	-72.0303
SAML	-8.9489	-63.1831
SC01	19.4272	-70.7277
SDD	18.4632	-69.9169
SDDR	18.9821	-71.2878
SDV	8.8839	-70.634

SDVV	8.8839	-70.634
SEK	-28.3233	27.625
SEUS	17.4928	-62.9814
SFS	36.4656	-6.2055
SHAI	5.88136	0.04389
SHEL	-15.9588	-5.7457
SHRB	11.2707	-67.3496
SIPC	9.3596	-63.0575
SJG	18.1091	-66.15
SLMB	-16.5705	-50.3455
SMN1	19.1878	-69.2733
SMPC	8.5127	-66.3219
SMRT	18.0505	-63.0746
SNIC	16.6201	-24.3467
SNVB	0.9051	-51.8771
SOMB	12.7209	-64.9313
SPB	-23.592	-47.432
SPB	-23.5927	-47.427
SPPT	-64.2955	-61.0514
SRP1	11.3184	-69.9004
SRPC	9.5825	-64.2942
SSB	45.279	4.542
STPC	8.1365	-66.2544
STVI	18.3524	-64.9565
STVI	18.3533	-64.9622
SUR	-32.3797	20.8117
SWZ	-27.1817	25.325
SWZ	-27.182	25.332
SYO	-69.0067	39.585
TAM	22.791	5.527

TEIG	20.2263	-88.2763
TEZI	-15.747	26.016
TRIS	-37.0681	-12.3152
TRMB	-18.0922	-44.929
TRQA	-38.0568	-61.9787
TRSB	-4.873	-42.7059
TSUM	-19.2022	17.5838
ULPC	8.8571	-67.3865
UPI	-28.3619	21.2527
UPI	-28.362	21.253
VABB	-23.0021	-46.9658
VCC01	-46.1207	-72.1607
VIPC	7.8605	-62.0655
VOH01	-48.4678	-72.5614
VTDF	-54.1388	-68.7061
WATN	-20.612	17.335
WIN	-22.5667	17.1
YNDE	3.87	11.456
ZOMB	-15.3833	35.35
ZUPC	8.3597	-65.1951

B. Events

List of Events used in the study

Date	Time	Latitude	Longitude
1997/03/20	02:17:09	-1.59	-12.71
1997/03/22	13:54:34	-58.66	-24.99
1997/04/05	18:13:51	-57.87	-25.39
1997/04/11	01:11:08	-58.1	-25.07
1997/04/25	09:11:41	-48.19	-9.41
1997/05/16	09:25:43	-60.58	-18.27
1997/05/21	20:23:04	0.03	-16.73
1997/05/29	00:12:36	-55.55	-27.07
1997/05/30	20:35:36	-54.18	6.83
1997/06/02	21:24:45	-57.96	-25.03
1997/06/13	08:07:18	-52.97	10.24
1997/06/15	13:01:14	-57.24	-24.83
1997/07/04	09:54:09	-58.39	-10.95
1997/07/22	19:10:41	4.73	-32.79
1997/08/10	22:03:32	-56.51	-27.2
1997/08/26	03:27:46	-58.44	-25.05
1997/09/01	12:36:36	-1.11	-15.61
1997/09/05	03:23:17	-56.59	-27.6
1997/09/10	20:27:46	-52.88	20.33
1997/09/11	00:47:31	-59.38	-16.65

1997/09/18	18:19:42	-61.29	-23.83
1997/09/26	14:00:09	0.16	-16.9
1997/10/05	18:04:38	-59.9	-28.92
1997/10/07	17:53:36	-52.14	16
1997/11/10	12:47:38	0.25	-16.84
1997/11/14	10:18:26	0.78	-27.21
1997/11/20	06:08:17	-59.32	-25.14
1997/12/14	02:39:25	-60.04	-25.72
1997/12/27	20:11:10	-55.97	-3.72
1997/12/29	05:12:26	-52.16	28.89
1998/01/03	06:10:17	-35.29	-15.8
1998/01/13	08:49:14	-55.64	-28.29
1998/02/06	13:01:20	-56.15	-27.14
1998/02/26	10:58:24	-56.05	-24.68
1998/03/01	06:58:30	-12.26	-14.51
1998/03/09	14:34:54	-60.06	-22.65
1998/03/27	00:30:57	-59.11	-24.78
1998/03/29	07:15:06	0.16	-17.87
1998/04/10	16:40:45	-1.18	-15.37
1998/04/25	06:07:37	-35.46	-16.93
1998/05/01	12:08:48	-56.08	-26.86
1998/05/28	11:32:04	-58.96	-24.76
1998/06/05	08:50:35	-55.8	-27.5
1998/06/12	13:47:33	-37.43	-17.07
1998/06/18	04:18:03	-11.61	-13.89
1998/06/23	14:37:01	-58.49	-13.33
1998/06/24	10:44:36	-37.36	-17.11
1998/07/10	08:20:42	-0.83	-15.37
1998/07/26	03:38:31	-0.3	-20.98
1998/07/30	23:36:35	-59.19	-24.82

1998/08/01	09:10:06	-31.43	-13.33
1998/08/04	12:28:40	-52.85	22.29
1998/08/05	07:31:00	5.68	-32.98
1998/08/13	05:55:03	-59.23	-24.48
1998/08/17	08:02:10	-3.34	-12.34
1998/08/29	08:30:26	-55.77	-26.96
1998/09/01	10:29:54	-58.5	-26.1
1998/10/03	01:13:39	-56.93	-25.35
1998/10/30	08:33:15	-54.66	5.7
1998/11/16	20:35:31	-58.34	-25.15
1998/12/05	07:19:37	-60.16	-26.44
1998/12/19	01:15:41	-1.52	-13.07
1998/12/26	12:14:40	-56.36	-26.72
1999/01/14	20:20:16	-23.13	179.99
1999/01/27	04:25:16	-37.85	-16.73
1999/02/04	19:43:20	1.25	-30.58
1999/02/05	04:23:12	-6.56	-11.68
1999/02/27	12:55:19	-49.31	-7.46
1999/03/16	14:42:59	0.47	-17.2
1999/03/26	14:27:48	-57.95	-24.95
1999/04/03	00:31:45	-56.8	-27.36
1999/04/26	12:10:17	-25.83	-13.78
1999/05/18	07:16:15	-35.02	-14.73
1999/06/09	04:05:48	-53.2	-47.41
1999/06/22	18:48:21	-56.18	-27.07
1999/07/03	16:36:07	7.92	-38.3
1999/08/04	05:40:30	-52.15	14.4
1999/08/21	21:51:20	-58.53	-13.05
1999/09/01	06:42:49	5.18	-32.7
1999/09/06	01:51:22	-14.48	-14.05

1999/10/18	02:43:29	-56.28	-26.27
1999/10/20	13:38:45	-57.53	-23.32
1999/11/02	23:18:22	-52.85	25.87
1999/11/05	12:00:15	28.4	-43.51
2000/01/21	05:04:19	-59.31	-17.06
2000/02/16	07:03:14	17.92	-61
2000/02/18	08:06:20	16.76	-46.51
2000/02/23	01:11:29	-60.46	-30.51
2000/03/01	08:48:06	-52.18	14.18
2000/03/17	11:51:23	-53.01	26.28
2000/03/27	02:55:39	32.02	-40.72
2000/04/18	00:12:10	-52.4	13.7
2000/05/18	09:50:31	-10.67	-13.55
2000/05/22	04:24:48	0.85	-25.75
2000/06/14	21:16:45	-4.68	-12.4
2000/06/16	17:59:09	-7.83	-13.74
2000/07/14	05:22:04	-0.87	-16.47
2000/07/15	03:13:28	-0.13	-19.6
2000/07/25	03:14:38	-53.57	-2.6
2000/07/26	05:37:48	0.63	-25.96
2000/07/27	10:58:44	-53.64	-2.32
2000/07/30	01:14:31	7.39	-33.94
2000/08/24	11:17:44	-28.01	-13.23
2000/08/31	20:30:09	0.88	-26.75
2000/09/10	21:37:48	-1.72	-13.11
2000/09/11	10:03:18	-58.08	-25.09
2000/10/05	13:39:17	31.74	-40.73
2000/10/18	08:02:58	23.69	-45.41
2000/10/21	11:36:10	-47.45	-12
2000/10/22	11:37:28	-57.53	-25.41

2000/10/27	09:10:10	-1.27	-23.77
2000/10/29	06:05:32	0.83	-28.1
2000/10/30	01:03:31	0.81	-25.67
2000/11/07	00:18:14	-55.34	-29.24
2000/11/12	03:29:58	-54.89	-29.85
2000/12/11	18:54:09	19.36	-66.97
2000/12/15	13:00:07	-50.43	-6.25
2001/01/02	19:37:39	1.08	-27.83
2001/01/05	08:06:38	16.11	-61.03
2001/01/05	11:54:18	-0.76	-22.21
2001/01/12	02:37:18	26.29	-44.46
2001/01/18	11:15:23	-55.28	-28.35
2001/01/19	09:04:37	-58.43	-9.59
2001/01/24	05:34:38	-0.46	-19.83
2001/01/31	06:02:35	-55.72	-28.04
2001/02/07	13:46:31	-55.49	-27.2
2001/02/13	00:28:14	-48.3	-9.7
2001/02/23	10:15:21	13.94	-44.89
2001/03/07	18:11:07	-6.93	-12.71
2001/03/30	18:11:50	-59.99	-25.86
2001/04/01	04:16:43	-52.42	17.49
2001/04/05	13:54:24	16.06	-60.98
2001/04/13	15:34:00	-60.04	-24.37
2001/06/07	09:16:19	0.54	-27.63
2001/06/12	14:22:19	14.53	-45.07
2001/06/21	11:02:09	-17.52	-14.4
2001/07/25	19:47:11	-11.83	-14.49
2001/07/30	19:50:15	-2.89	-12.47
2001/08/08	18:07:32	-56.25	-27.79
2001/08/28	17:40:41	-11.57	-13.47

2001/08/29	03:30:20	-52.94	18.44
2001/09/25	23:17:00	17.17	-61.36
2001/10/01	04:18:22	-58.58	-24.9
2001/10/10	10:02:04	5.56	-32.66
2001/10/16	15:27:29	19	-65.13
2001/10/17	11:29:14	19.19	-64.78
2001/10/23	22:51:21	-43.81	-16.09
2001/11/05	01:15:18	-58.44	-24.54
2001/11/08	22:57:57	-61.56	-25
2001/11/12	10:11:21	22.19	-44.81
2001/11/15	01:03:12	-1.14	-15.39
2001/12/05	07:46:41	-52.71	19.04
2001/12/06	11:59:12	-60.2	-25.63
2001/12/07	12:55:45	-52.92	13.37
2001/12/13	23:12:06	-53.73	25.35
2001/12/14	07:35:30	-53.38	25.23
2001/12/20	12:01:56	-56.94	-24.74
2002/01/07	00:48:02	-52.75	28.86
2002/02/10	01:47:12	-55.85	-28.81
2002/02/12	16:35:31	-60.18	-25.82
2002/02/19	12:33:29	-57.02	-25.35
2002/02/20	15:06:35	-52.37	16.23
2002/03/02	03:15:00	-35.45	-17.23
2002/03/07	07:10:19	-1.05	-24.3
2002/03/09	12:27:17	-56	-27.3
2002/03/11	14:24:06	19.05	-64.09
2002/03/14	21:03:24	3.54	-31.2
2002/03/24	14:36:02	24.35	-46.11
2002/03/28	05:48:37	23.38	-45.01
2002/04/01	19:20:30	-58.86	-24.24

2002/04/10	00:13:48	-44.44	-15.68
2002/04/14	11:17:06	11.49	-43.93
2002/04/18	14:17:28	-61.2	-25.73
2002/06/02	00:52:19	8.19	-37.49
2002/06/05	12:45:23	35.56	-36.19
2002/06/11	17:58:05	-40.82	-16.33
2002/06/12	19:52:53	-0.37	-20.73
2002/06/14	15:24:12	22.56	-44.67
2002/06/15	13:23:12	-53.45	24.08
2002/06/16	17:59:23	-53.46	24.03
2002/06/25	19:56:04	-5.09	-12.66
2002/06/26	01:00:14	-4.43	-12.67
2002/07/06	05:42:33	25.58	-44.97
2002/07/15	15:02:13	-44.19	-15.77
2002/07/29	07:13:44	6.58	126.79
2002/07/29	07:26:15	-55.97	-27.08
2002/07/30	06:55:11	-58.02	-23.02
2002/07/31	09:12:50	7.42	-36.36
2002/08/03	14:18:19	-0.86	-14.39
2002/08/04	15:16:34	-35.29	-16.17
2002/08/23	18:16:01	-55.97	-25.74
2002/08/27	06:48:16	-55.89	-25.82
2002/09/07	18:08:41	-57.84	-25.3
2002/09/26	12:55:33	-20.29	-12
2002/10/02	15:57:08	-0.62	-13.39
2002/10/22	06:38:51	-43.74	39
2002/11/08	18:45:25	-17.61	-13.23
2002/11/12	01:46:54	-56.49	-26.89
2002/11/13	20:27:02	18.85	-64.24
2002/11/14	15:30:34	-55.95	-35.43

2002/11/15	13:05:41	-55.79	-35.76
2002/11/16	10:16:31	-55.98	-34.98
2002/11/18	00:31:35	28.72	-43.21
2002/11/28	19:19:32	16.26	-46.5
2002/11/29	11:49:33	23.34	-44.81
2002/12/12	04:03:20	-31.86	-67.28
2002/12/12	04:16:09	-57.65	-25.36
2002/12/15	05:56:28	10.83	-43.3
2002/12/17	04:33:02	-57.03	-24.17
2002/12/18	01:47:16	-57.1	-24.66
2002/12/19	14:17:47	-56.97	-24.84
2002/12/21	14:12:42	-10.84	-13.18
2003/01/09	15:43:58	-59.76	-58.23
2003/01/11	07:30:13	-4.97	-11.37
2003/01/18	20:37:53	35.81	-35
2003/01/27	17:56:40	-45.43	35.28
2003/02/07	06:34:07	-56.3	-27.09
2003/02/08	08:50:01	-39.54	45.05
2003/02/11	19:42:12	-52.57	13.64
2003/02/12	17:16:33	-56.62	-26.55
2003/02/13	04:45:29	2.82	-31.47
2003/02/14	19:03:28	-61.7	-53.07
2003/02/22	11:37:50	-46.2	35.12
2003/03/02	16:43:05	-36.67	-20.67
2003/03/03	19:54:13	-55.24	-27.93
2003/03/07	12:23:16	0.89	-26.98
2003/03/21	01:09:55	18.34	-68.02
2003/03/21	01:23:56	-57.25	-25.01
2003/04/02	03:43:20	35.17	-35.65
2003/04/17	14:51:07	-54.32	2.49

2003/04/30	00:47:10	-54.85	5.77
2003/05/09	20:26:22	-47.91	32.25
2003/05/14	06:03:39	18.29	-58.72
2003/05/19	00:21:41	-60.24	-26.7
2003/06/21	05:56:03	10.55	-59.2
2003/06/25	01:38:46	28.57	-43.63
2003/06/30	00:07:28	17.28	-61.29
2003/07/08	08:51:32	-6.94	-21.76
2003/07/15	17:50:06	3.85	-30.91
2003/07/23	16:38:43	-15.69	-13.55
2003/08/01	01:37:20	-54.8	1.82
2003/08/02	17:30:38	35.13	-35.75
2003/08/04	04:37:42	-60.8	-43.21
2003/08/06	17:01:57	-60.34	-45.03
2003/08/14	08:41:33	-60.61	-42.37
2003/08/27	12:39:06	7.01	-34.23
2003/08/29	09:41:45	-59.81	-25.06
2003/09/05	07:46:55	-54.95	1.83
2003/09/06	15:47:06	-57.56	-25.51
2003/09/20	17:38:38	-55.91	-27.91
2003/09/21	23:15:21	-0.8	-13.77
2003/09/23	16:10:25	-22.72	-13.65
2003/09/25	18:43:13	35.34	-35.98
2003/09/29	22:07:18	-55.52	-26.8
2003/09/30	08:01:39	-60.49	-33.14
2003/10/05	18:29:13	-19.87	-11.61
2003/10/07	16:54:23	-47.16	-9.92
2003/10/11	23:08:48	-1.28	-15.43
2003/10/20	16:50:18	-58.21	-25.97
2003/10/23	07:47:23	-60.74	-25.93

2003/10/29	19:54:20	-61.05	-24.68
2003/10/30	06:00:51	-61.13	-24.43
2003/11/07	18:19:13	-57.44	-24.92
2003/11/09	19:52:52	-0.27	-19.26
2003/11/22	02:29:08	19.5	-78.38
2003/11/26	19:25:13	28.45	-43.39
2003/12/14	14:37:43	-55.44	-1.84
2003/12/21	07:41:06	-0.39	-20.13
2003/12/23	05:58:44	-0.52	-20.38
2004/01/15	10:56:22	10.94	-62.2
2004/01/16	18:07:58	7.79	-37.73
2004/01/18	14:07:08	-47.26	-10.88
2004/02/07	23:41:02	13.54	-44.87
2004/02/13	21:32:26	-39.2	-15.82
2004/02/27	13:45:29	-18.89	-12.36
2004/02/28	05:23:57	-18.75	-12.43
2004/03/03	20:24:49	-0.48	-16.13
2004/03/08	23:39:17	10.94	-43.28
2004/03/12	20:30:49	5.64	-32.85
2004/03/17	06:41:00	-7.12	-13.05
2004/03/18	23:09:46	32.48	-40.18
2004/04/04	18:04:38	-3.23	-12.18
2004/04/05	09:51:12	-56.86	-30.56
2004/04/08	10:23:01	-55.81	-27.78
2004/04/19	08:14:16	3.82	-32.21
2004/04/20	21:41:36	33.06	-39.34
2004/04/21	01:20:46	32.97	-39.41
2004/04/24	08:03:11	0.99	-27.05
2004/05/05	04:57:57	-58.32	-11.36
2004/05/07	09:50:33	-58.04	-25.11

2004/05/11	23:58:58	12.76	-44.48
2004/05/12	23:23:57	-1.2	-15.22
2004/05/13	07:14:41	-55.75	-27.64
2004/05/15	18:54:22	-47.67	32.03
2004/05/20	07:58:26	-52.28	14.1
2004/05/26	11:21:02	-52.82	18.94
2004/05/27	13:34:05	-52.82	18.98
2004/06/02	20:48:01	4.85	-32.6
2004/06/17	22:04:12	-41.33	-16.56
2004/07/06	15:02:59	-11.62	-13.51
2004/07/09	15:37:55	-39.84	-15.76
2004/07/16	07:18:01	-25.78	-13.64
2004/07/30	12:14:34	-57.51	-25.31
2004/08/05	21:51:24	23.79	-45.02
2004/08/10	19:10:23	-52.35	14.11
2004/08/23	00:57:18	-24.97	-13.58
2004/08/30	22:09:23	-56.6	-26.18
2004/09/06	12:43:07	-55.43	-28.79
2004/09/07	02:55:34	-55.26	-27.99
2004/09/08	15:40:27	-52.21	-4.87
2004/09/11	21:52:39	-58.13	-24.93
2004/09/13	17:15:08	17.75	-46.56
2004/09/18	07:07:52	23.28	-67.56
2004/09/21	02:47:47	-53.3	23.65
2004/09/22	20:50:05	-55.13	-28.63
2004/09/24	10:35:01	0.87	-25.66
2004/09/28	13:39:51	-12.87	-14.65
2004/09/29	02:01:03	-59.05	-25.18
2004/10/08	15:28:43	-56.54	-26.76
2004/10/09	23:38:26	-60.82	-51.19

2004/10/12	14:59:13	-28.93	-12.44
2004/10/15	18:52:31	-55.71	-1.41
2004/10/16	01:29:20	-46.39	33.8
2004/10/25	14:08:25	-57.05	-24.31
2004/10/26	20:48:17	-57.09	-24.26
2004/11/02	03:02:23	-44.85	-15.31
2004/11/07	02:41:45	-55.66	-29.23
2004/11/16	09:27:24	-52.65	28.2
2004/11/21	11:41:12	15.85	-61.65
2004/11/27	08:49:05	-46.11	-20.34
2004/11/30	18:25:36	-56.02	-24.21
2004/12/02	13:38:23	-57.36	-26.17
2004/12/03	03:46:48	10.31	-61.02
2004/12/11	19:45:45	18.76	-64.69
2004/12/15	19:35:33	-24.26	-13.14
2004/12/20	09:52:47	0.76	-25.29
2005/01/08	07:14:38	-55.29	-28.1
2005/01/12	08:40:22	-0.47	-20.53
2005/01/29	21:01:13	-1.2	-15.56
2005/01/31	13:56:42	-56.13	-27.15
2005/02/07	14:23:51	-60.18	-26.61
2005/02/14	18:06:03	15.89	-61.56
2005/02/16	10:54:12	35.44	-36.1
2005/02/17	01:19:22	-56.1	-27.12
2005/02/25	05:12:00	-49.1	-8.36
2005/03/05	00:07:43	-58.73	-25.87
2005/03/16	12:27:07	-56.26	-26.3
2005/03/21	16:14:40	-0.9	-24.5
2005/03/23	12:08:57	-55.74	-1.28
2005/03/24	06:08:42	-55.77	-27.34

2005/03/28	00:01:34	-0.09	-20.67
2005/03/31	05:19:55	-54.21	8.05
2005/04/05	19:58:43	-54.3	7.62
2005/04/09	15:53:57	-53.41	25.56
2005/04/12	13:55:54	-10.6	-13.03
2005/04/21	01:15:12	-52.32	13.99
2005/04/22	03:46:08	-10.25	-13.18
2005/04/27	13:25:36	-55.47	-27.9
2005/05/04	14:49:29	-58.18	-25.18
2005/05/10	06:40:24	-42.71	42.4
2005/05/18	09:10:58	-56.43	-26.5
2005/05/20	07:58:06	-58.98	-24.64
2005/06/05	01:04:52	-57.33	-25.82
2005/06/05	01:09:13	-53.14	22.51
2005/06/12	19:26:29	-56.4	-26.7
2005/06/15	13:14:01	-58.27	-24.57
2005/07/04	11:36:07	-41.94	42.65
2005/07/21	12:02:45	-59.18	-16.77
2005/07/22	12:16:44	-56.13	-27.31
2005/07/25	19:45:19	-56.23	-27.48
2005/08/04	12:11:22	-60.13	-25.38
2005/08/07	02:17:52	-46.8	33.62
2005/08/15	07:53:45	-1.5	-13.01
2005/08/21	07:12:18	-59.66	-25.09
2005/08/23	01:38:19	-59.75	-26.68
2005/08/28	03:44:06	-56.68	-26.9
2005/08/31	01:24:54	-59.49	-26.85
2005/09/03	12:38:26	-50	-8.55
2005/09/08	04:52:37	21.42	-45.86
2005/09/09	01:20:23	-55.65	-26.96

2005/09/22	16:19:45	-40.8	43.21
2005/09/22	16:37:49	-9.43	158.09
2005/10/02	06:55:02	0.92	-29.42
2005/10/03	10:28:34	-58.12	-24.73
2005/11/02	00:46:46	-54.55	5.58
2005/11/04	12:25:06	-35.59	53.46
2005/11/07	22:11:03	-56.06	-27.13
2005/11/09	12:37:29	-47.01	33.58
2005/11/11	14:58:57	-55.65	-26.97
2005/11/14	12:57:29	-43.86	41.73
2005/11/22	13:21:26	-61	-24.98
2005/12/11	04:42:35	15.36	-45.78
2005/12/19	14:44:52	3.34	-31.42
2005/12/23	18:04:01	8.15	-38.1
2005/12/25	18:47:33	-59.61	-24.38
2006/01/02	06:11:03	-61.12	-21.39
2006/01/05	08:40:54	-56.64	-24.58
2006/01/06	06:28:02	7.25	-34.44
2006/01/15	06:49:44	-54.07	7.31
2006/01/20	08:53:56	31.24	-41.44
2006/02/07	08:56:00	-59.06	-25.09
2006/02/17	13:24:10	-1.16	-15.13
2006/02/18	14:59:08	-6.05	-11.36
2006/02/20	19:26:48	-10.54	-13.2
2006/02/23	04:04:11	-54.64	1.95
2006/02/28	02:45:17	-35.37	54.12
2006/03/02	23:35:49	19.19	-63.9
2006/03/03	23:36:36	-55.92	-3.94
2006/03/04	00:53:34	1.09	-28.01
2006/03/09	09:59:59	-59.7	-29.7

2006/03/10	10:12:22	-60.67	-46.62
2006/03/18	14:13:41	-56	-27.28
2006/03/19	04:31:56	-58.15	-24.77
2006/03/27	01:10:37	7.22	-34.24
2006/03/28	04:09:54	-56.7	-25.99
2006/03/30	03:14:43	-1.11	-15.98
2006/04/04	01:43:35	-56.69	-26.71
2006/04/08	22:03:08	-0.03	-18.08
2006/04/10	06:26:18	7.77	-36.98
2006/04/14	09:51:24	-56.31	-26.77
2006/04/20	14:59:08	-49.62	-7.67
2006/04/28	07:22:46	3.96	-31.6
2006/04/30	03:51:35	-60.08	-25.82
2006/05/13	23:53:32	-56.32	-27.4
2006/05/24	17:58:11	3.94	-32.08
2006/05/26	11:52:42	-37.48	51.29
2006/05/29	05:20:45	-59.97	-25.79
2006/05/30	02:50:08	-45.92	-76.17
2006/06/03	19:21:41	-60.06	-25.97
2006/06/05	06:18:47	0.91	-27.99
2006/06/14	08:11:07	-52.98	25.59
2006/06/15	19:45:51	-55.89	-29.91
2006/06/18	18:28:06	32.97	-39.75
2006/06/20	00:42:28	-17.68	-13.85
2006/06/21	23:37:52	19.09	-46.04
2006/06/22	01:12:04	4.62	-32.76
2006/06/23	10:41:59	-47.24	32.5
2006/07/01	20:12:11	-56.69	-24.75
2006/07/06	15:11:27	-24.85	-13.43
2006/07/10	07:21:41	-11.54	-13.39

2006/07/13	19:13:45	-61.2	-36.65
2006/07/22	19:47:49	-17.74	-13.15
2006/07/25	07:57:32	-60.88	-24.71
2006/07/29	19:53:44	23.78	-64.01
2006/08/01	12:01:45	-6.92	-12.79
2006/08/04	13:41:42	10.07	-70.57
2006/08/17	20:11:57	-56.82	-5.63
2006/08/20	03:41:56	-61.27	-34.52
2006/08/22	00:09:27	-61.17	-34.1
2006/09/05	16:24:15	-58.11	-6.92
2006/09/06	11:42:45	-61.09	-34.09
2006/09/10	06:35:58	-58.08	-25.42
2006/09/14	01:08:47	-58.56	-29.71
2006/09/29	13:08:29	10.73	-61.39
2006/09/30	12:47:25	7.44	-34.64
2006/10/03	07:57:20	-53.24	23.17
2006/10/09	18:19:36	-51.09	28.85
2006/10/25	04:14:21	-55.61	-26.41
2006/10/26	14:28:39	38.65	15.41
2006/10/26	14:43:41	-55.53	-26.44
2006/10/31	06:42:43	-1.06	-24.38
2006/11/05	09:59:27	40.27	-29.56
2006/11/07	06:07:00	2.42	-32.08
2006/11/08	15:57:30	-56.98	-23.27
2006/11/13	08:54:00	-12.54	-14.7
2006/11/19	01:55:09	-55.74	-24.47
2006/11/22	05:20:50	-37.41	-17.18
2006/11/29	04:11:40	26.18	-44.81
2006/12/03	08:19:57	-0.38	-19.76
2006/12/06	12:05:51	-42.83	41.88

2006/12/13	18:25:14	-58.16	-25.06
2006/12/31	14:55:06	-38.04	-71.4
2007/01/01	01:05:16	32.75	-39.78
2007/01/15	07:58:15	-61.17	-34.01
2007/01/18	22:32:38	22.35	-44.96
2007/01/20	06:21:10	-55.31	-29.33
2007/01/23	04:16:10	-42.97	41.82
2007/01/23	04:37:20	-6.76	130.06
2007/02/04	03:33:23	35.34	-36.06
2007/02/05	16:37:07	-0.96	-14.39
2007/02/08	10:22:01	8.64	-39.43
2007/02/10	06:03:05	-43.26	-72.26
2007/02/14	02:42:01	36.37	-34.04
2007/02/16	01:15:29	-55.08	-26.34
2007/02/26	23:49:56	-44.79	35.36
2007/02/27	00:44:13	-20.15	173.02
2007/02/28	23:13:22	-55.28	-29.18
2007/03/01	22:45:33	26.58	-44.51
2007/03/01	23:11:55	26.54	-44.57
2007/03/04	11:26:16	33.75	-38.55
2007/03/04	11:43:44	33.76	-38.74
2007/03/07	23:01:27	3.17	-30.97
2007/03/08	11:14:37	-58.13	-7.93
2007/03/21	23:07:51	15.36	-45.61
2007/03/24	07:39:40	-42.57	42.19
2007/04/05	03:56:56	37.45	-24.44
2007/04/06	15:21:42	37.38	-24.35
2007/04/07	05:20:55	-39.8	46.19
2007/04/08	14:47:20	37.43	-24.43
2007/04/09	08:32:26	37.48	-24.5

2007/04/24	07:25:47	29.14	-43.26
2007/04/24	07:37:00	29.23	-43.3
2007/04/25	12:34:30	29.15	-43.07
2007/04/28	14:02:42	-61.04	-20.12
2007/05/04	12:06:58	-1.12	-14.92
2007/05/05	05:27:13	-58.73	-22.38
2007/05/19	10:38:40	-56.93	-24.37
2007/05/30	19:35:24	-60.61	-26.09
2007/06/02	14:06:41	30.74	-41.78
2007/06/03	11:17:41	-55.21	-29.36
2007/06/04	03:06:58	-56.04	-27.36
2007/06/05	15:27:09	-60.7	-26.12
2007/06/14	06:58:16	-56.45	-27.09
2007/06/15	03:48:38	-58.85	-25.89
2007/06/24	00:25:28	-55.78	-1.72
2007/07/01	23:45:33	-55.28	-28.07
2007/07/03	08:26:07	0.81	-30.04
2007/07/05	05:47:53	-60.06	-25.9
2007/07/08	07:28:40	-59.44	-25.97
2007/07/15	12:09:55	-60.24	-25.11
2007/07/20	20:00:11	-52.71	25.94
2007/07/25	19:38:27	44.45	-28.15
2007/07/31	02:42:53	-56.12	-27.57
2007/08/02	07:19:25	-52.55	17.92
2007/08/08	01:01:44	0.98	-29.23
2007/08/09	17:25:09	25.95	-45.03
2007/08/11	06:32:56	-5.44	-11.53
2007/08/12	08:01:30	-5.55	-11.46
2007/08/16	14:18:28	-3.43	-12.16
2007/08/16	14:44:11	-3.48	-12.16

2007/08/18	16:20:51	40.12	-29.71
2007/08/19	00:04:34	-60.85	-26.03
2007/08/19	00:41:32	-60.96	-26.03
2007/08/19	01:32:45	-60.77	-25.45
2007/08/20	12:37:11	-0.02	-18.14
2007/08/21	13:35:40	8.19	-39.16
2007/09/01	01:28:07	27.78	-44.1
2007/09/01	01:56:52	27.82	-44.07
2007/09/07	09:25:21	7.46	-34.71
2007/09/21	15:11:59	-47.65	-13.26
2007/09/22	06:35:32	42.93	-31.94
2007/09/26	18:39:38	-6.66	-11.59
2007/10/09	06:41:12	38.32	-30.37
2007/10/18	16:13:19	30.21	-42.65
2007/10/23	03:03:01	-1.63	-13.01
2007/11/03	13:52:10	-55.4	-29.64
2007/11/08	07:44:34	-56.06	-27.8
2007/11/17	08:42:21	-0.94	-13.13
2007/11/27	10:13:51	-1.11	-13.2
2007/11/29	19:00:32	15.06	-61.41
2007/12/06	17:12:06	22.75	-45
2007/12/12	22:10:06	-54.99	-33.49
2007/12/24	09:20:50	-54.12	-2.02
2007/12/28	01:42:43	-46.36	33.68
2008/01/12	08:32:48	-56.65	-26.88
2008/01/14	01:20:03	-35.31	53.85
2008/01/20	05:13:24	-59.65	-22.98
2008/01/29	14:57:30	-59	-24.65
2008/02/03	14:24:41	-56.38	-26.54
2008/02/04	07:43:58	19	-66.87

2008/02/06	16:10:37	-24.76	-13.33
2008/02/08	09:38:22	10.85	-41.71
2008/02/10	12:22:08	-61.05	-25.01
2008/02/11	07:00:43	-59.92	-58.49
2008/02/14	02:52:21	-0.77	-13.17
2008/02/20	02:12:43	-53.11	-46.66
2008/02/23	15:57:28	-57.12	-23.13
2008/02/26	10:31:14	-57.18	-23.09
2008/02/26	10:46:16	36.1	21.86
2008/02/29	16:10:32	-53.09	-46.7
2008/02/29	16:58:06	23.85	122.45
2008/03/08	18:47:39	-36.54	52.41
2008/03/09	15:27:54	-58.44	-24.58
2008/03/13	13:28:50	-45.32	35.08
2008/03/23	21:32:33	-0.99	-14.49
2008/04/01	11:05:25	-38.75	46.39
2008/04/14	09:45:20	-56.04	-27.75
2008/04/15	06:44:22	-55.82	-30.08
2008/04/16	20:28:46	-17.61	-12.98
2008/04/18	15:31:58	-53.08	21.36
2008/04/21	03:47:25	-55.65	-27.92
2008/04/24	12:15:05	-1.14	-23.87
2008/04/27	14:35:34	-35.44	-16.28
2008/04/28	14:33:19	-59.03	-24.14
2008/04/28	15:58:00	-59.04	-24.15
2008/04/29	09:00:18	-54.51	6.25
2008/05/15	14:23:33	-58.14	-25.19
2008/05/19	03:16:17	-47.72	32.16
2008/05/23	19:35:40	7.51	-35.01
2008/05/24	02:43:42	-42.17	-72.46

2008/05/25	15:39:47	-54.46	-56.12
2008/05/30	10:44:16	-54.92	1.51
2008/06/01	00:31:18	-54.91	1.59
2008/06/02	02:17:22	-37.65	-17.37
2008/06/13	20:06:51	-17.84	-13.59
2008/06/27	05:08:15	11.18	-62.28
2008/06/28	08:57:02	-33.12	-15.73
2008/06/30	06:17:51	-58.33	-21.77
2008/07/01	01:54:45	-58.35	-21.57
2008/07/03	06:34:56	10.26	-60.28
2008/07/07	21:39:28	-58.42	-21.77
2008/07/11	09:28:18	-11.76	-14.27
2008/07/15	05:07:18	-47.56	-11.93
2008/07/25	16:26:31	-59.9	-29.99
2008/07/27	21:15:47	-0.01	-18.16
2008/07/30	20:15:16	-60.04	-27.46
2008/08/06	14:45:42	-59.04	-24.6
2008/08/11	07:19:30	10.61	-64.17
2008/08/15	03:38:20	-58.69	-22.64
2008/08/17	15:39:12	-52.92	-4.1
2008/08/19	08:33:57	-8.09	-13.53
2008/08/21	19:13:46	-58.98	-24.72
2008/08/26	08:07:08	-52.63	26.66
2008/08/28	15:22:30	0.18	-17.37
2008/09/05	19:07:42	-0.88	-13.79
2008/09/10	13:08:21	8.18	-38.54
2008/09/16	07:28:30	0.95	-28.8
2008/09/17	21:03:42	-28.29	-12.65
2008/09/24	17:12:16	-22.77	-12.8
2008/10/03	05:26:26	7.76	-37

2008/10/04	07:56:59	-59.74	-25.42
2008/10/19	02:56:14	-56.01	-27.9
2008/10/21	21:21:55	-10.5	-13.11
2008/11/02	20:42:38	19.49	-66.28
2008/11/13	15:10:18	-56.05	-26.93
2008/11/14	02:05:13	-53.78	9.09
2008/11/22	18:49:50	-0.77	-13.8
2008/11/25	01:19:52	-47.09	-10.27
2008/12/08	01:51:05	13.51	-44.82
2008/12/13	17:21:16	8.11	-37.97
2008/12/14	20:36:32	-60.37	-18.44
2008/12/20	21:05:22	-31.23	-13.27
2009/01/02	19:42:32	0.94	-26.99
2009/01/17	05:17:15	-60.18	-26.21
2009/02/05	10:40:27	-56.6	-25.25
2009/02/06	02:58:36	-28.16	-71.62
2009/02/14	07:48:40	18.71	-68.93
2009/02/18	00:09:20	-53.08	21.07
2009/02/18	00:16:22	-53.1	21.37
2009/02/24	00:46:44	0.01	-18.33
2009/02/28	14:33:12	-61.03	-24.39
2009/03/03	06:05:02	-56.45	-26.67
2009/03/05	01:32:36	-30.78	-13.45
2009/03/09	09:47:20	-16.39	-11.15
2009/03/11	23:50:37	15.71	-46.69
2009/03/12	05:18:13	-61.15	-23.54
2009/03/20	16:01:19	-59.03	-24.76
2009/03/22	06:06:40	-12.86	-14.63
2009/03/22	06:35:17	-12.9	-14.6
2009/03/24	12:34:57	14.62	-44.95

2009/03/26	18:43:51	-6.9	-12.57
2009/03/27	10:00:48	-12.86	-14.58
2009/04/03	09:11:54	-60.08	-25.94
2009/04/04	18:39:22	-56.08	-27.54
2009/04/08	06:26:55	-58.04	-7.15
2009/04/09	03:31:32	-60.76	-50.19
2009/04/11	17:14:39	-60.13	-26.04
2009/04/16	14:57:16	-60.71	-26.55
2009/05/04	09:10:23	10.26	-67.15
2009/05/05	02:40:00	-44.12	-15.92
2009/05/11	14:32:34	-30.01	-13.75
2009/05/13	23:02:47	-55.86	-26.74
2009/05/19	03:26:23	-47.77	-13.26
2009/05/26	01:18:56	-34.76	54.34
2009/05/27	02:50:27	-33.13	-15.69
2009/05/28	21:07:44	-56.06	-27.77
2009/05/30	06:47:58	-60.75	-27.43
2009/06/01	04:35:09	19.91	-63.55
2009/06/03	04:36:45	-37.77	49.43
2009/06/04	17:25:32	-45.56	35.03
2009/06/06	20:33:33	23.94	-46.12
2009/06/09	15:15:36	-56.41	-26.34
2009/06/11	08:55:07	-24.97	-13.59
2009/06/16	20:06:01	-54.37	6.32
2009/06/24	11:12:26	0.3	-17.02
2009/06/25	12:34:19	-23.9	-13.34
2009/06/27	15:45:55	-33.09	-15.78
2009/07/02	03:20:53	-11.73	-14.08
2009/07/03	20:28:18	-49.84	-7.69
2009/07/11	01:54:37	-14.12	-13.8

2009/07/18	17:06:40	0.92	-29.24
2009/07/30	08:34:46	-22.94	-13.54
2009/08/12	14:50:20	-57.9	-24.9
2009/08/14	09:50:25	19.5	-65.81
2009/08/22	12:34:54	1.01	-28.4
2009/09/04	22:16:49	-48.34	31.6
2009/09/11	08:12:05	-56.06	-26.31
2009/09/11	08:49:16	48.14	154.66
2009/09/12	03:56:57	-45.83	-76.99
2009/09/21	23:18:36	3.99	-31.69
2009/09/23	07:29:59	-60.57	-33.1
2009/09/28	12:13:21	-25.77	-13.64
2009/10/02	06:30:45	-16.41	-172.83
2009/10/10	01:40:43	28.9	-43.46
2009/11/14	00:51:40	-38.94	-15.91
2009/11/18	01:42:50	-54	6.76
2009/11/19	00:05:25	-46.16	34.79
2009/11/20	19:31:32	0.1	-17.99
2009/11/22	22:07:51	-39.77	-75.46
2009/11/22	22:50:57	9.86	-60.84
2009/11/27	08:15:58	10.46	-69.73
2009/11/28	08:18:36	15.22	-59.31
2009/12/09	16:00:56	-0.62	-20.8
2009/12/12	03:34:47	-17.79	-13.32
2009/12/16	03:40:30	-55.53	-26.84
2009/12/24	22:04:59	-55.5	-26.87
2010/01/06	16:38:39	-41.71	-16.43
2010/01/12	21:53:17	18.61	-72.62
2010/01/13	00:59:10	18.66	-72.97
2010/01/15	18:00:50	10.55	-63.53

2010/01/20	11:03:47	18.67	-72.81
2010/01/24	22:43:24	16.15	-60.86
2010/01/26	15:22:10	-39.3	-15.7
2010/01/27	11:20:39	-39.08	-15.73
2010/02/03	02:18:32	-59.23	-25.08
2010/02/08	12:08:33	-56.39	-24.28
2010/02/11	11:51:58	-40.65	-16.63
2010/02/13	01:01:01	29.84	-42.79
2010/02/26	00:11:54	-55.96	-4.28
2010/02/27	19:54:34	10.83	-43.39
2010/02/28	16:13:47	-57.95	-7.93
2010/03/02	02:09:37	-39.86	-71.47
2010/03/10	02:41:52	-37.07	-73.13
2010/03/11	06:22:20	-57.46	-27.58
2010/03/12	14:39:48	-59.08	-25.22
2010/03/13	10:34:45	-37.78	-73.95
2010/03/14	22:33:23	-58.62	-23.34
2010/03/22	04:36:11	-17.71	-13.14
2010/03/26	09:36:58	-1.38	-15.92
2010/03/27	17:28:34	-52.81	25.79
2010/04/13	20:27:02	-56.55	-27
2010/04/16	22:41:38	-37.69	-74.25
2010/04/18	01:49:39	-37.41	-74.19
2010/04/20	01:00:46	-55.73	-26.79
2010/04/22	05:01:37	20.43	-45.56
2010/04/23	10:03:09	-37.69	-73.32
2010/04/25	21:09:51	-55.57	-27.67
2010/04/26	17:04:54	-56.25	-27.42
2010/05/01	16:29:00	-59	-25.65
2010/05/03	18:39:45	-37.36	-74.33

2010/05/04	16:38:49	-47.55	-11.8
2010/05/07	23:12:13	16.56	-60.88
2010/05/16	05:16:13	18.41	-67.13
2010/05/17	20:05:45	-16.36	-14.19
2010/05/20	01:43:56	-55.66	-26.19
2010/06/01	16:05:33	-36.93	-73.85
2010/06/02	01:49:08	-57.64	-26.11
2010/06/07	04:25:52	-0.74	-13.55
2010/06/24	04:07:30	-35.58	-17.38
2010/06/30	15:17:14	-55.4	-27.92
2010/07/09	22:57:16	-45.93	-76.41
2010/07/10	06:18:26	-40.17	-16.43
2010/07/20	17:19:54	-29.08	-12.99
2010/08/02	03:30:11	7.25	-34.38
2010/08/05	06:01:52	-37.7	-73.69
2010/08/14	08:40:47	11.38	-62.4
2010/08/20	13:09:00	-56.03	-27.85
2010/08/27	00:17:07	-56.1	-27.47
2010/08/29	06:37:52	-55.87	-26.66
2010/09/04	11:52:04	-59.28	-24.97
2010/09/09	07:28:05	-37.27	-74.16
2010/09/13	02:48:12	0.95	-29.02
2010/09/18	11:17:25	-0.4	-19.56
2010/09/26	05:29:53	-40.58	-73.14
2010/10/01	10:51:42	-59.19	-24.83
2010/10/05	23:42:40	-57.56	-24.18
2010/10/06	00:49:17	-52.84	10.88
2010/10/08	10:15:42	-59.23	-25.39
2010/10/09	20:01:26	-58.15	-8.99
2010/10/16	23:59:50	-55.48	-27.96

2010/10/27	18:46:02	-60.9	-24.06
2010/10/28	21:41:19	-0.38	-19.87
2010/11/04	12:29:35	12.87	-44.85
2010/11/10	13:25:41	-55.94	-4.28
2010/11/11	18:47:23	-60.01	-25.94
2010/11/13	04:35:41	17.97	-68.56
2010/11/14	11:21:47	-0.06	-18.04
2010/11/17	22:33:48	-7.49	-13.52
2010/11/22	05:09:57	8.26	-39.43
2010/11/26	13:01:56	10.91	-43.5
2010/11/27	02:44:57	10.93	-43.33
2010/11/29	01:37:17	-17.88	-13.59
2010/11/30	14:32:33	-28.67	-12.4
2010/12/07	04:27:25	-58.1	-7.29
2010/12/08	05:24:41	-56.49	-25.48
2010/12/09	14:40:16	-56.43	-25.48
2010/12/10	17:48:25	23.86	-45.71
2010/12/22	04:03:48	-4.82	-11.66
2010/12/24	23:43:44	18.49	-66.24
2010/12/27	00:48:39	-2.71	-12.29
2010/12/28	02:47:14	-52.71	27.78
2010/12/30	06:50:02	-56.07	-26.44
2010/12/31	16:30:59	0.81	-26.06
2011/01/04	18:17:37	-44.71	-15.69
2011/01/06	16:36:13	20.29	-45.62
2011/01/07	01:19:18	20.3	-45.6
2011/01/11	15:45:32	-6.38	-11.28
2011/01/17	01:35:33	-20.98	-11.49
2011/01/18	14:46:15	-57.37	-26.71
2011/01/20	03:44:22	-60.22	-26.84

2011/01/21	03:37:18	17.38	-63.16
2011/01/23	22:53:00	-56.66	-26.74
2011/01/25	05:39:38	-53.04	22.24
2011/01/30	01:03:43	-49.64	-10.59
2011/02/02	12:41:00	17.51	-63.54
2011/02/04	12:16:57	11.35	-61.96
2011/02/12	02:53:20	0.31	-17.05
2011/02/15	21:59:06	0.11	-17.9
2011/02/28	11:04:21	-59.3	-17.16
2011/03/01	03:46:32	-5.53	-11.46
2011/03/06	14:32:42	-56.41	-26.68
2011/03/07	23:35:42	-56.05	-27.59
2011/03/16	13:42:35	19.19	-67.84
2011/03/17	01:00:05	-58.05	-25.05
2011/03/19	03:03:15	-10.36	-13.08
2011/03/22	13:31:33	-33.11	-15.74
2011/03/26	11:38:59	1	-29.1
2011/04/13	04:28:59	18.98	-64.26
2011/04/19	23:29:12	-44.58	-15.71
2011/04/24	22:44:22	-35.47	-16.82
2011/05/15	13:08:22	0.87	-25.62
2011/05/21	00:16:28	-56.04	-26.92
2011/06/07	05:11:13	-44.44	-15.73
2011/06/07	05:18:35	-44.39	-15.75
2011/06/11	11:21:55	-58.47	-13.87
2011/06/19	08:37:48	-56.16	-27.21
2011/07/08	05:53:06	1.07	-26.4
2011/07/15	13:26:07	-61.12	-22.85
2011/07/27	23:00:33	10.9	-43.34
2011/08/07	04:01:10	13.75	-60.09

2011/08/10	23:45:48	-6.89	-12.6
2011/08/14	01:29:45	-0.96	-14.43
2011/08/16	20:24:05	-57.37	-25
2011/08/21	12:38:51	-56.58	-27.1
2011/09/03	04:49:03	-56.57	-26.44
2011/10/19	10:40:43	-32.14	-13.15
2011/11/28	10:36:00	19.07	-66.77
2011/11/29	00:30:35	-1.28	-15.6
2011/12/01	21:35:11	32.2	-40.35
2011/12/03	09:27:15	18.07	-59.7
2011/12/11	09:54:59	-55.97	-27.78
2011/12/16	12:02:57	-46	-76.43
2011/12/19	11:12:53	-56	-27.45
2011/12/23	19:12:39	-52.19	28.35
2012/01/05	09:35:34	18.48	-70.34
2012/01/12	14:11:11	-52.07	28.2
2012/01/13	15:54:45	-60.9	-26.71
2012/01/23	20:50:18	19.67	-70.08
2012/01/24	16:31:14	-56.42	-27.41
2012/02/09	08:49:32	-56.39	-25.58
2012/02/11	02:58:24	-37.54	-73.68
2012/02/23	05:08:16	-17.72	-13.2
2012/03/07	12:02:52	-58.2	-24.68
2012/04/10	05:09:12	-0.87	-13.92
2012/04/14	20:53:57	-57.03	-25.03
2012/04/17	19:04:00	-59.26	-16.34
2012/04/21	01:19:34	-35.39	-15.85
2012/05/09	14:49:54	-0.74	-13.41
2012/06/29	15:31:47	-24.63	-9.67
2012/07/04	21:29:27	18.32	-62.99

2012/07/28	16:01:16	4.61	-32.58
2012/08/16	12:08:22	7.7	-36.97
2012/08/30	08:04:40	-37.34	-74.04
2012/08/31	00:35:40	3.96	-32.24
2012/09/14	07:07:50	-39.56	-16.04
2012/09/14	07:18:41	-39.82	-15.77
2012/10/04	23:14:58	17.68	-46.47
2002/11/08	18:45:25	-17.61	-13.23
2002/11/12	01:46:54	-56.49	-26.89
2002/11/13	20:27:02	18.85	-64.24
2002/11/14	15:30:34	-55.95	-35.43
2002/11/15	13:05:41	-55.79	-35.76
2002/11/16	10:16:31	-55.98	-34.98
2002/11/18	00:31:35	28.72	-43.21
2002/11/28	19:19:32	16.26	-46.5
2002/11/29	11:49:33	23.34	-44.81
2002/12/12	04:03:20	-31.86	-67.28
2002/12/12	04:16:09	-57.65	-25.36
2002/12/15	05:56:28	10.83	-43.3
2002/12/17	04:33:02	-57.03	-24.17
2002/12/18	01:47:16	-57.1	-24.66
2002/12/19	14:17:47	-56.97	-24.84
2002/12/21	14:12:42	-10.84	-13.18
2007/10/18	16:13:19	30.21	-42.65
2010/07/09	22:57:16	-45.93	-76.41
2010/08/05	06:01:52	-37.7	-73.69
2012/08/30	08:04:40	-37.34	-74.04

C. PREM

Velocities for each layer used in the PREM starting model

Layer	Thickness (km)	V_P (kms^{-1})	V_S (kms^{-1}))	Density (kg m^{-1})
Water	4	1.5	0	1.05
Upper/Middle Crust	12	5.8	3.2	2.6
Lower Crust	9.4	6.8	3.9	2.9
Lithosphere	15.6	8.1	4.48	3.38
	20	8.091	4.48	3.38
	20	8.08	4.47	3.37
	35	8.05	4.46	3.37
LVZ	35	8.03	4.45	3.37
	35	8.01	4.43	3.36
	35	7.99	4.41	3.36
Transition zone	25	8.61	4.66	3.45
	25	8.66	4.68	3.46
	25	8.71	4.70	3.48
	25	8.76	4.72	3.50
	25	8.81	4.73	3.51
	25	8.85	4.75	3.52
Halfspace	0	8.85	4.75	3.52

D. Group velocity versus Sea floor age plots

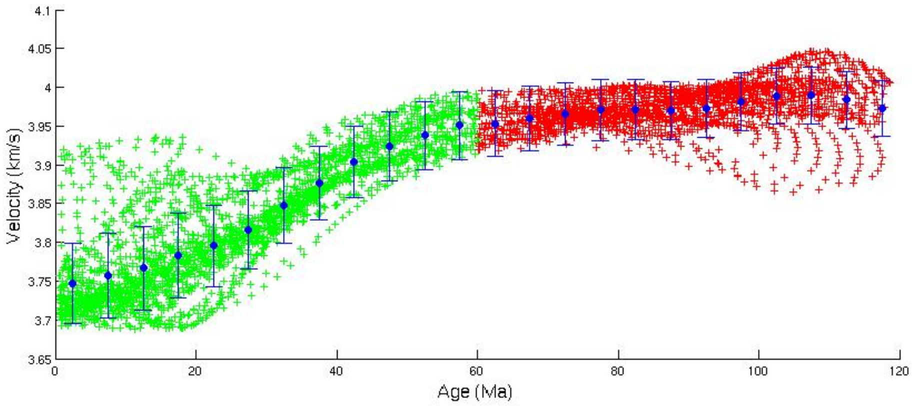

(a)

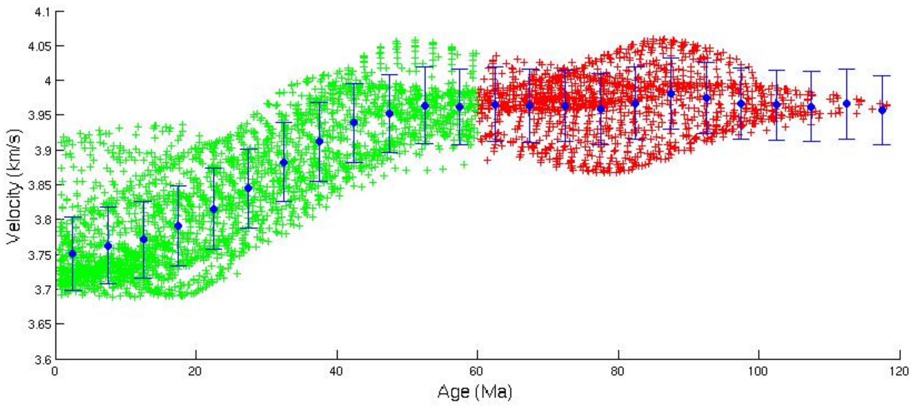

(b)

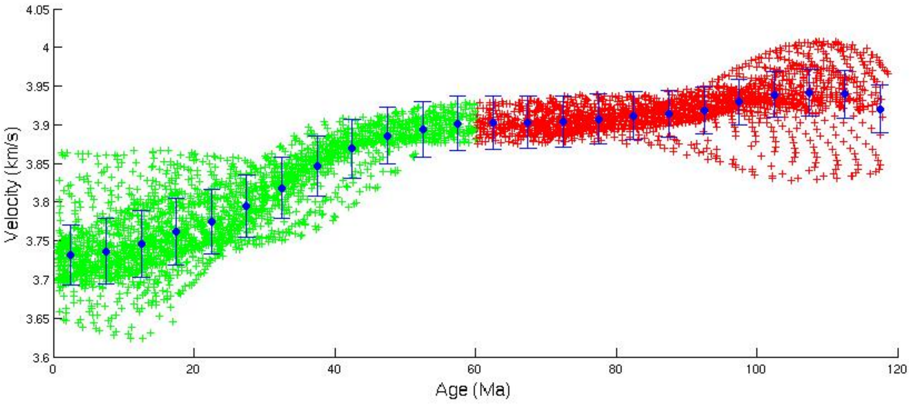

(c)

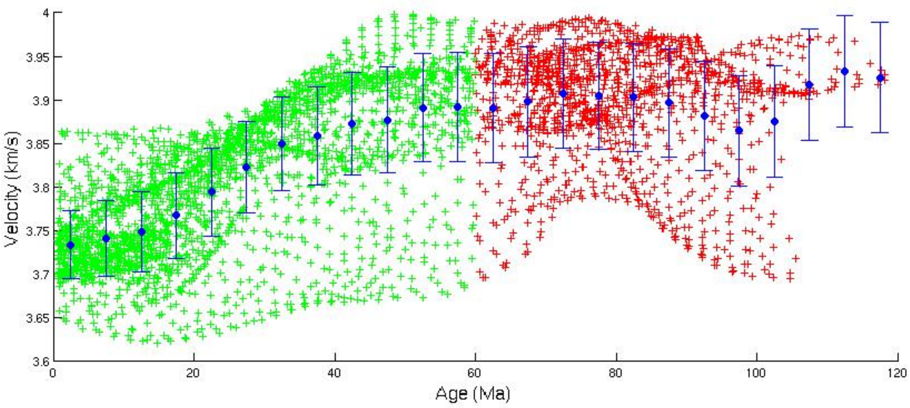

(d)

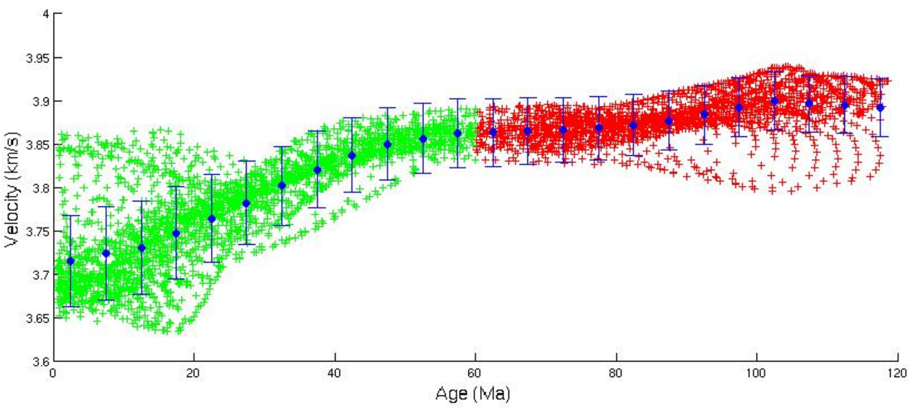

(e)

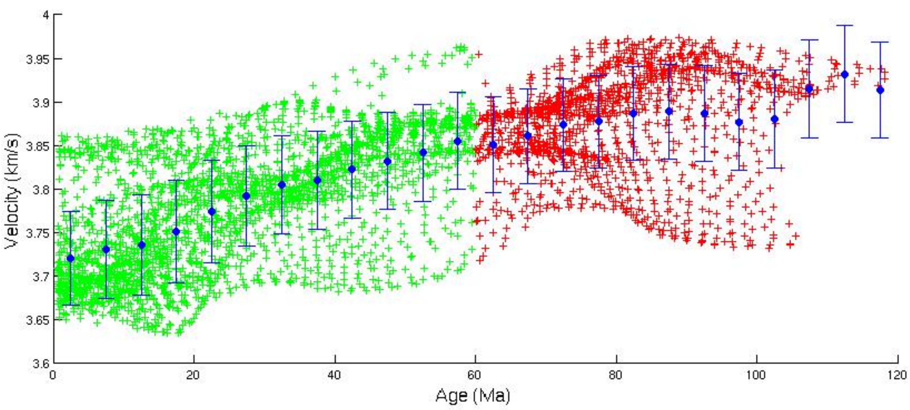

(f)

Group Velocity versus age plots for (a) 70 s east (b) 70 s west (c) 80 s east (d) 80 s west (e) 90 s east (f) 90 s west

E. 2D Profiles showing best fit thermal model to velocity structure

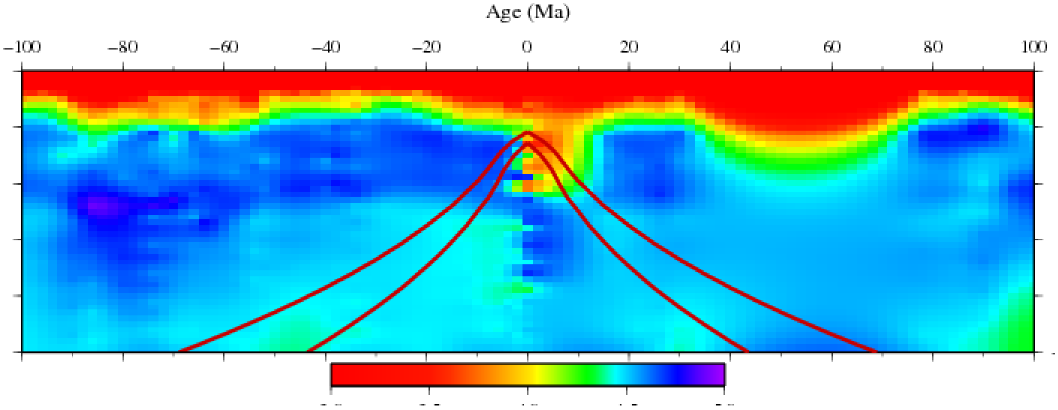
Age (Ma)
−100 −80 −60 −40 −20 0 20 40 60 80 100

(a)

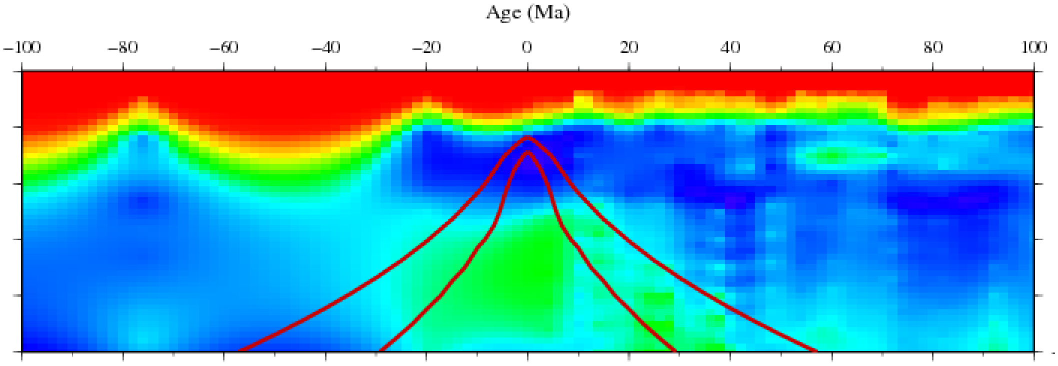
Age (Ma)
−100 −80 −60 −40 −20 0 20 40 60 80 100

(b)

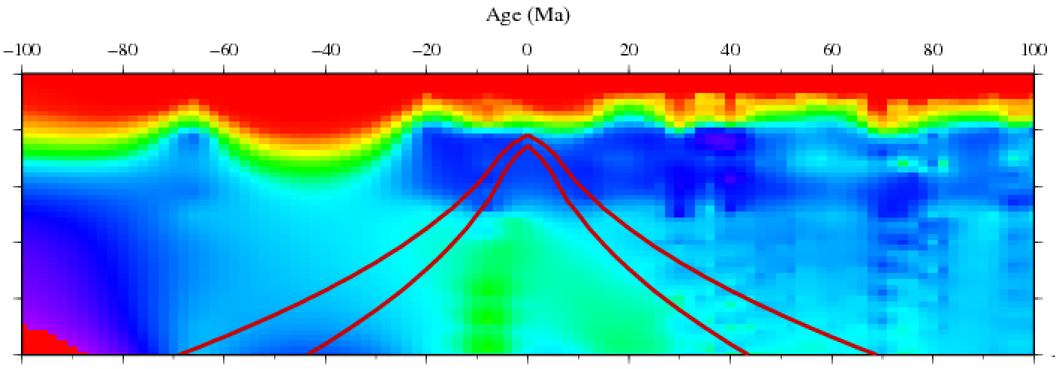
Age (Ma)
−100 −80 −60 −40 −20 0 20 40 60 80 100

(c)

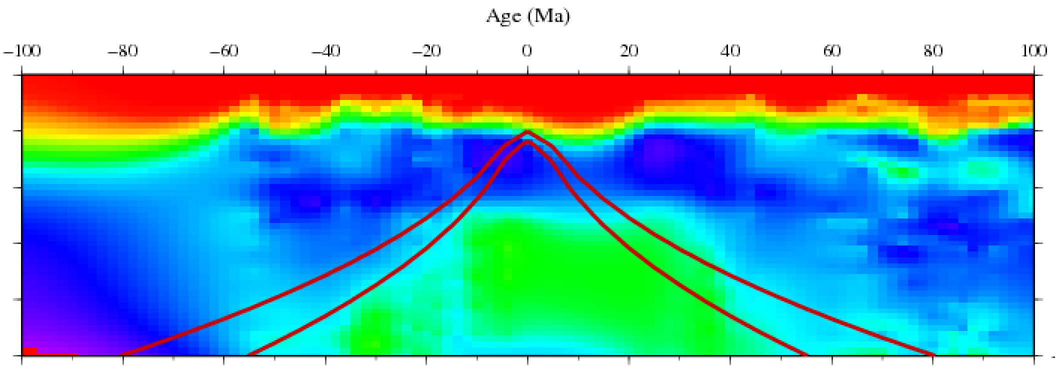

(d)

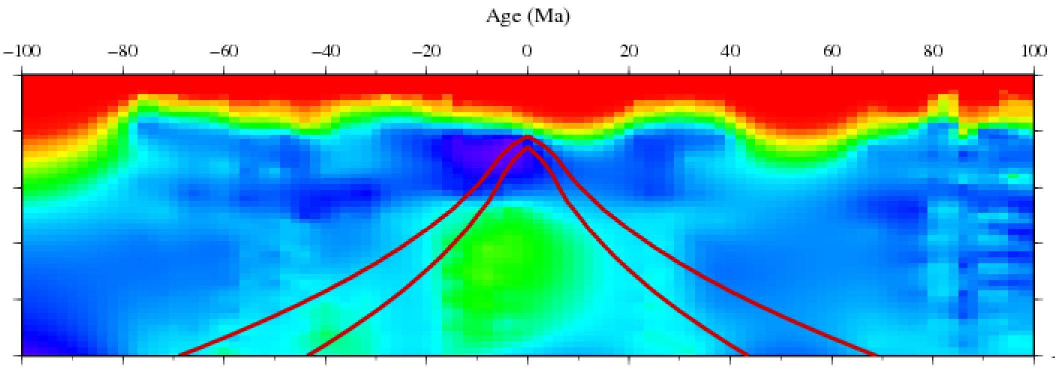

(e)

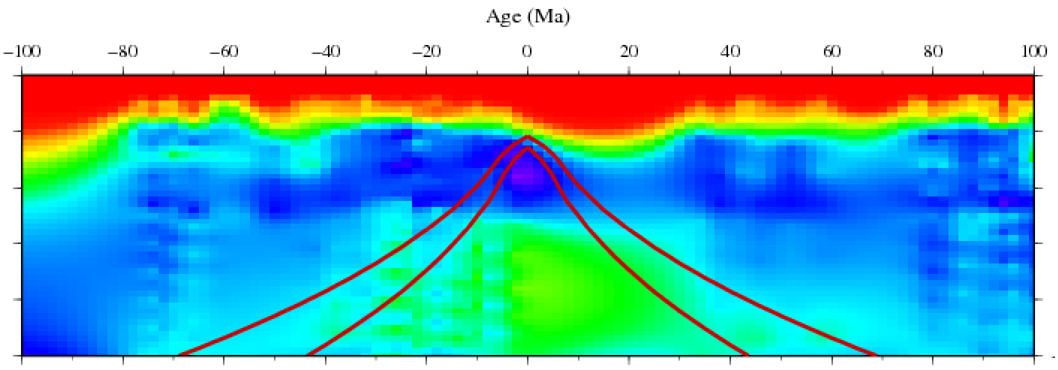

(f)

Velocity structure compared to thermal HSC model (red) for (a) Profile A: 5 °South and 1350 °CT_m in HSC (b) Profile B: 10 °South and 1300 °CT_m in HSC (c) Profile C: 15 °South and 1350 °CT_m in HSC (d) Profile E: 25 °Southand 1400 °CT_m in HSC (e)Profile F: 10 °South and 1350 °CT_m in HSC (f)Profile G: 15 °South and 1400 °CT_m in HSC

Bibliography

Abe, K., 1972. Group velocities of oceanic Rayleigh and love waves, *Physics of the Earth and Planetary Interiors*, **6**(5), 391–396.

Acton, C., Priestley, K., Gaur, V., & Rai, S., 2010. Group velocity tomography of the Indo-Eurasian collision zone, *Journal of Geophysical Research B: Solid Earth*, **115**(12).

Allerton, S., Escartìn, J., & Searle, R., 2000. Extremely asymmetric magmatic accretion of oceanic crust at the ends of slow-spreading ridge segments, *Geology*, **28**(2), 179–182.

Anderson, D., 1995. Lithosphere, asthenosphere, perisphere, *Reviews of Geophysics*, **33**(1), 124–149.

Anderson, D., 2007. *New Theory of the Earth*, Cambridge University Press.

Arroucau, P., Rawlinson, N., & Sambridge, M., 2010. New insight into cainozoic sedimentary basins and palaeozoic suture zones in southeast australia from ambient noise surface wave tomography, *Geophysical Research Letters*, **37**(7), n/a–n/a.

Assumpção, M., Feng, M., Tassara, A., & Julià, J., 2013. Models of crustal thickness for South America from seismic refraction, receiver functions and surface wave tomography, *Tectonophysics*, **609**, 82–96.

Bassin, C., L. G. & Masters, G., 2000. The current limits of resolution for surface wave tomography in North America, *EOS. Transactions of the American Geophysical Union*, **81**(F897).

Blackman, D. K. & Kendall, J.-M., 2002. Seismic anisotropy in the upper mantle 2. predictions for current plate boundary flow models, *Geochemistry, Geophysics, Geosystems*, **3**(9), 1 of 26–26 of 26.

Blaich, O., Faleide, J., & Tsikalas, F., 2011. Crustal breakup and continent-ocean transition at South Atlantic conjugate margins, *Journal of Geophysical Research: Solid Earth*, **116**(B1).

Bodin, T. & Sambridge, M., 2009. Seismic tomography with the reversible jump algorithm, *Geophysical Journal International*, **178**(3), 1411–1436.

Bown, J. & White, R., 1994. Variation with spreading rate of oceanic crustal thickness and geochemistry, *Earth and Planetary Science Letters*, **121**(3-4), 435–449.

Brune, J., 2013. *Surface Waves and Crustal Structure*, pp. 230–242, American Geophysical Union, Geophysical Monograph Series.

Canas, J. & Mitchell, B., 1981. Rayleigh wave attenuation and its variation across the Atlantic Ocean, *Geophysical Journal of the Royal Astronomical Society*, **67**(1), 159–176.

Cannat, M., 1996. How thick is the magmatic crust at slow spreading oceanic ridges?, *Journal of Geophysical Research: Solid Earth*, **101**(B2), 2847–2857.

Cannat, M., Mevel, C., Maia, M., Deplus, C., Durand, C., Gente, P., Agrinier, P., Belarouchi, A., Dubuisson, G., Humler, E., & Reynolds, J., 1995. Thin crust, ultramafic exposures, and rugged faulting patterns at the Mid-Atlantic Ridge (2224n), *Geology*, **23**(1), 49–52.

Chave, A., 1979. Lithospheric structure of the Walvis Ridge from Rayleigh wave dispersion, *Journal of Geophysical Research: Solid Earth*, **84**(B12), 6840–6848.

Chulick, G. S., Detweiler, S., & Mooney, W. D., 2013. Seismic structure of the crust and uppermost mantle of south america and surrounding oceanic basins, *Journal of South American Earth Sciences*, **42**(0), 260 – 276.

Colli, L., Fichtner, A., & Bunge, H.-P., 2013. Full waveform tomography of the upper mantle in the south atlantic region: Imaging a westward fluxing shallow asthenosphere?, *Tectonophysics*, **604**, 26–40, cited By (since 1996)1.

Colli, L., Stotz, I., Bunge, H.-P., Smethurst, M., Clark, S., Iaffaldano, G., Tassara, A., Guillocheau, F., & Bianchi, M., 2014. Rapid South Atlantic spreading changes and coeval vertical motion in surrounding continents: Evidence for temporal changes of pressure-driven upper mantle flow, *Tectonics*, **33**(7), 1304–1321.

Crosby, A., McKenzie, D., & Sclater, J., 2006. The relationship between depth, age and gravity in the oceans, *Geophysical Journal International*, **166**(2), 553–573.

Danesi, S. & Morelli, A., 2000. Group velocity of Rayleigh waves in the Antarctic region, *Physics of the Earth and Planetary Interiors*, **122**(1-2), 55–66.

Di Luccio, F. & Pasyanos, M., 2007. Crustal and upper-mantle structure in the eastern mediterranean from the analysis of surface wave dispersion curves, *Geophysical Journal International*, **169**(3), 1139–1152.

Doin, M.-P. & Fleitout, L., 1996. Thermal evolution of the oceanic lithosphere: An alternative view, *Earth and Planetary Science Letters*, **142**(1-2), 121–136.

Duennebier, F. & Sutton, G., 1995. Fidelity of ocean bottom seismic observations, *Marine Geophysical Researches*, **17**(6), 535–555.

Duncan, R. & Green, D., 1980. Role of multistage melting in the formation of oceanic crust, *Geology*, **8**(1), 22–26.

Dunn, R. & Toomey, D., 2001. Crack-induced seismic anisotropy in the oceanic crust across the East Pacific Rise $9°30'N), EarthandPlanetaryScienceLetters, \mathbf{189}(1-2), 9--17.$

Dziewonski, A., Bloch, S., & Landisman, M., 1969. Technique for the analysis of transient seismic signals, *Bulletin of the Seismological Society of America*, **59**(1), 427–444.

Dziewonski, A., Chou, T.-A., & Woodhouse, J., 1981. Determination of earthquake source parameters from waveform data for studies of global and regional seismicity, *Journal Geophysical Research*, **86**, 2825–2852.

Eaton, D. & Darbyshire, F., 2010. Lithospheric architecture and tectonic evolution of the Hudson Bay region, *Tectonophysics*, **480**(14), 1–22.

Ekström, G., 2011. A global model of love and rayleigh surface wave dispersion and anisotropy, 25-250 s, *Geophysical Journal International*, **187**.

Ekström, G. & Dziewonski, A. M., 1998. The unique anisotropy of the pacific upper mantle, *Nature*, **394**(6689), 168–172.

Ekström, G., Nettles, M., & Dziewonski, A., 2012. The global cmt project 2004-2010: Centroid-moment tensors for 13,017 earthquakes, *Physics of the Earth and Planetary Interiors*, **200-201**.

Faul, U. & Jackson, I., 2005. The seismological signature of temperature and grain size variations in the upper mantle, *Earth and Planetary Science Letters*, **234**(1-2), 119–134.

Feng, M., Assumpção, M., & Van der Lee, S., 2004. Group-velocity tomography and lithospheric s-velocity structure of the South American continent, *Physics of the Earth and Planetary Interiors*, **147**(4), 315–331.

Feng, M., van der Lee, S., & Assumpção, M., 2007. Upper mantle structure of South America from joint inversion of waveforms and fundamental mode group velocities of Rayleigh waves, *Journal of Geophysical Research: Solid Earth*, **112**(B4).

Fischer, K., Ford, H., Abt, D., & Rychert, C., 2010. The lithosphere-asthenosphere boundary, *Annual Review of Earth and Planetary Sciences*, **38**, 551–575.

Fishwick, S., 2010. Surface wave tomography: Imaging of the lithosphere-asthenosphere boundary beneath central and southern Africa?, *Lithos*, **120**(1-2), 63–73.

Fishwick, S. & Crosby, A., 2009. A comparison of surface wave tomography in the atlantic ocean with the plate model: Mismatches and implications for the lithosphere-asthenosphere system, *American Geophysical Union, Fall Meeting*, **ABSTRACT T11E-06**.

Fishwick, S., Heintz, M., Kennett, B. L. N., Reading, A. M., & Yoshizawa, K., 2008. Steps in lithospheric thickness within eastern australia, evidence from surface wave tomography, *Tectonics*, **27**(4).

Flament, N., Gurnis, M., Williams, S., Seton, M., Skogseid, J., Heine, C., & Müller, R., 2014. Topographic asymmetry of the South Atlantic from global models of mantle flow and lithospheric stretching, *Earth and Planetary Science Letters*, **387**, 107–119.

Forsyth, D., 1975. The early structural evolution and anisotropy of the oceanic upper mantle, *Geophysical Journal International*, **43**(1), 103–162.

Forsyth, D., 1977. The evolution of the upper mantle beneath mid-ocean ridges, *Tectonophysics*, **38**(1-2), 89–118.

Gaherty, J., Kato, M., & Jordan, T., 1999. Seismological structure of the upper mantle: A regional comparison of seismic layering, *Physics of the Earth and Planetary Interiors*, **110**(1-2), 21–41.

Gans, C., Beck, S., Zandt, G., Gilbert, H., Alvarado, P., Anderson, M., & Linkimer, L., 2011. Continental and oceanic crustal structure of the Pampean flat slab region, western Argentina, using receiver function analysis: New high-resolution results, *Geophysical Journal International*, **186**(1), 45–58.

Goutorbe, B., 2010. Combining seismically derived temperature with heat flow and bathymetry to constrain the thermal structure of oceanic lithosphere, *Earth and Planetary Science Letters*, **295**(3-4), 390–400.

Gregg, P., Lin, J., Behn, M., & Montési, L., 2007. Spreading rate dependence of gravity anomalies along oceanic transform faults, *Nature*, **448**, 183–187.

Grose, C. J., 2012. Properties of oceanic lithosphere: Revised plate cooling model predictions, *Earth and Planetary Science Letters*, **333**, 250–264.

Harmon, N., Forsyth, D. W., & Weeraratne, D. S., 2009. Thickening of young pacific lithosphere from high-resolution rayleigh wave tomography: A test of the conductive cooling model, *Earth and Planetary Science Letters*, **278**(1?2), 96 – 106.

Heintz, M., Debayle, E., & Vauchez, A., 2005. Upper mantle structure of the South American continent and neighboring oceans from surface wave tomography, *Tectonophysics*, **406**(1-2), 115–139.

Herrin, E. & Goforth, T., 1977. Phase-matched filters: Application to the study of Rayleigh waves, *Bulletin of the Seismological Society of America*, **67**(5), 1259–1275.

Herrmann, R. & Ammon, C., 2002. Computer programs in seismology, surface waves, receiver functions and crustal structure, *Saint Louis University, Saint Louis, Missouri, U.S.A.*.

Hirschmann, M., 2010. Partial melt in the oceanic low velocity zone, *Physics of the Earth and Planetary Interiors*, **179**(1-2), 60–71.

James, D., Assumpção, M., Snoke, J., Ribotta, L., & Kuehnel, R., 1993. Seismic studies of continental lithosphere beneath SE Brazil.

Jordan, T., 1975. The continental tectosphere, *Reviews of Geophysics and Space Physics*, **13**(3), 1–12.

Karato, S., 2012. On the origin of the asthenosphere, *Earth and Planetary Science Letters*, **321-322**, 95–103.

Kawakatsu, H., Kumar, P., Takei, Y., Shinohara, M., Kanazawa, T., Araki, E., & Suyehiro, K., 2009. Seismic evidence for sharp lithosphere-asthenosphere boundaries of oceanic plates, *Science*, **324**(5926), 499–502.

Korenaga, T. & Korenaga, J., 2008. Subsidence of normal oceanic lithosphere, apparent thermal expansivity, and seafloor flattening, *Earth and Planetary Science Letters*, **268**(1-2), 41–51.

Lago, B., Cazenave, A., & Marty, J.-C., 1990. Regional variations in subsidence rate of lithospheric plates: implication for thermal cooling models, *Physics of the Earth and Planetary Interiors*, **61**(3-4), 253–259.

Lay, T. & Wallace, T., 1995 *Modern Global Seismology*.

Lebedev, S., Adam, J.-C., & Meier, T., 2013. Mapping the Moho with seismic surface waves: A review, resolution analysis, and recommended inversion strategies, *Tectonophysics*, **609**, 377–394.

Lee, C.-T., Lenardic, A., Cooper, C., Niu, F., & Levander, A., 2005. The role of chemical boundary layers in regulating the thickness of continental and oceanic thermal boundary layers, *Earth and Planetary Science Letters*, **230**(3-4), 379–395.

Leeds, A. R., Knopoff, L., & Kausel, E. G., 1974. Variations of upper mantle structure under the pacific ocean, *Science*, **186**(4159), 141–143.

Lévěque, J., Debayle, E., & Maupin, V., 1998. Anisotropy in the Indian Ocean upper mantle from Rayleigh- and Love-waveform inversion, *Geophysical Journal International*, **133**(3), 529–540.

Levshin, A., Ritzwoller, M., & Resovsky, J., 1999. Source effects on surface wave group travel times and group velocity maps, *Physics of the Earth and Planetary Interiors*, **115**(3-4), 293–312.

Lodge, A. & Helffrich, G., 2006. Depleted swell root beneath the Cape Verde Islands, *Geology*, **34**(6), 449–452.

Maggi, A., Debayle, E., Priestley, K., & Barruol, G., 2006. Multimode surface waveform tomography of the Pacific Ocean: A closer look at the lithospheric cooling signature, *Geophysical Journal International*, **166**(3), 1384–1397.

Maggi, A., Debayle, E., Priestley, K., & Barruol, G., 2006. Azimuthal anisotropy of the Pacific region, *Earth and Planetary Science Letters*, **250**(1-2), 53–71.

Maupin, V. & Park, J., 2014. Seismic anisotropy: theory and observations, in *Treatise on Geophysics*, Elsevier, Amsterdam.

McKenzie, D., 1967. Some remarks on heat flow and gravity anomalies, *Journal of Geophysical Research*, **72**, 6261–6273.

McKenzie, D. & Bickle, M. J., 1988. The volume and composition of melt generated by extension of the lithosphere, *Journal of Petrology*, **29**(3), 625–679.

McKenzie, D., Jackson, J., & Priestley, K., 2005. Thermal structure of oceanic and continental lithosphere, *Earth and Planetary Science Letters*, **233**(3-4), 337–349.

Miller, M., Bataille, K., Priestley, K., Iwamori, H., & Calisto, I., 2005. Seismic imaging of a subducted ridge, southern Chile, *AGU Fall Meeting Abstracts*, p. A982.

Mocquet, A. & Romanowicz, B., 1990. Three-dimensional structure of the upper mantle beneath the Atlantic Ocean inferred from long-period Rayleigh waves: 2. Inversion, *Journal of Geophysical Research: Solid Earth*, **95**(B5), 6787–6798.

Morgan, J. & Chen, Y., 1993. The genesis of oceanic crust: Magma injection, hydrothermal circulation, and crustal flow, *Journal of Geophysical Research: Solid Earth*, **98**(B4), 6283–6297.

Moschetti, M., Ritzwoller, M., & Shapiro, N., 2007. Surface wave tomography of the western united states from ambient seismic noise: Rayleigh wave group velocity maps, *Geochemistry, Geophysics, Geosystems*, **8**(8).

Müller, R., Sdrolias, M., Gaina, C., & Roest, W., 2008. Age, spreading rates, and spreading asymmetry of the world's ocean crust, *Geochemistry, Geophysics, Geosystems*, **9**(4).

Mutter, J. & Carton, H., 2013. The Mohorovicic discontinuity in ocean basins: Some observations from seismic data, *Tectonophysics*, **609**, 314–330.

Neo, N., Yamazaki, S., & Miyashita, S., 2009. Data report: bulk rock compositions of samples from the iodp expedition 309/312 sample pool, odp hole 1256d, *Proceedings of the Integrated Ocean Drilling Program*, **309/312**.

Nettles, M. & Dziewonski, A., 2008. Radially anisotropic shear velocity structure of the upper mantle globally and beneath North America, *Journal of Geophysical Research B: Solid Earth*, **113**(2).

Nowacki, A., Kendall, J.-M., & Wookey, J., 2012. Mantle anisotropy beneath the Earth's mid-ocean ridges, *Earth and Planetary Science Letters*, **317-318**, 56–67.

O'Reilly, S., Zhang, M., Griffin, W., Begg, G., & Hronsky, J., 2009. Ultradeep continental roots and their oceanic remnants: A solution to the geochemical 'mantle reservoir' problem?, *Lithos*, **112, Supplement 2**, 1043 – 1054.

Oxburgh, E. & Turcotte, D., 1969. Increased estimate for heat flow at oceanic ridges [5], *Nature*, **223**(5213), 1354–1355.

Parsons, B. & Sclater, J., 1977. An analysis of the variation of ocean floor bathymetry and heat flow with age, *Journal Geophysical Research*, **82**(2), 803–827.

Pasyanos, M., 2010. Lithospheric thickness modeled from long-period surface wave dispersion, *Tectonophysics*, **481**(1-4), 38–50.

Pasyanos, M. & Nyblade, A., 2007. A top to bottom lithospheric study of Africa and Arabia, *Tectonophysics*, **444**(1-4), 27–44.

Pilidou, S., Priestley, K., Debayle, E., & Gudmundsson, Ó., 2005. Rayleigh wave tomography in the north atlantic: high resolution images of the iceland, azores and eifel mantle plumes, *Lithos*, **79**(3?4), 453 – 474, Mantle Plumes: Physical Processes, Chemical Signatures, Biological Effects.

Richardson, R., 1992. Ridge forces, absolute plate motions, and the intraplate stress field, *Journal of Geophysical Research: Solid Earth*, **97**(B8), 11739–11748.

Ritzwoller, M., Shapiro, N., & Zhong, S.-J., 2004. Cooling history of the Pacific lithosphere, *Earth and Planetary Science Letters*, **226**(1-2), 69–84.

Romanowicz, B., 2009. The thickness of tectonic plates, *Science*, **324**(5926), 474–476.

Russell, D., Herrmann, R., & Hwang, H., 1988. Application of frequency variable filters to surface wave amplitude analysis, *Bulletin of the Seismological Society of America*, **78**(1), 339–353.

Rychert, C. & Shearer, P., 2009. A global view of the lithosphere-asthenosphere boundary, *Science*, **324**(5926), 495–498.

Sclater, J., Parsons, B., & Jaupart, C., 1981. Oceans and continents: Similarities and differences in the mechanisms of heat loss, *Journal of Geophysical Research*, **86**(B12), 11535–11552.

Shapiro, N. & Singh, S., 1999. A systematic error in estimating surface-wave group velocity dispersion curves and a procedure for its correction, *Bulletin of the Seismological Society of America*, **89**(1), 1138–1142.

Shearer, P., 2009. *Introduction to Seismology*, Cambridge University Press.

Silveira, G. & Stutzmann, E., 2002. Anisotropic tomography of the Atlantic Ocean, *Physics of the Earth and Planetary Interiors*, **132**(4), 237–248.

Silveira, G., Stutzmann, E., Griot, D.-A., Montagner, J.-P., & Victor, L., 1998. Anisotropic tomography of the Atlantic Ocean from Rayleigh surface waves, *Physics of the Earth and Planetary Interiors*, **106**(3-4), 257–273.

Singh, D., 1988. Crust and upper-mantle velocity structure beneath the northern and central Indian Ocean from the phase and group velocity of Rayleigh and Love waves, *Physics of the Earth and Planetary Interiors*, **50**(3), 230–239.

Singh, D., 2005. Rayleigh-wave group-velocity studies beneath the Indian Ocean, *Bulletin of the Seismological Society of America*, **95**(2), 502–511.

Sleep, N., 2005. Evolution of the continental lithosphere, *Annual Review of Earth and Planetary Sciences*, **33**, 369–393.

Souza, J. L. D., 1996. S wave velocity in the south atlantic oceanic lithosphere, *Anais da Academia Brasileira de Ciencias*, **68**(1), 41–64.

Stein, C. & Stein, S., 1992. A model for the global variation in oceanic depth and heat flow with lithospheric age, *Nature*, **359**(6391), 123–129.

Stein, S. & Wysession, M., 2008. Blackwell Publishing.

Tang, Q. & Zheng, C., 2013. Crust and upper mantle structure and its tectonic implications in the South China Sea and adjacent regions, *Journal of Asian Earth Sciences*, **62**, 510–525.

Tibi, R., Larson, A., Nyblade, A., Shore, P., Wiens, D., Nnange, J., Tabos, C., & Bekoa, A., 2005. A broadband seismological investigation of the Cameroon Volcanic Line, *EOS. Transactions of the American Geophysical Union*, **86**(1), Abstract S11B–0170.

Tong, C., White, R., Warner, M., & Group, A. W., 2004. Effects of tectonism and magmatism on crack structure in oceanic crust: A seismic anisotropy study, *Geology*, **32**(1), 25–28.

Torsvik, T., Rousse, S., Labails, C., & Smethurst, M., 2009. A new scheme for the opening of the South Atlantic Ocean and the dissection of an Aptian salt basin, *Geophysical Journal International*, **177**(3), 1315–1333.

Trampert, J. & Woodhouse, J., 2003. Global anisotropic phase velocity maps for fundamental mode surface waves between 40 and 150 s, *Geophysical Journal International*, **154**(1), 154–165.

Turcotte, D. & Oxburgh, E., 1967. Finite amplitude convective cells and continental drift, *Journal of Fluid Mechanics*, **28**(1), 29–42.

Turcotte, D. & Schubert, G., 2002. *Geodynamics, Second Edition*, Cambridge University Press.

Wang, G.-Q., Tang, G.-Q., Boore, D. M., Burbach, G. V. N., Jackson, C. R., Zhou, X.-Y., & Lin, Q.-L., 2006. Surface waves in the western taiwan coastal plain from an aftershock of the 1999 chi-chi, taiwan, earthquake, *Bulletin of the Seismological Society of America*, **96**(3), 821–845.

Wegener, A., 1966. *The Origin of Continents and Oceans*, Dover Earth Science Series, Dover Publications.

White, R., 1988. The earth's crust and lithosphere, *Journal of Petrology*, **Special Volume**(1), 1–10.

Wiens, D., 1998. Seismic experiment in Patagonia and Antarctica (SEPA), *IRIS Newsletter*, (17), 9–11.

Winterbourne, J., Crosby, A., & White, N., 2009. Depth, age and dynamic topography of oceanic lithosphere beneath heavily sedimented Atlantic margins, *Earth and Planetary Science Letters*, **287**(1-2), 137–151.

Yoshii, T., 1975. Regionality of group velocities of Rayleigh waves in the Pacific and thickening of the plate, *Earth and Planetary Science Letters*, **25**(3), 305–312.

Yu, G.-K. & Mitchell, B. J., 1979. Regionalized shear velocity models of the pacific upper mantle from observed love and rayleigh wave dispersion, *Geophysical Journal International*, **57**(2), 311–341.

Zhang, Y.-S. & Lay, T., 1999. Evolution of oceanic upper mantle structure, *Physics of the Earth and Planetary Interiors*, **114**(1), 71–80.

Zoback, M., Zoback, M., Adams, J., Assumpção, M., Bell, S., Bergman, E., Blümling, P., Brereton, N., Denham, D., Ding, J., Fuchs, K., Gay, N., Gregersen, S., Gupta, H., Gvishiani, A., Jacob, K., Klein, R., Knoll, P., Magee, M., Mercier, J., Müller, C., Paquin, C., Rajendran, K., Stephansson, O., Suarez, G., Suter, M., Udias, A., Xu, Z., & Zhizhin, M., 1989. Global patterns of tectonic stress, *Nature*, **341**, 291–298.